

© 2013

Robert Raymond Lindner

ALL RIGHTS RESERVED

# THE GROWTH OF MASSIVE GALAXIES AND CLUSTERS AT HIGH REDSHIFT

by

ROBERT RAYMOND LINDNER

A dissertation submitted to the  
Graduate School—New Brunswick  
Rutgers, The State University of New Jersey  
in partial fulfillment of the requirements  
for the degree of  
Doctor of Philosophy  
Graduate Program in Physics and Astronomy

Written under the direction of

Andrew J. Baker

and approved by

---

---

---

---

---

New Brunswick, New Jersey

October, 2013

## ABSTRACT OF THE DISSERTATION

# The Growth of Massive Galaxies and Clusters at High Redshift

by Robert Raymond Lindner

Dissertation Director: Andrew J. Baker

Massive galaxies and galaxy clusters gain much of their mass by merging with their neighbors; this hierarchical structure formation is the foundation of our understanding of galaxy evolution. Nevertheless, the detailed evolutionary processes needed to form the structures we see in the local Universe remain poorly understood. This thesis comprises four projects examining the growth of galaxies and clusters at high redshift by using radio, sub/millimeter, and X-ray observations to provide empirical constraints on their cosmic evolution. Chapter 2 presents deep 1.2 mm imaging of the inner  $20' \times 20'$  of the Lockman Hole North (LHN) field to search for submillimeter galaxies (SMGs), rapidly star-forming, high-redshift galaxy mergers. We detect 41 SMGs with  $S/N > 4.0$  and use Monte Carlo simulations to estimate their number counts and angular clustering properties. Chapter 3 investigates the nuclear accretion properties of the LHN SMGs. In the sample's average rest-frame X-ray spectrum, we detect strong  $\text{Fe K}\alpha$  emission (equivalent width  $\text{EW} \gtrsim 1 \text{ keV}$ ) from highly-ionized Fe species – evidence

that beneath the galaxies’ heavy obscuration, supermassive black holes may be growing rapidly. Chapter 4 describes a new 345 GHz and 2.1 GHz imaging campaign to study the intracluster media (ICM) of eleven massive Sunyaev Zel’dovich Effect (SZE)-detected clusters from the Atacama Cosmology Telescope (ACT) southern survey. In six of eleven, 345 GHz SZE increments are detected and used to characterize the spatial distribution and energy content of the ICM at high ( $19.2''$ ) resolution. This work helps us understand how SZE-mass scaling relations are affected by contamination from other sources along the line of sight and by dynamical properties of the ICM. Chapter 5 studies the non-thermal radio emission in one exceptional  $z = 0.870$  binary cluster merger (ACTJ0102-4915, “El Gordo”) with the help of newly-acquired radio observations. El Gordo is the highest-redshift cluster known to host double radio “relics” and a radio “halo,” and by characterizing the morphology, intensity, spectral index, and polarization of these structures, we extend our knowledge of ICM shocks and magnetic fields to an era when the Universe was only  $\simeq 50\%$  its current age.



## Acknowledgements

I would like to first thank my research adviser, Andrew Baker. Even in the potentially infinite expanses of the Universe, one cannot find a better role model and mentor of all things science and career related.

Thank you Jack Hughes, Chuck Keeton, Ron Gilman, and David Spergel for reading and commenting on my thesis, and Alain Omont and Jack Hughes for writing letters of recommendation on my behalf during job season. I would like to thank the Rutgers faculty for always being available and eager to help think through a research idea or a homework problem, and the Rutgers graduate student cohort, especially fellow radio astronomer Chelsea Sharon, for so many helpful science conversations over the years.

I would not be here finishing my Ph.D. if it were not for the love and support of my parents Jim and Gail Lindner, who have always and relentlessly encouraged me to pursue my interests. To my parents, thank you.

A special heartfelt gratitude is for my wife and best friend, Alison Lindner, who supports me unconditionally and forever stands by my side.

Portions of this dissertation have been published or will be published in the near future. Chapters 2 and 3 are published as Lindner et al. (2011) and Lindner et al. (2012), respectively, and I would like to thank my coauthors in these works (Andrew Baker, Alain Omont, Alexandre Beelen, Frazer Owen, Frank Bertoldi, Herve Dole, Nicolas Fiolet, Andrew Harris, Rob Ivison, Carol Lonsdale, Dieter Lutz, and Mari Polletta). Chapters 4 and 5 are in preparation as Lindner et al. (2013a) and Lindner et al. (2013b), respectively, and I would like to thank my closest collaborators in

these works (Paula Aguirre, Andrew Baker, Nick Battaglia, Filiberto Braglia, Sudeep Das, Neeraj Gupta, Carlos Hernández Monteagudo, Jack Hughes, Polo Infante, Kenda Knowles, Marcos Lima, Toby Marriage, Felipe Menanteau, Karl Menten, Kavi Moodley, Erik Reese, Neelima Sehgal, Jon Sievers, Raghunathan Srianand, and Axel Weiss). I would especially like to thank Paula Aguirre, Neeraj Gupta, and Toby Marriage for their help and guidance. Chapter 4 makes use of observations from the Atacama Cosmology Telescope (ACT); I very much appreciate the hard work and insights of all my fellow members of the ACT collaboration. Finally, I would like to thank Melanie Johnston-Hollitt and Reinout van Weeren for helpful discussions, and Kenda Knowles, Breezy Ocaña, Shane O’Sullivan, Raghunathan Srianand and Robin Wark for help with observations.

This work has been supported by NSF grants AST-0708653, AST-0955810, and a GAANN fellowship.

# Table of Contents

<b>Abstract</b> . . . . .	ii
<b>Acknowledgements</b> . . . . .	iv
<b>List of Figures</b> . . . . .	xiii
<b>List of Abbreviations</b> . . . . .	xvii
<b>1. Introduction</b> . . . . .	1
1.1. Cosmology background . . . . .	2
1.1.1. The expanding Universe . . . . .	2
1.1.2. Hierarchical structure formation . . . . .	4
1.1.3. Distance measures . . . . .	5
1.1.4. Flux density . . . . .	7
1.1.5. The k-correction . . . . .	8
1.1.6. Flux density versus luminosity . . . . .	8
1.2. Galaxies . . . . .	10
1.2.1. Galaxy types . . . . .	10
1.2.2. Star formation . . . . .	11
1.2.3. Nuclear accretion . . . . .	13
Active galactic nuclei . . . . .	14
Fe K $\alpha$ emission in AGNs . . . . .	15
The M- $\sigma$ relation in local galaxies . . . . .	18
1.2.4. Thermal dust emission . . . . .	18

1.2.5.	Synchrotron radiation . . . . .	20
1.2.6.	Radio-IR correlation in star-forming galaxies . . . . .	21
1.2.7.	Submillimeter galaxies (SMGs) . . . . .	23
	The negative k-correction in SMGs . . . . .	24
	Constraining models of galaxy evolution with SMG surveys . . .	26
1.3.	Galaxy clusters . . . . .	27
1.3.1.	Anatomy of a cluster . . . . .	27
	The dark matter halo . . . . .	27
	The intracluster medium . . . . .	28
	The cluster galaxies . . . . .	28
1.3.2.	The Sunyaev Zel'dovich effect . . . . .	29
1.3.3.	Galaxy clusters as cosmological probes . . . . .	31
1.3.4.	Galaxy clusters as gravitational lenses . . . . .	32
1.3.5.	Nonthermal emission in galaxy clusters . . . . .	33
	Spectral aging . . . . .	34
	Rotation measure . . . . .	36
<b>2.</b>	<b>A Deep 1.2 mm Map of the Lockman Hole North . . . . .</b>	<b>37</b>
2.1.	Introduction . . . . .	37
2.2.	Observations . . . . .	40
2.3.	Data reduction . . . . .	43
2.3.1.	Signal maps . . . . .	43
2.3.2.	Noise maps . . . . .	44
2.3.3.	Simulated maps . . . . .	48
2.4.	$P(D)$ analysis of the pixel flux distribution . . . . .	49
2.5.	Analysis of bright sources . . . . .	58

2.5.1.	Source extraction . . . . .	58
2.5.2.	Comparison of results for best and full maps . . . . .	64
2.5.3.	Confusion . . . . .	69
2.5.4.	Spurious sources . . . . .	70
2.5.5.	Completeness . . . . .	72
2.5.6.	Flux boosting . . . . .	73
2.5.7.	Direct calculation of number counts . . . . .	77
2.5.8.	Clustering . . . . .	77
2.6.	Counterpart identification . . . . .	83
2.6.1.	20 cm radio counterparts . . . . .	83
2.6.2.	50 cm radio counterparts . . . . .	84
2.6.3.	90 cm radio counterparts . . . . .	85
2.6.4.	24 $\mu$ m counterparts . . . . .	85
2.6.5.	X-ray counterparts . . . . .	85
2.7.	Discussion . . . . .	86
2.7.1.	Number counts vs. previous deep fields . . . . .	86
2.7.2.	Fractional counterpart identification . . . . .	89
2.7.3.	Redshift distribution . . . . .	92
2.7.4.	Spatial correlation with 20 cm sources . . . . .	97
2.7.5.	Resolving the 1.2 mm CIB . . . . .	98
2.8.	Conclusions . . . . .	100
2.9.	Appendix: Notes on individual detections . . . . .	101
2.9.1.	MM J104700.1+590109 = ID # 1 . . . . .	101
2.9.2.	MM J104631.4+585056 = ID # 3 . . . . .	102
2.9.3.	MM J104638.4+585613 = ID # 6 . . . . .	102

2.9.4.	MM J104704.9+585008 = ID # 9 . . . . .	103
2.9.5.	MM J104556.5+585317 = ID # 11 . . . . .	103
2.9.6.	MM J104728.3+585213 = ID # 15 . . . . .	103
2.9.7.	MM J104610.4+590242 = ID # 17 . . . . .	105
2.9.8.	MM J104617.0+585444 = ID # 20 . . . . .	105
2.9.9.	MM J104522.8+585558 = ID # 26 . . . . .	105
2.9.10.	MM J104620.9+585434 = ID # 28 . . . . .	105
2.9.11.	MM J104556.1+590914 = ID # 29 . . . . .	107
2.9.12.	MM J104539.6+585419 = ID # 32 . . . . .	108
2.9.13.	MM J104608.1+590744 = ID # 36 . . . . .	108
2.9.14.	MM J104610.8+585242 = ID # 37 . . . . .	108
2.9.15.	MM J104611.9+590231 = ID # 39 . . . . .	108

### 3. Detection of Iron $K\alpha$ Emission from a Complete Sample of

<b>Submillimeter Galaxies</b> . . . . .	109
3.1. Introduction . . . . .	109
3.2. Data and Sample Selection . . . . .	111
3.2.1. Millimeter observations and stacking sample . . . . .	111
3.2.2. <i>Chandra</i> ACIS-I Observations . . . . .	112
3.3. Stacking Analysis . . . . .	113
3.3.1. Image-based stacking . . . . .	113
3.3.2. Optimized broad-band stacking . . . . .	114
3.3.3. Optimized spectral stacking . . . . .	118
3.3.4. Estimating $L_X$ and $L_{\text{Fe}K\alpha}$ . . . . .	124
3.4. Obscuration and Star Formation Rate . . . . .	125
3.5. Discussion . . . . .	129

3.5.1.	Comparison to previous surveys . . . . .	129
	Detection rate . . . . .	129
	$L_{\text{Fe K}\alpha}$ vs. $L_{\text{IR}}$ vs. $L_{20\text{ cm}}$ . . . . .	131
	Fe K $\alpha$ emission properties . . . . .	132
3.5.2.	Origin of the Fe K $\alpha$ emission . . . . .	137
	Supernovae . . . . .	137
	Galactic-scale winds . . . . .	139
	AGN activity . . . . .	140
3.6.	Conclusions . . . . .	143
3.7.	Appendix . . . . .	144
3.7.1.	Detailed descriptions of calculations . . . . .	144
	Optimized spectral stacking method . . . . .	144
	Fe K $\alpha$ energy flux . . . . .	145
<b>4.</b>	<b>The LABOCA/ACT Survey of Clusters at All Redshifts . . . . .</b>	<b>146</b>
4.1.	Introduction . . . . .	146
4.2.	Cluster sample . . . . .	149
4.3.	Observations and data reduction . . . . .	149
4.3.1.	345 GHz APEX/LABOCA . . . . .	149
	LABOCA observations . . . . .	151
	LABOCA data reduction . . . . .	153
	Iterative multi-scale algorithm . . . . .	155
	Systematic uncertainties of iterative pipeline . . . . .	157
4.3.2.	148 GHz and 218 GHz ACT . . . . .	161
4.3.3.	2.1 GHz ATCA . . . . .	162
	ATCA Observations . . . . .	162

4.3.4.	<i>Herschel</i> /SPIRE observations . . . . .	164
4.3.5.	The Sunyaev Zel’dovich effect . . . . .	165
4.4.	Point source contamination . . . . .	166
4.4.1.	Radio sources . . . . .	166
	2.1 GHz number counts . . . . .	167
	Radio contamination extrapolated to 148 GHz . . . . .	168
4.4.2.	SMGs . . . . .	173
4.5.	Peculiar velocities . . . . .	174
4.6.	Conclusions . . . . .	180
4.7.	Appendix . . . . .	180
4.7.1.	“La Flaca” and El Gordo . . . . .	180
 <b>5. The Radio Halo and Relics of El Gordo, a Massive <math>z = 0.870</math> Cluster</b>		
	<b>Merger . . . . .</b>	<b>183</b>
5.1.	Introduction . . . . .	183
5.2.	ACT J0102-4915, “El Gordo” . . . . .	185
5.3.	Observations and data reduction . . . . .	186
5.3.1.	2.1 GHz ATCA . . . . .	186
5.3.2.	610 MHz GMRT . . . . .	188
5.4.	Radio relics . . . . .	188
5.4.1.	Geometries . . . . .	190
5.4.2.	Spectral indices . . . . .	190
5.4.3.	Rotation measure and $B_{\parallel}$ . . . . .	194
5.4.4.	Polarization . . . . .	198
5.4.5.	Shock properties and $B_{\perp}$ . . . . .	201
5.5.	Radio halo . . . . .	202



5.5.1. Geometry . . . . .	205
5.5.2. Spectral index . . . . .	206
5.5.3. Luminosity . . . . .	209
5.6. Conclusions . . . . .	209
<b>6. Conclusions . . . . .</b>	<b>212</b>

## List of Figures

1.1. Hierarchical merger tree . . . . .	5
1.2. Hierarchical structure in the Millenium Simulation . . . . .	6
1.3. Elliptical and spiral galaxies . . . . .	11
1.4. Anatomy of an active galactic nucleus (AGN) . . . . .	16
1.5. X-ray photoelectric absorption . . . . .	17
1.6. Thermal dust spectra versus redshift . . . . .	25
1.7. The Sunyaev Zel’dovich effect . . . . .	31
2.1. MAMBO 1.2 mm S/N map . . . . .	45
2.2. MAMBO 1.2 mm weight map . . . . .	46
2.3. Pixel flux distributions of MAMBO 1.2 mm S/N maps . . . . .	48
2.4. Effective MAMBO point spread function (PSF) . . . . .	50
2.5. Pixel flux distribution in MAMBO 1.2 mm map . . . . .	52
2.6. Likelihood spaces for parametrized number counts . . . . .	56
2.7. Uncertainties in the positions of extracted SMGs . . . . .	59
2.8. Change in S/N for 17 sources common to “best” and “full” maps . . . . .	66
2.9. Flux density comparison for the 17 highest S/N detections . . . . .	67
2.10. Flux density comparison for on-off and on-the-fly observing modes . . . . .	68
2.11. Spurious detections as a function of S/N within noise maps. . . . .	71
2.12. Completeness as a function of flux density . . . . .	73
2.13. Deboosted posterior probability distributions . . . . .	75

2.14. Monte Carlo simulation to test Bayesian flux boosting corrections . . . .	76
2.15. Integral and differential 1.2 mm number counts . . . . .	78
2.16. Landy-Szalay correlation function estimator $w(\theta)$ . . . . .	81
2.17. Integral distribution of nearest neighbors . . . . .	82
2.18. 50/20 cm spectral index vs. 20 cm flux density for SMG radio counterparts.	93
2.19. 350/1.4 GHz spectral index versus redshift . . . . .	95
2.20. Redshift distribution of significant detections . . . . .	96
2.21. MAMBO source positions versus 20 cm radio source density . . . . .	99
2.22. MAMBO source MM J104631.4+585056 = ID # 03 . . . . .	102
2.23. MAMBO source MM J104728.3+585213 = ID # 15 . . . . .	104
2.24. MAMBO sources MM J104610.4+590242 (ID # 17) and MM J104611.9+590231 (ID # 39) . . . . .	106
2.25. MAMBO source MM J104556.1+590914 = ID # 29 . . . . .	107
3.1. SMG positions inside the LHN compared to <i>Chandra</i> X-ray depth . . .	112
3.2. Stacked X-ray images in the <i>Chandra</i> energy bands . . . . .	114
3.3. Stacked S/N versus broadening kernel size $\sigma_{\text{kernel}}$ . . . . .	116
3.4. Redshift distribution of stacking sample . . . . .	119
3.5. Stacked observed-frame X-ray spectrum . . . . .	121
3.6. Stacked rest-frame X-ray spectrum . . . . .	122
3.7. Bootstrap-Monte Carlo analysis of Fe K $\alpha$ counts . . . . .	123
3.8. X-ray luminosity versus infrared luminosity . . . . .	133
3.9. X-ray luminosity versus 20 cm spectral power . . . . .	134
3.10. S/N of Fe K $\alpha$ emission versus bin position and width . . . . .	136
3.11. Fe K $\alpha$ line luminosity $L_{\text{K}\alpha}$ versus $L_{\text{IR}}$ . . . . .	138
4.1. APEX/LABOCA spiral sampling pattern . . . . .	152

4.2. LABOCA focal plane . . . . .	154
4.3. LABOCA iterative pipeline performance . . . . .	155
4.4. LABOCA 345 GHz maps . . . . .	158
4.5. Iterative pipeline transfer function efficiency . . . . .	160
4.6. 2.1 GHz number counts . . . . .	169
4.7. 2.1 GHz number counts vs. angular radius . . . . .	170
4.8. 2.1 GHz number counts vs. physical radius . . . . .	171
4.9. Radio source spectral index distribution . . . . .	172
4.10. Best-fit SZE spectra . . . . .	178
4.11. $Y'_{\text{SZ}}$ vs. $v_p$ likelihood . . . . .	179
4.12. Spectral energy distribution for “La Flaca” . . . . .	181
5.1. 2.1 GHz ATCA image of El Gordo . . . . .	187
5.2. 610 GHz GMRT image of El Gordo . . . . .	189
5.3. Spectral index ( $\alpha_{610}^{2.1}$ ) map of the NW relic . . . . .	192
5.4. Spectral index ( $\alpha_{1.6}^{2.6}$ ) map of the NW relic . . . . .	193
5.5. Spectral index ( $\alpha_{610}^{2.1}$ ) map of the E and SE relics . . . . .	193
5.6. Rotation measure transfer function . . . . .	195
5.7. Integrated RM synthesis spectrum for the NW relic . . . . .	197
5.8. Rotation measure of NW relic . . . . .	198
5.9. Polarization fraction of the NW relic . . . . .	199
5.10. 2.1 GHz polarization fraction and angle . . . . .	200
5.11. Radial profile of the NW relic . . . . .	203
5.12. Shock width vs. magnetic field strength . . . . .	204
5.13. Radio halo spectral index $\alpha_{610}^{2.1}$ . . . . .	207
5.14. Radio spectral index vs. X-ray gas temperature . . . . .	208

5.15. $L_{1,4}$ vs. $L_X$ . . . . .	210
-------------------------------------	-----

## List of Abbreviations

<b>ACIS</b>	Advanced CCD Imaging Spectrometer
<b>ACT</b>	Atacama Cosmology Telescope
<b>AGN</b>	Active Galactic Nucleus
<b>AIPS</b>	Astronomical Image Processing Software
<b>ALMA</b>	Atacama Large Millimeter/submillimeter Array
<b>APEX</b>	Atacama Pathfinder Experiment
<b>ASTE</b>	Atacama Submillimeter Telescope Experiment
<b>ATCA</b>	Australia Telescope Compact Array
<b>BH</b>	Black Hole
<b>BOA</b>	Bolometer Data Analysis
<b>CABB</b>	Compact Array Broadband Backend
<b>CASA</b>	Common Astronomy Software Applications
<b>CCD</b>	Charge Coupled Device
<b>CDF-N</b>	<i>Chandra</i> Deep Field-North
<b>CDM</b>	Cold Dark Matter
<b>CfA</b>	Center for Astrophysics (Harvard-Smithsonian)
<b>CIAO</b>	Chandra Interactive Analysis of Observations
<b>CIB</b>	Cosmic Infrared Background
<b>CIZA</b>	Clusters in the Zone of Avoidance
<b>CMB</b>	Cosmic Microwave Background
<b>CO</b>	Carbon monoxide
<b>COSMOS</b>	Cosmic Evolution Survey
<b>CXC</b>	<i>Chandra</i> X-ray Center
<b>Dec.</b>	Declination

**ECDF-S** Extended *Chandra* Deep Field-South

**ESO** European Southern Observatory

**EW** Equivalent width

**FIR** Far infrared

**FRMS** Faraday Rotation Measure Synthesis

**FWHM** Full Width at Half Maximum

**GILDAS** Grenoble Imaging and Line Data Analysis

**GOODS-N** Great Observatories Origins Survey - North

**GOODS-S** Great Observatories Origins Survey - South

**GMRT** Giant Meter-wave Radio Telescope

**HerMES** *Herschel* Multi-tiered Extragalactic Survey

**HPBW** Half Power Beam Width

**HR** Hardness ratio

**IC** Index Catalog

**ICM** Intracluster Medium

**IMF** Initial Mass Function

**IR** Infrared

**IRAC** Infrared Array Camera

**IRAM** Institut de Radioastronomie Millimétrique

**IRAS** Infrared Astronomical Satellite

**ISM** Interstellar Medium

**JCMT** James Clerk Maxwell Telescope

**KS** Kolmogorov-Smirnov

**kSZ** kinematic Sunyaev Zel'dovich

**LABOCA** Large APEX Bolometer Camera

**LASCAR** LABOCA/ACT Survey of Clusters at All Redshifts

**LESS** LABOCA survey of the ECDFS Submillimeter Survey

**LHE** Lockman Hole East

**LHN** Lockman Hole North

**LIRG** Luminous Infrared Galaxy

**LST** Local Sidereal Time

**MACS** Massive Cluster Survey

**MAMBO** Max-Planck Millimeter Bolometer Array

**MCMCMH** Markov Chain Monte Carlo Metropolis Hastings

**MHD** Magnetohydrodynamic

**MIPS** Multiband Imaging Photometer

**MPIfR** Max Planck Institute for Radio Astronomy

**NASA** National Aeronautics and Space Administration

**NFW** Navarro-Frenk-White

**NGC** New General Catalog

**NOAO** National Optical Astronomy Observatory

**NSF** National Science Foundation

**PACS** Photodetector Array Camera and Spectrometer

**P(D)** Probability of Fluctuation

**PFD** Pixel Flux Distribution

**PIMMS** Portable Interactive Multi-Mission Simulator

**PSF** Point Spread Function

**QSO** Quasi-Stellar Object

**R.A.** Right Ascension

**RFI** Radio Frequency Interference

**RIAF** Radiatively Inefficient Accretion Flow

**RM** Rotation Measure

**RMTF** Rotation Measure Transfer Function

**RMS** Root Mean Squared

**SAA** Shift-and-Add

**SAD** Search And Destroy



**SCUBA** Submillimeter Common-User Bolometer Array

**SED** Spectral Energy Distribution

**SFR** Star Formation Rate

**SFRD** Star Formation Rate Density

**SHADES** SCUBA Half-Degree Extragalactic Survey

**SMG** Submillimeter Galaxy

**S/N** Signal-to-Noise

**SN** Supernova

**SNR** Signal-to-noise ratio

**SPIRE** Spectral and Photometric Imaging Receiver

**SPT** South Pole Telescope

**SUMSS** Sydney University Molonglo Sky Survey

**SWIRE** *Spitzer* Wide-area Infrared Extragalactic survey

**SXDF** Subari XMM-Newton Deep Field

**SZE** Sunyaev Zel'dovich Effect

**ULIRG** Ultra-luminous infrared galaxy

**VLA** Very Large Array

**WFI** Wide-Field Imager

**WIYN** Wisconsin Indiana Yale NOAO telescope

**WMAP** Wilkinson Microwave Anisotropy Probe

**XMM-Newton** X-ray Multi-Mirror Mission Newton

# Chapter 1

## Introduction

My thesis investigates how massive galaxies and galaxy clusters grow at high redshift, a process that is often associated with merging. At least some of the most massive present-day galaxies formed in rapidly star-forming systems at high redshift, like submillimeter galaxies (SMGs). SMGs are dusty starbursts triggered by mergers of gas-rich progenitor systems. Chapter 2 presents an SMG survey of the Lockman Hole North (LHN) to study the statistical properties of dust-obscured high-redshift starburst galaxies. Chapter 3 examines the X-ray properties of the LHN SMGs using a stacking analysis to search for merger-triggered, concurrent growth of the galaxies' super-massive black holes. Massive galaxy clusters at all redshifts are readily detectable using the distortion they introduce to the cosmic microwave background (CMB), known as the Sunaev Zel'dovich Effect (SZE). Chapter 4 presents submillimeter imaging of the SZE signal of eleven massive galaxy clusters originally detected by the Atacama Cosmology Telescope (ACT) southern survey to investigate how dynamical state and SMG and radio galaxy contamination can affect the SZE signals of massive clusters. In our hierarchical Universe, the most massive clusters also tend to be recent mergers. The energy released in cluster-cluster mergers, the most energetic events since the Big Bang, can produce shocks that can accelerate ultra-relativistic cosmic rays that reveal information about clusters' dynamical states and magnetic field properties. Chapter 5 presents a detailed analysis of the radio halo and relics in one exceptional high-redshift cluster merger. Although systems that are undergoing rapid growth events like mergers and starbursts

are relatively rare compared to their quiescent counterparts, their observational signatures are readily identifiable even at great distances and therefore serve as beacons to help us observe mass assembly at high redshifts where other observables fade away. A summary and conclusions are presented in Chapter 6.

Chapter 1 explains the main concepts and recurring conventions that are used throughout the thesis. Section 1.1 describes the large-scale cosmological properties of the Universe that are important in understanding observations of galaxies and clusters. Sections 1.2 and 1.3 explain the basic properties of galaxies and galaxy clusters, and provide background into the theoretical concepts of each that are important in studying their growth through cosmic time.

## 1.1 Cosmology background

### 1.1.1 The expanding Universe

The early Universe lacked stars and galaxies. Instead, baryonic matter (astronomers' nomenclature for protons, neutrons, *and* electrons) was distributed in a smooth fog of hot plasma. The thermal glow that this primordial plasma emitted, known as the cosmic microwave background (CMB) radiation, still travels through the Universe today and was detected by scientists Arno Penzias and Robert Wilson in New Jersey in 1965 (Penzias & Wilson, 1965). This discovery provided strong support for the “Big Bang” cosmological model, a solution to the dynamical equations of space-time that predicts the Universe (under the assumptions of homogeneity and isotropy on large scales) is undergoing homogeneous expansion.

A useful concept in cosmology is that of the comoving distance. Comoving distance, unlike proper distance which is measured in an inertial frame, is measured on a grid that is fixed in space-time and expanding with the Universe. The size of the Universe at a time  $t$  since the Big Bang is parameterized by the scale factor  $a$ , the ratio of a

proper distance element to a comoving distance element. In the past  $a < 1$ , while  $a = 1$  today. The scale factor is related to the observed cosmological redshift  $z$  by

$$\frac{1}{a} \equiv 1 + z = \frac{\nu_{\text{emit}}}{\nu_{\text{obs}}}, \quad (1.1)$$

where  $\nu_{\text{emit}}$  and  $\nu_{\text{obs}}$  represent, respectively, the frequencies of photons emitted from a source at redshift  $z$  and observed today at  $z = 0$ . The Universe contains three types of energy density that scale differently with the size of the Universe and equivalently the scale factor  $a$ . Matter density  $\rho_m(a) = \rho_{m0} a^{-3}$  scales with volume, radiation density  $\rho_r(a) = \rho_{r0} a^{-4}$  scales with both volume and photon wavelength, and dark energy density  $\rho_\Lambda(a) = \rho_{\Lambda0}$  we assume is constant in time (i.e., a “cosmological constant”);  $\rho_{m0}$ ,  $\rho_{r0}$ , and  $\rho_{\Lambda0}$ , respectively, represent the matter, radiation, and dark energy density today where  $a = 1$ . It is convenient to refer to the  $\rho_i$  in terms of their relative contributions to the critical density of the Universe,  $\rho_{c0} = 3H_0^2/8\pi G$ , as  $\Omega_i = \rho_i/\rho_{c0}$ , where  $G$  is the gravitational constant. The critical density represents the total energy density required to have a geometrically flat Universe. To high precision, our Universe is flat and therefore the total energy density is equal to the critical density.

The expansion rate of the Universe is given by the Hubble parameter  $H(a) \equiv \dot{a}/a$  in units of  $\text{km s}^{-1} \text{Mpc}^{-1}$  ( $1 \text{ Mpc} = 3.09 \times 10^{22} \text{ m}$ ). In a homogeneous and isotropic flat Universe filled with matter, radiation, and dark energy, the expansion rate is given by the Friedmann equation:

$$H^2(z) = H_0^2 [\Omega_m a^{-3} + \Omega_r a^{-4} + \Omega_\Lambda]. \quad (1.2)$$

The Hubble parameter today is  $H_0 = 73.8 \pm 2.4 \text{ km s}^{-1} \text{Mpc}^{-1}$  (Riess et al., 2011).

### 1.1.2 Hierarchical structure formation

The total matter density of the Universe is composed of 16% baryonic matter and 84% dark matter (Planck Collaboration et al., 2013 XVI). Dark matter is gravitating mass that does not interact via the electromagnetic force. Within the expanding space-time, the mutual gravitational attraction of dark matter pulls the mass distribution into clumps. This clumping is seeded by primordial density fluctuations that were established during the earliest moments of the Universe’s existence. Positive density fluctuations attract nearby matter and grow larger as time elapses. Therefore, in contrast to the Universe’s smooth beginnings, the Universe today is heterogeneous and filled with dense, self-gravitating dark matter structures called dark matter halos. Massive galaxies and galaxy clusters live in the centers of massive dark-matter halos.

Over time, small halos merge together to form larger and larger halos. Therefore, the largest objects at any given redshift have only recently been formed through a merging together of smaller objects. This process is known as “hierarchical structure formation” (e.g., Lacey & Cole, 1993). Figure 1.1 illustrates the hierarchical formation of a massive dark matter halo using a merger tree. As time passes, the halo progenitors (branches) merge together to form a single, massive object at  $t = t_0$ . Dark matter halos gain mass predominantly by merging; therefore, galaxy-galaxy and cluster-cluster collisions are common and influential in their respective evolutionary tracks. Violent mergers in the early Universe are important for our understanding of submillimeter galaxies (Chapter 2), and in the study of radio halos and relics in galaxy clusters (Chapter 5).

The theory of dark matter-driven hierarchical structure formation occurring within an expanding dark matter and dark energy-dominated Universe is referred to as the  $\Lambda$  Cold Dark Matter ( $\Lambda$ CDM) model of cosmology.  $\Lambda$ CDM has been very successful in explaining the observed properties of Universe. The predicted mass function of dark matter halos from the early analytic approximation and the  $\sim 10^3$ -particle simulation

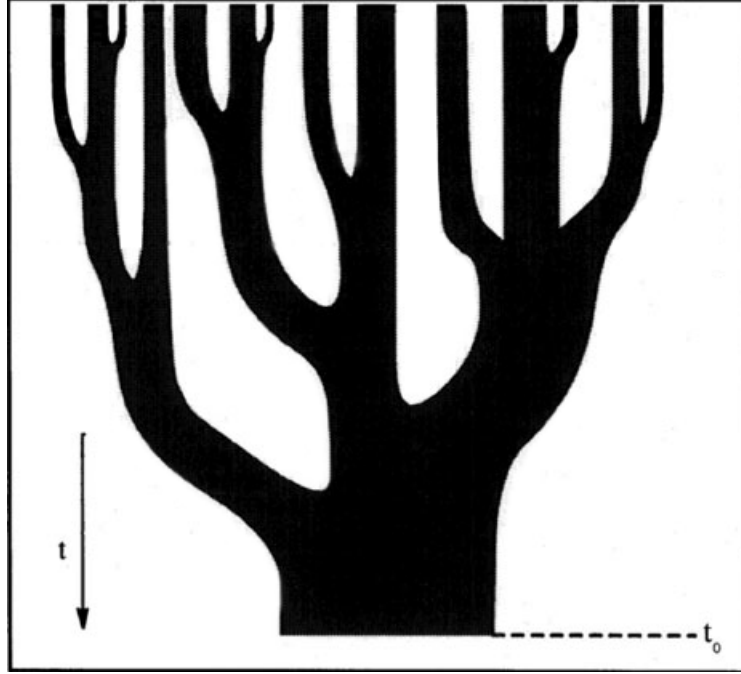


Figure 1.1: Illustration of a dark-matter merger tree from Lacey & Cole (1993). Time advances downwards as progenitor halos merge into one final dark matter halo at  $t = t_0$ .

of Press & Schechter (1974) has held up to observations and remains consistent when compared to more recent predictions using the  $\sim 10^{10}$ -particle simulations from Springel et al. (2005). Figure 1.2 presents a slice through the Springel et al. (2005) “Millenium” simulation at redshift  $z = 0$ , showing hierarchical structure from individual halos up to large-scale cosmic filaments. Large-scale structures like cosmic filaments and voids can be detected by measuring the spatial correlation between galaxies (e.g., Chapter 2). Overall, the  $\Lambda$ CDM theory of cosmology is very successful and can explain all major CMB datasets using only *six* free parameters (Calabrese et al., 2013; Planck Collaboration et al., 2013 XVI).

### 1.1.3 Distance measures

In an expanding Universe, our common intuition of “distance” is unreliable. This section will explain the different types of cosmological distance measures and how they

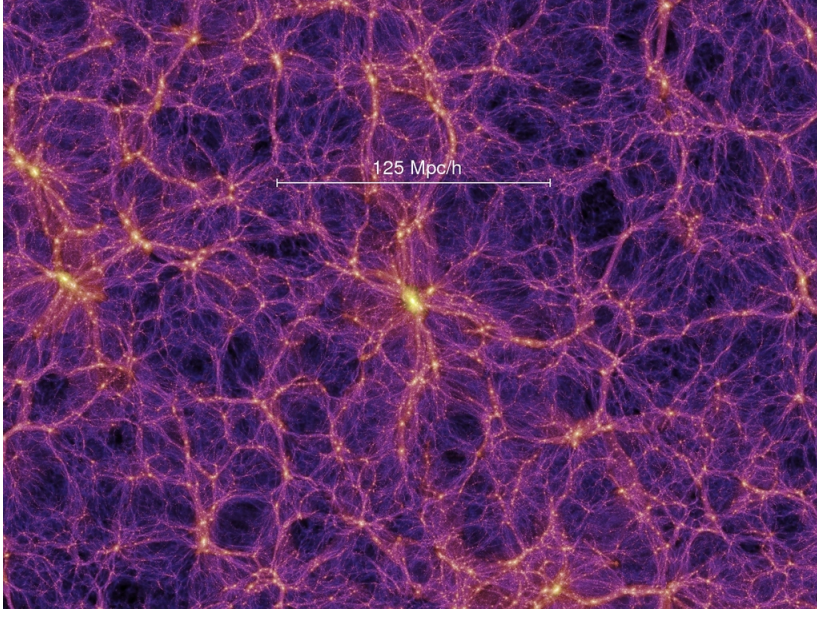


Figure 1.2: Snapshot at  $z = 0$  of a slice through the “Millennium” (Springel et al., 2005) supercomputer simulation of the dark matter distribution in the Universe showing the hierarchical and filamentary distribution of matter on large scales.

are used in observational astrophysics (for a complete review, see Dodelson, 2003).

The most fundamental distance is the comoving distance  $\chi$ , which is measured on an expanding grid that is fixed in space-time. Consequently, even in an expanding Universe, the comoving distance to a galaxy at redshift  $z$  does not change in time, and is equal to the integral of comoving distance elements  $dx = c dt/a$  from  $a(z)$  to  $a(z = 0) = 1$ . With the definition of  $H(a)$  (Equation 1.2), we substitute  $dt = H da/a$  and obtain

$$\chi(a) = \int_a^1 \frac{c da'}{a'^2 H(a')}. \quad (1.3)$$

The angular diameter distance  $D_A$  is the quantity used to relate the apparent angular size  $\theta$  of an object to its physical size  $l$  through the traditional relation  $\theta = l/D_A$ . In a flat Universe, the angular diameter distance to redshift  $z(a)$  can be expressed in terms of  $\chi$  via

$$D_A(a) = a \chi(a). \quad (1.4)$$

Similarly, the luminosity distance  $D_L$  is the quantity used to relate the observed flux  $f$  ( $\text{W m}^{-2}$ ) from a distant emitter to its bolometric power  $L$  (W) through the relation  $f = L/4\pi D_L^2$ . In terms of  $\chi$ ,

$$D_L(a) = \chi(a) / a. \quad (1.5)$$

The relative factor of  $a^2$  between  $D_L$  and  $D_A$  identifies a classically unintuitive relationship between the apparent sizes and the observed fluxes of sources at cosmological distances. For example, at redshifts  $z = 1$  and  $z = 5$  in a standard  $\Lambda$ CDM cosmology, the luminosity distance  $D_L = 6700$  Mpc and  $48000$  Mpc, while  $D_A = 1700$  Mpc and  $1300$  Mpc, respectively. Therefore, the apparent angular size of objects in the Universe is not a steadily decreasing function of redshift, and actually *increases* for  $z \gtrsim 1$ . This behavior of  $D_A$  has important implications for the detectability of SZE-selected galaxy clusters (Chapter 4).

#### 1.1.4 Flux density

The equation above relating the observed flux from a distant source to its bolometric power,  $f = L/4\pi D_L^2$ , assumes that the measurement uses an ideal detector that responds equally to all wavelengths of radiation. In real telescopes, for either engineering or scientific reasons, receivers are only sensitive to radiation within a specified bandpass, e.g., with center frequency  $\nu_{\text{obs}}$  and bandwidth  $\Delta\nu = \nu_2 - \nu_1$ , where  $\nu_2 > \nu_{\text{obs}} > \nu_1$ .

Flux measurements of a particular source will vary from telescope to telescope if their receivers have different bandwidths. Therefore, rather than using flux, the brightness of a source is commonly described using *flux density*  $S$ , the flux per unit bandwidth. Flux density is measured in Jansky ( $\text{Jy} = 10^{-26} \text{ W Hz}^{-1} \text{ m}^{-2}$ ), and does not change for a flat-spectrum source as the telescope bandwidth varies. For sources at cosmological distances, the radiation falling inside a fixed observing bandwidth  $\Delta\nu$  originates from a wider rest-frame bandwidth  $(\Delta\nu)_{\text{rest}} = (1+z)\Delta\nu$ . This redshifted bandwidth serves



to increase the apparent flux density relative to naive expectation of a flat-spectrum source as  $z$  increases.

### 1.1.5 The k-correction

Similar to the difference between flux and flux density, the spectral power  $F$ , or spectral energy distribution (SED), is the bolometric power per unit bandwidth and describes the radiation spectrum of a source. The flux density measured from a source at redshift  $z$  at frequency  $\nu_{\text{obs}}$  probes the source's rest-frame SED at  $\nu = (1 + z)\nu_{\text{obs}}$ . If the SED increases or decreases with  $\nu$ , then varying a source's redshift also varies the location in the rest-frame SED that is probed by observations. The change in apparent brightness due to this mismatch between observed and rest-frame frequencies is called, for historical reasons, the *k-correction*.

To compare the observed flux densities of two galaxies at different redshifts in matching rest-frame bandpasses, one needs to compensate for their different k-corrections. The k-correction is traditionally defined in terms of magnitudes,<sup>1</sup> where the magnitude  $m$  at frequency  $\nu$  is given by  $m = -2.5 \log(S_\nu/S_0)$ . Therefore, a positive k-correction decreases the observed brightness, and a negative k-correction increases the brightness. The k-correction is important in the study of submillimeter galaxies because their SEDs in the spectral regions probed by submillimeter observations are rapidly increasing functions of frequency (see Section 1.2.7).

### 1.1.6 Flux density versus luminosity

After taking into account the redshifted bandwidth and the k-correction, the final expression for the average flux density within bandwidth  $\Delta\nu = \nu_2 - \nu_1$ , centered on  $\nu_{\text{obs}}$ ,

---

<sup>1</sup> Magnitudes are *relative* quantities defined in terms of a reference flux density value  $S_{\nu 0}$ . The SED of the star Vega (Vega magnitudes) and the constant value of 3631 Jy (AB magnitudes) define common reference values.

of a source with rest-frame spectral power  $F(\nu)$  [ $\text{W Hz}^{-1}$ ] at redshift  $z$  is

$$S_\nu = \frac{(1+z)}{4\pi D_L^2} \frac{1}{\Delta\nu} \int_{\nu_1}^{\nu_2} F[(1+z)\nu'] d\nu', \quad (1.6)$$

where the bolometric power  $L = \int_{-\infty}^{+\infty} F(\nu') d\nu'$ .

If the bandwidth is very narrow compared to the scale of variation in the SED, then the integral in equation 1.6 can be approximated as

$$\lim_{\Delta\nu \rightarrow 0} \frac{1}{\Delta\nu} \int_{\nu-\Delta\nu/2}^{\nu+\Delta\nu/2} F[(1+z)\nu'] d\nu' = \int_{-\infty}^{+\infty} \delta(\nu' - \nu) F[(1+z)\nu'] d\nu' \quad (1.7)$$

$$= F[(1+z)\nu], \quad (1.8)$$

giving

$$S_\nu = \frac{(1+z)}{4\pi D_L^2} F[(1+z)\nu]. \quad (1.9)$$

For a power-law-shaped SED of the form  $F(\nu) = F_0 \nu^{-\alpha}$ ,  $F[(1+z)\nu] = (1+z)^{-\alpha} F(\nu)$ , and Equation 1.9 becomes

$$S_\nu = \frac{1}{4\pi D_L^2} F(\nu) (1+z)^{1-\alpha}. \quad (1.10)$$

This formulation is useful in the study of high-redshift star-forming galaxies because the submillimeter and radio portions of their spectra are well-described by power-law functions. The submillimeter power law is from the Rayleigh-Jeans regime of thermal dust emission (Section 1.2.4), and the radio power law is from synchrotron radiation (Section 1.2.5). When the SED of a source can be described by  $F \propto \nu^{-\alpha}$ ,  $\alpha$  is called the spectral index. The two-point spectral index between two frequencies  $\nu_1$  and  $\nu_2$ , given by  $\alpha = -\log(S_{\nu_1}/S_{\nu_2})/\log(\nu_1/\nu_2)$  can also be used as a measure of the effective spectral shape of a source whether or not the SED really is a single power law.

## 1.2 Galaxies

$\Lambda$ CDM is successful in explaining the large-scale, statistical properties of the Universe. A great challenge remains in explaining the formation and relative abundances of galaxies of different types, masses, and compositions. Galaxy properties like these are influenced by smaller-scale astrophysics like star formation, black hole accretion, mergers, and supernovae, which are poorly understood compared to cosmological dynamics. In this section, we discuss some important processes that occur in galaxies.

### 1.2.1 Galaxy types

In approximate order of mass fraction, galaxies are composed of dark matter, stars, gas, dust, and a central super-massive black hole. The first galaxies formed when the primordial gas of the early Universe accreted onto dark matter halos. Since this time, hierarchical merging, continued gas accretion, and small-scale astrophysics has guided the evolution of galaxies. Galaxies are classified by their visual morphologies using a scale created by Edwin Hubble (Hubble, 1926) that ranges from “elliptical” to “spiral,” with a “Hubble sequence” connecting them. Elliptical galaxies have smooth, ellipsoidal stellar distributions and tend to be more massive and to contain less dust than spirals, which are disk-shaped with prominent spiral arms and plenty of interstellar gas and dust. The spiral end of the Hubble sequence is split between barred and unbarred spirals. Barred spiral galaxies have bar-shaped structures in their centers made of stars. The stellar age distribution in spiral galaxies is split between a younger population of stars in the disk, and an older population of stars in a spheroidal bulge component. Stars can populate the bulge through in situ formation, by being scattered out of their disk orbits by gravitational interactions with other galaxies, or through internal secular evolution processes (e.g., Kormendy & Kennicutt, 2004). Spiral galaxies with no bulge component, called bulgeless spirals, have likely not yet had strong encounters with other



Figure 1.3: *left*: Elliptical galaxy ESO 306-17 at distance 145 Mpc. Composite image is  $4.1'$  (173 kpc) wide and uses wavelengths 480 nm and 920 nm. *right*: Spiral galaxy NGC 4826 at distance of 5.2 Mpc. Composite image is  $1.5'$  (2.3 kpc) wide and uses wavelengths 450 nm, 540 nm, 660 nm, and 800 nm. Credit: NASA, ESA, and the Hubble Heritage (STScI/AURA)-ESA/Hubble Collaboration; Michael West, Stephen Smartt.

galaxies. Galaxies that *have* had strong encounters can end up as “peculiar galaxies”, which are the scattered remnants of systems likely destroyed through gravitational interactions with their neighbors.

Figure 1.3 shows examples of an elliptical and a spiral galaxy in the local Universe. The dark clouds in NGC 4826 reveal massive dust reservoirs that obscure the optical light from the galaxy’s disk and bulge; ESO 306-17, in contrast, contains little dust. Galaxy evolution research strives to understand the important physical processes and evolutionary tracks that lead to galaxies of different types. The most massive elliptical galaxies in the present-day Universe were likely created during an SMG phase of intense star formation at high redshift.

### 1.2.2 Star formation

Star formation is the production of new stars from clouds of interstellar molecular gas and dust. Molecular gas is made predominately of molecular hydrogen ( $\text{H}_2$ ) and is able

to form within clouds of atomic hydrogen (HI) when the density is high enough to shield  $\text{H}_2$  from photodissociation by the interstellar radiation field.

Star formation is one of the primary ways for a galaxy to increase its stellar mass; the other is to accrete new stars from other galaxies through mergers. New stars are born when a cloud of molecular gas grows to the point where its internal thermal and magnetic pressure can no longer support its gravitational weight. The cloud subsequently collapses and fragments into a population of newly-born stars that support their weight against the pull of gravity using pressure unlocked by nuclear fusion in their cores. The star-formation rate (SFR) of a galaxy is measured in solar masses<sup>2</sup> per year ( $M_\odot \text{ yr}^{-1}$ ). The Milky Way is currently forming stars at a rate of  $\sim 1 M_\odot \text{ yr}^{-1}$ , while some extreme “starburst” galaxies at high redshift can reach  $> 1000 M_\odot \text{ yr}^{-1}$ . The newly-ignited stars heat and drive winds and supernova shocks into the surrounding gas. This negative feedback makes the star-formation efficiency (SFE), the total fraction of gas turned into stars per unit time, of a given molecular cloud relatively low. For example, the SFE in 23 nearby star-forming galaxies is  $\simeq 5.3 \times 10^{-10} \text{ yr}^{-1}$  (Leroy et al., 2008).

A galaxy’s SFR depends on the amount of gas available – no gas, no star-formation. The relation for projected SFR density  $\Sigma_{\text{SFR}}$  ( $M_\odot \text{ yr}^{-1} \text{ pc}^{-2}$ ) takes the form of a power law of the projected gas density  $\Sigma_{\text{gas}}$  ( $M_\odot \text{ pc}^{-2}$ ):  $\Sigma_{\text{SFR}} \propto \Sigma_{\text{gas}}^n$ , where  $n \simeq 1.4$  (Schmidt, 1959; Kennicutt, 1998). There is evidence that this star-formation relation is different for nearby star-forming galaxies and high-redshift starburst galaxies (e.g., Bigiel et al., 2008; Sharon et al., 2013).

The relative distribution of individual stellar masses in a newly-born population of stars is phenomenologically parametrized using an “initial mass function” (IMF). In the local Universe, the IMF for stars more massive than the Sun is described well by

---

<sup>2</sup> solar mass  $M_\odot = 2.0 \times 10^{30} \text{ kg}$

a single power-law function  $dN \propto M^{-2.35} dM$  (Salpeter, 1955), indicating that massive stars are much rarer than lower-mass stars. For example, at the time of formation we would expect about one star with mass  $50 M_{\odot}$  for every  $10^4$  stars with mass  $1 M_{\odot}$ . As well as being rare, the high-mass stars also have very short lifetimes compared to their less-massive counterparts because the high pressures and temperatures in massive stars' cores deplete their hydrogen fuel supplies rapidly. The death of a massive star results in a core-collapse supernova, a powerful explosion that can outshine an entire galaxy and drive shock waves into the nearby interstellar medium (ISM). A more recent “broken power-law” model by Kroupa (2001) describes the mass function down to much lower stellar masses, where the mass function flattens out. For example, between  $0.01 \leq M/M_{\odot} < 0.08$ ,  $dN \propto M^{-0.3(\pm 0.7)} dM$  (Kroupa, 2001).

### 1.2.3 Nuclear accretion

Most massive elliptical and bulged-spiral galaxies have super-massive ( $M_{\text{BH}} \gtrsim 10^6 M_{\odot}$ ) black holes living in their centers, identifiable by the gravitational effects they have on the velocities of stars and gas clouds in galaxies' nuclei (e.g., Magorrian et al., 1998). Stars and interstellar gas can fall into these central black holes, a process known as accretion. This in-falling matter settles into an accretion flow around the black hole. Viscosity in the accretion flow redistributes angular momentum from the inner regions to the outer regions, allowing matter to accrete onto the black hole. The viscosity may be caused by turbulence from magnetorotational instabilities in the magnetized accretion disk (Balbus & Hawley, 1991). Accretion releases gravitational potential energy, which produces thermal and non-thermal radiation, cosmic rays, and relativistic outflows. Very low accretion rates can produce radiatively inefficient accretion flows (RIAFs), where the released gravitational potential energy is transported inwards with the accretion flow into the black hole before it can radiate, resulting in low-luminosity

or undetectable accreting systems.

### **Active galactic nuclei**

Accreting galaxies that efficiently couple accretion energy to radiation are called active galaxies; the central nucleus itself is known as an active galactic nucleus (AGN). During episodes of rapid accretion, the AGN becomes very luminous and can outshine the combined light of its host galaxy. Accretion processes can also redistribute energy, heat the ISM, and eject material from the nucleus or even the entire galaxy.

As well as having an accretion flow of hot material, an AGN will typically contain a dusty torus, a larger toroidal cloud of gas and dust surrounding the accretion disk; a hot corona, a cloud of relativistic electrons above the accretion disk; and sometimes relativistic jets, collimated, bipolar, high-energy outflows of relativistic particles away from the black hole. AGNs are classified into two categories, Type I and Type II. Type II AGNs are observed to have only narrow optical emission lines from low-velocity material far away from the accretion disc. In contrast, Type I AGNs exhibit narrow emission lines as well as broad emission lines from high-velocity material near the black hole. Whether an AGN is a Type I or Type II is determined by viewing angle, as shown in Figure 1.4. Type I AGNs are oriented to allow a privileged view down into the central engine, while Type II systems are oriented more edge-on, so that the torus obscures the direct light from their central regions. Figure 1.4 also shows an image of the nearby Type II AGN Centaurus A (NGC 5128), where the prominent dust lane obscures direct views to the central black hole.

Intervening gas, dust, and heavy elements along the line of sight to an AGN can absorb and scatter the light emitted by accretion processes. In the X-ray waveband (0.5–10 keV photons), the attenuation is mostly due to Compton scattering and photoelectric

absorption, with both increasing in strength as gas metallicity<sup>3</sup> increases. The hydrogen column density  $N_{\text{H}}$  is the number of hydrogen atoms per unit area projected along a given line of sight  $N_{\text{H}} [\text{cm}^{-2}] = \int n_{\text{H}} dl$ , where  $n_{\text{H}} (\text{cm}^{-3})$  is the hydrogen volume density. As described previously, because of the complex geometry of the obscuring dust torus, the optical signatures of AGNs vary with viewing angle. Therefore, a defining characteristic of an AGN is taken to be a power-law spectrum in the hard X-ray waveband (photon energies  $> 2 \text{ keV}$ ), which is relatively insensitive to viewing angle because hard X-rays can penetrate an entire galaxy's worth of gas column density. For example, the column density required to achieve an optical depth of unity at an energy of  $6.5 \text{ keV}$  is given by

$$\tau \equiv \int \sigma n_{\text{H}} dl = \sigma N_{\text{H}} = 1$$

$$n_{\text{H}, \tau=1} \simeq 6 \times 10^{23} \text{ cm}^{-2},$$

where the  $6.5 \text{ keV}$  photoelectric cross section of a solar abundance gas is  $\sigma \simeq 1.6 \times 10^{-24} \text{ cm}^2$  (Morrison & McCammon, 1983). In contrast, the hydrogen column density through the Milky Way is  $N_{\text{H}} \sim 10^{19} \text{ cm}^{-2}$ .

AGNs produce hard X-ray emission through inverse Compton scattering when thermal photons from the accretion disc scatter off relativistic electrons in the corona. This X-ray emission takes the form of a power-law and is characterized by a photon index  $\Gamma$  as  $dN \propto E^{-\Gamma} dE$  for the number of photons  $N$  with energy between  $E$  and  $dE$ . Typical values for  $\Gamma$  in the hard X-ray spectra of AGNs are between 1.5–2.5.

### **Fe K $\alpha$ emission in AGNs**

The Fe K $\alpha$  line is a ubiquitous spectral feature in AGNs. It is produced when inverse-Compton X-ray radiation from the corona shines on the material in the accretion flow

---

<sup>3</sup> Metallicity is the relative fraction of heavy elements in the gas compared to hydrogen and is usually measured with respect to the solar metallicity  $Z_{\odot}$ .



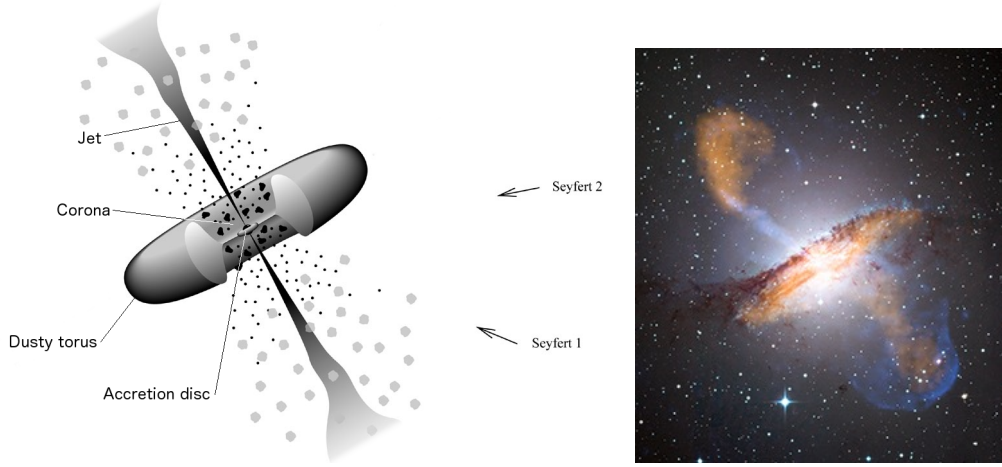


Figure 1.4: *left:* Diagram of a typical active nucleus. The dusty torus extends to approximately 0.03 pc (Urry & Padovani, 1995). Figure adapted from Urry & Padovani (1995). *Right:* Nearby Type II active galaxy Centaurus A (NGC 5128) at a distance of 11 Mpc (image is 12' (38 kpc) wide). Composite image shows 870  $\mu\text{m}$  (orange) and X-ray (blue); starlight is approximately true color. Credit: X-ray: NASA/CXC/CfA/R.Kraft et al.; Submillimeter: MPIfR/ESO/APEX/A. Weiss et al.; Optical: ESO/WFI

and the inner surface of the surrounding dusty torus. The  $\text{Fe K}\alpha$  line is produced by atomic transitions from the first excited state to the ground state of iron. The energy of the neutral  $\text{Fe I K}\alpha$  line can be approximated using the Rydberg equation and Moseley's law:

$$E(\text{Fe I K}\alpha) = 13.6 \text{ eV} (Z - 1)^2 \left( \frac{1}{n_1^2} - \frac{1}{n_2^2} \right) \simeq 6.4 \text{ keV}, \quad (1.11)$$

where  $Z_{\text{Fe}} = 26$ ,  $n_1 = 1$ , and  $n_2 = 2$ .

In heavily obscured systems ( $N_{\text{H}} \gtrsim 10^{24} \text{ cm}^{-2}$ ), the  $\text{Fe K}\alpha$  emission line is very powerful compared to the X-ray continuum. The strength of an X-ray spectral line compared to the surrounding X-ray continuum is measured using the equivalent width (EW), the energy width of continuum radiation that would contain the same flux as the spectral line. The  $\text{Fe K}\alpha$  emission in heavily obscured AGNs has a large equivalent width of  $\text{EW} \gtrsim 1 \text{ keV}$  because the primary hard X-ray continuum is absorbed while the  $\text{Fe K}\alpha$  line is partially reflected into the line of sight from more distant cooler gas. In contrast, lines of sight that allow views directly to the central accretion disc will have a

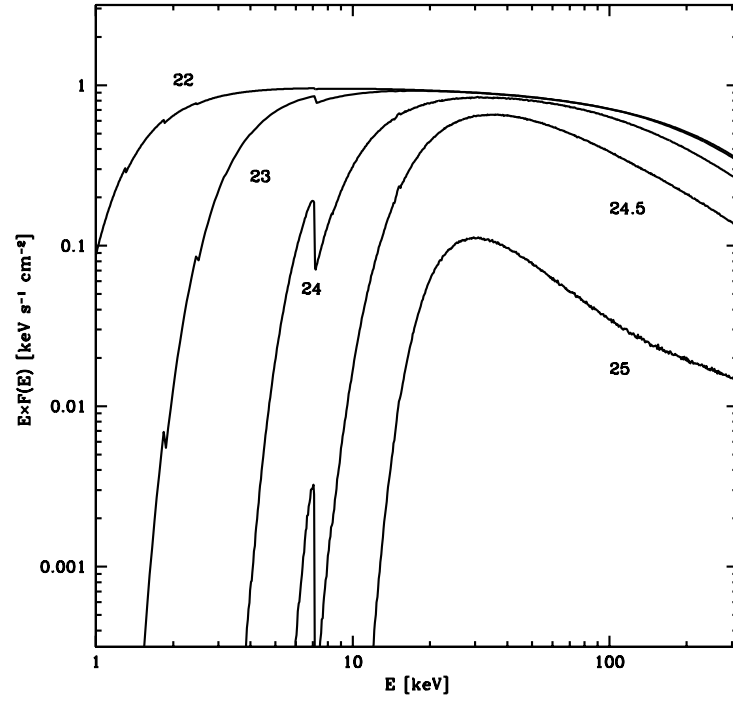


Figure 1.5: Typical observed X-ray flux spectrum of an AGN with photon index  $\Gamma = 2$  as a function of hydrogen column density. The numbers in the figure represent the obscuration ( $\log(N_{\text{H}}/\text{cm}^{-2})$ ) of each spectrum. Figure from Comastri (2004).

more diluted signal of  $\text{EW} \sim 100 \text{ eV}$ . Figure 1.5 shows typical X-ray continuum spectra of AGNs as a function of increasing hydrogen column density.

### The $M$ – $\sigma$ relation in local galaxies

A curious fact about super-massive black holes is that their masses  $M_{\text{BH}}$  are tightly correlated to the total stellar mass  $M_{\text{bulge}}$  of their host galaxies’ stellar bulges<sup>4</sup>, with  $M_{\text{bulge}} \simeq 1000 \times M_{\text{BH}}$  (e.g., Magorrian et al., 1998). An even tighter correlation is found between  $M_{\text{BH}}$  and the stellar-bulge velocity dispersion  $\sigma$  (Ferrarese & Merritt, 2000; Gebhardt et al., 2000; Merritt & Ferrarese, 2001). Dynamically speaking, these correlations are unexpected because the black hole and stellar bulge hardly know about each other. The black hole sits at the center of a sphere of mass, immune to the gravitational influence of the stars, and the gravitational attraction of the black hole on the stars is negligible because  $M_{\text{bulge}} \gg M_{\text{BH}}$ . Therefore, the observed  $M_{\text{bulge}}$ – $M_{\text{BH}}$  correlation in nearby galaxies is an *artifact* of the galaxies’ past evolution, providing clues about a past interaction between star-formation history and accretion history. Submillimeter galaxies may represent an evolutionary stage in the lives of galaxies that reflects this regulation between accretion and star formation (Chapter 3).

#### 1.2.4 Thermal dust emission

Interstellar dust grains, composed of silicate and graphite cores with ice mantles, represent the solid phase of the ISM in galaxies. Dust efficiently absorbs the optical and ultraviolet light from stellar photospheres and hot nuclear accretion disks (e.g., see dust lanes in Figure 1.3) and thermally re-emits this energy as thermal radiation. This is known as “dust reprocessing” of short-wavelength radiation into the infrared. The far-infrared (FIR) region of a galaxy’s SED is dominated by the thermal emission from cool

---

<sup>4</sup>  $M_{\text{bulge}}$  refers to the stellar mass in the bulge for spiral galaxies, and to the total stellar mass for elliptical galaxies.

interstellar dust grains. Dust also serves as an important medium for gas chemistry, and along with CO emission lines, as a source of radiative cooling inside proto-stellar gas clouds. Dust masses  $M_{\text{dust}}$  for a sample of 65 nearby ( $< 30$  Mpc) galaxies spanning a representative range of galaxy properties are between  $10^5$  and  $10^8 M_{\odot}$  (Draine et al., 2007).

At rest-frame wavelengths  $\lambda \gtrsim 100 \mu\text{m}$ , dust emission can be described by a modified black body spectrum  $f_{\nu} = \epsilon(\tau, \nu) B_{\nu}$ , where  $\epsilon$  is the emissivity of the dust and  $B_{\nu}$  is the Planck function. The Planck function  $B_{\nu}$  depends only on the average dust temperature  $T_{\text{D}}$ , while the dust emissivity  $\epsilon$  falls with frequency because the dust couples inefficiently to the radiation field for wavelengths larger than the typical grain size of  $0.01\text{--}1 \mu\text{m}$  (Kim et al., 1994). This frequency-dependent emissivity is parameterized by the emissivity index  $\beta$  as  $\epsilon \propto \nu^{\beta}$ , where  $\beta \simeq 1.5$ . Typical values for  $T_{\text{D}}$  in the interstellar radiation field of a galaxy range between  $19\text{--}30$  K (Tielens, 2005).

Near the peak of the thermal SED ( $\lambda \simeq 100 \mu\text{m}$ ), the dust turns optically thick and the spectrum approaches that of a pure blackbody  $B_{\nu}$ . Therefore, the full spectrum is described by

$$f_{\nu} = (1 - e^{-\tau}) B_{\nu}, \quad (1.12)$$

where

$$B_{\nu} = \frac{2h\nu^3}{c^2} \frac{1}{e^{\frac{h\nu}{k_{\text{B}}T_{\text{D}}}} - 1}, \quad (1.13)$$

$k_{\text{B}}$  is the Boltzmann constant, and  $\tau = (\nu/\nu_0)^{\beta}$ . The parameter  $\nu_0$  represents the frequency where the optical depth equals unity, and is expected to be  $\simeq 3000$  GHz ( $c/100 \mu\text{m}$ ; Draine, 2006). As  $h\nu/kT_{\text{dust}} \rightarrow 0$  (the Rayleigh-Jeans regime), the shape of the spectrum approaches that of a power law with spectral index  $\alpha = 2 + \beta$  (here defined as  $S_{\nu} \propto \nu^{\alpha}$ ).

### 1.2.5 Synchrotron radiation

Synchrotron radiation is emitted when ultra-relativistic charged particles are accelerated by the Lorentz force around magnetic field lines. The SED of a single relativistic electron increases as a power law until approximately the critical frequency

$$\omega_c = \frac{3\gamma^2 q B}{2m_e c}, \quad (1.14)$$

after which it falls as an exponential. The total power emitted by a single relativistic particle with charge  $q$ , mass  $m$ , and total energy  $\gamma mc^2$  in a magnetic field with strength  $B$  is given by Rybicki & Lightman (1979) as

$$P = \frac{1}{6\pi} \sigma_{TC} \beta^2 \gamma^2 B^2, \quad (1.15)$$

where  $\beta = v/c$ . The frequency dependence of synchrotron radiation for a population of electrons with a power-law energy distribution,  $dN = E^{-p} dE$ , is

$$P(\nu) \propto \nu^{-(p-1)/2}, \quad (1.16)$$

which is also a power law with spectral index  $\alpha = (p - 1)/2$ .

Radio synchrotron emission occurs in many astrophysical environments when electrons are accelerated via magnetohydrodynamical shocks or turbulence. For example, supernova remnants, the intracluster gas reservoirs inside merging galaxy clusters, and jets from AGNs all produce synchrotron radiation. The compression ratio  $r$  of a strong shock (Mach number  $\mathcal{M} \gg 1$ ) in a monatomic gas is given by the Rankine-Hugoniot shock conditions as  $r \equiv \rho_f/\rho_i = 4$  (Longair, 2011), where  $\rho_f$  and  $\rho_i$  are the post-shock and pre-shock gas densities, respectively. In a magnetized gas, free electrons and ions repeatedly reflect off magnetic irregularities in the forward and reverse shocks, gaining energy with each crossing of the shock surface, and escape with a number distribution  $N(E) \propto E^{-p}$ , where  $p = (r + 2)/(r - 1) \simeq 2$  (Drury, 1983). The synchrotron spectrum

emitted from the strong shock-energized electrons is therefore a power law with spectral index  $\alpha = 0.5$  (see Equation 1.16).

In star-forming galaxies, synchrotron radiation is the dominant source of radio-waveband emission at frequencies  $\lesssim 30$  GHz (Condon, 1992), and is produced when short-lived, massive stars explode as supernovae. The shock fronts sweep up the local ISM, aligning and amplifying ambient magnetic fields, and accelerating electrons to relativistic energies. The typical radio spectral index for star-forming galaxies is  $\alpha \simeq 0.8$  (Condon, 1992).

### 1.2.6 Radio-IR correlation in star-forming galaxies

In star-forming galaxies, there is a tight correlation between power radiated in the infrared and at radio wavelengths near 20 cm (1.4 GHz). Although the details remain mysterious, the basic picture that it is caused by ongoing star formation is agreed upon.

Stars form in massive clouds of gas and dust, and some small fraction of the newly formed stars will be massive with short lifetimes (Section 1.2.2). These massive stars are very hot, and after a short time, explode as core-collapse supernovae. The intense optical and ultraviolet radiation from the massive stars' hot photospheres is absorbed by the dust in the surrounding molecular cloud or ambient ISM, then reprocessed into infrared radiation. The ongoing supernovae also fill the nearby ISM with supersonic  $\mathcal{M} > 1$  shock waves that accelerate free electrons to ultra-relativistic energies, and also sweep up, compress, and amplify the ambient magnetic field to produce synchrotron radiation. Observations of nearby star-forming galaxies suggest the emitted infrared power is linearly proportional to the radio synchrotron radiation (Condon, 1992).

Carilli & Yun (1999) take advantage of the proportionality between the infrared and radio emission in star-forming galaxies to estimate the galaxies' redshifts. Near 350 GHz, the observed flux density of a high-redshift star-forming galaxy is dominated

by thermal dust, while near 1.4 GHz, synchrotron emission dominates. In this discussion, we follow the convention of Carilli & Yun (1999) and define  $\alpha$  using  $S_\nu \propto \nu^\alpha$ . In this case, the observed flux densities (Equation 1.10) near 350 GHz and 1.4 GHz, respectively, are

$$S_\nu^{\text{submm}} = C_1 \left( \frac{\text{SFR}}{M_\odot \text{ yr}^{-1}} \right) \frac{1}{4\pi D_L^2} \left( \frac{\nu}{350 \text{ GHz}} \right)^{\alpha_{\text{submm}}} (1+z)^{1+\alpha_{\text{submm}}} \quad (1.17)$$

$$S_\nu^{\text{radio}} = C_2 \left( \frac{\text{SFR}}{M_\odot \text{ yr}^{-1}} \right) \frac{1}{4\pi D_L^2} \left( \frac{\nu}{1.4 \text{ GHz}} \right)^{\alpha_{\text{radio}}} (1+z)^{1+\alpha_{\text{radio}}}. \quad (1.18)$$

$C_1$  and  $C_2$  are constants that encode the physics of the proportionality, and are given in Carilli & Yun (1999). The spectral index between  $S_\nu^{\text{radio}}$  and  $S_\nu^{\text{submm}}$  ( $\alpha_{1.4}^{350}$ ) is then independent of SFR, and can be used to estimate the redshift  $z$ . The spectral index  $\alpha_{1.4}^{350}$  is given by

$$\begin{aligned} \alpha_{1.4}^{350} &= \log \left( S_\nu^{\text{submm}} / S_\nu^{\text{radio}} \right) / \log (350/1.4) \\ &= \frac{\log (C_1/C_2)}{\log (350/1.4)} + \frac{(\alpha_{\text{submm}} - \alpha_{\text{radio}}) \log(1+z)}{\log (350/1.4)} \\ &= -0.24 - [0.42 \times (\alpha_{\text{radio}} - \alpha_{\text{submm}})] \log(1+z) \end{aligned} \quad (1.19)$$

We can now solve for  $z$  to provide an estimate of the source redshift  $z_{\text{CY}}$  as a function of  $\alpha_{1.4}^{350}$ :

$$z \sim z_{\text{CY}} = 10^X - 1, \quad (1.20)$$

where

$$X = \frac{\alpha_{1.4}^{350} + 0.24}{0.42 \times (\alpha_{\text{submm}} - \alpha_{\text{radio}})}. \quad (1.21)$$

The Carilli & Yun (1999) technique is powerful because it can provide redshift estimates for all sources suspected to be dominated by star formation that have submillimeter/radio counterpart pairs without additional spectroscopic follow-up observations. However, redshifts estimated using this technique have significant systematic uncertainties tied to the assumptions about the shape of the typical SED. Notably, the values assumed for  $\alpha_{\text{submm}}$  and  $\alpha_{\text{radio}}$  have a strong impact on the results. Roseboom

et al. (2012) find typical discrepancies between Carilli & Yun (1999) and spectroscopic redshifts of  $|\Delta z_{\text{CY}}|/(1+z) = 0.24$  for 22 millimeter-selected SMGs.

### 1.2.7 Submillimeter galaxies (SMGs)

Submillimeter galaxies (SMGs) are a special class of high-redshift system that are bright and readily detected in the “submillimeter” waveband, loosely defined to be wavelengths between  $1\text{ mm} > \lambda > 0.5\text{ mm}$ . They commonly have infrared (IR) luminosities<sup>5</sup>  $L_{\text{IR}} \gtrsim 10^{12} L_{\odot}$ , where  $L_{\text{IR}}$  is defined as the integrated power between rest-frame wavelengths  $8\text{ }\mu\text{m}$  and  $1000\text{ }\mu\text{m}$ . In the local Universe, galaxies with  $L_{\text{IR}} > 10^{12} L_{\odot}$  are called ultra-luminous infrared galaxies (ULIRGs). The nearest ULIRG is a merging system named Arp 220 (Soifer et al., 1984) at a distance of 77 Mpc with  $L_{\text{IR}} = 2 \times 10^{12} L_{\odot}$ . In 1997, the first submillimeter-waveband telescopes discovered that ULIRG-class objects at high redshift were  $\sim 1000$  times more numerous (per comoving volume) than they are in the local Universe (Smail et al., 1997), implying that these extreme systems were much more common in the past. This conclusion is consistent with results from optical/ultraviolet studies that have found the Universe is winding down from a period of intense, global starburst activity that ended near  $z \sim 1$  (e.g., Connolly et al., 1997). However, the SMGs revealed a different population of starburst galaxies that were unaccounted for in previous optical/ultraviolet surveys of cosmic star-formation due to their complete dust obscuration.

Most low-luminosity ULIRGs ( $L_{\text{IR}} \lesssim 10^{12.4} L_{\odot}$ ; Tran et al., 2001) do not have the hard X-ray signatures of an AGN. They instead have strong emission lines from the vibrational modes of polycyclic aromatic hydrocarbons (PAHs), large molecules of bonded benzene rings, which are destroyed by AGNs’ powerful ultraviolet and X-ray emission. Therefore, their infrared dust luminosities are thought to be primarily powered by star

---

<sup>5</sup> solar luminosity  $L_{\odot} = 3.85 \times 10^{26}\text{ W}$



formation buried under thick clouds of gas and dust. In the local Universe, ULIRGs are usually involved in mergers or have disturbed morphologies indicating recent merger activity (Veilleux et al., 2002). Numerical simulations (e.g., Toomre & Toomre, 1972) demonstrated that reservoirs of gas can be funneled into the dense galactic nucleus during a major merger, and this increased gas density may cause a violent episode of star-formation. Resolved submillimeter and rest-frame optical imaging of SMGs suggest they too are related to merger activity (Engel et al., 2010; Aguirre et al., 2013).

As of their discovery in 1997, the name “SMG” was an adequate term to describe this galaxy population because the observations were only sensitive enough to detect the most luminous sources, thereby yielding a population of violent starburst galaxies. Now the term SMG is becoming outdated because sensitive submillimeter observations from new observatories can detect fainter sources with a wider range of intrinsic properties at many different wavelengths.

### **The negative k-correction in SMGs**

SMGs, like any other dusty star-forming galaxy population, have a remarkable property that make them a powerful tool for studying intense star formation through cosmic time. Their SEDs are dominated by a thermal dust spectrum which, when observed in the submillimeter waveband, provides a strong, negative k-correction with increasing redshift. At redshifts  $z \sim 1\text{--}10$ , the gain in observed flux density from the k-correction is even competitive with the losses from the increasing luminosity distance. This effect is shown in Figure 1.6, where a typical SMG thermal dust spectrum with  $T_D = 35\text{ K}$ ,  $\beta = 1.5$  and  $L_{\text{IR}} = 2 \times 10^{12} L_\odot$  is shown for redshifts between 1–10. The shaded regions show the bandpasses for the Max-Planck Millimeter Bolometer (MAMBO) array and Large APEX Bolometer Camera (LABOCA). As redshift increases, the observed flux density in each band *increases* with redshift. Therefore, as the galaxies move farther

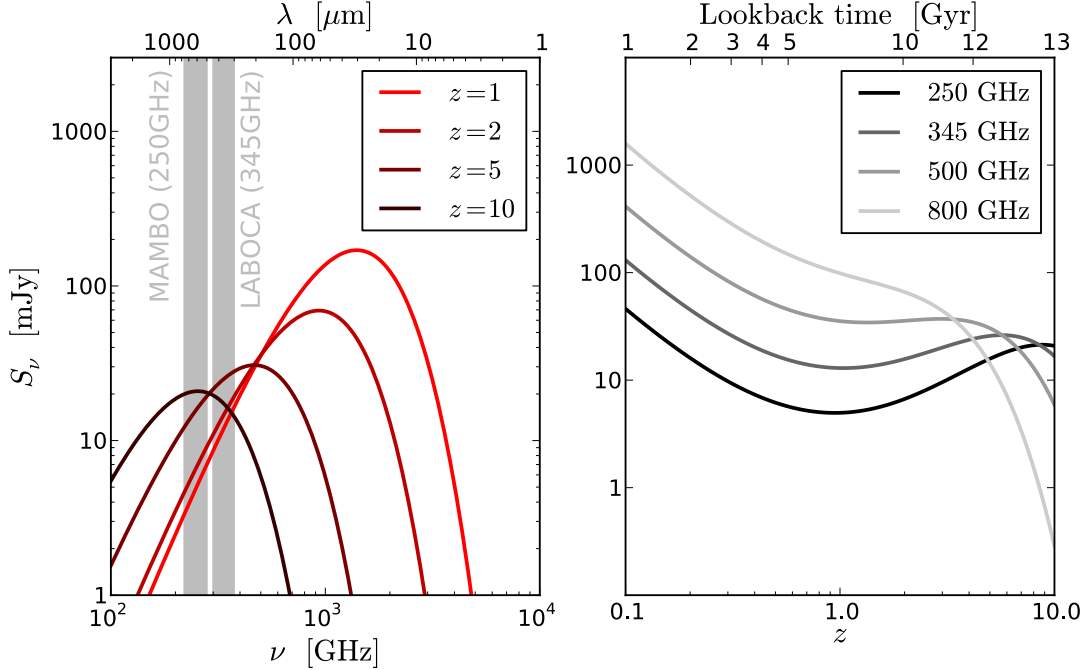


Figure 1.6: *Left:* Observed flux densities of a model SMG with a thermal dust spectrum ( $T_D = 35$  K,  $\beta = 1.5$  and  $L_{\text{IR}} = 2 \times 10^{12} L_\odot$ ) at different redshifts. The shaded regions represent the bandpasses of the MAMBO and LABOCA bolometer arrays. *Right:* Observed flux density versus redshift for the same model SMG in different observing bands. Calculations use  $H_0 = 70 \text{ km s}^{-1} \text{ Mpc}^{-1}$ ,  $\Omega_\Lambda = 0.73$ , and  $\Omega_m = 0.27$ .

away, they get brighter. The right panel of Figure 1.6 shows the observed flux density in four submillimeter wavebands as a function of redshift. It is not until  $z \gtrsim 10$ , when the peak of the thermal dust SED gets redshifted entirely through the bandpass, that the flux density begins to fall.

This peculiar effect means that a galaxy with a given infrared luminosity  $L_{\text{IR}}$  and dust temperature  $T_D$  will have approximately constant observed flux density between  $1 < z < 10$ , where the luminosity distance, respectively, ranges between approximately  $7 \times 10^3 \text{ Mpc} < D_L < 11 \times 10^4 \text{ Mpc}$ . Therefore, the selection function of deep submillimeter surveys is more sensitive to the intrinsic properties of the galaxies than it is to redshift.

## Constraining models of galaxy evolution with SMG surveys

Because SMGs can be detected with equal efficiency from redshifts  $z \sim 1\text{--}10$ , it is difficult to constrain the individual systems' redshifts with submillimeter data alone. Therefore, statistical metrics that do not rely on having a redshift-complete galaxy sample are often used to compare observations to models of galaxy evolution.

One such metric is the *number counts*, a measure of the projected density of galaxies on the sky. The differential number counts  $dN/dS$  represent the number of galaxies detected with flux density between  $S$  and  $dS$  per square degree. This result can then be compared to predictions to constrain models of galaxy evolution. The technique is usually limited by the observations' inability to constrain the very faint and very bright ends of the number counts function. The faintest galaxies eventually will fall below the sensitivity limit of the survey, and the brightest galaxies are usually so rare that the typical solid angle of a surveyed region of sky is unlikely to contain a single one. Progress is being made on the faint end by targeting fields that also contain massive galaxy clusters to magnify faint galaxies above the detection threshold of the survey, and on the bright end as new instrumentation is able to increase the mapping speed of submillimeter surveys.

The redshift distribution of SMGs can also be used to constrain models of galaxy evolution. It is complementary to the number counts function, which is less sensitive to SMG redshifts. Because the poor angular resolution of typical wide-field SMG surveys ( $\sim 10\text{--}30''$ ) allows for many possible optical counterparts for each source, an SMG's redshift is commonly determined by first matching the source to a 1.4 GHz radio counterpart. The number counts of 1.4 GHz radio sources are much lower than those of optical galaxies, so an unambiguous match is more likely. This technique is biased only to measure the redshifts of sources that have radio counterparts. Because radio synchrotron emission does not benefit from a negative k-correction, this introduces a bias

to find SMGs at lower redshifts (e.g., Chapman et al., 2005). Measuring the properties of *complete* samples of SMGs with radio counterparts can help provide an unbiased measurement of the redshift distribution of SMGs (Chapter 2).

### 1.3 Galaxy clusters

#### 1.3.1 Anatomy of a cluster

Galaxy clusters are massive ( $\gtrsim 10^{14} M_{\odot}$ ) gravitationally-bound structures made of dark matter, hot ionized gas, and galaxies. The total mass fraction in the hot gas component, although it varies between clusters, and within individual clusters when measured at different locations, is approximately 10% (Vikhlinin et al., 2006). The galaxies make up an additional  $\sim 1\%$  (Lin et al., 2012), leaving  $\sim 90\%$  of the mass in the form of dark matter.

#### The dark matter halo

Galaxy clusters began in the early Universe as peaks in the primordial mass density field. As time passed, their self gravity pulled them out of the expanding “Hubble flow,” and they collapsed into virialized halos. During the collapse, the initial phase space configuration of the material is lost and virial pressure equilibrium is established, a process known as “violent relaxation” (Lynden-Bell, 1967).

The resulting post-collapse equilibrium dark-matter density profile has been measured using numerical dark matter simulations to be (Navarro et al., 1997):

$$\rho(r) = \frac{\rho_0}{cx(1+cx)^2}, \quad (1.22)$$

where  $x = r/r_{500c}$ ,  $r_{500c}$  is the radius that encloses a mean matter density of  $500 \rho_c$ , and the concentration parameter  $c$ .

### The intracluster medium

The volume between a cluster's galaxies is filled with low density ( $10^{-3} \text{ cm}^{-3}$ ), high temperature ( $\sim 10^8 \text{ K}$ ) ionized gas called the intracluster medium (ICM). In the X-ray waveband, this gas glows via thermal bremsstrahlung, which is continuum radiation emitted when free electrons are accelerated by Coulomb deflections off other electrons and ions in the thermal plasma. The electron temperature in the ICM of a massive cluster is  $kT_e \sim 5 \text{ keV}$ . The gas temperature agrees with the velocity dispersion of the galaxies, confirming they are orbiting inside the same potential well established by the cluster dark matter halo. Gas in the ICM is both accreted onto the cluster from beyond the virial radius, and also stripped out from galaxies within the cluster.

The equilibrium gas pressure profile has been measured using observations and numerical simulations to be (Navarro et al., 1997; Nagai et al., 2007):

$$\frac{P(r)}{P_{500}} = \frac{P_0}{(c_{500} x)^\gamma [1 + (c_{500} x)^\alpha]^{(\beta-\gamma)/\alpha}}. \quad (1.23)$$

The best fitting parameters based on X-ray observations are consistent with those from SZE observations and are (Arnaud et al., 2010; Sayers et al., 2013):  $[P_0, c_{500}, \gamma, \alpha, \beta] = [8.130h_{70}^{-3/2}, 1.156, 0.3292, 1.0620, 5.4807]$ .

### The cluster galaxies

Elliptical galaxies are the most common galaxy type found inside galaxy clusters. This is likely due to the environmental effects of living inside a galaxy cluster. For example, the force of ram pressure ( $F_{\text{ram}} \simeq n_e v^2$ ) acting on a typical cluster member galaxy as it moves through the ICM will easily overcome the galaxy's gravitational hold on its gas supply (Gunn & Gott, 1972). Evidence of ram-pressure stripping is found in the increased HI content of galaxy clusters as a function of cluster-centric radius and the inverse correlation between spiral fraction and velocity dispersion in clusters (Sarazin,

1988, and references therein). The removal of a spiral galaxy's gas reservoir by itself will not create an elliptical galaxy, because the disk-like orbits of the remaining stars will remain unchanged. However, the frequent interactions and mergers occurring within the dense cluster environment can help scramble stellar orbits and produce elliptical-looking galaxies (Toomre & Toomre, 1972).

### 1.3.2 The Sunyaev Zel'dovich effect

When CMB photons travel through the volume of a galaxy cluster, they are inverse-Compton scattered by the hot ICM electrons. For a single-temperature gas in the single-scattering limit, the Compton  $y$  parameter gives the total fractional energy increase per photon, equal to the fractional increase per collision times the optical depth to Compton scattering

$$y \equiv \frac{k_B T_e}{m_e c^2} \int n_e \sigma_T dl, \quad (1.24)$$

where  $m_e$  is the electron mass,  $\sigma_T$  is the Thomson cross section, and  $T_e$  is the electron temperature. The optical depth of Compton scattering  $\tau_e = \int n_e \sigma_T dl \ll 1$ . The distortion that this process introduces to the spectrum of the CMB along the cluster line of sight is known as the Sunyaev Zel'dovich effect (SZE; Zeldovich & Sunyaev, 1969; Sunyaev & Zeldovich, 1970). In the non-relativistic limit of Compton scattering,  $k_B T_e / m_e c^2 \ll 1$ , the CMB temperature deflection along a line of sight through a cluster that is at rest with respect to the CMB is given by (Sunyaev & Zeldovich, 1970):

$$\frac{\Delta T_{tSZ}}{T_{\text{CMB}}} = y \left( x \frac{e^x + 1}{e^x - 1} - 4 \right), \quad (1.25)$$

where  $x = h\nu / kT_{\text{CMB}}$ . This temperature-dependent signal is referred to as the thermal SZE (tSZ).

For a cluster with line-of-sight peculiar velocity  $v_p$  with respect to the CMB, there is an additional signal due to the Doppler effect of the bulk motion of the gas. This is

known as the kinetic SZE (kSZ) and is given in the non-relativistic limit by (Sunyaev & Zeldovich, 1972)

$$\frac{\Delta T_{\text{kSZ}}}{T_{\text{CMB}}} = -\tau_e \left( \frac{v_{\text{pec}}}{c} \right). \quad (1.26)$$

The corresponding change in surface brightness for the thermal and kinetic SZE signal is found by multiplying each by the derivative of the Planck function with respect to temperature

$$\frac{dB_\nu}{(dT_{\text{SZE}}/T_{\text{CMB}})} = I_0 \frac{x^4 e^x}{(e^x - 1)^2}. \quad (1.27)$$

The ratio of the intensities of thermal to kinetic SZE signals depends on frequency as

$$\frac{\Delta T_{\text{tSZ}}}{\Delta T_{\text{kSZ}}} = \frac{\theta}{\beta} \left( x \frac{e^x + 1}{e^x - 1} - 4 \right), \quad (1.28)$$

where  $\beta = v_{\text{pec}}/c$  and  $\theta = kT_e/m_e c^2$ . For LABOCA observations ( $\nu = 345$  GHz,  $x = 6.1$ ) of a massive cluster with  $kT_e = 10$  keV, and  $v_p = 500$  km s<sup>-1</sup>,  $\Delta T_{\text{tSZ}}/\Delta T_{\text{kSZ}} \simeq 25$ .

Figure 1.7 presents the SZE signal  $\Delta I_{\text{CMB}}$  for a typical massive cluster as a function of  $y$ ,  $T_e$ , and  $v_p$ . The LABOCA and ACT observing bands are represented by the grey regions. The curves in Figure 1.7 were produced using numerical integration software (Chluba et al., 2012, 2013) and include relativistic effects.

The total SZE signal for a cluster is given by the integral of the Compton  $y$  parameter over solid angle,  $Y_{\text{SZ}} = \int y d\Omega$ . Pressure profiles of galaxy clusters measured using X-ray and submillimeter imaging (Arnaud et al., 2010; Sayers et al., 2013) find a shape consistent with a generalized NFW profile (Navarro et al., 1997). Because the SZE signal smoothly extends to zero, the relative size and  $Y_{\text{SZ}}$  properties are commonly defined with respect to  $r_{500c}$ . The self-similar nature of galaxy mass profiles enforces that clusters of similar mass will have similar  $r_{500c}$  values. Similarly, the quantity  $Y_{500c}$  is the spherical integral of  $y$  within radius  $r_{500c}$ .

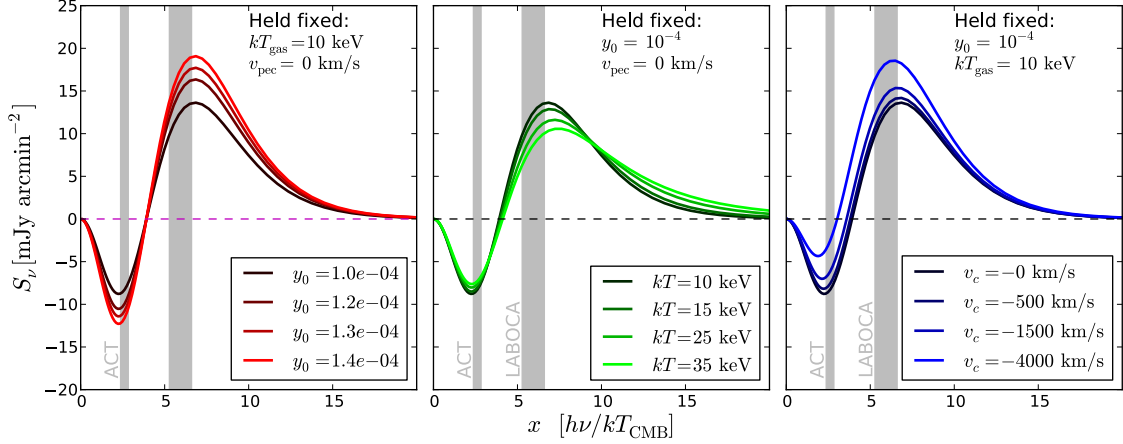


Figure 1.7: Intensity deflection  $\Delta I_{\text{CMB}}$  of the SZE signal versus  $x$  through the center of a typical massive galaxy cluster. The three panels show how  $\Delta I_{\text{CMB}}(x)$  is affected by varying  $y$  (left),  $T_{\text{gas}}$  (center), and  $v_p$  (right). The shaded regions represent the ACT and LABOCA bandpasses.

### 1.3.3 Galaxy clusters as cosmological probes

The time it takes a primordial density fluctuation of a given size to collapse, the subsequent growth rate, and the total number of collapsed halos all depend on the cosmological initial conditions. Therefore, the mass function of clusters  $N(M)$ , the number of galaxy clusters per comoving volume with masses between  $M$  and  $dM$ , can be used to constrain these cosmological parameters. The cluster mass function at late times  $z \sim 0$  is sensitive to  $\Omega_m$  and  $\sigma_8$ , and its evolution as a function of redshift is sensitive to dark energy through the dark energy equation of state parameter  $w$ .

Using the SZE signal  $Y_{\text{SZ}}$  is a good way to search for galaxy clusters. The SZE temperature deflection  $\Delta T_{\text{tSZ}}$  does not depend on redshift (Equation 1.25), and the angular diameter distance  $D_A$  and consequently the subtended solid angle of a given cluster changes little beyond redshift  $z \gtrsim 1$  (see Section 1.1.3). Therefore, the detectability of a given cluster, given by  $Y_{\text{SZ}}$ , is unchanging as a function of redshift, allowing SZE surveys to place strong constraints on cosmological parameters by detecting the most massive clusters out to arbitrarily high redshifts. For example, the



large mass ( $\simeq 2.2 \times 10^{15} M_{\odot}$ ) and high redshift ( $z = 0.870$ ) of the exceptional cluster ACT-CL J0102–4915 (Menanteau et al., 2012) is such that we expect to only find a few such systems in the entire observable Universe. In contrast, surveys that use optical or X-ray observations to detect clusters will be limited by the luminosity distance  $D_L$ , which is a rapidly increasing function of redshift.

Recent high-resolution SZE cluster surveys have located hundreds of moderate-to-high redshift SZE-selected clusters (Vanderlinde et al., 2010; Marriage et al., 2011; Williamson et al., 2011; Menanteau et al., 2013), and the next generation of SZE surveys will find many times more (e.g., Niemack et al., 2010). Therefore, the ability for SZE surveys to constrain cosmology is beginning to be limited by the systematic uncertainties in predicting cluster mass from SZE signal, and not by Poisson uncertainties based on the number of clusters. The research described in Chapter 4 helps to characterize this systematic uncertainty with high-resolution SZE increment imaging of a representative sample of massive ACT clusters.

#### 1.3.4 Galaxy clusters as gravitational lenses

It can be advantageous to search for distant galaxies in fields containing foreground massive galaxy clusters. Light from the background galaxy is lensed as it passes through the gravitational potential well of the galaxy cluster. If the image of the background galaxy is magnified, then it will appear brighter than it would have if the cluster were not there. In surveys with a fixed flux-density threshold for detection, gravitational lensing allows for galaxies with intrinsically fainter (unlensed) flux densities to be detected and studied. This strategy was employed in the first SMG surveys (Smail et al., 1997), and continues to be used to probe the population statistics at fainter levels than could be observed otherwise (Knudsen et al., 2008; Johansson et al., 2011).

The research presented in Chapter 4 uses deep  $870\mu\text{m}$  images of massive galaxy

clusters. In this waveband, the data contain SZE increment signal from the clusters superimposed on the gravitationally-lensed images of thermal dust emission from background SMGs. Disentangling the SZE signal from the thermal dust emission is accomplished using information at multiple frequencies and multiple spatial scales.

### 1.3.5 Nonthermal emission in galaxy clusters

Some massive merging cluster systems contain populations of high-energy cosmic-ray electrons with Lorentz factors  $\Gamma \sim 1000\text{--}5000$  that produce radio-band synchrotron radiation on large ( $\sim 1$  Mpc) scales. These non-thermal radio features are categorized as (1) radio halos with diffuse emission filling much of the cluster volume, and (2) radio relics with extended filamentary emission near the cluster outskirts.

The diffusion speed of the electrons through the ICM (of order  $100\text{ km s}^{-1}$ , set by the Alfvén speed in the magnetized plasma) is low compared to their radiative lifetimes ( $\sim 10^8$  yr), so the radiating particles are unlikely to be supplied by active cluster galaxies and must be energized locally (Ferrari et al. 2008). There are two categories of theories that try to explain the non-thermal emission of radio halos and relics. The first category includes what are called “primary models.” Primary models predict that the cosmic-ray electrons are accelerated by shocks or turbulence in the ICM. Examples include the first-order Fermi process in strong shocks (Ensslin et al., 1998) and the turbulent reacceleration process in stochastic MHD turbulence (Brunetti et al., 2001). In both scenarios, the initial seed population of low/moderate energy free electrons is provided by active galaxies in the cluster and/or by populations of previously accelerated electrons. In primary models, energy injection depends on the local state of the ICM gas. Therefore, they generally predict that the emission strength and spectral shape should be spatially associated with cluster turbulence or shocks.

The second category includes what are known as “secondary models,” which predict

that the cosmic ray electrons are created by inelastic hadronic collisions between thermal protons in the ICM and relativistic cosmic-ray protons. The cosmic-ray protons have a much longer radiative lifetime, and are thought to be accelerated during mergers throughout the lives of clusters (Dennison, 1980). In secondary models, the energies of the proton-proton collisions do not depend on the local ICM properties. Therefore, the resulting emission should be spherically symmetric and the spectral shape should be constant throughout the cluster.

Primary models are the favored explanation for both radio relics and halos. Radio relics have properties that are broadly consistent with the first-order Fermi process occurring at shock fronts in the ICM. Radio halos are also observed to have asymmetric morphologies and spatially-varying spectral shapes, which are predictions of primary models. It was also recently found that the  $\gamma$ -ray flux from the Coma cluster, the most luminous and best-studied radio halo cluster, is inconsistent with predictions of secondary radio-halo models (Brunetti et al., 2012).

### Spectral aging

Higher-energy electrons radiate their energy away through synchrotron radiation more rapidly than lower-energy electrons (Equation 1.15). Therefore, the synchrotron spectrum steepens as time passes; this process is known as spectral aging. In radio relics, spectral aging can be used to identify the down-stream region of a shock front in the ICM, and also can help provide an estimate of the ICM magnetic field strength at the location of the relic.

The time required for an electron to radiate away its energy through synchrotron radiation  $t_{syn}$  is estimated by the electron's total energy divided by its total radiating power (e.g., Equation 1.15):

$$t_{syn} = \frac{\gamma m_e c^2}{\frac{1}{6\pi} \sigma_T c \beta^2 \gamma^2 B^2}. \quad (1.29)$$

After substituting  $\gamma$  for the critical photon energy (Equation 1.14), and taking into account the  $k$ -correction and the energy losses through collisions off CMB photons, we get (e.g., van Weeren et al., 2011b)

$$t_{syn} = 3.2 \times 10^{10} \frac{B^{1/2}}{B^2 + B_{\text{CMB}}^2} \frac{1}{\sqrt{\nu(1+z)}} \text{ yr}, \quad (1.30)$$

where  $B$  and  $B_{\text{CMB}}$  are in  $\mu\text{G}$  and  $\nu$  is in  $\text{MHz}$ .  $B_{\text{CMB}}$  is the magnetic field strength that would produce a synchrotron radiative power equivalent to the energy lost through inverse Compton scattering off CMB photons at redshift  $z$ ,  $B_{\text{CMB}}(z) \simeq 3.2(1+z)^2 \mu\text{G}$ . When combined with the observed width of the radio relic  $d_{\text{relic}}$ ,  $t_{syn}$  provides an estimate of the shock velocity  $v$  through the relation  $d_{\text{relic}} = v t_{syn}$ .

An independent estimate of the shock velocity is gained by inspecting the radio relic spectral index  $\alpha$ . The spectral index is a function of the particle energy distribution index  $p$  ( $dN \propto E^{-p} dE$ ), which is related to the shock compression ratio  $r = \rho_f / \rho_i$  in a first order Fermi process (Drury, 1983):

$$p = \frac{r+2}{r-1}. \quad (1.31)$$

The compression ratio  $r$  is a function of the shock Mach number  $\mathcal{M}$  (Longair, 2011):

$$\frac{1}{r} = \frac{\gamma-1}{\gamma+1} + \frac{2}{\gamma+1} \frac{1}{\mathcal{M}^2}. \quad (1.32)$$

Finally, the Mach number can be converted to a shock velocity using the sound speed  $c_s$  of the gas, which can be provided by X-ray observations. The sound speed

$$\begin{aligned} c_g &= \sqrt{\gamma k T_{\text{gas}} / m} \\ &\simeq 400 \sqrt{\frac{k T_{\text{gas}}}{1 \text{ keV}}} \text{ km s}^{-1}, \end{aligned} \quad (1.33)$$

where in an ionized gas  $m$  is the mass of a proton and  $\gamma = 5/3$ .

After combining all information one can solve for the magnetic field strength  $B$  at the location of the relic. This powerful technique allows measurements of the magnetic

field perpendicular to the line of sight at great distances from the cluster center (e.g., van Weeren et al., 2010).

### Rotation measure

The polarization angle of a linearly polarized electromagnetic wave, defined as

$$\Psi = 1/2 \tan^{-1}(U/Q) \quad (1.34)$$

in terms of the Stokes parameters  $Q$  and  $U$ , will rotate as it travels through a magnetized plasma. This effect is known as Faraday rotation, and can be used to probe the magnetic field strength parallel to the line of sight. The measurement of Faraday rotation is complementary to the above technique using spectral aging, which measures of magnetic field intensity perpendicular to the line of sight.

The amount of Faraday rotation is given by  $\Psi_{\text{obs}} - \Psi_{\text{emit}} = \text{RM} \lambda^2$ , where  $\lambda$  is the observing wavelength and RM is the rotation measure given by Burn (1966) as

$$\text{RM} = 0.81 \int n_e B_{\parallel} dl \text{ rad m}^{-2}, \quad (1.35)$$

with  $n_e$  in  $\text{cm}^{-3}$  and  $B$  in  $\mu\text{G}$ . The rotation measure is a well-defined quantity for a single source of polarized radiation behind a screen of magnetized plasma. Given a dataset consisting of Stokes parameters  $Q$  and  $U$  at a series of wavelengths  $\lambda_i$ , RM can be measured by fitting a line to the plot of  $\Psi$  versus  $\lambda^2$ . For multiple sources of polarized radiation along the line of sight, each subjected to different amounts of rotation measure, it is necessary instead to solve for the Faraday spectrum  $F$ . The Faraday spectrum gives the total polarized flux density as a function of Faraday depth, and can be derived from the  $(Q, U, \lambda^2)$  dataset using a technique called RM-synthesis (Brentjens & de Bruyn, 2005). In Chapter 5, RM-synthesis is used to measure the RM structure across the radio relic in the high-redshift cluster merger El Gordo.

## Chapter 2

### A Deep 1.2 mm Map of the Lockman Hole North

#### 2.1 Introduction

Over a decade ago, measurement of the cosmic infrared background (CIB: Puget et al., 1996; Fixsen et al., 1998) revealed that approximately half of all of the light in the universe emerges at far-infrared wavelengths due to reprocessing by dust (e.g., Dole et al., 2006). With the advent of the Submillimeter Common-User Bolometer Array (SCUBA; Holland et al., 1999), it became clear around the same time that not all of this reprocessed emission originated in galaxy populations that could be easily detected with optical telescopes. Instead, SCUBA surveys at  $850\,\mu\text{m}$  revealed the existence of a population of bright submillimeter galaxies (SMGs; Smail et al., 1997; Barger et al., 1998; Hughes et al., 1998) with faint or undetectable optical counterparts. Optical spectroscopy of the least obscured members of the population (Ivison et al., 1998, 2000), followed up by detections of CO emission (Frayser et al., 1998, 1999), confirmed that SMGs were indeed a high- $z$  population. Their faint X-ray counterparts (Alexander et al., 2003, 2005a) as well as mid-infrared spectroscopy (Valiante et al., 2007; Menéndez-Delmestre et al., 2007, 2009; Pope et al., 2008) indicated that they were not predominantly powered by accretion, but rather by star formation. These observations suggest that SMGs may play an important role in the cosmic star formation history. However, the details of their star formation remain uncertain. Different schools of thought exist about whether SMGs are major mergers (e.g., Conselice et al., 2003;

Narayanan et al., 2009, 2010) or host bursts triggered by the inflow of intergalactic gas along filaments (Davé et al., 2010). Likewise, galaxy evolution models that consider SMGs have disagreed on whether they are (Baugh et al., 2005) or are not (Hayward et al., 2011) forming stars with an unusually top-heavy initial mass function (IMF).

Understanding how SMGs fit into the overall history of cosmic star formation has been impeded by their high obscuration in the optical and the coarse angular resolution of the (sub)millimeter bolometer arrays used to detect them. An important advance came with the use of deep, high-resolution radio continuum maps with the Very Large Array (VLA) to localize SMGs on the basis of the far-IR/radio correlation. Keck followup of radio-preselected SMG samples (Ivison et al., 2002; Chapman et al., 2003, 2005) broke the logjam for determining SMGs’ redshifts, allowing a dramatic expansion of SMG samples with CO-confirmed spectroscopic redshifts and spatially resolved maps (Neri et al., 2003; Greve et al., 2005; Tacconi et al., 2006). Although these developments have been important and exciting, there are a number of caveats on the current state of our knowledge. First, not all SMGs have counterparts in VLA maps of typical depths, and not all that have counterparts yield optical spectroscopic redshifts; this has led to uncertainties in the population’s overall redshift distribution, especially at the high- $z$  end. Second, we have come to realize that the  $850\,\mu\text{m}$  waveband at which the influential early SCUBA work was done does not give us a complete picture of all dusty galaxy populations at high redshift: observations at shorter/longer wavelengths preferentially detect populations with higher/lower dust temperatures and/or lower/higher redshifts (e.g., Chapman et al., 2004; Valiante et al., 2007; Magnelli et al., 2010; Chapman et al., 2010; Magdis et al., 2010). Finally, with the exception of highly lensed systems, our direct knowledge is restricted to bright individual detections for which limited sensitivity and angular resolution (vs. confusion) are not fatal obstacles. Understanding the lower- $L_{\text{IR}}$  galaxy populations that produce the bulk of the CIB is challenging, and efforts to

determine their properties are not always consistent with the CIB’s normalization (e.g., Scott et al., 2010).

To fill in some of the gaps in our knowledge, we need to obtain deep mapping at multiple (sub)millimeter wavelengths, at high angular resolution, over a large area that has good multiwavelength coverage (and especially, very deep radio continuum data). This combination of properties can in principle allow us to (a) optimize the identification of counterparts at other wavelengths, and therefore the determination of redshifts and the assessment of SMGs’ detailed evolutionary states; (b) defeat cosmic variance and optimize sensitivity to clustering and large-scale structure, a key first step in connecting the properties of SMGs to the properties of the dark matter halos that host them; and (c) strongly constrain the parameters of SMG number counts down to faint flux densities, so that we can accurately compare the census of obscured star formation to the constraint of the CIB.

In this paper, we report 1.2 mm observations at  $11''$  resolution of a unique deep field that satisfies many of these needs. Our map is both larger and more sensitive than previous deep maps made at 1.2 mm (e.g., Greve et al., 2004; Bertoldi et al., 2007; Greve et al., 2008), and compared to recent work done with other instruments, displays a competitive combination of attributes. Surveys made at 1.1 mm using ASTE/AzTEC have mapped equal or wider fields to a greater depth, but with much lower spatial resolution (e.g., Scott et al., 2010; Hatsukade et al., 2011). Maps using JCMT/AzTEC and APEX/LABOCA generally achieve wider fields or greater depths, but not both, and also have coarser spatial resolution (e.g., Scott et al., 2008; Perera et al., 2008; Weiß et al., 2009; Austermann et al., 2010). The powerful combination of resolution, depth, and extent of our MAMBO map, together with the rich supplementary data available for our target field, make it a powerful tool for studying the properties of SMGs.

Our map lies within the Lockman Hole North (LHN) field, centered at 10:46:00



and +59:01:00 (J2000), which was one of the targets of the *Spitzer* Wide-Area Infrared Extragalactic (SWIRE) survey (Lonsdale et al., 2003). In addition to SWIRE coverage in all four IRAC and all three MIPS bands, the LHN has been the subject of extremely deep 20 cm continuum mapping with the Very Large Array (VLA) by Owen & Morrison (2008), who produced an ABCD configuration synthesis image with a central  $1\sigma$  RMS sensitivity of  $2.7\,\mu\text{Jy}$ . These data have been further supplemented by 90 cm VLA mapping (Owen & Morrison, 2009), 50 cm GMRT mapping (Fiolet et al., 2009; Owen, 2013a), deep *Spitzer*  $24\,\mu\text{m}$  imaging (Owen, 2013b), optical spectroscopy with WIYN (Owen & Morrison, 2009), X-ray imaging from the *Chandra*/SWIRE survey (Polletta et al., 2006; Wilkes et al., 2009), and determination of photometric redshifts from multicolor optical and near-IR imaging (Strazzullo et al., 2010). The LHN is also one of the targets of the *Herschel* Multi-tiered Extragalactic Survey (HerMES; Oliver et al., 2010).

## 2.2 Observations

We used the 117-element Max-Planck millimeter bolometer (MAMBO) array (Kreysa et al., 1998) at the IRAM 30 m telescope to obtain on-the-fly mapping of the LHN at an effective wavelength of 1.2 mm. Our observations were obtained over the course of five semesters from 2006 through 2010 (Table 2.1). Due to telescope control software problems during the first two semesters – an error in computing corrections for atmospheric refraction, which undermined the quality of the pointing during the first semester, and tracking jitter that undermined map reconstruction during both semesters – we have restricted our initial analysis (e.g., §2.4) to a “best” map that includes only the data from our final three semesters of observations. We have also constructed a “full” map using data from all five semesters, whose reliability we can validate based on comparison with the “best” map (§2.5.2), and which we therefore use for our analysis of the

Table 2.1. MAMBO observations

Season	Maps	Hours	Tracking jitter?	Bad refraction correction?	Chop throws (arcsec)
2006 winter	76	78.9	X	X	36/48
2008 summer	12	12.3	X		42/36
2008 winter	39	40.3			42/36
2009 summer	8	8.0			42/36
2009 winter	52	53.0			42/36
Total “best”	99	101.3			
Total “full”	183	192.5			

Note. — “Best” data use maps from winter 2008, summer 2009, and winter 2010. “Full” data use maps from all seasons in the table.

bright source population in the field. 101.3 hr and 192.5 hr of data were combined to produce the “best” and “full” maps with areas of  $514 \text{ arcmin}^2$  and  $566 \text{ arcmin}^2$ , and average depths of  $0.90 \text{ mJy beam}^{-1}$  and  $0.75 \text{ mJy beam}^{-1}$ , respectively.

During all five semesters, our MAMBO data were acquired during the weeks that IRAM dedicates to pooled observations of multiple bolometer projects. As a result, most of our data were taken with 250 GHz zenith opacity  $\leq 0.3$ , low sky noise, and essentially no cloud cover. Observations were limited to LST ranges when the LHN had elevation  $\geq 40^\circ$  (to minimize opacity corrections and pointing anomalies) and  $\leq 80^\circ$  (to avoid slewing errors and sudden accelerations of the MAMBO array). We built up coverage of our field by making many small  $\sim 300'' \times 320''$  (azimuth  $\times$  elevation) maps, each of which required 41 minutes to complete. The pointing centers of these small maps were arranged in a rectangular grid with  $2'$  spacings between map centers.

We planned the observations so that before (and usually after) each 41-minute map, the telescope was pointed on a nearby quasar— typically J1033+609 at a distance of  $1.9^\circ$  from field center, with  $S_{1.2 \text{ mm}} \sim 0.3 \text{ Jy}$ . Every 1–2 maps, a skydip was performed to

measure the zenith opacity, confirm that weather conditions remained good, and allow the interpolation of opacity corrections during the maps themselves. Standard flux calibrators were observed roughly every four hours; these coincided with large slews, to force resets of the telescope’s inclinometers. Focus measurements on bright quasars or planets were made at the beginning of each observing session as well as after sunrise and sunset. We required all of these calibrations so as to minimize pointing errors and anomalous refraction, as is important for the detection of faint point sources in a wide-area map.

The IRAM 30 m uses a chopping secondary mirror to subtract low-frequency sky noise from on-the-fly MAMBO maps. This chopping gives the telescope an effective double-beam point spread function (PSF) on the sky, with one positive and one negative beam separated in azimuth and symmetric about the nominal pointing center. During shift-and-add (SAA) reconstruction (see §2.3), negative-beam data are inverted and combined (for a given sky position) with their positive-beam counterparts. The end result is a triple-beam pattern that is a well-defined function of position for any single observation: two negative sidelobes bracket a positive beam in azimuth. The SAA algorithm thus conserves the mean flux of the observations, in that the negative sidelobes together contain as much integrated flux as the positive beam. When many observations are combined into a single mosaicked image, the effective PSF is a superposition of many triple-beam patterns that can vary substantially with position.

Since a given sky position within the LHN usually falls within several of our small maps, varying the chop throw and scan direction tends to scatter the negative flux into a uniform annulus around the positive central Gaussian, reducing its peak intensity and minimizing its deleterious effects on the fluxes of nearby pixels. We therefore (a) used different chop throws for alternating columns in our grid of pointing centers, and (b) recorded the scan direction of each map in equatorial coordinates, so that observers

(to the best of their ability) could observe new grid positions at LSTs such that scan directions would not match those of (existing) adjacent maps. In the central regions of our final maps (i.e., where we extract sources), peak intensities of the negative sidelobes reach only 5% of the peak positive flux thanks to our adoption of these strategies.

During our first two semesters of observations, we obtained maps of 88 grid positions out of 100 in a  $10 \times 10$  grid centered on the LHN field center stated in §2.1. During our last three semesters, which contribute to the “best” map, we observed 97 positions of 99 in a  $9 \times 11$  grid, extending  $2'$  farther east but  $2'$  less far south than the original grid, as well as two additional grid locations in the southeast corner. Between the first and second semesters, we swapped which sets of pointing centers were observed with which chop throws ( $36''$  and  $48''$  throws vs.  $42''$  and  $36''$  throws for alternating columns). Due to the differences in spatial coverage and weather conditions during the observations, the areas where the “best” map and the “full” map are respectively deepest overlap but do not match perfectly (see Figure 2.2).

## 2.3 Data reduction

### 2.3.1 Signal maps

The raw bolometer time stream data were reduced using Robert Zylka’s MOPSIC<sup>1</sup> pipeline, which is distributed in parallel with IRAM’s GILDAS package. MOPSIC is the standard package for reducing deep MAMBO on-the-fly maps (see e.g., Greve et al., 2004; Voss et al., 2006; Bertoldi et al., 2007; Greve et al., 2008). We now briefly outline the steps of the MOPSIC reduction pipeline; for further details see Greve et al. (2004). The pipeline removes spikes in the time stream data stronger than  $5 \times$  the instantaneous bolometer RMS noise. It also subtracts a third-order polynomial baseline in time and

---

<sup>1</sup> see <http://www.iram.es/IRAMES/mainWiki/CookbookMopsic>

performs correlated signal filtering on the bolometer time streams to identify and remove foreground atmospheric emission that affects many bolometers simultaneously. Each bolometer is correlated with an annulus of neighboring bolometers within a  $150''$  radius, and the average signal of the twelve most highly correlated bolometers is subtracted away. The filtered time streams are then binned into  $3.5'' \times 3.5''$  pixels, and a signal map is reconstructed using the SAA algorithm. The individual signal maps are combined into a mosaic image by averaging the map flux density at each pixel weighted by the local inverse variance. Our “optimally filtered” signal map (Figure 2.1) was created by applying a PSF-matched filter to the final mosaic image (§2.5.1).

In addition to the signal map, the MOPSIC pipeline also produces a weight map that is locally proportional to the inverse variance in the signal map. By enforcing that the Gaussian distribution of the S/N map pixel distribution has a standard deviation of unity, we normalize the weight map so that it can be used to find the local RMS noise,  $\sigma = 1/\sqrt{W}$ , in the image (see Figure 2.2). Using the weight map as a guide to find the local RMS noise for a detection is more robust than using the nearby pixels themselves, because locally the pixels are affected by the negative residual sidelobes of SAA reconstruction, as well as those of other bright nearby sources.

### 2.3.2 Noise maps

Because of the telescope’s effective triple-beam PSF, each source in the field injects negative as well as positive flux into the map. To generate realizations of source-free maps, hereafter referred to as “noise maps,” we removed the negative and positive flux from undetected as well as bright sources using two different techniques. We go on to use the different results for different purposes.

We constructed the first type of noise map with a technique common in MAMBO data analysis (see, e.g., Greve et al., 2004; Bertoldi et al., 2007; Greve et al., 2008),

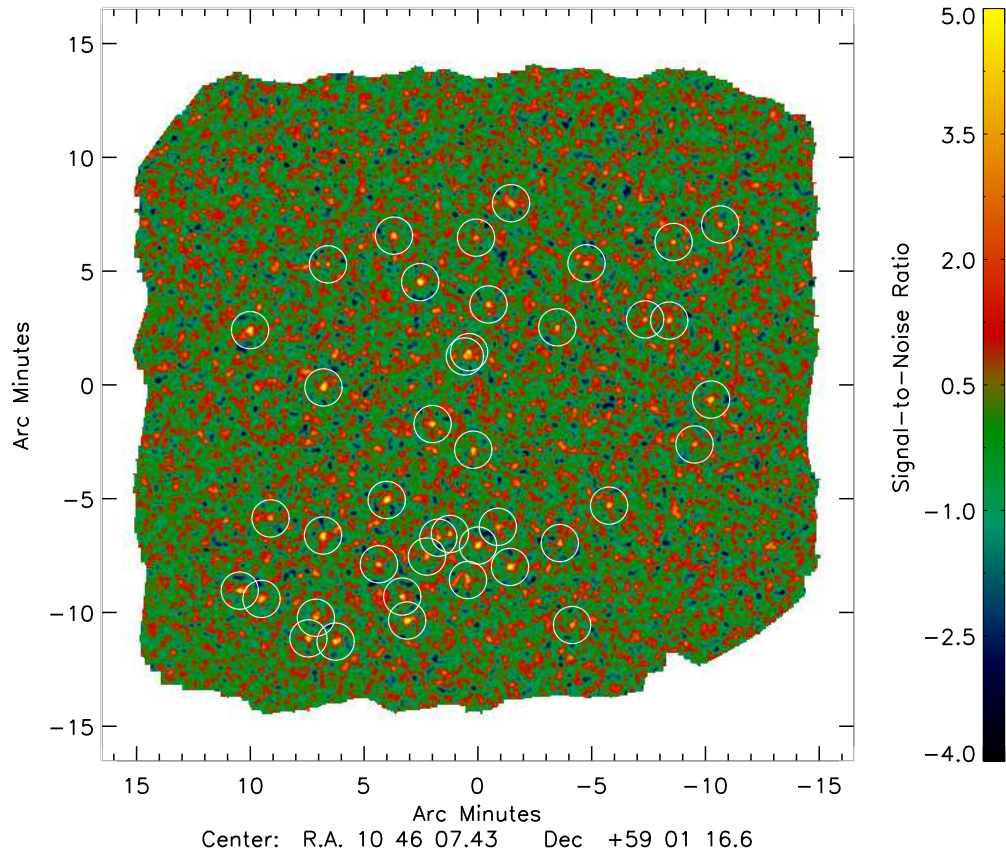


Figure 2.1: The complete, optimally filtered S/N map of the “full” dataset, with white circles showing the locations of our 41 detections with  $S/N > 4.0$ .

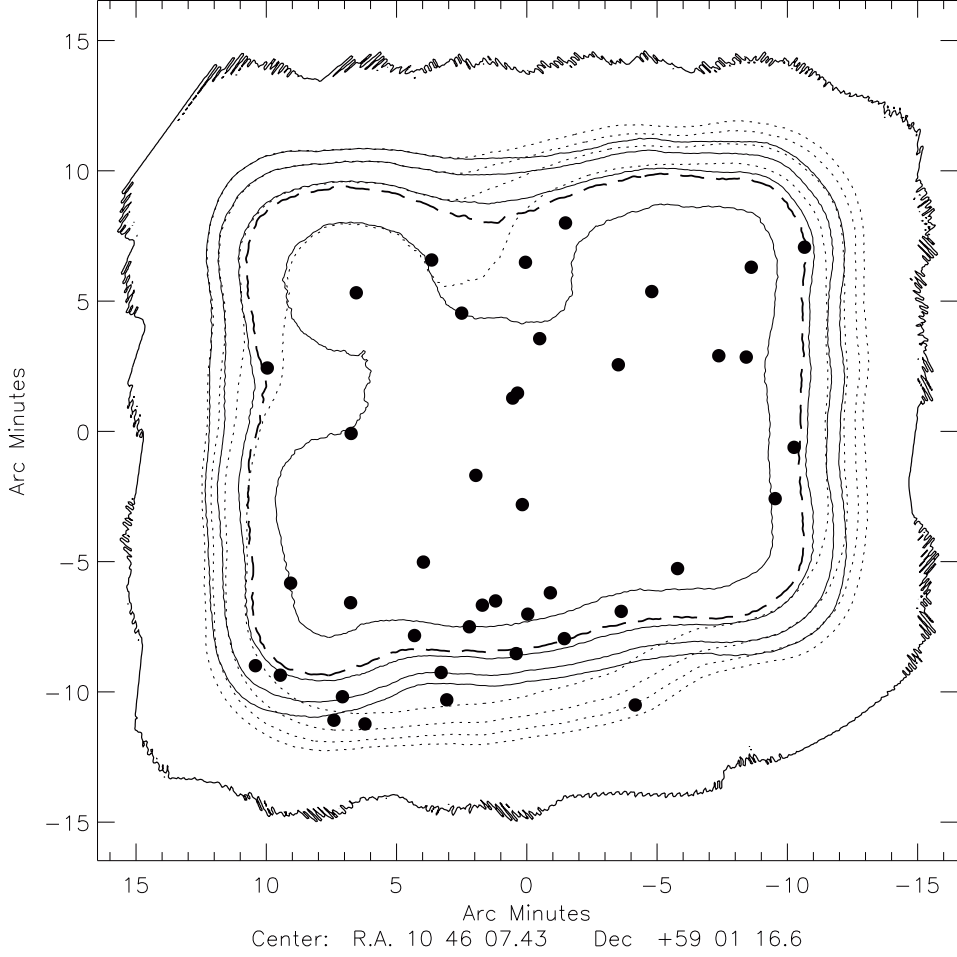


Figure 2.2: Weight map. Contours denote post-filtering RMS noise levels of 0.8, 1.0, 1.2, and 1.4  $\text{mJy beam}^{-1}$  in the “best” data (solid contours) and the “full” data (dotted contours). Thick dashed contour shows the map region used for the  $P(D)$  analysis of the “best” data. Circles show the locations of detected sources with  $S/N \geq 4.0$ . The thick outer edge shows the extent of the full map. The effective areas comprising the “best” and “full” maps (RMS noise  $< 1.5 \text{ mJy beam}^{-1}$  after filtering) are 514 and 566  $\text{arcmin}^2$ , respectively.

using the data reduction pipeline to scramble the known locations of the bolometers within the image plane. During reconstruction of the time stream data, this has the effect of smearing the flux from any one source into an area on the sky of approximately  $200 \text{ arcmin}^2$ , reducing the intensity of the source’s peak flux contributions by a factor of  $\sim 10^3$  and making the peak flux contribution from our strongest sources  $\sim 200$  times fainter than the RMS noise. Because the telescope’s chopping ensures that the mean of the map is zero, there is no residual baseline increase as the negative flux contributions are identically smoothed. These “shuffled noise maps” are simple to construct, but it is cumbersome to produce large numbers of them since each requires a full reduction of the data using the MOPSIC pipeline. Therefore, we use the shuffled noise maps only to estimate the noise of our “full” data during source extraction (§2.5.1) as well as in the Monte Carlo simulation of completeness (§2.5.5).

We needed to develop a different technique for creating noise maps in order to quickly generate thousands of independent noise realizations of chopped data for our  $P(D)$  analysis. For this we subtracted subsets of the data that are “jackknifed” in the sense that we remove fractions of the original data first. One *full* image of our field is created using the data from only *one* bolometer in the array at a time. All bolometers other than the one of interest are masked away after the correlated signal filter is applied, so the data still receive the benefit of correlated sky noise subtraction. Two half-sets of these images are then selected at random and subtracted from each other to produce one realization of noise. This technique is similar to the jackknifing by scan commonly used for AzTEC data (see, e.g., Scott et al., 2008, 2010; Perera et al., 2008; Austermann et al., 2010), in that each jackknifed subset uses the scanning information of every available map. Use of this information is especially important for our chopped data if we are to remove negative flux artifacts from the triple-beam PSF as well as positive flux. These “jackknifed noise maps” are more amenable to mass production,



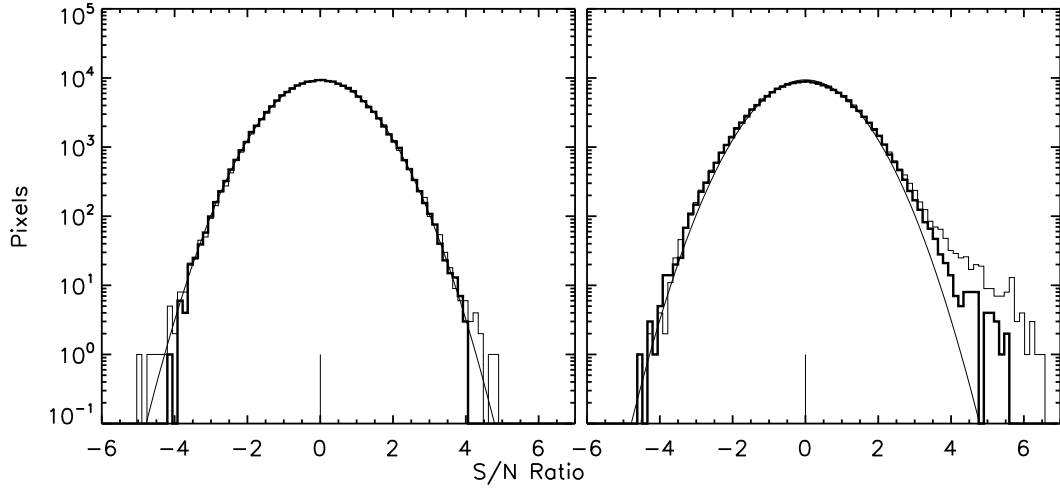


Figure 2.3: Pixel flux distributions of the S/N maps. Left: Histograms are shown for both shuffled (thin) and jackknifed (thick) noise maps. Right: S/N map histogram for the “best” map (thick) and the “full” map (thin). Over-plotted in both panels is a Gaussian function with unit standard deviation and zero mean, normalized to the area under the histograms. All maps have a mean value consistent with zero (shown as the vertical line segment), enforced by the chopped observing mode of the IRAM 30m telescope and SAA reconstruction. The “full” map has more pixels with high S/N because it reaches a higher sensitivity. The histograms were created with maps trimmed to a noise level of  $1.5 \text{ mJy beam}^{-1}$ .

and are guaranteed to remove all contributions from a source however faint, so they are used in our pixel flux distribution (PFD) analysis (§2.4) and in our Monte Carlo simulations to estimate numbers of spurious detections (§2.5.4).

The PFDs for S/N maps created with both jackknifed and shuffled noise exhibit random Gaussian noise to high precision (Figure 2.3), with reduced chi-square for standard normal distribution fits of  $1.0 \pm 0.2$  and  $1.2 \pm 0.2$ , respectively.

### 2.3.3 Simulated maps

Our simulated sky maps are constructed by populating noise maps with simulated sources. Careful construction of these maps is important for the fluctuation analysis

described below (§2.4), for which our method relies entirely on our ability to authentically reproduce the signal from the MAMBO array so as to faithfully reproduce the PFD. Thus, when adding sources into a noise map, we need to take into account the position-dependent negative sidelobes as well as the position-independent positive flux profile for each injected source.

To handle the varying PSF properly, we take an approach similar to that of Greve et al. (2008) and model the changes in the PSF explicitly as a function of position. We use the MOPSIC pipeline script `map_negres.mopsic`, which will calculate the expected negative residual pattern on the sky in equatorial coordinates for a given set of observations and an ideal, gridded, input source model. As an input we used an array of ideal Gaussian point source profiles, each with  $11''$  FWHM, spanning the entire field and spaced as closely as possible without having the sidelobes overlap. This minimum spacing is set by our larger chop throw ( $42''$  for all of our “best” data and the overwhelming majority of our “full” dataset). The result is an array showing the full PSF near any location in the map (see Figure 2.4). Because the  $\sim 84''$  spacing is less than the  $300''$  extent of each individual map and the  $120''$  separation between map pointing centers, the PSF morphologies change slowly from one to the next. We thus generate an authentic point source response in a simulated map by using the closest available PSF relative to the position of a given injected source.

## 2.4 $P(D)$ analysis of the pixel flux distribution

We constrained the 1.2 mm number counts below our nominal sensitivity and confusion limits by performing a fluctuation analysis, also known as a  $P(D)$  analysis (Condon, 1974). The  $P(D)$  analysis has the advantage of using information from the entire PFD of the map (see Figure 2.5) to constrain the number counts, rather than using only those pixels above the source detection threshold (e.g., by counting bright sources).

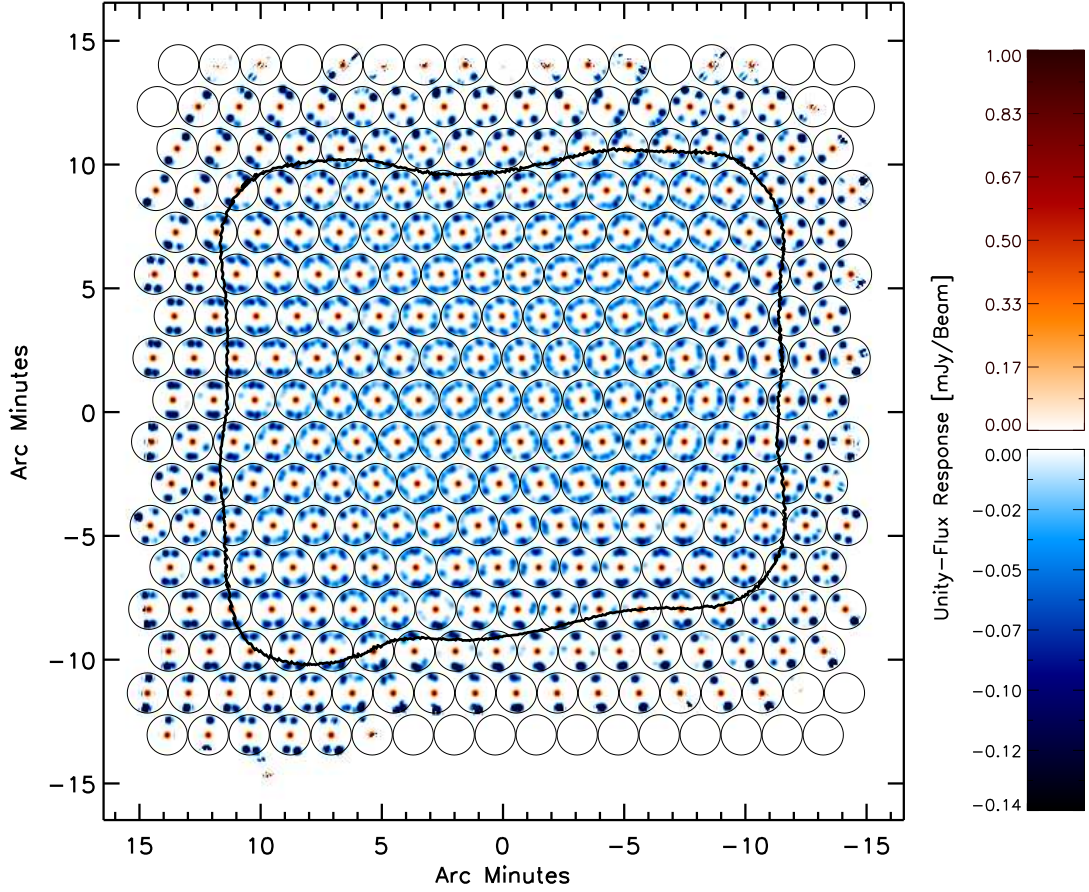


Figure 2.4: The effective PSF (including negative residuals) as a function of position across our “best” map. Red/blue represents a positive/negative signal response. The thick solid contour encloses the area where the “best” map has RMS noise  $< 1.5 \text{ mJy beam}^{-1}$ . The map is centered on coordinates  $10^{\text{h}}46^{\text{m}}43^{\text{s}}$ ,  $+59^{\circ}01'16''.6$  (J2000).

This distinction makes the  $P(D)$  analysis robust against the small number statistics of counting detections in the map. Additionally, the nature of the Monte Carlo simulation described below allows us to minimize uncertainties in flux boosting and completeness, as well as the effects of confusion and source blending, because they are built into the simulation through the injection of model sources. These benefits have led Monte Carlo simulation  $P(D)$  analyses (e.g., Maloney et al., 2005; Scott et al., 2010), as well as Markov Chain Monte Carlo Metropolis-Hastings (MCMCMH)  $P(D)$  analyses (e.g., Patanchon et al., 2009; Valiante et al., 2010; Glenn et al., 2010), to be applied to both chopped and unchopped data at many wavelengths. Our implementation of a Monte Carlo simulation  $P(D)$  analysis, which is best suited to handle our position-dependent PSF, adopts the methods of Scott et al. (2010).

The basic approach of our  $P(D)$  analysis is to parametrize the differential number counts and add a simulated map of sources obeying these number counts (along with their position-dependent negative sidelobes; see §2.3.3) to a jackknifed noise map (see §2.3.2), thereby creating a fully simulated MAMBO sky image. Because of its simple form, our initial parametrization is a single power law with normalization  $N_{4\text{mJy}}$  and index  $\delta$ , such that the differential number counts have the form

$$\frac{dN}{dS} = N_{4\text{mJy}} \left( \frac{4\text{mJy}}{S} \right)^\delta \quad (2.1)$$

We adopt this form from Laurent et al. (2005), so as to minimize the degeneracy between the normalization and slope of the number counts at the flux density of our typical significant detection ( $\simeq 4\text{mJy}$ ). Next, we optimally filter this fully simulated sky image and compare its PFD to that of the real data using the likelihood (see below) as a goodness-of-fit statistic. We then compute the average likelihood of the data for ten iterations of these model parameters, choose new parameters, and repeat the process. After filling parameter space with likelihood statistics, we identify the

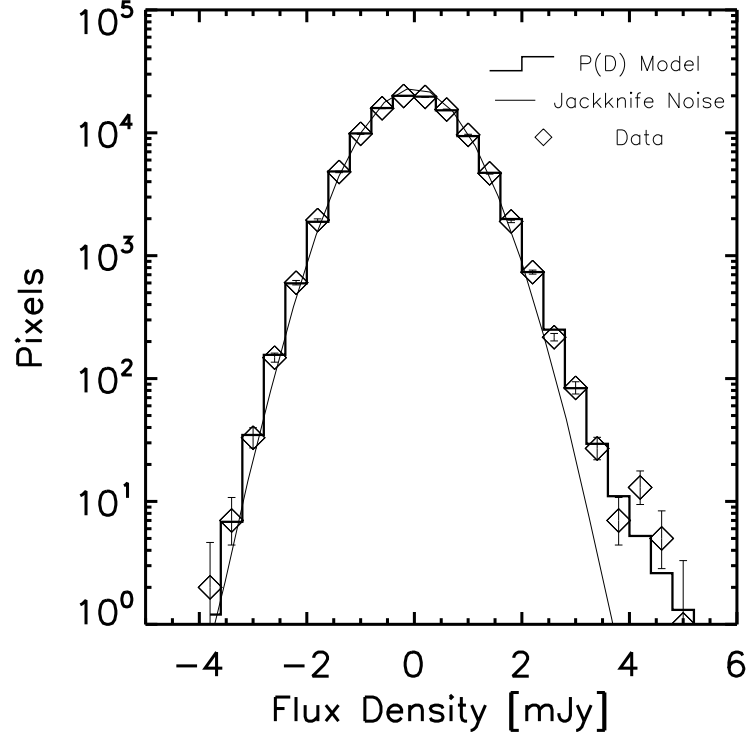


Figure 2.5: Pixel flux distribution showing the agreement between the data and the average best-fit (Schechter function) model from the  $P(D)$  analysis. Points represent the PFD of the optimally filtered “best” data. The solid histogram shows the mean PFD of 100 random sky realizations of the best fitting number counts embedded in random jackknifed noise maps. The thin curve represents the mean histogram of only the jackknifed noise maps. The single larger flux density bin that spanned 4–5 mJy for the  $P(D)$  analysis (see §2.4) is shown here broken down into small bins matching the rest of the distribution.

best-fit parameters as those giving the maximum likelihood. After the location of this peak in parameter space is identified, we return and sample this one position  $\sim 10^3$  times in order to constrain the absolute likelihood value enough to discriminate between fits using different flux density cut-off values (see below).

The likelihood for each sky realization is calculated as follows. Assuming the PFD's flux bins are uncorrelated, the probability of observing  $n_i$  pixels in the  $i$ th flux bin given an expectation value of  $\lambda_i$  is given by a Poisson distribution:

$$P(n_i|\lambda_i) = \frac{\lambda_i^{n_i} e^{-\lambda_i}}{n_i!} \quad (2.2)$$

Therefore, the natural logarithm of the probability  $P[n_i]$  of observing the full PFD  $\{n_i\}$  for a model PFD  $\{\lambda_i\}$  (the log-likelihood) is given by

$$\ln P[n_i] = \sum_i \ln \left( \frac{\lambda_i^{n_i} e^{-\lambda_i}}{n_i!} \right) = \sum_i n_i \ln \lambda_i - \ln n_i! - \lambda_i \quad (2.3)$$

We limit the comparison to bins in which  $n_i \geq 10$  and use Stirling's approximation to write the sum as

$$\ln P[n_i] \simeq \sum_i n_i - \lambda_i - n_i \ln \left( \frac{n_i}{\lambda_i} \right) \quad (2.4)$$

In reality our histogram bins are *not* uncorrelated, since our beam solid angle is  $\sim 10\times$  larger than the area of one pixel; thus, this expression will serve simply as a comparative metric for choosing a set of best-fitting parameters. The properly calibrated error bars for this estimate can then be found via a Monte Carlo simulation using synthetic images generated from the best-fit model.  $P[n_i]$  is therefore a function over the two-dimensional parameter space of  $(N_{4\text{ mJy}}, \delta)$ , within which the best-fitting model parameters are those that minimize  $-\ln P[n_i]$ .

We apply the  $P(D)$  analysis to the region in the “best” map where the local RMS noise  $\sigma \leq 1.25 \text{ mJy beam}^{-1}$  before filtering (see Figure 2.2). This threshold was chosen to maximize the discriminating power of the simulation. If the noise threshold is very low, the region used for analysis has very high sensitivity, but there are fewer pixels

available for comparison. If the noise threshold is too high (e.g., we use the full extent of the “best” map), too many regions with differing local noise properties are included, and the signal from the interior of the map is washed out. Our choice of threshold represents a compromise between these two limits, including as many pixels in the analysis as possible while keeping their noise properties as uniform as possible.

Our initial expression of the PFD in terms of 15 bins between  $-3.5$  and  $+4.0$  mJy beam $^{-1}$ , chosen so that all flux bins had  $\geq 10$  pixels, failed to constrain the model parameters with a unique maximum likelihood. Because the brightest (and most model-constraining) pixels in the histogram are in the sparsely populated bins above 4.0 mJy beam $^{-1}$ , our simulations produced only a best-fit *arc* in parameter space. When we increased the sensitivity to the brightest pixels by adding an additional bin spanning from 4.0 – 5.0 mJy beam $^{-1}$ , wide enough to include  $\geq 10$  pixels, a well-defined global maximum appeared along the previously degenerate arc.

In order to keep the models from diverging at low flux densities, we also imposed a faint-end cutoff in flux density,  $S_{\text{cut}}$ , which we crudely treated as a third parameter in the  $P(D)$  analysis. By stepping through the values  $S_{\text{cut}} = 0.3, 0.2, 0.1, 0.05$ , and  $0.01$  mJy, testing each with a full set of fitting parameters, we found the maximum likelihood values for the power law to be  $41.7 \pm 0.4\%$ ,  $47.7 \pm 0.2\%$ ,  $52.1 \pm 0.2\%$ ,  $53.0 \pm 0.3\%$ , and  $49.7 \pm 0.5\%$ , respectively. The fits improved steadily with decreasing  $S_{\text{cut}}$  down to 0.05 mJy but then worsened at 0.01 mJy. Thus, the overall best fitting parameters for the power law were  $N_{4\text{ mJy}} = 19.7^{+4.1}_{-8.8} \text{ deg}^{-2} \text{ mJy}^{-1}$ ,  $\delta = 3.14^{+0.14}_{-0.18}$ , and  $S_{\text{cut}} = 0.05$  mJy (we quote marginalized 68% double-sided error bars).

Our second number counts parametrization was a Schechter (1976) function of the form

$$\frac{dN}{dS} = N'_{4\text{ mJy}} \left( \frac{4\text{ mJy}}{S} \right)^{\delta'} \exp \left( -\frac{S - 4\text{ mJy}}{S'_{\text{exp}}} \right) \quad (2.5)$$

Because the full four-dimensional parameter space of the Schechter function ( $N'_{4\text{ mJy}}$ ,  $\delta'$ ,

$S'_{\text{exp}}, S'_{\text{cut}}$ ) is too large to probe with a blind grid-searching routine, we began by fixing  $S'_{\text{cut}}$  equal to the solution for the power-law model (0.05 mJy). We then alternated the  $P(D)$  analysis between varying the parameters  $(N'_{4\text{mJy}}, S'_{\text{exp}})$  and  $(N'_{4\text{mJy}}, \delta')$  until the solutions converged on the same values for all three parameters (convergence was achieved after three iterations). The initial seed guess for  $S'_{\text{exp}}$  was motivated by naively scaling the  $P(D)$  solution at 1.1 mm, found by Scott et al. (2010) using AzTEC data in the GOODS-S field ( $S'_{\text{exp}, 1.1\text{mm}} = 1.30\text{ mJy}$ ), to 1.2 mm (see §2.7.1). The results converged to the exponential scaling flux density of  $S'_{\text{exp}} = 1.05\text{ mJy}$ , which was then held fixed while we proceeded to make full searches over the parameters  $(N'_{4\text{mJy}}, \delta')$  while varying  $S'_{\text{cut}}$ .

The quality-of-fit for the Schechter function was also greatest for a flux density cutoff of  $S'_{\text{cut}} = 0.05\text{ mJy}$ . The maximum likelihood values for  $S'_{\text{cut}} = 0.2, 0.1, 0.05,$  and  $0.01\text{ mJy}$  were  $23.8 \pm 0.1\%$ ,  $26.9 \pm 0.1\%$ ,  $28.3 \pm 0.2\%$ , and  $26.7 \pm 0.4\%$ , respectively. The final set of best-fitting parameters for the Schechter function were  $N'_{4\text{mJy}} = 14.5^{+7.1}_{-2.7}\text{ deg}^{-2}\text{mJy}^{-1}$ ,  $\delta' = 1.86^{+0.20}_{-0.23}$ ,  $S'_{\text{exp}} = 1.05\text{ mJy}$ , and  $S'_{\text{cut}} = 0.05\text{ mJy}$ .

Figure 2.6 shows full 68% and 95% confidence regions around the parameters of maximum likelihood for both the power law and Schechter function parametrizations. The uncertainty contours were generated via Monte Carlo sampling (used, e.g., in Scott et al., 2010) by taking the best-fit model parameters and using them to generate additional simulated sky realizations. A  $P(D)$  analysis was then carried out on each of these realizations to recover a set of new (scattered) best-fit model parameters. This process was performed  $\sim 100$  times with the same model inputs in order to generate a likelihood density map around the best-fit model parameters.

As an additional constraint on our model fitting and a means of choosing between parametrizations, we also require that the number counts model obey the constraint of



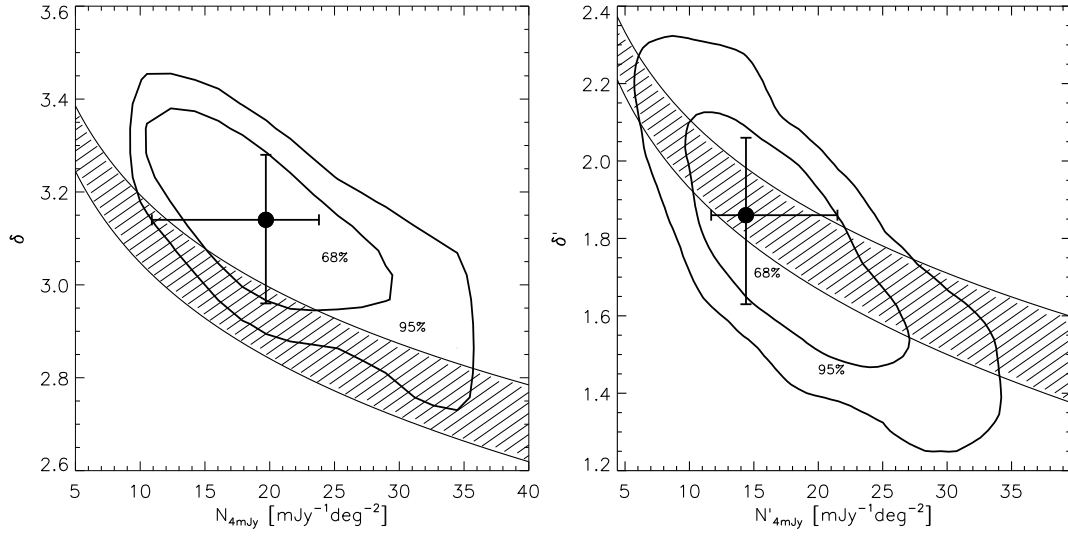


Figure 2.6: Likelihood parameter spaces for different parametrizations of the 1.2 mm differential number counts. The points mark the best fitting parameters and the marginalized 68% double-sided error bars. The contours bound the 68% and 95% confidence regions found through Monte Carlo simulations. The shaded bands show the regions in parameter space that reproduce the observed intensity of the 1.2 mm CIB, assuming a lower-limit flux density cutoff of 0.05 mJy. *Left*: Power law model, with best fitting parameters  $N_{4\text{mJy}} = 19.7^{+4.1}_{-8.8} \text{ deg}^{-2} \text{ mJy}^{-1}$  and  $\delta = 3.14^{+0.14}_{-0.18}$ . *Right*: Schechter function model, with best fitting parameters  $N'_{4\text{mJy}} = 14.5^{+7.1}_{-2.7} \text{ deg}^{-2} \text{ mJy}^{-1}$  and  $\delta' = 1.86^{+0.20}_{-0.23}$ .

the 1.2 mm CIB (see §2.7.5), which is shown as the shaded region in Figure 2.6. It is evident in Figure 2.6 that although the power law parametrization can fit our observations well, it significantly overpredicts the 1.2 mm CIB. In contrast, the Schechter function parametrization is in excellent agreement with the constraint of the CIB. We therefore adopt the Schechter function parametrization as our fiducial model (e.g., Figure 2.5) for the remainder of the paper. At the highest flux densities the Schechter function and power-law models nominally predict very different behavior; however, our fluctuation analysis is not sensitive to the number counts at flux densities higher than those of our brightest detected sources.

The fact that both the power-law and Schechter function models of the differential number counts fit best when  $S_{\text{cut}} = 0.05$  mJy suggests that the 1.2 mm number counts do not keep rising far beyond 0.05 mJy; formally, they may begin to fall between 0.05 and 0.01 mJy, or may already be decreasing by 0.05 mJy. The former case is in agreement with recent surveys of lensing clusters (e.g., Knudsen et al., 2008) that show SMG number counts increase at least as far down as  $\simeq 0.1$  mJy at  $850\ \mu\text{m}$ . At 1.2 mm, this corresponds to  $S_{1.2\text{ mm}} \simeq 0.03 - 0.04$  mJy using the submillimeter spectral indices determined from matching detections at  $850\ \mu\text{m}$ , 1.1 mm, and 1.2 mm in the GOODS-N and COSMOS fields (Greve et al. 2008; Chapin et al. 2009; Austermann et al. 2010; see §2.7.1) This result is in contrast to the analysis of Scott et al. (2010), who found that the choice of  $S_{\text{cut}}$  did not affect their results. The discrepancy may be due to the fact that their lower resolution ( $28''$  HPBW) reduces the effective depth that can be reached before sources begin crowding in the beam, thereby reducing the sensitivity of the  $P(D)$  technique.

## 2.5 Analysis of bright sources

### 2.5.1 Source extraction

We extracted sources from our “best” and “full” maps in a three-step process. First, we minimized the chi-square statistic for a two-dimensional Gaussian profile with an  $11''$  FWHM fit at each pixel center. This minimization was achieved quickly by using a matched filter convolution (see, e.g., Serjeant et al., 2003). Given a signal image  $S_{ij}$ , an image of the local RMS noise  $\sigma_{ij}$ , and a smaller array describing the telescope’s PSF  $P_{xy}$ , the chi-square statistic for a source with flux  $F$  located at pixel  $(i, j)$  can be written

$$\chi^2(F|i, j) = \sum_{xy} \left( \frac{S_{i-x, j-y} - FP_{xy}}{\sigma_{i-x, j-y}} \right)^2 \quad (2.6)$$

We ignored the position-dependent negative sidelobes when we applied the matched filter and used only the central Gaussian profile, since the negative residual flux reaches only  $\leq 5\%$  of the peak positive intensity (see Figure 2.4) in the map interior. Additionally, our significant detections are on average farther away from each other than the largest chop throw used during the observations ( $48''$ ), so their effect on our flux measurements will be less than 5% of our strongest sources’ flux densities (i.e.,  $\lesssim 0.25$  mJy).

By finding the minimum of  $\chi^2(F|i, j)$  as a function of  $F$  and determining the associated uncertainty  $\Delta F$  (Serjeant et al., 2003), we obtained

$$\frac{d\chi^2}{dF} = 0 \longrightarrow \frac{F}{\Delta F} = \frac{\sum_{xy} S_{i-x, j-y} W_{i-x, j-y} P_{xy}}{\sqrt{\sum_{xy} W_{i-x, j-y} P_{xy}^2}} \quad (2.7)$$

as the S/N of each pixel, in terms of the weight map  $W$  defined in §2.3.1. Next, we located the centroid of each source to sub-pixel precision by fitting the PSF to the region in the original signal map at the location of each significant peak in the S/N map, allowing the position of the Gaussian to vary. Figure 2.7 shows the uncertainty in this best-fit centroid position, derived via Monte Carlo simulations. For the typical

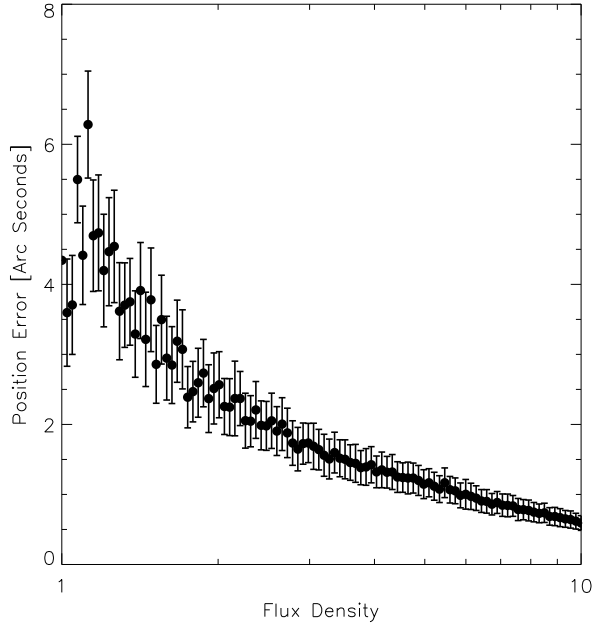


Figure 2.7: Average angular separation between injected and recovered source locations as a function of flux density. The injection process was performed 1000 times for each flux density value. The scatter increases at low flux densities because of incompleteness.

flux densities of our significant detections, the average offset between injected and recovered centroids is  $1'' - 3''$ . Finally, we computed the best-fit flux density by taking the matched-filter weighted average of the flux map, this time with the PSF kernel shifted by interpolation to the more precise location of the source centroid. After the flux density of each source was recorded, the source was removed from the map by subtracting the flux-scaled PSF from the source location before we searched for the next most significant detection.

By propagating the uncertainty in the signal image through the  $\chi^2$ -minimization process, Serjeant et al. (2003) have shown that the uncertainty in the resulting best-fit flux density at position  $(i, j)$  is

$$\Delta F(i, j) = \frac{1}{\sqrt{\sum_{xy} W_{i-x, j-y} P_{xy}^2}} \quad (2.8)$$

We find that this expression consistently *underestimates* the uncertainty in our map. The reason is simply that the derivation by Serjeant et al. (2003) implicitly assumes that the Gaussian noise in the flux image is spatially uncorrelated. In our images, the noise is correlated on a length exactly matching the FWHM of the telescope PSF, and pure noise fluctuations can be amplified along with the real point sources. In order to correct for this underestimate we (1) produce an optimally filtered image and weight map, (2) use this filtered image and weight map to make a S/N ratio map, and (3) rescale the filtered weight map such that the standard deviation of the S/N map equals unity. This empirical calibration corrects for the effects of correlated noise and produces a map with accurate post-filtered flux density uncertainties. The accuracy of the method is evidenced by its matching the *predicted* number of positive excursions in a correlated Gaussian field as a function of S/N level (see §2.5.4).

The quoted  $1\sigma$  errors (see columns  $S_{\nu}^{\text{Best}}$  and  $S_{\nu}^{\text{Full}}$  in Table 2.2) for each detection correspond to the rescaled version of  $\Delta F$  evaluated using the shuffled noise map at the location of the source (see §2.3.2). This noise map describes the Gaussian noise of the observations more faithfully than the original signal map, which overestimates the noise by  $\sim 5\%$  due to the positive and negative sidelobes from bright sources. Because our noise is well above the estimated confusion limit (§2.5.3), Gaussian random fluctuations are the dominant source of uncertainty in our measurements.

Table 2.2. MAMBO detections

ID	Source name	$S_{\nu}^{\text{Best}^a}$ (mJy)	$S_{\nu}^{\text{Full}^b}$ (mJy)	$S_{\nu}^{\text{Deboosted}^c}$ (mJy)	$P(< 0)^d$	$z$	$D_{20\text{ cm}}^e$ (arcsec)	$P_{20\text{ cm}}^f$	$S_{20\text{ cm}}^g$ ( $\mu\text{Jy}$ )	$S_{50\text{ cm}}^h$ ( $\mu\text{Jy}$ )	$S_{90\text{ cm}}^i$ ( $\mu\text{Jy}$ )	$P_{24\text{ }\mu\text{m}}^j$	$S_{24\text{ }\mu\text{m}}^k$ ( $\mu\text{Jy}$ )
S/N $\geq 4.5$													
1	MM J104700.1+590109	3.7 $\pm$ 0.8	4.1 $\pm$ 0.6	3.5 $^{+0.6}_{-0.6}$	< 0.01	2.562 <sup>l</sup>	2.0	<b>0.0025</b>	278 $\pm$ 6	490 $\pm$ 11	687 $\pm$ 72	<b>0.0018</b>	1280 $\pm$ 9
2	MM J104627.1+590546	4.5 $\pm$ 0.8	4.7 $\pm$ 0.7	3.8 $^{+0.7}_{-0.7}$	< 0.01	4.29 <sup>m</sup>	3.0	<b>0.037</b>	35 $\pm$ 6	49 $\pm$ 23 <sup>t</sup>		0.11	41 $\pm$ 6
3	MM J104631.4+585056	6.1 $\pm$ 1.8	4.7 $\pm$ 0.7	3.8 $^{+0.8}_{-0.7}$	< 0.01	1.8 <sup>n</sup>	0.5	<b>0.0001<sup>r</sup></b>	458 $\pm$ 9	937 $\pm$ 10	1633 $\pm$ 85		
4	MM J104607.4+585413	2.8 $\pm$ 0.8	3.2 $\pm$ 0.5	2.7 $^{+0.5}_{-0.5}$	< 0.01	4.4 <sup>n</sup>	0.5	<b>0.0025</b>	29 $\pm$ 3	50 $\pm$ 11			
5	MM J104725.2+590339	4.9 $\pm$ 0.9	5.2 $\pm$ 0.8	4.0 $^{+0.8}_{-0.8}$	< 0.01	3.00 <sup>m</sup>	3.4	<b>0.028</b>	51 $\pm$ 5	115 $\pm$ 10		<b>0.0099</b>	395 $\pm$ 26
6	MM J104638.4+585613	3.1 $\pm$ 0.7	2.7 $\pm$ 0.5	2.3 $^{+0.4}_{-0.4}$	< 0.01	2.03 <sup>o</sup>	2.1	<b>0.0043</b>	159 $\pm$ 5	321 $\pm$ 9	442 $\pm$ 70	<b>0.0074</b>	662 $\pm$ 8
7	MM J104700.1+585439	2.8 $\pm$ 0.7	2.8 $\pm$ 0.5	2.3 $^{+0.4}_{-0.5}$	< 0.01	4.2 <sup>n</sup>	2.0	<b>0.016</b>	41 $\pm$ 4	60 $\pm$ 10		0.10	329 $\pm$ 18
8	MM J104633.1+585159	4.5 $\pm$ 1.2	3.4 $\pm$ 0.6	2.7 $^{+0.6}_{-0.6}$	< 0.01	3.3 <sup>n</sup>	0.4	<b>0.0003</b>	97 $\pm$ 9	145 $\pm$ 10		<b>0.0022</b>	342 $\pm$ 8
9	MM J104704.9+585008	5.6 $\pm$ 1.5	5.1 $\pm$ 0.9	3.8 $^{+1.0}_{-0.9}$	< 0.01	3.9 <sup>n</sup>	0.6	<b>0.0043<sup>s</sup></b>	23 $\pm$ 5	67 $\pm$ 11			
10	MM J104622.9+585933	3.6 $\pm$ 0.7	2.9 $\pm$ 0.5	2.4 $^{+0.5}_{-0.5}$	< 0.01	2.6 <sup>n</sup>	2.1	<b>0.0083</b>	78 $\pm$ 5	153 $\pm$ 11	383 $\pm$ 73	0.14	221 $\pm$ 8
11	MM J104556.5+585317	3.5 $\pm$ 0.9	3.4 $\pm$ 0.6	2.7 $^{+0.6}_{-0.6}$	< 0.01	1.95 <sup>o</sup>	3.5	<b>0.0057</b>	314 $\pm$ 10	427 $\pm$ 9	662 $\pm$ 74	<b>0.017</b>	684 $\pm$ 7
12	MM J104448.0+590036	5.1 $\pm$ 0.9	3.5 $\pm$ 0.6	2.7 $^{+0.6}_{-0.7}$	< 0.01	2.16 <sup>m</sup>	3.0	<b>0.0049</b>	273 $\pm$ 13	421 $\pm$ 20	815 $\pm$ 140	<b>0.037</b>	597 $\pm$ 27
13	MM J104609.0+585826	2.7 $\pm$ 0.7	2.7 $\pm$ 0.5	2.1 $^{+0.5}_{-0.5}$	< 0.01	1.14 <sup>m</sup>	3.1	<b>0.0067</b>	197 $\pm$ 3	461 $\pm$ 10	1101 $\pm$ 151	0.28	128 $\pm$ 8
14	MM J104636.1+590749	4.3 $\pm$ 0.8	4.3 $\pm$ 0.8	3.0 $^{+0.9}_{-0.9}$	< 0.01	2.26 <sup>m</sup>	2.4	<b>0.0079</b>	97 $\pm$ 3	215 $\pm$ 14		<b>0.0055</b>	596 $\pm$ 7
15	MM J104728.3+585213	5.1 $\pm$ 1.1	4.5 $\pm$ 0.9	3.0 $^{+0.9}_{-1.0}$	< 0.01	2.76 <sup>m</sup>	2.4	<b>0.0044<sup>r</sup></b>	180 $\pm$ 15	245 $\pm$ 12		<b>0.0081</b>	834 $\pm$ 23
16	MM J104720.9+585151	2.3 $\pm$ 1.0	3.8 $\pm$ 0.7	2.7 $^{+0.8}_{-0.8}$	< 0.01	4.9 <sup>n</sup>	1.5	<b>0.0088</b>	47 $\pm$ 6	55 $\pm$ 15		0.13	307 $\pm$ 9
17	MM J104610.4+590242	3.4 $\pm$ 0.7	2.6 $\pm$ 0.5	2.0 $^{+0.5}_{-0.5}$	< 0.01	4.0 <sup>n</sup>	1.1	<b>0.0099<sup>s</sup></b>	27 $\pm$ 3	< 45		<b>0.025</b>	293 $\pm$ 19

Table 2.2 (cont'd)

ID	Source name	$S_{\nu}^{\text{Best}^a}$ (mJy)	$S_{\nu}^{\text{Full}^b}$ (mJy)	$S_{\nu}^{\text{Deboosted}^c}$ (mJy)	$P(<0)$	$z$	$D_{20\text{ cm}}^e$ (arcsec)	$P_{20\text{ cm}}^f$	$S_{20\text{ cm}}^g$ ( $\mu\text{Jy}$ )	$S_{50\text{ cm}}^h$ ( $\mu\text{Jy}$ )	$S_{90\text{ cm}}^i$ ( $\mu\text{Jy}$ )	$P_{24\text{ }\mu\text{m}}^j$	$S_{24\text{ }\mu\text{m}}^k$ ( $\mu\text{Jy}$ )
18	MM J104655.7+585000	4.6 $\pm$ 0.9	2.9 $^{+1.1}_{-1.1}$	2.9 $^{+1.1}_{-1.1}$	0.017	1.30 <sup>n</sup>	5.0	<b>0.024</b>	104 $\pm$ 6	202 $\pm$ 11 <sup>t</sup>	385 $\pm$ 73	<b>0.026</b>	679 $\pm$ 9
19	MM J104502.1+590404	2.6 $\pm$ 0.5	2.0 $^{+0.6}_{-0.6}$	2.0 $^{+0.6}_{-0.6}$	< 0.01	4.1 <sup>n</sup>	1.8	<b>0.020</b>	28 $\pm$ 4	47 $\pm$ 12			
20	MM J104617.0+585444	2.3 $\pm$ 0.5	1.7 $^{+0.5}_{-0.5}$	1.7 $^{+0.5}_{-0.5}$	< 0.01	> 4.6 <sup>n</sup>	5.0	0.12 <sup>s</sup>	15 $\pm$ 4	< 33		<b>0.027</b>	67 $\pm$ 8
21	MM J104530.3+590636	2.4 $\pm$ 0.5	1.8 $^{+0.5}_{-0.5}$	1.8 $^{+0.5}_{-0.5}$	< 0.01	3.1 <sup>n</sup>	0.9	<b>0.0057</b>	36 $\pm$ 3	82 $\pm$ 12		<b>0.017</b>	196 $\pm$ 8
22	MM J104603.8+590448	2.7 $\pm$ 0.6	2.0 $^{+0.6}_{-0.6}$	2.0 $^{+0.6}_{-0.6}$	< 0.01	1.44 <sup>m</sup>	3.4	<b>0.0094</b>	165 $\pm$ 5	355 $\pm$ 15	485 $\pm$ 72	<b>0.019</b>	595 $\pm$ 9
23	MM J104641.0+585324	2.2 $\pm$ 0.5	1.7 $^{+0.5}_{-0.5}$	1.7 $^{+0.5}_{-0.5}$	< 0.01	3.6 <sup>n</sup>	1.6	<b>0.016</b>	31 $\pm$ 4	56 $\pm$ 12			
24	MM J104500.5+590731	2.4 $\pm$ 0.5	1.8 $^{+0.6}_{-0.6}$	1.8 $^{+0.6}_{-0.6}$	< 0.01	3.24 <sup>m</sup>	2.3	<b>0.011</b>	67 $\pm$ 7	132 $\pm$ 10		0.089	264 $\pm$ 18
25	MM J104540.3+590347	2.3 $\pm$ 0.5	1.7 $^{+0.6}_{-0.6}$	1.7 $^{+0.6}_{-0.6}$	< 0.01	3.5 <sup>n</sup>	2.3	<b>0.036</b>	24 $\pm$ 6	53 $\pm$ 15		<b>0.0071</b>	119 $\pm$ 7
26	MM J104522.8+585558	2.5 $\pm$ 0.6	1.8 $^{+0.7}_{-0.7}$	1.8 $^{+0.7}_{-0.7}$	< 0.01	> 5.0 <sup>n</sup>			< 14	< 40		0.11	239 $\pm$ 20
27	MM J104702.4+585102	3.1 $\pm$ 0.7	2.0 $^{+0.8}_{-0.9}$	2.0 $^{+0.8}_{-0.9}$	0.018	2.9 <sup>n</sup>	0.2	<b>0.0002</b>	77 $\pm$ 12	49 $\pm$ 12		<b>0.030</b>	237 $\pm$ 9
$4.0 \leq S/N < 4.5$													
28	MM J104620.9+585434	2.1 $\pm$ 0.5	1.5 $^{+0.5}_{-0.5}$	1.5 $^{+0.5}_{-0.5}$	< 0.01	3.8 <sup>n</sup>	2.1	<b>0.029<sup>s</sup></b>	25 $\pm$ 6	< 60			
29	MM J104556.1+590914	2.8 $\pm$ 0.7	1.8 $^{+0.8}_{-0.8}$	1.8 $^{+0.8}_{-0.8}$	0.022	0.044 <sup>p</sup>	4.7	<b>0.0092</b>	307 $\pm$ 39	567 $\pm$ 85		<b>0.0012</b>	4838 $\pm$ 23
30	MM J104510.3+590408	2.2 $\pm$ 0.5	1.5 $^{+0.6}_{-0.6}$	1.5 $^{+0.6}_{-0.6}$	0.011	2.4 <sup>n</sup>	1.2	<b>0.0034</b>	74 $\pm$ 6	155 $\pm$ 10		<b>0.012</b>	56 $\pm$ 7
31	MM J104624.7+585344	2.1 $\pm$ 0.5	1.5 $^{+0.6}_{-0.6}$	1.5 $^{+0.6}_{-0.6}$	< 0.01	2.90 <sup>m</sup>	2.9	<b>0.027</b>	43 $\pm$ 3	72 $\pm$ 9		0.079	236 $\pm$ 7
32	MM J104539.6+585419	2.5 $\pm$ 0.6	1.7 $^{+0.7}_{-0.7}$	1.7 $^{+0.7}_{-0.7}$	0.023	2.40 <sup>q</sup>	5.2	0.056	46 $\pm$ 3	113 $\pm$ 9		0.059	485 $\pm$ 7
33	MM J104535.5+585044	5.2 $\pm$ 1.2	2.7 $^{+1.2}_{-1.2}$	2.7 $^{+1.2}_{-1.2}$	0.20	3.7 <sup>n</sup>	6.3	<b>0.049</b>	70 $\pm$ 9	101 $\pm$ 10		0.19	245 $\pm$ 7
34	MM J104453.7+585838	2.4 $\pm$ 0.6	1.5 $^{+0.7}_{-0.7}$	1.5 $^{+0.7}_{-0.7}$	0.022	3.5 <sup>n</sup>	3.0	<b>0.031</b>	40 $\pm$ 8	65 $\pm$ 10		0.13	76 $\pm$ 7

Table 2.2 (cont'd)

ID	Source name	$S_{\nu}^{\text{Best}^a}$ (mJy)	$S_{\nu}^{\text{Full}^b}$ (mJy)	$S_{\nu}^{\text{Deboosted}^c}$ (mJy)	$P(<0)$ <sup>d</sup>	$z$	$D_{20\text{ cm}}^e$ (arcsec)	$P_{20\text{ cm}}^f$	$S_{20\text{ cm}}^g$ ( $\mu\text{Jy}$ )	$S_{50\text{ cm}}^h$ ( $\mu\text{Jy}$ )	$S_{90\text{ cm}}^i$ ( $\mu\text{Jy}$ )	$P_{24\text{ }\mu\text{m}}^j$	$S_{24\text{ }\mu\text{m}}^k$ ( $\mu\text{Jy}$ )
35	MM J104717.9+585523	$2.4 \pm 0.6$	$2.4 \pm 0.6$	$1.5^{+0.7}_{-0.7}$	0.025	3.71 <sup>m</sup>	2.4	<b>0.014</b>	$60 \pm 5$	$68 \pm 11$		0.099	$297 \pm 23$
36	MM J104608.1+590744	$2.9 \pm 0.7$	$2.9 \pm 0.7$	$1.7^{+1.1}_{-0.9}$	0.052	4.5 <sup>n</sup>	2.1	<b>0.041<sup>s</sup></b>	$16 \pm 3$	$< 47$		0.11	$396 \pm 39$
37	MM J104610.8+585242	$2.3 \pm 0.6$	$2.3 \pm 0.6$	$1.5^{+0.8}_{-0.7}$	0.030	1.72 <sup>q</sup>	2.3	<b>0.0052</b>	$160 \pm 7$	$320 \pm 10$	$450 \pm 75$	<b>0.026</b>	$401 \pm 8$
38	MM J104444.5+590817	$2.8 \pm 0.7$	$2.8 \pm 0.7$	$1.5^{+0.7}_{-0.6}$	0.052	3.6 <sup>n</sup>	2.8	<b>0.017</b>	$68 \pm 16$	$77 \pm 10$		0.12	$153 \pm 8$
39	MM J104611.9+590231	$2.1 \pm 0.5$	$2.1 \pm 0.5$	$1.4^{+0.7}_{-0.6}$	0.023	2.6 <sup>n</sup>	2.2	<b>0.024<sup>s</sup></b>	$34 \pm 3$	$99 \pm 13$		<b>0.024</b>	$634 \pm 8$
40	MM J104658.7+590633	$3.0 \pm 0.8$	$3.0 \pm 0.8$	$1.5^{+1.2}_{-1.1}$	0.074	2.9 <sup>n</sup>	2.6	<b>0.017</b>	$56 \pm 4$	$102 \pm 11$		<b>0.032</b>	$229 \pm 8$
41	MM J104600.7+585502	$2.1 \pm 0.5$	$2.1 \pm 0.5$	$1.4^{+0.7}_{-0.6}$	0.025	2.6 <sup>n</sup>	3.1	<b>0.018</b>	$71 \pm 11$	$67 \pm 9$			



### 2.5.2 Comparison of results for best and full maps

As discussed in §2.2, control software problems during our first two semesters of observations undermined our confidence in the reliability of the resulting maps. To assess whether the “full” map could be trusted for bright source extraction, we performed two comparisons between our “full” data and observations with pristine calibration. For the first comparison, we carried out the source extraction steps described in Section 2.5.1 for *both* the “best” and the “full” datasets and compared the properties of the sources recovered from each. Specifically, we began by choosing the eight sources with  $S/N \geq 4.5\sigma$  detections in our “best” map: above this threshold, we expect to see fewer than one spurious detection (§2.5.4). All eight of these sources are recovered with  $\geq 5.0\sigma$  significance in the “full” map. Figure 2.8 shows the locations of these sources in the field, and the locations of the additional  $\geq 5.0\sigma$  detections in the “full” map. Each of the eight sources increases in significance between the “best” and the “full” maps. Additionally, all but one of the “full” map’s  $17 \geq 5.0\sigma$  sources are identified in the “best” data at lower significance. One source kept the same significance because it lies in the northeast corner of the field, where observations in the first two semesters contribute little additional sensitivity. Further, for these 17 sources, the ratio of the flux densities in the “best” and “full” maps is consistent with unity (Figure 2.9).

Next, we compared our “full” map to MAMBO on-off photometry by Fiolet et al. (2009) of *Spitzer*-selected high-redshift starburst candidates in the LHN. We tabulated the map flux densities at the positions of the 13 galaxies in their sample that lie within our map’s footprint (two of these turn up as significant detections in our “full” map; we use these sources’ non-deboosted flux densities here) and compared them to the flux densities reported by Fiolet et al. (2009). We found that the flux densities from the two significant detections as well as those from 10 of the 11 non-detections are consistent to within  $1\sigma$  (see Figure 2.10; one source is only consistent to within  $\sim 1.5\sigma$ ).

Table 2.2 (cont'd)

ID	Source name	$S_{\nu}^{\text{Best}^a}$ (mJy)	$S_{\nu}^{\text{Full}^b}$ (mJy)	$S_{\nu}^{\text{Deboosted}^c}$ (mJy)	$D_{20\text{ cm}}^e$ (arcsec)	$z^d$	$P_{20\text{ cm}}^f$ ( $\mu\text{Jy}$ )	$S_{20\text{ cm}}^g$ ( $\mu\text{Jy}$ )	$S_{50\text{ cm}}^h$ ( $\mu\text{Jy}$ )	$S_{90\text{ cm}}^i$ ( $\mu\text{Jy}$ )	$P_{24\text{ }\mu\text{m}}^j$	$S_{24\text{ }\mu\text{m}}^k$ ( $\mu\text{Jy}$ )
----	-------------	---------------------------------	---------------------------------	--------------------------------------	-------------------------------	-------	---	---	---	---	-------------------------------	--

Note. —  $P$  values in boldface type denote a likely counterpart ( $P < 0.05$ ).

<sup>a</sup>Raw flux density extracted from our “best” map (see §2.5.2).

<sup>b</sup>Raw flux density extracted from our “full” map(see §2.5.2).

<sup>c</sup>Flux density extracted from our “full” map, and corrected for flux boosting (see §2.5.6).

<sup>d</sup>Total probability that the deboosted flux density is  $\leq 0$  mJy (see §2.5.6)

<sup>e</sup>Angular separation between MAMBO detection and 20 cm counterpart.

<sup>f</sup>Probability of chance association with 20 cm counterpart.

<sup>g</sup>Flux density of 20 cm counterpart (Owen & Morrison, 2008).

<sup>h</sup>Flux density of 50 cm counterpart (Owen, 2013a).

<sup>i</sup>Flux density of 90 cm counterpart (Owen et al., 2009).

<sup>j</sup>Probability of chance association with 24  $\mu\text{m}$  counterpart.

<sup>k</sup>Flux density of 24  $\mu\text{m}$  counterpart (Owen, 2013b).

<sup>l</sup> $z_{\text{spec}}$  from Polletta et al. (2006).

<sup>m</sup> $z_{\text{phot}}$  from Strazzullo et al. (2010).

<sup>n</sup> $z_{\alpha}$  estimated from Carilli & Yun (1999) spectral index (see §2.7.3).

<sup>o</sup> $z_{\text{spec}}$  from Fiolet et al. (2010).

<sup>p</sup> $z_{\text{spec}}$  from Owen & Morrison (2009).

<sup>q</sup> $z'_{\text{phot}}$  from Magdis et al. (2010).

<sup>r</sup>There are two radio counterparts within  $8''$  of MAMBO source with  $P < 0.05$ ; see Section 2.9.

<sup>s</sup>The catalog of Owen & Morrison (2008) does not contain this radio counterpart (see §2.6.1).

<sup>t</sup>Flux density is uncertain due to blending (see §2.6.2).

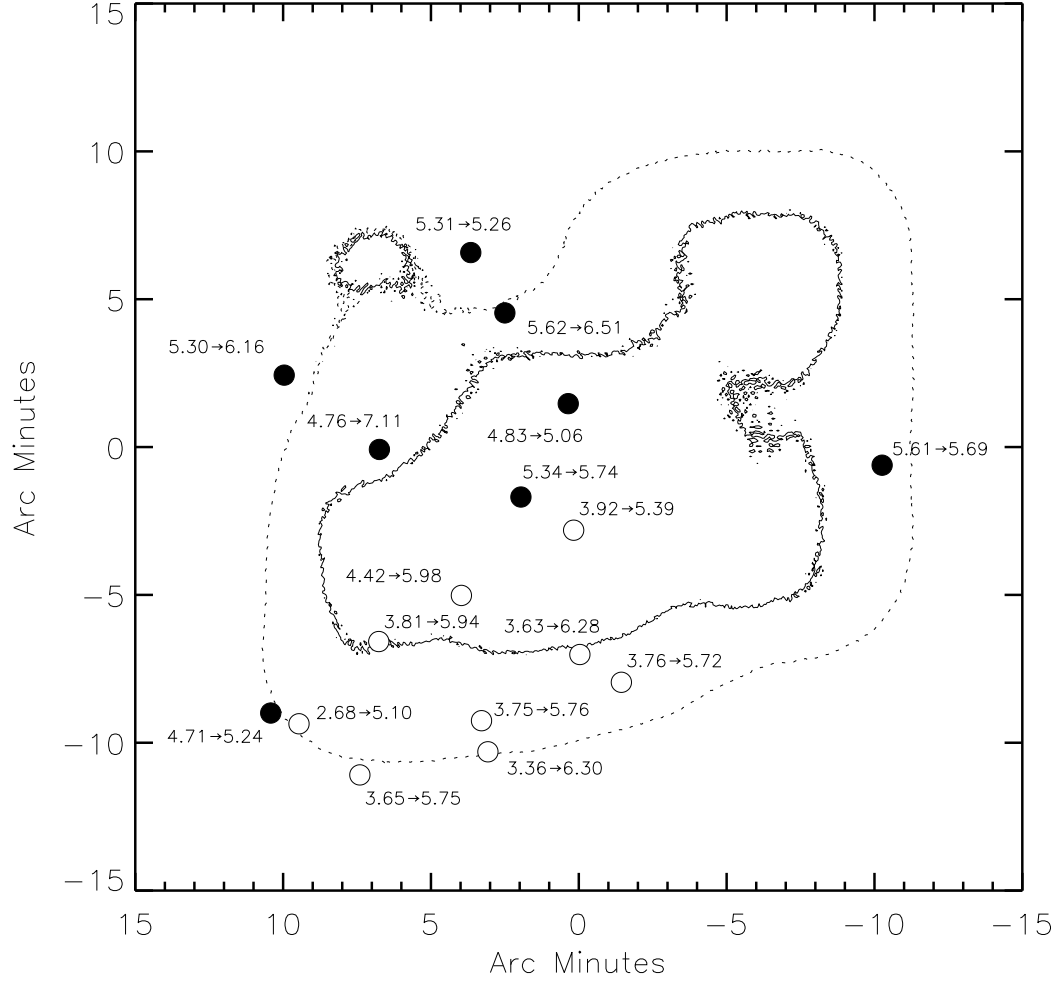


Figure 2.8: The change in S/N of our 17 comparison sources in the “best” and “full” datasets. Filled circles show eight sources in the “best” map with  $S/N \geq 4.5$ . In the “full” map, we recover all of these detections, plus others shown as empty circles, above a threshold  $S/N \geq 5.0$ . The solid/dashed contour denotes the  $1 \text{ mJy beam}^{-1}$  RMS noise threshold in the maps of the “best”/“full” data. The numbers near each detection show the S/N ratio of that source in the “best” data  $\rightarrow$  “full” data.

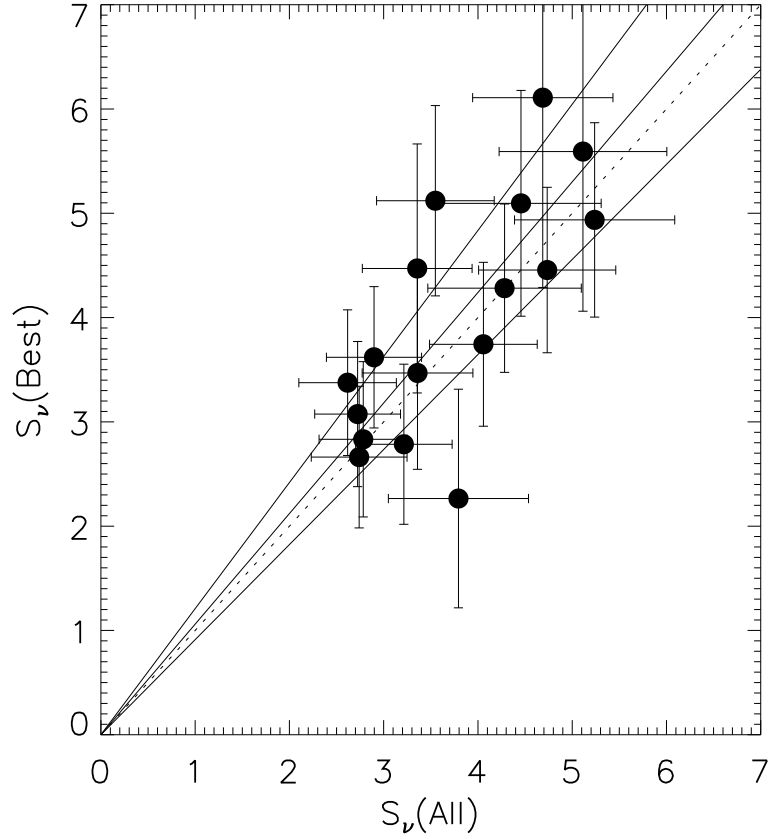


Figure 2.9: Flux density comparison between the 17 highest S/N detections in the “full” data and their counterparts in the “best” data (these sources are plotted in Figure 2.8). The solid lines show the best fit slope with  $2\sigma$  uncertainties of a line constrained to cross the origin. For illustration, the dotted line has unit slope. The chi-square minimization with  $x$  and  $y$  errors was performed using the IDL script `mpfit.pro` (Markwardt, 2009). The best fitting slope is  $m = 1.06 \pm 0.07$  ( $\pm 1\sigma$  uncertainties).

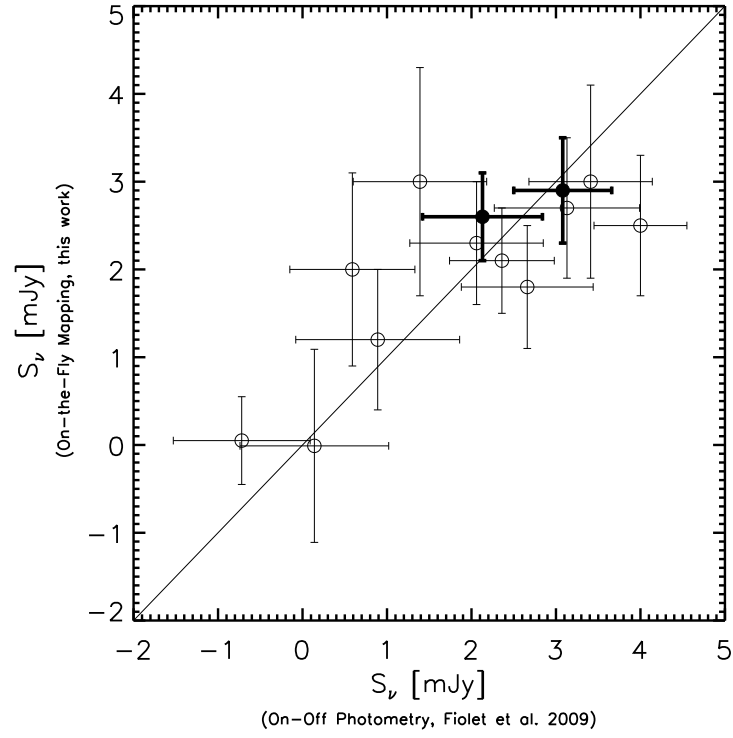


Figure 2.10: Flux density comparison between on-off photometry-mode (Fiolet et al., 2009) and on-the-fly mapping (this work) of 13 *Spitzer*-selected starburst galaxies in the LHN that lie within our “full” map coverage. Symbols with thick (thin) lines represent 2 (11) of the sources from Fiolet et al. (2009) with significant detections (non-detections) in our full map.

These two successful consistency checks lead us to conclude that the errors in our first two semesters’ data are not at a level that compromises point source detection, at least for high-significance sources. We have therefore proceeded to define our source catalog on the basis of the “full” map. Since the fluctuation analysis described in §2.4 relies on the authentic reproduction of the field’s noise properties and low-S/N fluctuations, we have restricted this analysis to the “best” data only.

### 2.5.3 Confusion

Random Gaussian noise is the uncertainty in the total flux density inside any single *beam* on the sky due to random fluctuations, while confusion noise is an additional uncertainty in the flux density of a single *source* due to the contributions of faint sources within that beam. The “confusion limit” is defined as the flux density threshold at which confusion noise significantly affects the measured flux density of a source, and is commonly taken to be the flux density above which the integrated number counts of all brighter sources reach  $\simeq 0.033$  per beam (Condon, 1974). In our map, this rule gives  $\simeq 0.9$  mJy using  $\theta_B = 15.6''$  (in the smoothed  $\leftrightarrow$  filtered version of our “full” map) and assuming our best-fit number counts (§2.4).

We have also made a direct estimate of the confusion noise by comparing the noise in the central regions of the filtered “best” map to the same region in a series of filtered jackknifed noise maps. Since the jackknifed noise maps remove confused as well as bright sources, the increase in average RMS noise in this relatively uniform region indicates our map contains confusion noise at the level of  $\sigma_C \simeq 0.24$  mJy beam $^{-1}$ . As a consistency check, we have also estimated the confusion noise by generating simulated maps with source populations following our best-fit number counts from 0.05 mJy up to the confusion limit of 0.9 mJy. Due to the central limit theorem, these faint and

confused maps with zero mean have roughly Gaussian PFDs and provide approximations of the confusion noise, assuming our model of the number counts. The standard deviation in these maps is  $0.21 \text{ mJy beam}^{-1}$ , in agreement with the measured confusion noise within the uncertainties of the number counts model. We therefore adopt the measured value of  $\sigma_C \simeq 0.24 \text{ mJy}$  as our estimate of the confusion noise. The average uncertainty in the flux density of a source in our catalog is  $0.62 \text{ mJy}$ , indicating that confusion does not dominate our noise budget.

#### 2.5.4 Spurious sources

We estimated the number of spurious detections as a function of S/N by running our source extraction algorithm on various noise maps (see §2.3.2). We tested jackknifed noise maps, shuffled noise maps, and simple Gaussian random numbers. The Gaussian random numbers had a spatially varying standard deviation matched to the weight map of the observations. Figure 2.11 shows the mean total numbers of spurious detections found in  $10^3$  jackknifed and Gaussian number noise maps, and in  $10^2$  shuffled noise maps, as a function of S/N. All three styles of noise map are consistent with each other in their ability to produce spurious detections with  $S/N \geq 3.0$ . This result confirms that for the purposes of extracting high-significance detections, the shuffled noise maps are just as “source-free” as the jackknifed noise maps. Additionally, both are consistent with a Gaussian distribution down to  $3.0\sigma$  (and likely consistent with Gaussian noise at all S/N, as implied by the PFD histograms in §2.3). The over-plotted curve in Figure 2.11 shows the expected number of excursions above a given S/N level in any isotropic and homogenous Gaussian random field, derived (and thus only formally valid) for high excursions (see, e.g., Chapter 6 of Adler, 1981). The agreement at high S/N indicates that our noise maps and source extraction algorithm are well-behaved. For both the “best” and “full” maps, we expect 0.8 (5.4) spurious sources with  $S/N \geq 4.5$  (4.0).

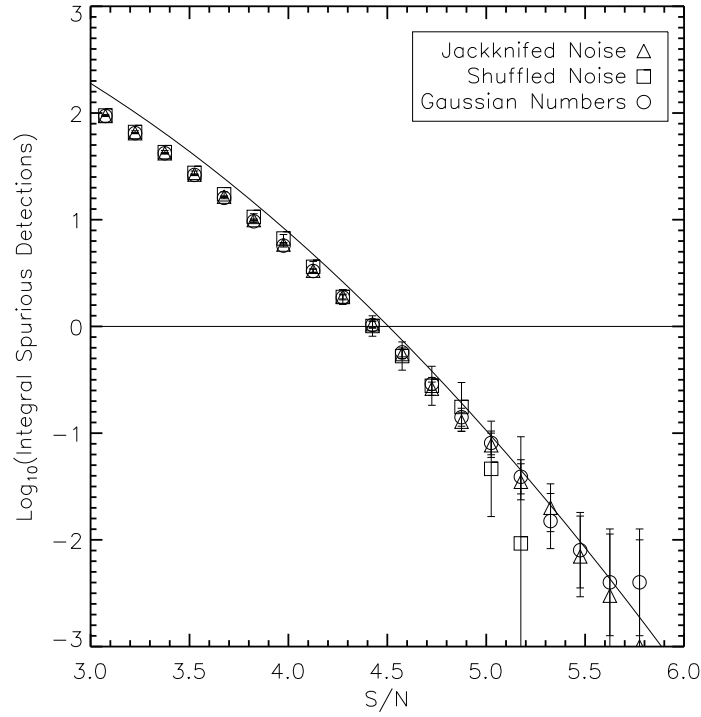


Figure 2.11: Integral numbers of spurious detections as a function of  $S/N$  within jackknifed noise maps, shuffled noise maps, and maps of random Gaussian numbers. We expect to detect 0.8 spurious sources with  $S/N \geq 4.5$  and  $\simeq 5.4$  spurious sources with  $S/N \geq 4.0$ . The curve shows the expected number of excursions above a given  $S/N$  level within a Gaussian random field in the limit of high  $S/N$  (Adler, 1981).



A source at high risk of being a spurious detection can be identified by calculating the total probability that the deboosted flux density is  $\leq 0$  mJy (see, e.g., Austermann et al., 2010; Scott et al., 2010), hereafter referred to as  $P(S < 0)$ . Using the threshold of  $P(S < 0) \geq 0.10$  used by Austermann et al. (2010), we identify only one (ID # 33) high-risk spurious detection in our  $S/N > 4.0$  sample (see Table 2.2).

### 2.5.5 Completeness

We estimate the completeness in our data using the Monte Carlo method of searching for injected sources of varying flux density. The inhomogeneous noise in our map means that sources of identical flux density have different probabilities of being detected in different locations. We account for this effect statistically by performing the completeness simulation assuming sources have equal probability of being located anywhere in the map during the injection process. Although the high-redshift star-forming galaxy population that our observations trace is likely to exhibit clustering, with the brightest galaxy mergers occurring in the most massive dark matter halos (see, e.g., Weiß et al., 2009), the large  $\Delta z$  interval to which millimeter selection is sensitive tends to weaken angular clustering signatures (see however §2.5.8). We inject model sources with known flux density into our original signal map one at a time at random positions and search for them using the same source extraction algorithm used to create our source list. If an artificial source is recovered with  $S/N \geq 4.0$  within  $11''$  of the injected location, it is considered detected. The injection process was repeated  $10^3$  times for each flux density in a logarithmic grid from 1.0 mJy to 10.0 mJy; the average recovery percentage is shown in Figure 2.12. Our map is 80% complete at 3.7 mJy and 50% complete at 2.6 mJy. We also tabulated the angular separations between the injected and recovered source positions to characterize the uncertainties in the positions of our actual significant detections (ignoring telescope pointing errors). For  $S_{1.2\text{mm}} \gtrsim 2$  mJy, the average

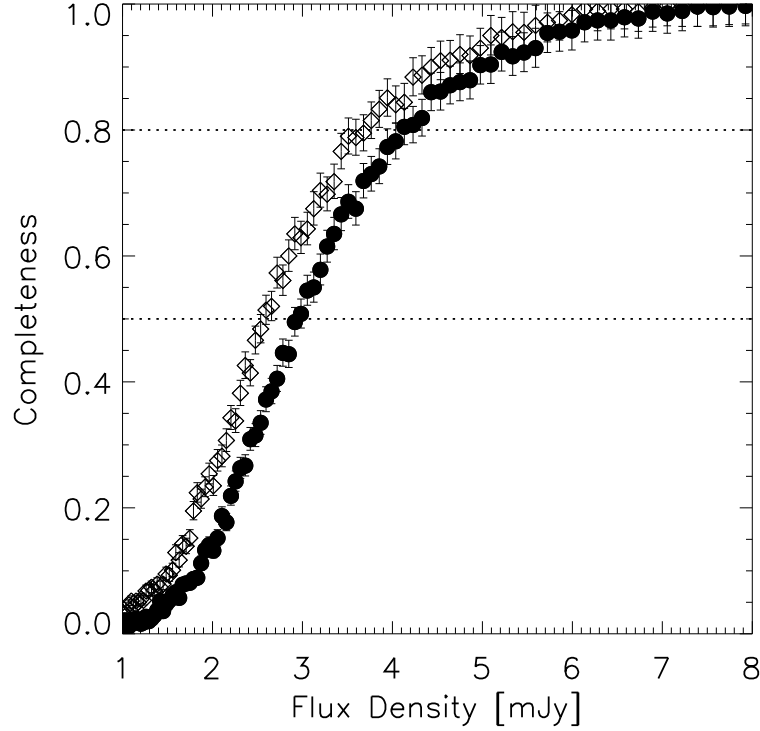


Figure 2.12: Completeness as a function of flux density. The circles/diamonds represent  $4.5\sigma/4.0\sigma$  source extraction thresholds for detection. The number count calculation uses a threshold of  $4.5\sigma$ , while our source catalog includes sources down to  $4.0\sigma$ . Horizontal lines represent 80% and 50% completeness limits.

position error  $\langle\Delta\theta\rangle \leq 3''$  (see Figure 2.7).

### 2.5.6 Flux boosting

To correct the measured flux densities of our detections for the effect of “flux boosting,” we use the Bayesian technique described in Coppin et al. (2005), which because of its versatility in handling both chopped and unchopped data has been adapted for use at many wavelengths (e.g., Coppin et al., 2006; Greve et al., 2008; Scott et al., 2008; Perera et al., 2008; Scott et al., 2010; Austermann et al., 2010). Using Bayes’s Theorem and the prior information of the number counts functional form found from our  $P(D)$  analysis (§2.4), the probability that a source has true flux density  $S_0$  given a measurement  $S$

with uncertainty  $\sigma$  is equal to

$$P(S_0|S, \sigma) = \frac{P(S, \sigma|S_0)P(S_0)}{P(S, \sigma)} \quad (2.9)$$

where  $P(S, \sigma|S_0)$  is the posterior probability,  $P(S_0)$  is the prior flux density distribution,  $P(S, \sigma|S_0)$  is the likelihood, and  $P(S, \sigma)$  is the prior measurement distribution.  $P(S, \sigma)$  is independent of  $S_0$ , so only acts to normalize the expression such that  $\int P(S_0|S, \sigma)dS_0 = 1$ ; hereafter, it will be ignored. We have shown that the uncertainty in our map is dominated by Gaussian random noise, so  $P(S, \sigma|S_0)$  takes the form

$$P(S, \sigma|S_0) \propto \exp \left[ -\frac{(S - S_0)^2}{2\sigma^2} \right] \quad (2.10)$$

To estimate the prior flux distribution in the map ( $P(S_0)$ ), we assembled a PFD containing the pixels from  $10^4$  noise-free random sky realizations that used the best-fit number count parameters from our  $P(D)$  analysis. The peak value and 68% double-sided confidence intervals of the resulting posterior probability function ( $P(S_0|S, \sigma)$ ) were found numerically for each measured flux density and uncertainty. Figure 2.13 shows four examples of the deboosting process, each in a different regime of source S/N. If the S/N is too low, and the integration of the confidence intervals does not converge, we instead use an analytic formula to estimate the deboosted flux density. For this, we generalize the formalism of Hogg & Turner (1998) to a Schechter function, and locate the maximum of the posterior flux distribution:

$$P(S_0|S, \sigma) \propto S_0^{-\delta'} \exp \left[ -\frac{S_0}{S'_{\text{exp}}} - \frac{(S - S_0)^2}{2\sigma^2} \right] \quad (2.11)$$

where  $\delta'$  and  $S'_{\text{exp}}$  are the power-law slope and exponential scale factor of the Schechter function, respectively. By solving for  $S_0$  when the derivative of the above expression vanishes, we find the highest posterior probability to be achieved for

$$S_{\text{true}} = \frac{S S'_{\text{exp}} - \sigma^2 + \sqrt{(\sigma^2 - S S'_{\text{exp}})^2 - 4 \delta' S'^2_{\text{exp}} \sigma^2}}{2 S'_{\text{exp}}} \quad (2.12)$$

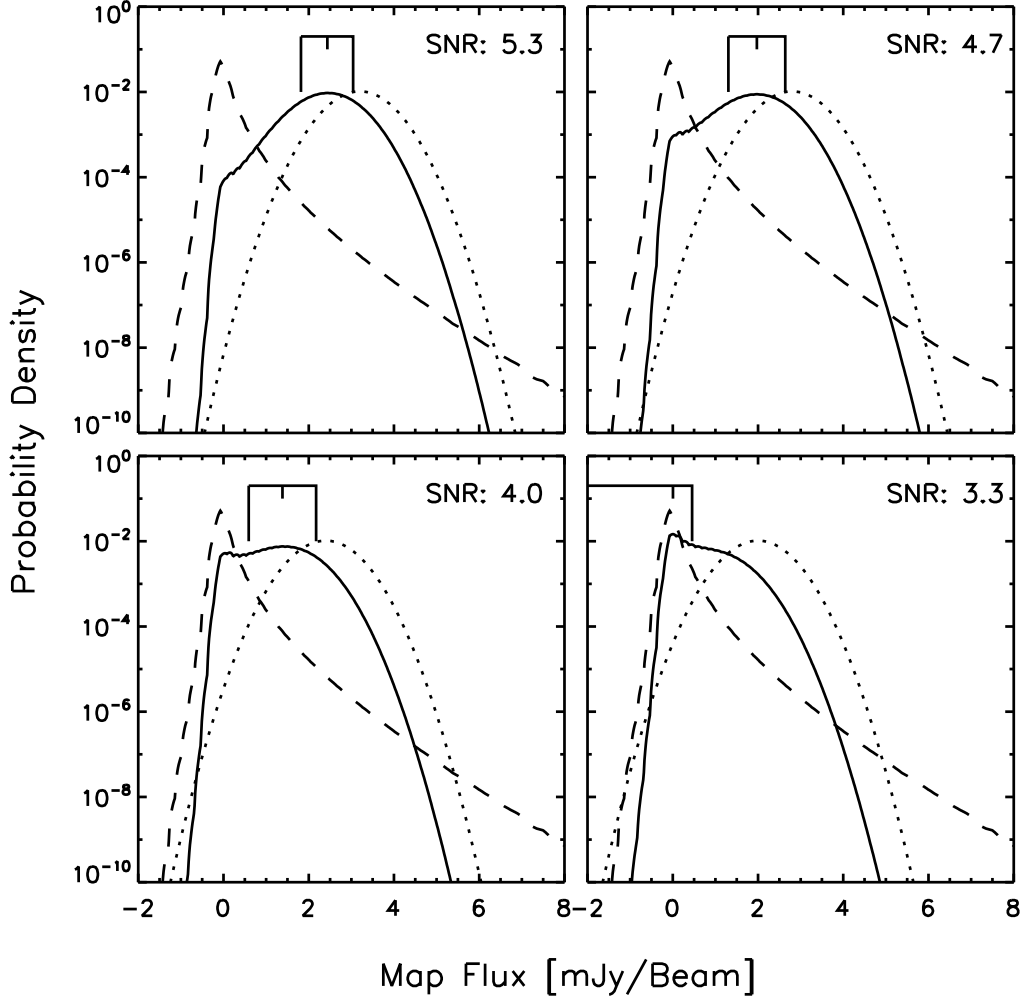


Figure 2.13: Posterior probability distributions of four characteristic S/N regimes. The dotted lines represent the Gaussian probability distributions for each of the four measurements (the likelihoods), all assuming  $\sigma = 0.6$  mJy and varying mean. The dashed lines represent the prior flux distribution constructed from Monte Carlo simulations, and the solid lines represent the normalized posterior probability distributions. The brackets above the curves denote the peak likelihood values (the deboosted flux densities) along with the left and right 38% confidence intervals. When the S/N is too low for either the left or the right confidence interval to converge, as is the case in the final panel, we use instead the analytic formula from Equation 2.12.

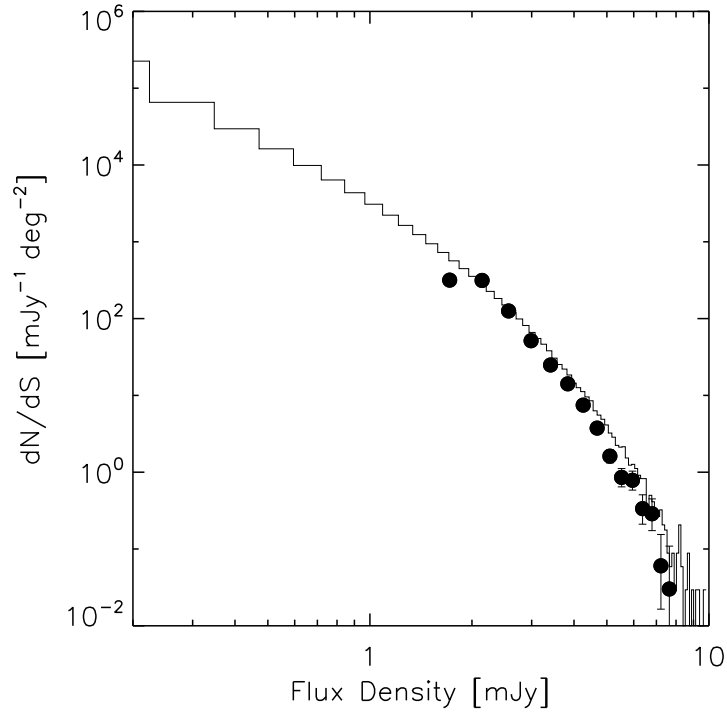


Figure 2.14: Monte Carlo simulation to test our Bayesian flux boosting correction. The histogram shows the average number counts model used to inject sources into realistic noise maps. The circles show the average number counts calculated from the raw counts by using the Bayesian method to deboost the flux density of each recovered source. Error bars represent only the Poisson uncertainty in the average (Gehrels, 1986).

To ensure that our adaption of the Bayesian method of flux deboosting returns a properly corrected estimate of the true number counts, we performed a Monte Carlo simulation to directly calculate the observed number counts of random sky realizations populated with source distributions following our best-fit number counts (see, e.g., Coppin et al., 2006). Figure 2.14 shows the results of this consistency check. This simulation demonstrates that the Bayesian method of flux deboosting performs well in recovering the original injected number counts. The residual scatter of the average recovered number counts around the average input model in Figure 2.14 demonstrates the level of systematic error in the algorithm, which is significantly smaller than the statistical error of our differential number counts estimate (see Figure 2.15).

Table 2.3. 1.2 mm number counts

Flux Bin (mJy)	Differential		Integral	
	Flux Density (mJy)	$dN/dS$ (deg <sup>-2</sup> mJy <sup>-1</sup> )	Flux Density (mJy)	$N(> S)$ (deg <sup>-2</sup> )
1.68–2.14	1.91	$435^{+369}_{-228}$	1.68	$366^{+212}_{-122}$
2.14–2.59	2.36	$128^{+200}_{-94}$	2.14	$166^{+128}_{-63}$
2.59–3.05	2.82	$156^{+151}_{-89}$	2.59	$108^{+90}_{-46}$
3.05–3.51	3.28	$18^{+80}_{-17}$	3.05	$37^{+58}_{-22}$
3.51–3.97	3.74	$62^{+97}_{-45}$	3.51	$28^{+44}_{-21}$

### 2.5.7 Direct calculation of number counts

While our catalog of detections includes all sources with  $S/N > 4.0$ , we use only detections with  $S/N > 4.5$  for our direct calculation of the number counts because above this threshold, we expect to detect less than one spurious source (see Figure 2.11). Table 2.3 presents integral and differential number counts after correction for completeness and flux boosting. Figure 2.15 shows our directly calculated number counts, along with the 95% confidence regions for the best-fit power law and Schechter function models of the differential number counts found from the  $P(D)$  analysis. These two independent methods of estimating the number counts are in agreement with each other. This consistency is encouraging because the  $P(D)$  analysis and the direct estimate of number counts depend on the faint and bright pixel values in different ways.

### 2.5.8 Clustering

The group of sources in the southeast corner of our field, as well as the large void in the center, prompted us to perform a clustering analysis to determine whether or not the distribution of sources in our map is statistically clustered or not. To perform the

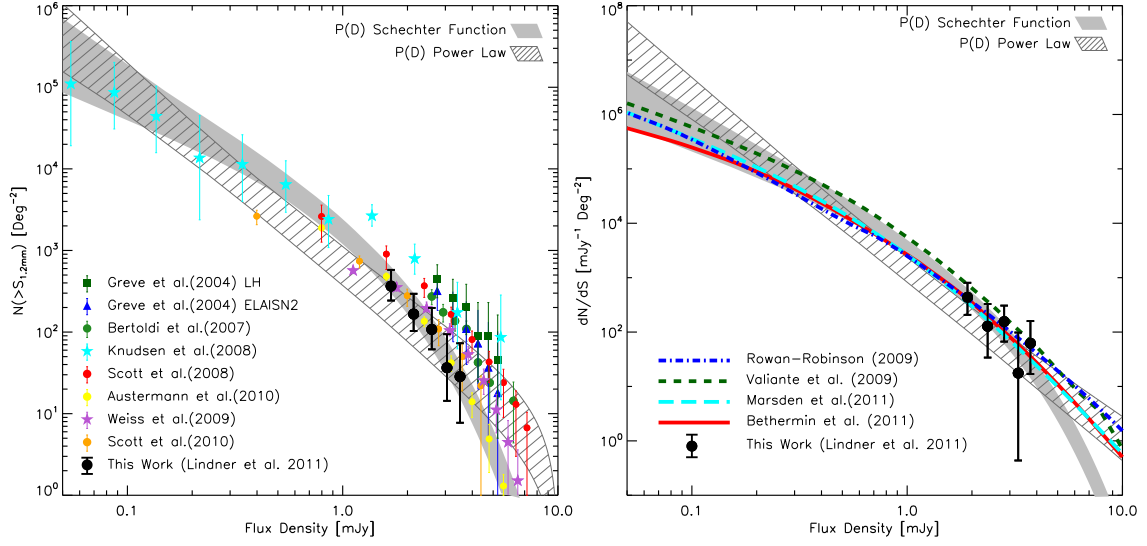


Figure 2.15: *Left*: 1.2 mm integral number counts, compared to the  $P(D)$  analysis best fit models and other observed number counts from the literature. Filled black circles show our Bayesian deboosted number counts with 95% confidence error bars including the Poisson uncertainty and the uncertainty in the completeness correction. The solid filled region shows the 95% confidence region for the best fitting Schechter function from the  $P(D)$  analysis. The cross-hatched region shows the same for the best fitting power law. MAMBO counts: LH and ELAIS-N2 (green squares and blue triangles; Greve et al., 2004), COSMOS (green circles; Bertoldi et al., 2007). LABOCA counts: ECDF-S (purple stars; Weiß et al., 2009). AzTEC counts: GOODS-S (orange circles; Scott et al., 2010), SHADES (yellow circles; Austermann et al., 2010), COSMOS (red circles; Scott et al., 2008). SCUBA lensing cluster counts from Knudsen et al. (2008) are shown as red stars. The counts at  $850\,\mu\text{m}$  (SCUBA),  $870\,\mu\text{m}$  (LABOCA), and  $1.1\,\text{mm}$  (AzTEC) have been scaled to  $1.2\,\text{mm}$  (see §2.7.1). *Right*: 1.2 mm differential number counts and  $P(D)$  models compared to the predictions of galaxy evolution models. Lines represent different differential counts predictions by Rowan-Robinson (2009), blue dot-dashed; Valiante et al. (2009), green short-dashed; Béthermin et al. (2011), red solid; Marsden et al. (2011), cyan long-dashed. Models with predictions only for the  $1.1\,\text{mm}$  waveband were scaled in order to compare to our observations (see §2.7.1).

analysis, we used the Landy & Szalay (1993) correlation function estimator:

$$w(\theta) = \frac{DD - 2DR + RR}{RR} \quad (2.13)$$

with variance

$$\langle \Delta w(\theta) \rangle^2 \simeq \frac{(1 + w(\theta))^2}{RR} \quad (2.14)$$

(Gawiser et al., 2006). In the equations above,  $DD$ ,  $RR$ , and  $DR$  represent the normalized numbers of unique galaxy-galaxy, random-random, and galaxy-random pairs with angular separations  $\theta \pm d\theta/2$ . This estimator is used frequently in extragalactic deep field analyses (e.g., Borys et al., 2003; Scott et al., 2006; Weiß et al., 2009), and has been shown to have nearly Poisson variance and zero bias (Landy & Szalay, 1993). We take into account the geometric boundary of the map and the variation in detectability with position by generating the random locations with the same Monte Carlo algorithm used for the  $P(D)$  analysis. We inject ensembles of sources following our best fitting number counts into a noise map at random locations and use the positions of sources detected with  $S/N > 4.0$  as our random coordinates. This Monte Carlo technique is important for ensuring that we do not misinterpret depth variation in the map as a clustering signal.

To confirm that this technique is unbiased, we also performed the full clustering analysis on only random positions to check that we recovered a flat  $w(\theta) = 0$  response (see Figure 2.16). For small separations ( $\lesssim 2'$ ), however, it turns out that  $w(\theta)$  does not return zero in our data: depending on the position within the map, the negative sidelobes can suppress the flux densities of nearby sources enough to lower their  $S/N$  ratios below the detection threshold. This effect begins to have an effect at  $\simeq 2 \times$  the chop throw (of which the maximum used in any semester was  $48''$ ), and has a strong effect at separations  $\leq 1 \times$  chop throw. Because this effect suppresses the detection of  $RR$  and  $DD$  pairs but not  $DR$  pairs, the zero-clustering baseline for chopped data like ours is less than zero at these small angles. In order to assess the clustering in the map



while taking this bias into account, we measure the effective clustering relative to the zero-clustering baseline for these separations ( $\lesssim 2'$ ).

The result of our Monte Carlo clustering analysis is shown in Figure 2.16. We find a small clustering signal when using all detections with  $S/N > 4.0$  that agrees reasonably well with the angular correlation function measured by Scott et al. (2006), who combined many different SCUBA 850  $\mu\text{m}$  blank field maps, and that shows stronger clustering (albeit at lower  $S/N$ ) than the correlation function measured by Weiß et al. (2009) at 870  $\mu\text{m}$  in the ECDF-S. Williams et al. (2011) have analyzed the clustering of  $3.0\text{--}3.5\sigma$  1.1 mm detections in a  $0.72\text{ deg}^2$  map of the COSMOS field with ASTE/AzTEC, concluding that it is difficult to recover reliable clustering parameters for SMGs from maps whose angular resolution and total area are limited. This result argues for caution in interpreting our clustering analysis, although we do benefit to an extent from MAMBO’s relatively high angular resolution. An interesting feature in our correlation function is the spike near  $\theta \simeq 4'$ . This signal is due to the rich group of sources in the southeastern corner of the map, all at typical relative spacings of a few arcminutes from each other (see also §2.7.4). It may be noteworthy that Weiß et al. (2009) find a  $\sim 2.4\sigma$  spike above their best fitting model of  $\omega(\theta)$  at a scale of  $\sim 5'$ , near where Williams et al. (2011) also detect a slight positive excess in  $\omega(\theta)$ . When performing the analysis on only our (27) most significant sources with  $S/N > 4.5$ , we find no significant clustering signal.

Following the analysis of, e.g., Borys et al. (2003) for the SCUBA “Supermap,” we also use the method of Scott & Tout (1989) to analyze the cumulative distribution of nearest neighbors to test whether our galaxy positions are consistent with being drawn from a random distribution (see Figure 2.17). Because the nearest neighbor analysis is sensitive to the total number of positions used, we use the 41 most significant detections in *each* Monte Carlo realization, instead of all of those detections with  $S/N > 4.0$  as in

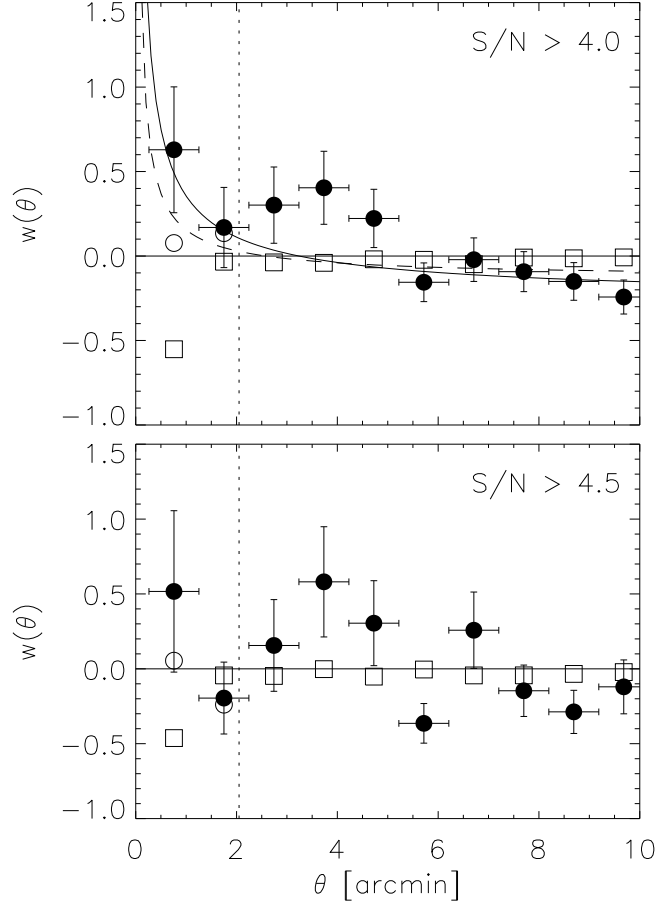


Figure 2.16: Landy-Szalay correlation function estimator  $w(\theta)$  as a function of angular separation. Top panel uses our 41 detections with  $S/N > 4.0$ . Bottom panel uses 27 sources with  $S/N > 4.5$ . The vertical dashed line shows upper limit in  $\theta$  on the clustering suppression effect introduced by chopping (see §2.5.8). Open squares show the results from using random positions to check the zero-clustering baseline; open circles show the raw clustering signal, which are corrected for the zero-clustering baseline to deliver the filled circles.

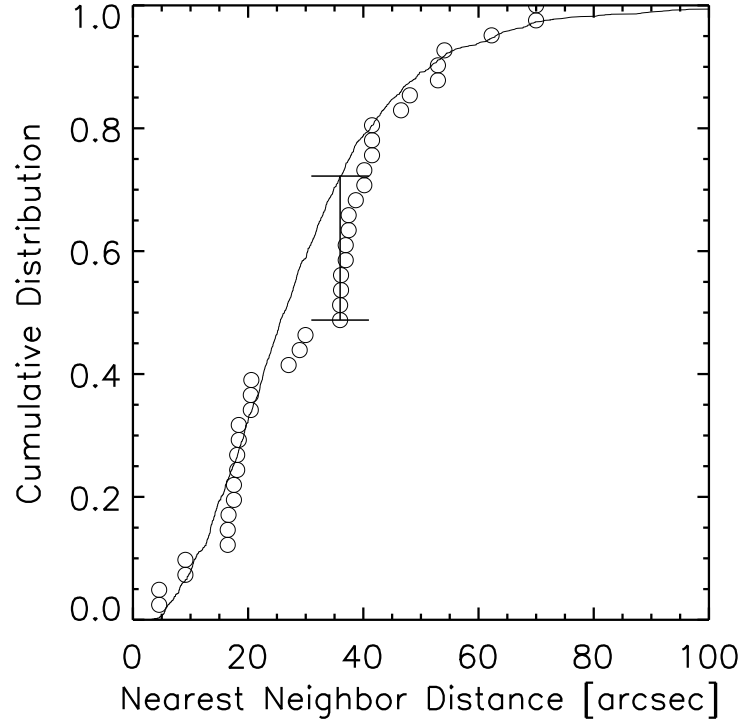


Figure 2.17: Integral distribution of nearest neighbors. Solid line shows the distribution from Monte-Carlo generated random positions. Circles show the distribution of our 41 significant detections. The vertical line segment denotes the maximum difference between the two distributions. A Kolmogorov-Smirnov test rules out the hypothesis that our sources are drawn from a random distribution at 95% confidence.

the correlation function analysis. Because the number counts rise quickly, the S/N of the least significant discovered source varies, but is always close to 4.0. A Kolmogorov-Smirnov test rules out the null hypothesis that our significant detections are drawn from a random position distribution at the 95% confidence level, implying that the source locations in the map (e.g., defining the southeastern clump and the central void) are not arranged randomly.

## 2.6 Counterpart identification

We have calculated the corrected probability of chance associations ( $P$ ; Downes et al., 1986) between our MAMBO detections and possible counterparts at the other wavelengths at which the LHN has been observed (see Table 2.2). The  $P$  statistic is defined by

$$P = 1 - e^{-E} \quad (2.15)$$

for  $E = P^*[1 + \ln(P_c/P^*)]$ ,  $P^* = \pi r^2 N(> S)$ , and  $P_c = \pi r_s^2 N_c$ , in terms of the brightness of the counterpart  $S$ , the source separation  $r$ , the search radius  $r_s$ , the number density of sources brighter than  $S$   $N(> S)$ , and the number density of sources at the sensitivity limit  $N_c$ . Based on the results of the position error analysis (see Figure 2.7), we chose a counterpart search radius of  $8''$ . Because positional uncertainty  $\sigma \propto \text{FWHM} \times \text{SNR}^{-1}$ , our  $11''$  beam is the dominant source of error, and we ignore the positional uncertainties at other wavelengths. We consider  $P < 0.01$  to define a robust counterpart,  $0.01 \leq P < 0.05$  a likely counterpart, and  $P \geq 0.05$  an unlikely association.

### 2.6.1 20 cm radio counterparts

We used the NRAO VLA Sky Survey (NVSS) and the deep SWIRE number counts of Condon et al. (1998) and Owen & Morrison (2008), respectively, in the calculation of  $P$  to assess the significance of 20 cm counterparts. The 20 cm VLA pointing of the LHN has a central RMS sensitivity of  $2.7 \mu\text{Jy}$ , rising to  $\sim 4\text{--}5 \mu\text{Jy}$  near the edges of our MAMBO map. When we compare our 41  $\text{S/N} > 4.0$  detections to the  $5\sigma$  20 cm catalog of Owen & Morrison (2008), 44% (18) have robust counterparts, and 41% (17) have likely counterparts. We have also reexamined the 20 cm map in the vicinity of the remaining MAMBO sources and have identified one additional robust

counterpart (ID # 9), two likely counterparts (ID # 28 and # 36), and one unlikely counterpart (ID # 20) at the  $4\text{--}5\sigma$  level. We also deblended one likely counterpart into one robust and one unlikely counterpart (ID # 17). After including these additional sources, 49% (20) of our MAMBO detections have robust counterparts, 44% (18) have likely counterparts, and 7% (3) have unlikely or no detected counterparts. We performed a Monte Carlo simulation to test the reliability of our  $P$  values and found that  $4.9 \pm 0.2\%$  of randomly chosen positions within our MAMBO field have a likely radio counterpart ( $P < 0.05$ ) within  $8''$ , confirming the validity of the high number of robust associations. We expect  $\sim 5$  spurious detections above  $S/N > 4.0$ ; thus, the handful of sources with unlikely or no radio counterparts may be spurious detections if they do not lie at a very high redshift. One MAMBO source (ID # 32) with an unlikely ( $P_{20\text{ cm}} = 0.056$ ) radio counterpart also has a likely ( $P_{250\text{ }\mu\text{m}} = 0.016$ ) *Herschel* counterpart (Magdis et al., 2010), arguing against its being a spurious detection.

### 2.6.2 50 cm radio counterparts

We have extracted 50 cm flux densities from the GMRT map (Owen, 2013a) with the same technique used at 20 cm and 50 cm (see Owen & Morrison, 2008; Owen et al., 2009). The uncertainties listed in Table 2.2 reflect the local RMS noise in the image and do not include a  $\sim 3\%$  calibration error or a spatially varying GMRT pointing error. Two of the 50 cm detections are heavily blended with bright neighbors, so for these counterparts we report only tentative fluxes. Of the 40 tabulated 20 cm counterparts (including the two with  $P > 0.05$ ), all 40 have 50 cm counterparts. The one 20 cm non-detection (within  $8''$ ) is also a 50 cm non-detection.

### 2.6.3 90 cm radio counterparts

To search for 90 cm counterparts, we used the 90 cm radio catalog of Owen et al. (2009), which has an RMS sensitivity of  $10\ \mu\text{Jy}$ . Of our 41 MAMBO sources, 24% (10) have 90 cm counterparts. Each of the ten 90 cm counterparts is also detected at 50 and 20 cm with  $P_{20\text{ cm}} < 0.05$ .

### 2.6.4 24 $\mu\text{m}$ counterparts

In addition to SWIRE 24  $\mu\text{m}$  observations of the LHN ( $3\sigma$  depth of  $209\ \mu\text{Jy}$ ), there exist deeper *Spitzer*/MIPS data with a  $3\sigma$  depth of  $18\ \mu\text{Jy}$  (Owen, 2013b). We searched for 24  $\mu\text{m}$  counterparts to our MAMBO detections in this deeper MIPS image. To calculate  $P$  statistics for 24  $\mu\text{m}$  counterparts, we used the counts of Béthermin et al. (2010). A Monte Carlo simulation of the 24  $\mu\text{m}$   $P$ -statistic finds that  $4.7 \pm 0.3\%$  of random positions yield a counterpart with  $P < 0.05$ . Within our sample of 41 MAMBO sources, 20% (8) have robust 24  $\mu\text{m}$  counterparts, and 29% (12) have likely counterparts.

### 2.6.5 X-ray counterparts

Only one source (MM J104522.8+585558 = ID # 26) has a likely X-ray counterpart (CXOSW J104523.6+585601; Wilkes et al., 2009). The X-ray source is at a distance of  $7.2''$  and has a broad band (0.3–8.0 keV) flux of  $(2.5 \pm 1.1) \times 10^{-15}\ \text{erg cm}^{-2}\ \text{s}^{-1}$  (Polletta et al., 2006). By using the 2.5–7 keV flux of  $1.58 \times 10^{-15}\ \text{erg cm}^{-2}\ \text{s}^{-1}$  together with the *Chandra*/SWIRE counts from 2–8 keV (Wilkes et al., 2009) we can set an upper limit on the probability of chance association of  $P \lesssim 0.02$ .

## 2.7 Discussion

### 2.7.1 Number counts vs. previous deep fields

Previous deep surveys at 1.2 mm using MAMBO (e.g., Greve et al., 2004; Bertoldi et al., 2007) have returned directly calculated 1.2 mm number counts in the Lockman Hole East (LHE), ELAIS-N2, and COSMOS fields. The parameters of these surveys are listed in Table 2.4; we compare their results to our directly calculated counts, as well as to our best-fit  $P(D)$  models, in Figure 2.15. We find that our power-law slope is consistent with their results, but our results have a lower overall normalization. This difference in normalization might be due to the different methods used in the number counts calculations. We have used the Bayesian method of flux deboosting presented in Coppin et al. (2005), and only include our most significant detections in the calculation. The analyses of Greve et al. (2004) and Bertoldi et al. (2007) use the method of injecting sources into noise maps to determine their flux deboosting correction, and include sources with lower S/N in their number counts calculation. In principle, any S/N cutoff would be acceptable for the latter calculation as long as the completeness correction uses the same threshold; however, lower S/N thresholds will lead to more spurious detections. Both of these effects could be contributing to their higher normalization. However, considering the relatively large error bars on all the measurements and the internal variation among the ELAIS-N2, LHE, and COSMOS datasets themselves, the results are still nearly consistent.

Because a single power-law parametrization of the number counts is commonly used to compare the results of deep surveys, we begin by noting that our best-fit power law index ( $\delta = 3.14^{+0.14}_{-0.18}$ ) is consistent with the results of surveys at other wavelengths that fit their number counts using a similar (single power-law) model. Coppin et al. (2006) find 850  $\mu$ m power-law indices of  $\delta = 2.9 \pm 0.2$  and  $\delta = 3.0 \pm 0.3$  in the LHE

Table 2.4. Area surveyed

Reference	Instrument	Field	Area (deg <sup>2</sup> )	Depth (mJy beam <sup>-1</sup> )	HPBW (arcsec)
Greve et al. (2004)	MAMBO 1.2 mm	ELAIS-N2 & LH	0.099	0.8	11
Bertoldi et al. (2007)	MAMBO 1.2 mm	COSMOS	0.11	1.0	11
Scott et al. (2008)	AzTEC/JCMT 1.1 mm	COSMOS	0.15	1.3	18
Perera et al. (2008)	AzTEC/JCMT 1.1 mm	GOODS-N	0.068	0.96-1.16	18
Wei et al. (2009)	LABOCA/APEX 870 $\mu$ m	ECDF-S	0.25	1.2	19.2
Austermann et al. (2010)	AzTEC/JCMT 1.1 mm	LHE & SXDF	0.5	1	18
Scott et al. (2010)	AzTEC/ASTE 1.1 mm	GOODS-S	0.14	0.48-0.73	30
Hatsukade et al. (2011)	AzTEC/ASTE 1.1 mm	AKARI, SXDF, & SSA	0.25	0.32-0.71	30
<i>This Work</i>	MAMBO 1.2 mm	LHN	0.16	0.75	11

and Subaru/XMM-Newton deep fields, respectively. Using Bolocam data at 1.1 mm, Laurent et al. (2005) estimate a power-law index of  $\delta = 3.16$  from directly calculated counts in the Lockman Hole. However, Maloney et al. (2005) performed a  $P(D)$  analysis on the same 1.1 mm Bolocam data and find  $\delta = 2.7^{+0.18}_{-0.15}$ . Although it is well within the  $1\sigma$  uncertainties of the Laurent et al. (2005) result, the latter slope differs from ours by  $> 2\sigma$ . In this case, differences in the methods of our  $P(D)$  analyses might be the differentiating factor. Maloney et al. (2005) also used chopped observations in their analysis, for example, but ignored the effects of chopping on the PFD. It is possible that by not including the negative residual flux in their  $P(D)$  analysis, they required many fewer faint sources to match the pixel distribution of the real data (and therefore derived a shallower power law slope). However, a value of  $\delta \simeq 2.7$  is also the best-fit single power-law slope found by Scott et al. (2010) for their  $P(D)$  analysis of unchopped 1.1 mm AzTEC data in the GOODS-S field.

In Figure 2.15 (see also Table 2.4), we also compare our results to those for deep field observations at 1.1 mm by AzTEC of the COSMOS (Scott et al., 2008), GOODS-N (Perera et al., 2008), GOODS-S (Scott et al., 2010), SHADES (Austermann et al., 2010), and AKARI, SSA-N2, and SXDF (Hatsukade et al., 2011) deep fields. (For clarity, the observations of Hatsukade et al. (2011) and Perera et al. (2008) are not shown in the



plot because their data points lie within the scatter of the other AzTEC observations.) We also compare our results to the extremely deep SMG counts measured in lensing fields at  $850\,\mu\text{m}$  by Knudsen et al. (2008) as well as the recent wide map by Weiß et al. (2009) using LABOCA at  $870\,\mu\text{m}$  in the ECDF-S. In order to compare our number counts directly to the results of these surveys at other wavelengths, we rescale their flux densities. Our choice of rescaling factor is based on the direct comparisons between  $S_{850\,\mu\text{m}}$ ,  $S_{1.1\text{mm}}$ , and  $S_{1.2\text{mm}}$  for galaxies in the GOODS-N field. The average flux density ratio for sources with robust SCUBA and AzTEC detections in the GOODS-N field is  $S_{850\,\mu\text{m}}/S_{1.1\text{mm}} \simeq 1.8 - 2.0$  (Perera et al., 2008; Chapin et al., 2009). When comparing SCUBA and MAMBO detections, Greve et al. (2008) find  $S_{850\,\mu\text{m}}/S_{1.2\text{mm}} \simeq 2.5$ . By coadding the MAMBO and AzTEC observations in the GOODS-N field into a map at an effective wavelength of  $\lambda = 1.16\text{ mm}$ , Penner et al. (2011) find an average value of  $S_{1.16\text{mm}}/S_{1.1\text{mm}} \sim 0.88$  and  $S_{1.16\text{mm}}/S_{1.2\text{mm}} \sim 1.14$ . All of these results are consistent with a single modified blackbody spectrum, for  $\beta = 1.5$  and  $T_d = 30\text{ K}$ , observed at  $z \simeq 2.5$ . Therefore, we adopt this fiducial galaxy model when comparing fluxes at different wavelengths and use  $S_{850\,\mu\text{m}}/S_{1.2\text{mm}} = 2.3$ ,  $S_{870\,\mu\text{m}}/S_{1.2\text{mm}} = 2.2$ , and  $S_{1.1\text{mm}}/S_{1.2\text{mm}} = 1.2$ . Our directly calculated counts are in excellent agreement with the rescaled results of the AzTEC surveys. Additionally, our prediction for the shape of the number counts below our sensitivity threshold, afforded by our  $P(D)$  analysis, agrees well with the deepest AzTEC number counts and is even in rough agreement with the deepest SMG counts by Knudsen et al. (2008).

Figure 2.15 also compares our results to various number count predictions derived from backward evolution models that incorporate multi-waveband observations of number counts and redshift distributions, as well as limits imposed by the CIB light. We have restricted this comparison to models that offer predictions at wavelengths of  $1.2\text{ mm}$  (Béthermin et al., 2011) or at  $1.1\text{ mm}$  (Valiante et al., 2009; Rowan-Robinson,

2009; Marsden et al., 2011), to which we can apply the rescaling described above. Although flux scaling will generally not provide a precise representation of a model’s predictions at 1.2 mm, the extrapolation from 1.1 mm to 1.2 mm is fairly modest. At flux densities equal to or less than those of our significant detections, we find that our observations are generally consistent with all model predictions, although the Valiante et al. (2009) model slightly overpredicts our  $P(D)$  curve near 1 mJy. At the high flux density limit, all models uniformly overpredict the counts from our best-fitting Schechter function model, while remaining consistent with the predictions from our power-law result (which is only marginally compatible with the CIB; see Figure 2.6). However, we cannot draw any conclusions from this apparent discrepancy, as our  $P(D)$  analysis cannot constrain the differential counts at flux densities greater than those of our brightest detections.

### 2.7.2 Fractional counterpart identification

Here we investigate the question of whether our radio counterpart identification rate ( $R_{1.4\text{ GHz}}$ ) of  $\simeq 93^{+4}_{-7}\%$  (38/41) in the LHN is intrinsically greater than is seen in other surveys, or if it is simply a function of the increased 20 cm sensitivity in this field. We compare our identification rate to those found for previous deep surveys at 850  $\mu\text{m}$ , 870  $\mu\text{m}$ , 1.1 mm, and 1.2 mm. Table 2.5 lists recent millimeter and submillimeter deep field surveys from the GOODS-N, LHE, SXDF, COSMOS, and ECDF-S fields (Borys et al., 2003, 2004; Ivison et al., 2007; Bertoldi et al., 2007; Schinnerer et al., 2007; Perera et al., 2008; Chapin et al., 2009; Weiß et al., 2009; Biggs et al., 2011), along with their 20 cm radio counterpart identification rates and 20 cm map sensitivities. Because the surveys have different definitions of “significant” (sub)millimeter detections, different data reduction techniques, and different standards for radio counterpart associations, we marginalize over all of these variables by looking at the average radio counterpart

identification rate, and the average 20 cm map sensitivity. Using the surveys listed in Table 2.5, we find  $\langle\sigma_{1.4\text{ GHz}}\rangle \simeq 7.2\,\mu\text{Jy}$  and  $\langle R_{1.4\text{ GHz}}\rangle \simeq 57\%$ .

If we imagine that our field had a sensitivity  $\langle\sigma_{1.4\text{ GHz}}\rangle \simeq 7.2\,\mu\text{Jy}$ , six of our likely radio counterparts would fall below the  $4.0\sigma$  limit of  $S_{1.4\text{ GHz}} < 29\,\mu\text{Jy}$  and would not be detected. Four additional likely 20 cm counterparts would appear at the  $4\text{--}5\sigma$  level and would be at high risk of not being detected due to the usual completeness effects. Therefore, our radio counterpart identification rate would be  $68^{+8\%}_{-9\%}\text{--}78^{+7\%}_{-8\%}$ . This range is only marginally greater than the average value of 57%, and well within the scatter of the previous surveys. Therefore, we attribute our high radio identification rate to the extremely sensitive VLA map of this field, rather than to unusual properties of 1.2 mm-selected sources at this depth.

Because we expect  $\sim 5$  spurious detections among our 41 sources with  $S/N > 4.0$  and we find only 2–3 detections with unlikely or no radio counterparts, there is little room left to accommodate a substantial, extremely high-redshift ( $z > 5$ ) population of radio-undetected SMGs (see also Ivison et al., 2005). This work suggests that with a deep enough radio image, perhaps all SMGs might have their radio counterparts identified, auguring well for upcoming deep surveys that exploit the dramatically expanded correlator bandwidth of the EVLA.

We find that  $7.3^{+6.7\%}_{-4.0\%}$  (3/41) of our detections have two likely radio counterparts (MAMBO ID # 3, 15, and 39). If we consider the fact that 5% of all randomly chosen positions within our MAMBO map will have counterparts within  $8''$  with  $P \leq 0.05$ , then we would expect to find a double radio counterpart rate of  $\sim 4.6\%$  from chance associations. Previous studies have found that  $\sim 10\%$  of SMGs host multiple likely radio counterparts (see, e.g., Ivison et al., 2002, 2007; Pope et al., 2006), probably due to the effects of confusion within the submm/mm image, physical interactions, or the extended jets of radio-loud AGN. Although our SMG sample in the LHN is too small

Table 2.5. 20 cm counterpart identification rates

Reference	Instrument	Field	$\sigma_{1.4\text{ GHz}}$ ( $\mu\text{Jy beam}^{-1}$ )	ID rate
Borys et al. (2004)	SCUBA 850 $\mu\text{m}$	GOODS-N	9.0	58% (11/19)
Iverson et al. (2007)	SCUBA 850 $\mu\text{m}$	LHE & SXDF	4.2 & 7	52% (62/120)
Bertoldi et al. (2007)	MAMBO 1.2 mm	COSMOS	8.5	73% (11/15)
Scott et al. (2008)	AzTEC 1.1 mm	COSMOS	10.5	44% (12/47)
Chapin et al. (2009)	AzTEC 1.1 mm	GOODS-N	4.5	76% (22/29)
Biggs et al. (2011)	LABOCA 870 $\mu\text{m}$	ECDF-S	6.5	37% (47/126)
<i>This Work</i>	MAMBO 1.2 mm	LHN	2.7	93% (38/41)

to be able to constrain the fraction of multiple radio counterparts to better than  $\pm 5\%$ , we note that the pair separations of the radio counterparts are  $2.1''$ ,  $7.7''$ , and  $7.4''$ , and that two of the three MAMBO sources have deboosted flux densities in the top 25% of our sample. These results may be in agreement with the trend identified in Ivison et al. (2007) that multiple radio counterparts are preferentially associated with the brightest SMGs, and have pair angular separations  $\Delta\theta \simeq 2''\text{--}6''$ .

### 2.7.3 Redshift distribution

As listed in Table 2.2 and detailed in Section 2.9, of our 41 significant individual detections, two have optical spectroscopic redshifts (Polletta et al., 2006; Owen & Morrison, 2009), two have mid-IR spectroscopic redshifts (Fiolet et al., 2010), and two have high-quality photometric redshifts based on *Herschel* far-IR photometry that we will denote in what follows as “ $z'_{\text{phot}}$ ” (Magdis et al., 2010). For those of the remaining 35 sources with robust or likely radio counterparts, we generally adopt the optical photometric redshifts (denoted  $z_{\text{phot}}$  in what follows) determined by Strazzullo et al. (2010) for the radio catalog of Owen & Morrison (2008). The exception to this rule comes for  $\{z_{\text{phot}}\}$  to which Strazzullo et al. (2010) assign a goodness-of-fit quality flag of “C”; these redshifts are less reliable, and in particular are more likely to manifest catastrophic errors. For such sources, as well as for the one 1.2 mm detection that lacks a radio counterpart altogether, we instead derive our own redshift estimates ( $z_\alpha$ ) using the radio-submillimeter spectral index redshift indicator of Carilli & Yun (1999):

$$\alpha_{1.4}^{350} = -0.24 - [0.42 \times (\alpha_{\text{radio}} - \alpha_{\text{submm}}) \times \log_{10}(1 + z_\alpha)] \quad (2.16)$$

(see also Carilli & Yun, 2000; Yun & Carilli, 2002). For  $\alpha_{\text{radio}}$  we use, in order of priority and availability,  $\alpha_{20\text{cm}}^{90\text{cm}}$ ,  $\alpha_{20\text{cm}}^{50\text{cm}}$ , or  $-0.68$ . We use  $\alpha_{20\text{cm}}^{50\text{cm}}$  only for sources with clean, unblended 50 cm detections. For these unblended 50 cm counterparts, we find an average value of  $\langle \alpha_{20\text{cm}}^{50\text{cm}} \rangle = -0.68 \pm 0.06$  (see Figure 2.18), in agreement with the

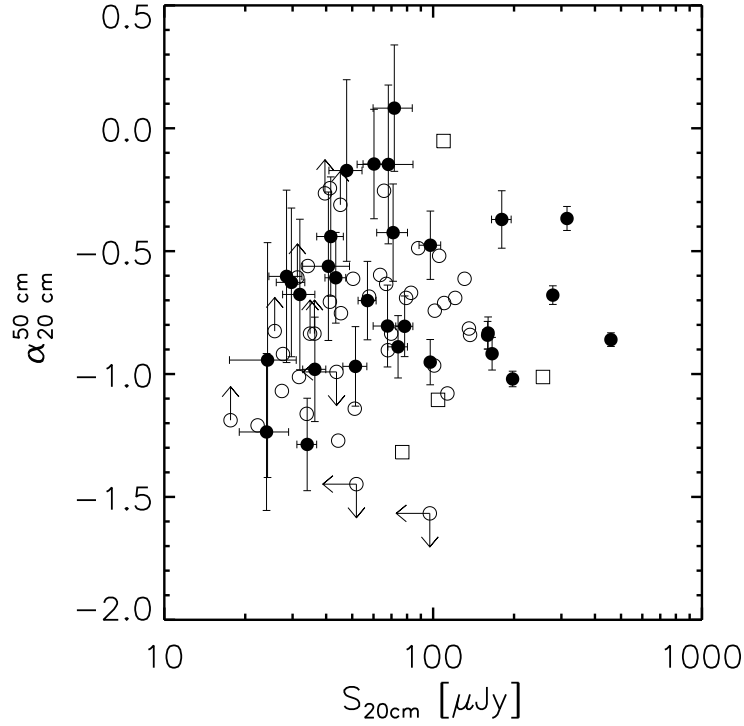


Figure 2.18: 50/20 cm spectral index vs. 20 cm flux density for SMG radio counterparts. Solid circles represent the 20 unblended 50 cm radio counterparts to our MAMBO detections. Open circles (squares) represent non AGN-dominated (AGN-dominated) SMGs in the LHE field (Ibar et al., 2010).

average spectral index of SMGs in the LHE field of  $\langle \alpha_{20\text{ cm}}^{50\text{ cm}} \rangle = -0.75 \pm 0.06$  (Ibar et al., 2009, 2010). We adopt this mean value of  $\alpha_{20\text{ cm}}^{50\text{ cm}}$  ( $-0.68$ ) for redshift determination of sources with *only* 20 cm radio counterparts, or whose 50 cm counterparts are confused. For  $\alpha_{\text{submm}}$ , we use the spectral index at 1.2 mm of the fiducial high-redshift dusty galaxy SED ( $\alpha_{\text{submm}} = 3.2$ ), as motivated in §2.7.1. For our detection with no likely radio counterpart, we estimate a redshift lower bound by using the local  $S_{20\text{ cm}}$   $4\sigma$  upper limit in Equation 2.16.

Figure 2.19 illustrates why we exclude C-quality photometric redshifts from our catalog. Plotted is the  $\alpha_{1.4}^{350}$  spectral index of the detections as a function of  $z_{\text{phot}}$ . The points are coded according to photometric redshift quality flag (Strazzullo et al., 2010). The points with the best photometric redshift fit quality (AA) are shown as black

circles, followed by blue squares (A), green diamonds (B), and red triangles (C). The shaded region shows the Carilli & Yun (1999) relation for  $-\alpha_{\text{radio}} = 0.52 - 0.80$ , where  $-0.52$  represents the median  $\alpha_{20\text{cm}}^{90\text{cm}}$  spectral index in the LHN field (Owen et al., 2009) and  $-0.80$  is the fiducial synchrotron value (Condon, 1992). The over-plotted lines show the empirical relations recovered by redshifting the SEDs of nearby star-forming galaxies M82 and Arp 220 (Klein et al., 1988; Scoville et al., 1991). The highest quality photometric redshifts agree with their galaxies’ spectral indices in that they either follow the Carilli & Yun relation, or are consistent with an M82 or Arp 220 SED. In contrast, the C-quality photometric redshifts are scattered almost uniformly in  $z$  for a given  $\alpha_{1.4}^{350}$ , demonstrating their lack of robustness.

Figure 2.20 shows the redshift distribution of our catalog, including all spectroscopic, photometric, and  $\alpha_{1.4}^{350}$ -estimated redshifts. It is apparent in Figure 2.20 that the 17 spectroscopic and high-quality (*Herschel* and AA/A/B-grade optical) photometric redshifts are biased towards lower redshifts. The median redshift for this 41% of our sample is  $z_{\text{median}} = 2.26$ , with an inter-quartile range of 1.72–2.90. For all galaxies,  $z_{\text{median}} = 2.90$ , with an inter-quartile range of 2.33–3.70. This systematic bias has two causes. First, the highest-redshift galaxies have the faintest counterparts, and will necessarily be detected in fewer optical bands, which results in a poorer fit. This trend is in contrast to the full radio catalog, for which the median  $z_{\text{phot}}$  is  $\sim 1$  and the fraction of photometric redshifts with AA/A/B quality ( $\sim 85\%$ ) is much higher than for our MAMBO sources. Second, the SEDs in the Strazzullo et al. (2010) galaxy template library are most representative of nearby galaxies, potentially resulting in a poor fit if they are applied to high- $z$  galaxies whose SEDs are not included in that library.

The median redshift for our sample ( $z_{\text{median}} = 2.90$ ) is larger than the median redshift determined by Pope et al. (2006) for a complete sample of  $850\mu\text{m}$ -selected SMGs with spectroscopic redshifts ( $z_{\text{median}} = 2.0$ ). Although our redshift distribution

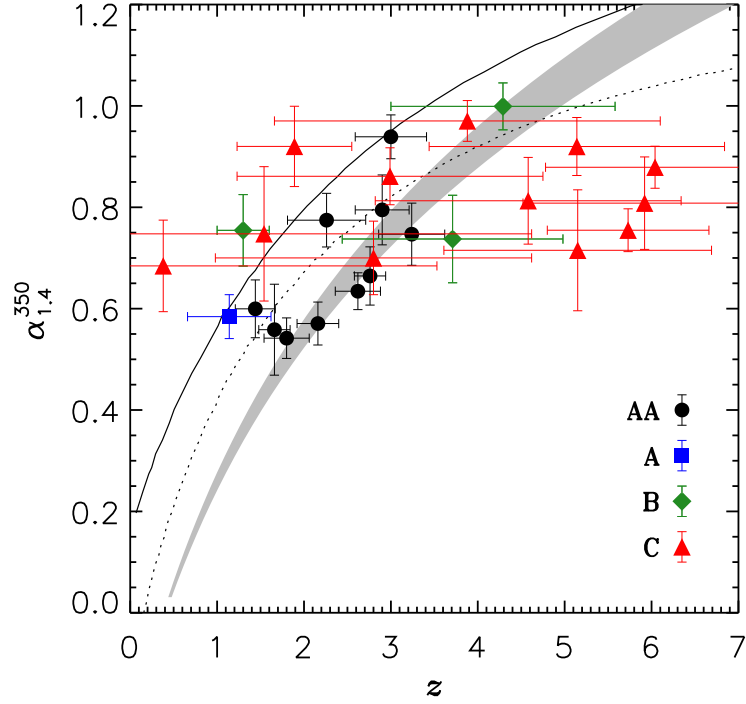


Figure 2.19: 350/1.4 GHz spectral index ( $\alpha_{1.4}^{350}$ ) vs.  $z$ . Black circles, blue squares, green diamonds, and red triangles have  $z_{\text{phot}}$  with fit qualities of AA, A, B, and C, respectively. The shaded area shows the expected behavior of  $\alpha_{1.4}^{350}$  for the Carilli & Yun (1999) spectral index redshift indicator, with  $-\alpha_{\text{radio}}$  ranging from 0.52–0.80. The solid and dashed lines show the empirical relations obtained by redshifting the SEDs of nearby starburst galaxies Arp 220 and M82, respectively.



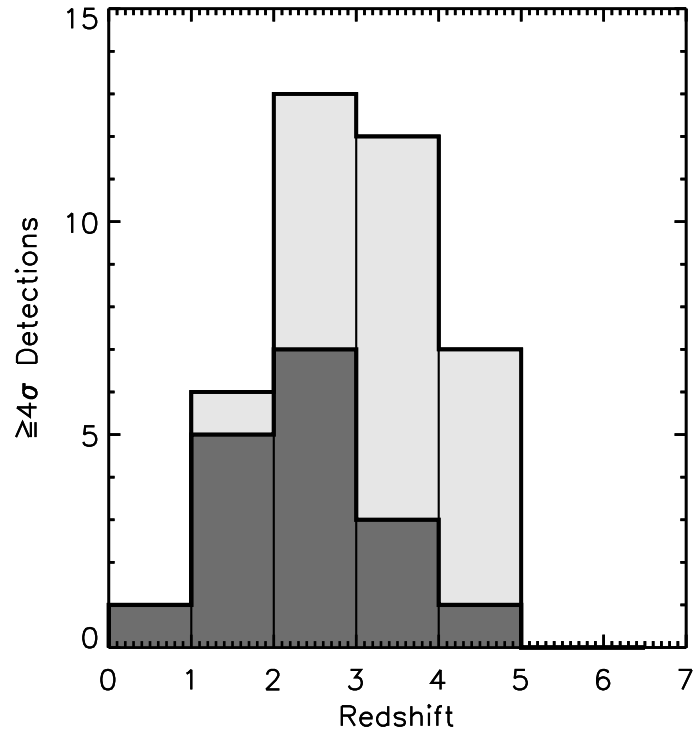


Figure 2.20: Redshift distribution of significant detections. The light grey histogram includes all sources. The dark grey histogram includes only sources with spectroscopic or high-quality (*Herschel* or AA/A/B-grade optical) photometric redshifts.

has greater uncertainties because it relies heavily on photometric redshifts and spectral index redshift estimates, it is in agreement with the results of Chapin et al. (2009), who have shown that, with high statistical significance, galaxies in a sample selected at 1.1 mm are detected at higher redshift ( $z_{\text{median}} = 2.7$ ) than those selected at  $850\ \mu\text{m}$ . Our median redshift is also greater than that of the sample of 68 galaxies selected at  $870\ \mu\text{m}$  from the LABOCA survey of the ECDF-S. Using 17-band optical through mid-IR photometry, Wardlow et al. (2011) find  $z_{\text{median}} = 2.2$ .

#### 2.7.4 Spatial correlation with 20 cm sources

The results from the  $w(\theta)$  and nearest neighbor analyses (§2.5.8) suggest that our sources are clustered to some degree. The spike in  $w(\theta)$  on  $\sim 4'$  scales is an intriguing result that is consistent with the visual impression of Figure 2.1 (i.e., the southeastern overdensity and the central void) and hints at the existence of large-scale structure (LSS) in this field. To investigate whether the spatial distribution of our detections traces LSS that can also be seen at other wavelengths, we compare our source positions to the distribution of radio sources within the LHN. In order to compare our MAMBO sources to radio sources at comparable redshifts, we include only radio sources with  $1.5 < z_{\text{phot}} < 4.5$  (excluding all that only have a C-quality  $z_{\text{phot}}$ ). Additionally, we only consider radio sources with sizes greater than  $1.0''$ . These larger sources will be preferentially gas-rich mergers with extended star formation or radio-loud AGN, which we would naively expect to trace environmental overdensities on the basis of studies at lower redshift (e.g., Hill & Lilly, 1991; Best, 2004; Best et al., 2005; Wake et al., 2008). From a practical standpoint, they can also be detected over the full area of the MAMBO map, allowing for a fair comparison; sources with 20 cm sizes  $\leq 1''$ , in contrast, tend to be fainter, and therefore have systematically lower surface densities farther from the center of the VLA map.

In Figure 2.21, we plot our 1.2 mm source positions over a  $3'$ -resolution smoothed surface density map of the 307 radio sources in the Owen & Morrison (2008) VLA catalog that satisfy our selection cuts. We find that the distributions of the two populations agree quite well: (1) the density map shows a deficiency of radio sources at the location of our central MAMBO void, (2) every radio source density peak ( $\langle \Sigma_{20\text{ cm}} \rangle \geq 0.5 \text{ arcmin}^{-2}$ ) is associated with at least one MAMBO detection, and (3)  $\sim 66\%$  of our MAMBO detections are located in regions with higher than average ( $\langle \Sigma_{20\text{ cm}} \rangle \geq 0.34 \text{ arcmin}^{-2}$ ) radio source density, whose area comprises only 45% of the total. This striking agreement seems to argue for a real physical correlation between our MAMBO detections and 20 cm radio galaxies at similar redshifts. Following Austermann et al. (2009), we have also compared our SMG catalog to an identical number of homogeneously distributed, randomly chosen positions. The experiment confirms the spatial correlation at a confidence level of 90%. However, when using random positions derived from our simulated maps that take into account the spatially varying sensitivity, we find that our MAMBO detections, although significantly correlated with each other, are not significantly spatially correlated with this sample of high- $z$  20 cm galaxies.

### 2.7.5 Resolving the 1.2 mm CIB

At 1.2 mm, the cosmic infrared background (CIB) intensity is  $I_\nu \simeq 15 - 24 \text{ Jy deg}^{-2}$  (Puget et al., 1996; Fixsen et al., 1998). By adding up the deboosted flux densities of our detections with  $S/N > 4.0$ , we recover  $\simeq 0.58 \text{ Jy deg}^{-2}$  of the CIB, or about  $\sim 3\%$ . Figure 2.6 shows that our best fitting Schechter function estimate of the differential number counts is entirely consistent with the intensity of the CIB, while the power-law model is only marginally compatible with it. The analysis performed by Scott et al. (2010) on ASTE/AzTEC data in the GOODS-S field finds that the best-fit power law model from their  $P(D)$  analysis can account for the CIB, although only if they integrate

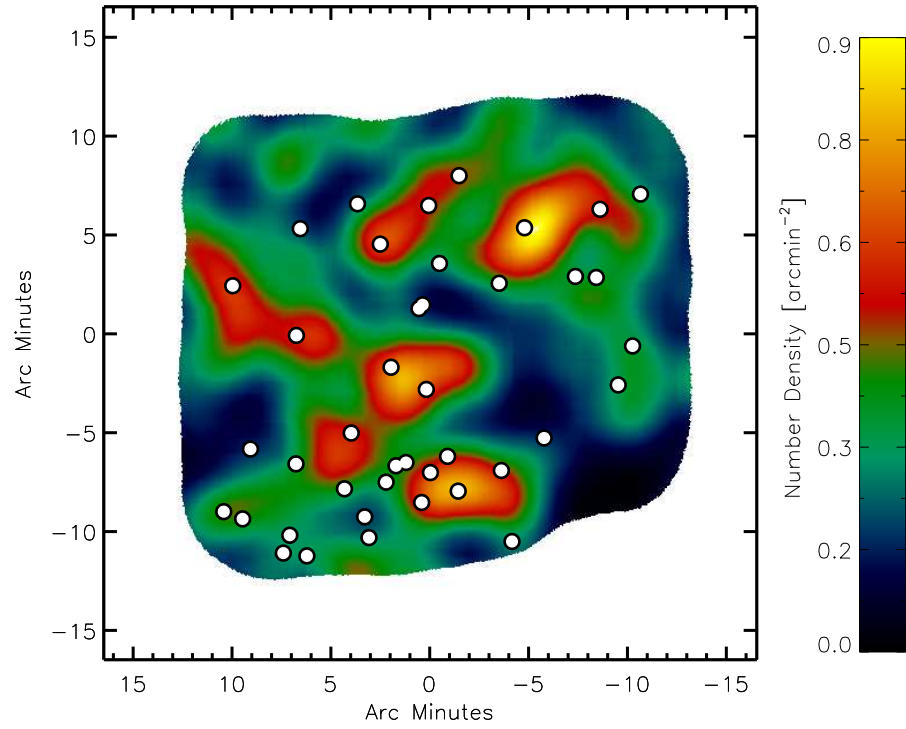


Figure 2.21: Distributions of individually detected MAMBO sources and the smoothed surface density of 20 cm radio sources with  $1.5 < z_{\text{phot}} < 4.5$  (excluding radio sources with C-quality photometric redshifts) and sizes  $\geq 1''$ . The area shown is the region in the “full” map used for source extraction.

the counts past the cutoff used for that analysis. They also find that their Schechter function model is incompatible with the CIB, and can only recover  $\sim 30\%$  of the 1.1 mm background when integrated down to  $S'_{1.1\text{ mm}} = 0$  mJy. These results may be due to their a priori choice of a faint-end power-law index  $\delta' = 1.0$ . We fit for this parameter directly and find that a steeper value of  $\delta' \simeq 1.86$  is optimal for our data and produces enough faint sources to account fully for the CIB light at 1.2 mm.

## 2.8 Conclusions

We have presented a  $566 \text{ arcmin}^2$  map of the Lockman Hole North field with an average optimally filtered point source sensitivity  $\simeq 0.75 \text{ mJy beam}^{-1}$ . By making use of previously developed and original techniques to handle chopped bolometer array data, along with  $P(D)$ -based number counts and clustering analyses, we have assembled a comprehensive picture of the 1.2 mm sky. Our results provide valuable new constraints for models of the evolution of dusty starburst galaxies through cosmic time.

We detect 41 1.2 mm sources at  $S/N > 4.0$  in our final map. Of these 41 detections, 38 have robust or likely ( $P < 0.05$ ) 20 cm radio counterparts, and 20 have robust or likely counterparts at  $24 \mu\text{m}$ . Based on Monte-Carlo simulations, we expect  $\sim 5$  of these detections to be spurious, and only  $\sim 2$  20 cm counterparts with  $P < 0.05$  to be chance associations. This result gives our MAMBO/LHN map the highest single-field SMG radio counterpart identification rate ever observed ( $93^{+4}_{-7}\%$ ), which we have shown can be explained entirely by the extraordinary depth of our 20 cm VLA map. The enhanced sensitivity of the EVLA will be able to make high counterpart fractions routine for future SMG samples. Based on the spectroscopic, photometric, and radio/far-infrared spectral index redshifts of these counterparts, the median redshift of our sample is  $z_{\text{median}} = 2.9$ , higher than has been determined for  $850 \mu\text{m}$ -selected SMG samples in fields with shallower VLA coverage.

We estimate the number counts of 1.2 mm sources both directly and by using a  $P(D)$  analysis and find a similar slope but a lower overall normalization relative to previous MAMBO surveys. However, our results are in close agreement, after a scaling in flux density, with those of recent surveys at 1.1 mm. The compatibility of our directly calculated counts and  $P(D)$  analysis with the constraint of the 1.2 mm CIB demonstrate the robustness of our results. In particular, we find that for  $S_{1.2\text{mm}} \lesssim 0.05\text{ mJy}$  the SMG differential number counts cannot keep rising with the faint-end slope observed for  $S_{1.2\text{mm}} > 0.05\text{ mJy}$ , and that the bright SMG population contributes at most a small fraction to the 1.2 mm CIB.

The high resolution afforded by the IRAM 30 m telescope, the large extent of our map, and the use of analysis methods that thoroughly take into account the negative residuals of the chopped triple-beam PSF have allowed us to demonstrate possible clustering in the 1.2 mm population. The SMG correlation function, a nearest neighbors analysis, and, to a lesser extent, the spatial correlation of our significant detections with large radio sources over the same redshift range all suggest that our sample traces some degree of large scale structure at high redshift. Our work prepares the 1.2 mm waveband for the ALMA era by creating a better understanding of this population’s statistical properties and setting new 1.2 mm constraints for galaxy evolution models.

## 2.9 Appendix: Notes on individual detections

### 2.9.1 MM J104700.1+590109 = ID # 1

Polletta et al. (2006) report an optical  $z_{\text{spec}} = 2.562$  for this source. It also has a  $70\text{ }\mu\text{m}$  counterpart with  $S_{70\text{ }\mu\text{m}} = 10.4 \pm 1.7\text{ mJy}$  at a distance of  $3.2''$ , and a  $160\text{ }\mu\text{m}$  counterpart with  $S_{160\text{ }\mu\text{m}} = 24.1 \pm 1.9\text{ mJy}$  at a distance of  $1.7''$  (Owen, 2013b).

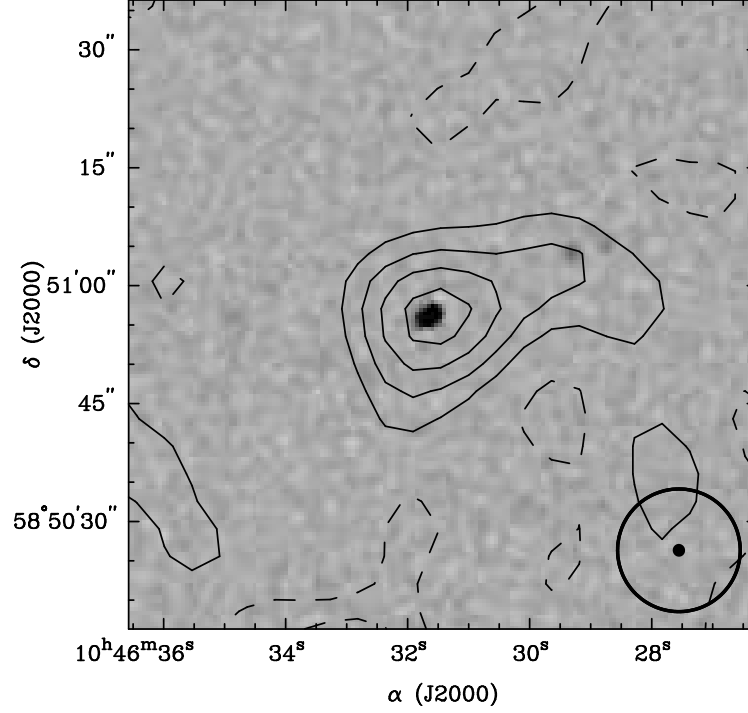


Figure 2.22: 1.2 mm contours (multiples of  $1.0 \text{ mJy beam}^{-1}$ ) for MAMBO source MM J104631.4+585056 = ID # 03, overlaid on 20 cm map showing double counterpart. The black circle and small filled ellipse at lower right represent the  $15.6''$  MAMBO beam (after filtering) and the  $1.63'' \times 1.57''$  VLA beam, respectively.

### 2.9.2 MM J104631.4+585056 = ID # 3

In addition to the robust 20 cm counterpart listed in Table 2.2, this source has an additional likely counterpart with  $S_{20 \text{ cm}} = 30 \mu\text{Jy}$ , separation  $2.6''$ , and  $P = 0.034$ , with which it is nearly blended. Neither radio counterpart has an estimated photometric redshift. Figure 2.22 shows 1.2 mm contours overlaid on a 20 cm cutout image that includes both counterparts.

### 2.9.3 MM J104638.4+585613 = ID # 6

We identify this source with LHN8 in the *Herschel* catalog of Magdis et al. (2010), from which it is separated by  $2.0''$  ( $P = 0.0084$ ), and with SWIRE4-J104638.68+585612.5 = ID # L14 in the *Spitzer* sample of Fiolet et al. (2010), who report a mid-IR  $z_{\text{spec}} = 2.03$ .

Fiolet et al. (2009) report an on-off flux density measurement of  $S_{1.2\text{ mm}} = 2.13 \pm 0.71\text{ mJy}$ , which is consistent with our (non-deboosted)  $S_{1.2\text{ mm}} = 2.7 \pm 0.5\text{ mJy}$  within the uncertainties.

#### 2.9.4 MM J104704.9+585008 = ID # 9

The radio counterpart to this source ( $P = 0.0043$ ) is not in the catalog of Owen & Morrison (2008) because it has a S/N ratio of 4.8.

#### 2.9.5 MM J104556.5+585317 = ID # 11

We identify this source with LHN1 in the *Herschel* catalog of Magdis et al. (2010), from which it is separated by  $3.4''$  ( $P = 0.0057$ ), and with SWIRE4-J104556.90+585318.8 = ID # L11 in the *Spitzer* sample of Fiolet et al. (2010), who report a mid-IR  $z_{\text{spec}} = 1.95$  in good agreement with the optical  $z_{\text{phot}} = 1.80$  reported by Strazzullo et al. (2010). Fiolet et al. (2009) report an on-off flux density measurement of  $S_{1.2\text{ mm}} = 3.08 \pm 0.58\text{ mJy}$ , which is consistent with our (non-deboosted)  $S_{1.2\text{ mm}} = 3.4 \pm 0.6\text{ mJy}$  within the uncertainties. This source also has a  $160\text{ }\mu\text{m}$  counterpart (Owen, 2013b) with  $S_{160\text{ }\mu\text{m}} = 11.8 \pm 1.5\text{ mJy}$  at a distance of  $4.3''$

#### 2.9.6 MM J104728.3+585213 = ID # 15

This source has two radio counterparts; the primary counterpart listed in Table 2.2 has  $z_{\text{phot}} = 2.76$ , while the second (with  $P = 0.032$ ) has  $z_{\text{phot}} = 1.06$ . In the 20 cm map, we see a quadruple radio source (see Figure 2.23). At a low level of significance, the 1.2 mm emission appears to be elongated in the same direction as the radio source(s). This system also has a  $160\text{ }\mu\text{m}$  counterpart (Owen, 2013b) with  $S_{160\text{ }\mu\text{m}} = 12.7 \pm 1.5\text{ mJy}$  at a distance of  $6.8''$ .



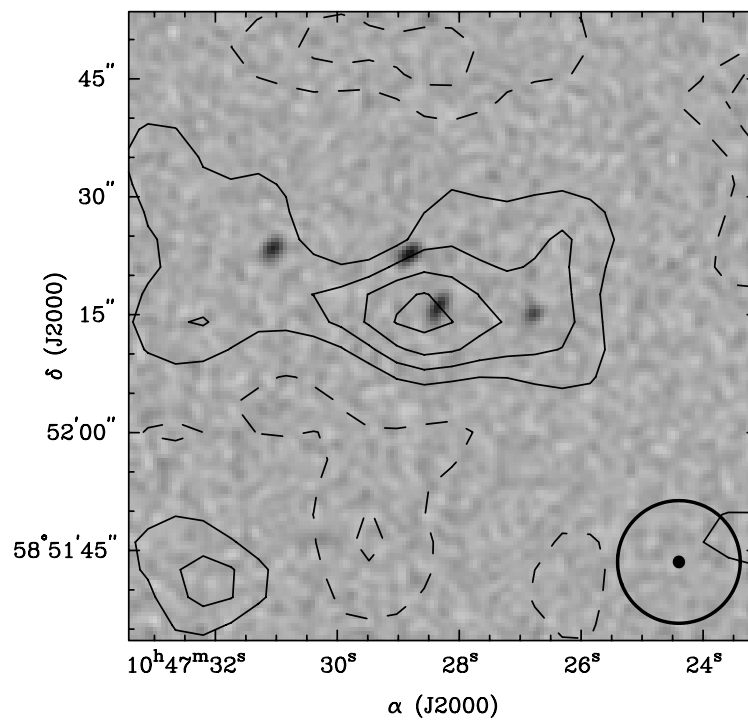


Figure 2.23: 1.2 mm contours (multiples of  $1.0 \text{ mJy beam}^{-1}$ ) for MAMBO source MMJ104728.3+585213 = ID # 15, overlaid on 20 cm map showing multiple counterparts. Other notation is as in Figure 2.22.

### 2.9.7 MM J104610.4+590242 = ID # 17

This source is separated by only  $\sim 15''$  from MM J104611.9+590231 = ID # 39. The catalog of Owen & Morrison (2008) includes a single radio source whose nominal position is midway between two very faint sources (one resolved, one unresolved) that are visible in the original 20 cm map (see Figure 2.24). These two sources, with peak flux densities of  $15.6 \mu\text{Jy}$  and  $13.5 \mu\text{Jy}$ , are only identifiable because they lie very close to the center of the VLA map, where the local RMS noise is only  $2.9 \mu\text{Jy beam}^{-1}$ . After attributing the flux of the catalogued source to its two constituents, we find that one is a robust radio counterpart for the MAMBO source ( $1.0''$  separation with  $P = 0.0099$ ), while the other is probably a chance association ( $3.3''$  separation with  $P = 0.077$ ).

### 2.9.8 MM J104617.0+585444 = ID # 20

This source has an unlikely 20 cm radio counterpart ( $P = 0.12$ ) with  $S/N = 4.2$  ( $S_{20\text{ cm}} = 15.0 \pm 3.6 \mu\text{Jy}$ ), and is therefore not in the catalog of Owen & Morrison (2008), which includes only sources with  $S/N > 5.0$ .

### 2.9.9 MM J104522.8+585558 = ID # 26

This source has no radio counterpart within  $8''$  and no likely  $24\mu\text{m}$  counterpart, although it does have an X-ray counterpart (see §2.6.5).

### 2.9.10 MM J104620.9+585434 = ID # 28

This source has a likely 20 cm radio counterpart ( $P = 0.029$ ) with  $S/N = 4.3$  ( $S_{20\text{ cm}} = 24.8 \pm 5.8 \mu\text{Jy}$ ), and is therefore not in the catalog of Owen & Morrison (2008), which includes only sources with  $S/N > 5.0$ .

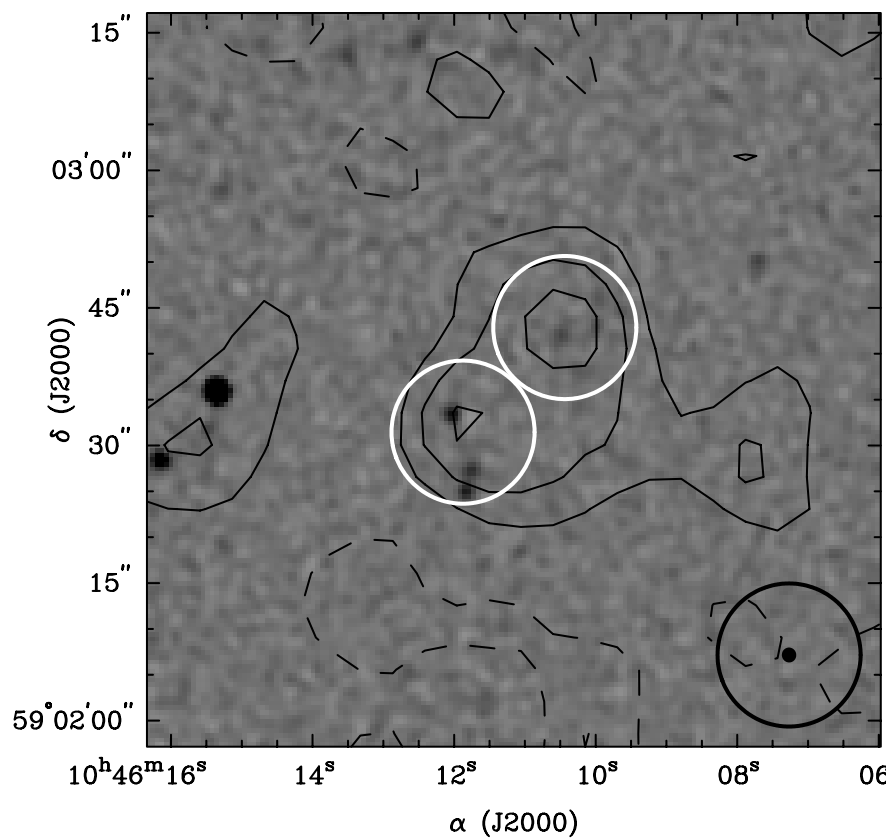


Figure 2.24: Nearly blended MAMBO sources MM J104610.4+590242 (ID # 17), which has one likely 20 cm counterpart, and MM J104611.9+590231 (ID # 39), which has two likely 20 cm counterparts. 1.2 mm contours (multiples of  $0.7 \text{ mJy beam}^{-1}$ ) are overlaid on 20 cm greyscale. White circles are centered on the positions of the extracted MAMBO sources; other notation is as in Figure 2.22.

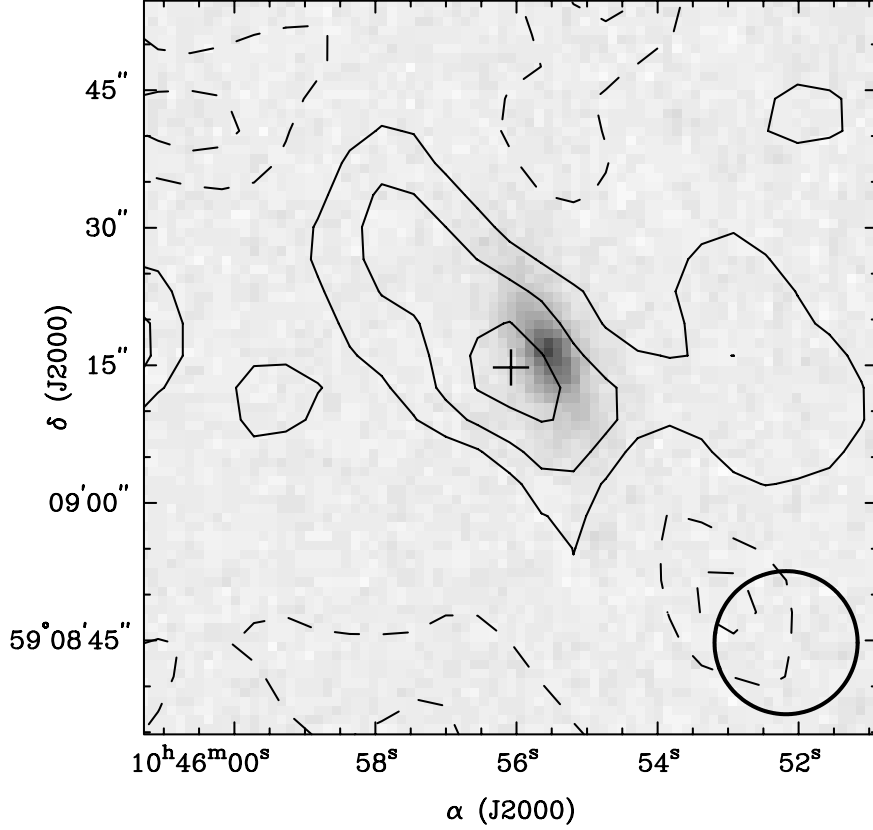


Figure 2.25: 1.2 mm contours (multiples of  $0.8 \text{ mJy beam}^{-1}$ ) for MAMBO source MM J104556.1+590914 = ID # 29, overlaid on a DSS red image of SDSS J104555.49+590915.9 at  $z_{\text{spec}} = 0.044$  (Owen & Morrison, 2009). Other notation is as in Figure 2.22.

### 2.9.11 MM J104556.1+590914 = ID # 29

We identify this source with SDSS J104555.49+590915.9, an optically bright galaxy for which Owen & Morrison (2009) report an optical  $z_{\text{spec}} = 0.044$ . Figure 2.25 shows a red optical image overlaid with 1.2 mm contours, which at a low level of significance are elongated in the same direction as the galaxy's stars. This  $\simeq 20''$  source is heavily resolved at 20 cm and 50 cm. It is also detected at  $160 \mu\text{m}$  (Owen, 2013b) with  $S_{160 \mu\text{m}} = 15.8 \pm 1.4 \text{ mJy}$  (at a separation of  $6.6''$ ), and at  $250 \mu\text{m}$  (*Herschel*/SPIRE; Smith et al., 2012) with  $S_{250 \mu\text{m}} = 133 \pm 8 \text{ mJy}$  (at a separation of  $3.6''$ ).

### 2.9.12 MM J104539.6+585419 = ID # 32

We identify this source with LHN3 in the *Herschel* catalog of Magdis et al. (2010), from which it is separated by  $5.2''$  ( $P = 0.016$ ). Magdis et al. (2010) estimate  $z'_{\text{phot}} = 2.40$  on the basis of their PACS and SPIRE photometry, which we list in Table 2.2 rather than the Strazzullo et al. (2010) optical  $z_{\text{phot}} = 1.32$ , due to the close connection between far-IR and millimeter emission.

### 2.9.13 MM J104608.1+590744 = ID # 36

This source has a 20 cm radio counterpart ( $P = 0.041$ ) with  $S/N = 4.9$  ( $S_{20\text{ cm}} = 16.1 \pm 3.3 \mu\text{Jy}$ ), and is therefore not in the catalog of Owen & Morrison (2008), which includes only sources with  $S/N > 5.0$ .

### 2.9.14 MM J104610.8+585242 = ID # 37

We identify this source with LHN4 in the *Herschel* catalog of Magdis et al. (2010), from which it is separated by  $2.4''$  ( $P = 0.013$ ). Magdis et al. (2010) estimate  $z'_{\text{phot}} = 1.72$  on the basis of their PACS and SPIRE photometry, which we list in Table 2.2; this is in good agreement with the optical  $z_{\text{phot}} = 1.66$  reported by Strazzullo et al. (2010).

### 2.9.15 MM J104611.9+590231 = ID # 39

This source is separated by only  $\sim 15''$  from MM J104610.4+590242 = ID # 17. It also has a pair of likely radio counterparts within an  $8''$  search radius. Figure 2.24 shows 1.2 mm contours overlaid on a 20 cm cutout image. This source is not identified in the catalog of Owen & Morrison (2008).

## Chapter 3

### Detection of Iron $K\alpha$ Emission from a Complete Sample of Submillimeter Galaxies

#### 3.1 Introduction

Submillimeter galaxies (SMGs) are distant star-forming systems with tremendous infrared luminosities ( $L_{\text{IR}}[8\text{--}1000\,\mu\text{m}] \gtrsim 10^{12} L_{\odot}$ ). In the (sub)millimeter waveband they are observable out to high redshifts due to the strong negative  $K$ -correction in the Rayleigh-Jeans regime of their thermal spectrum (see, e.g., Blain et al., 2002). The prevalence of SMGs at  $z > 1$  (Chapman et al., 2005) in combination with their high rates of dust-obscured star-formation imply that they may be responsible for the production of a significant fraction of all the stellar mass in present-day galaxies. X-ray (Alexander et al., 2003, 2005a) and mid-infrared (Valiante et al., 2007; Menéndez-Delmestre et al., 2007, 2009; Pope et al., 2008) spectroscopy shows that SMGs frequently contain active galactic nuclei (AGN) as well as powerful starbursts. This connection between star formation and accretion at high redshift may help explain the black hole mass-bulge mass relation in present-day galaxies (e.g., Alexander et al., 2005b). However, it remains hard to determine the relative importance of accretion and star formation for the SMG population as a whole because of the challenge of assembling large, statistically unbiased SMG samples.

Studying the X-ray properties of SMGs is difficult for two main reasons. First, the X-ray counterparts to SMGs are extremely faint. The count rate is so low that even

the deepest *Chandra* and *XMM-Newton* spectra of SMGs cannot resolve features that serve as sensitive diagnostics of the physical conditions inside galaxies, like the Fe K $\alpha$  emission line. Fe K $\alpha$  emission is a ubiquitous feature in spectra of optically-selected AGN up to  $z \simeq 3$  (e.g., Brusa et al., 2005; Chaudhary et al., 2010; Iwasawa et al., 2011), but the Fe K $\alpha$  emission properties of SMGs remain considerably more uncertain (Alexander et al., 2005a). Second, the requirement that SMGs need radio, (sub)millimeter, or mid-IR counterparts capable of nailing down their positions in high-resolution X-ray maps can lead to concessions of inhomogeneously-selected samples (e.g., including radio-selected galaxies; Alexander et al., 2005a), yielding results that conflict with X-ray studies of purely submillimeter-selected SMG samples (Laird et al., 2010; Georgantopoulos et al., 2011). To disentangle the relationship between SMGs and X-ray selected AGN, we need to overcome the uncertainty introduced by inhomogeneously selected samples, requiring X-ray spectral analyses of large, flux-limited samples of (sub)millimeter-selected SMGs with robust counterparts.

In this work, we report on an X-ray stacking analysis of a sample of 38 SMGs detected in a 1.2 mm map of the Lockman Hole North (LHN), one of the fields in the *Spitzer* Wide-Area Infrared Extragalactic (SWIRE) Survey (Lonsdale et al., 2003), using data from the *Chandra*-SWIRE survey (Polletta et al., 2006; Wilkes et al., 2009). The high radio counterpart identification rate of the LHN SMG sample (93%; Lindner et al., 2011) is afforded by the extremely deep 20 cm map of the same field (Owen & Morrison, 2009), and allows for reliable X-ray photometry. The sample benefits from spectroscopic (Polletta et al., 2006; Owen & Morrison, 2009; Fiolet et al., 2010) and optically-derived photometric (Strazzullo et al., 2010) redshifts. Additionally, analyses of *Herschel* observations of the LHN (Magdis et al., 2010; Roseboom et al., 2012) have delivered reliable photometric redshifts and infrared luminosities for a large fraction of the sample by fitting far-IR photometry with thermal-dust spectral energy distribution

(SED) models.

In §2, we describe the observations used in our analysis. §3 outlines our X-ray stacking technique, and our method for deriving rest-frame luminosities. In §4, we compare our results to previous X-ray studies of SMGs, and discuss the possible origins of the Fe K $\alpha$  emission seen in our stacked spectrum. In §5, we present our conclusions. In our calculations, we assume a *WMAP* cosmology with  $H_0 = 70 \text{ km s}^{-1} \text{ Mpc}^{-1}$ ,  $\Omega_M = 0.27$ , and  $\Omega_\Lambda = 0.73$  (Komatsu et al., 2011).

## 3.2 Data and Sample Selection

### 3.2.1 Millimeter observations and stacking sample

Our SMG sample consists of 38 of the 41 significant detections in the 1.2 mm map (Lindner et al., 2011) of the LHN made using the Max Planck Millimeter Bolometer (MAMBO; Kreysa et al., 1998) array on the Institut de Radioastronomie Millimétrique 30 m telescope. We exclude one source that lacks a plausible 20 cm radio counterpart (L20), one that has a likely X-ray counterpart (L26), and one nearby galaxy at  $z = 0.044$  (L29) from the stacking sample. Of our final sample of 38 galaxies, 37 (97%) have robust 20 cm radio counterparts with a chance of spurious association ( $P$ ; Downes et al., 1986) of  $P < 0.05$ ; the remaining galaxy, L32, has  $P = 0.056$ . Stacking is performed with the coordinates of the SMGs' radio counterparts, which have a mean offset of  $2.4''$  with respect to the SMG centroids. Five of our stacking targets have positions that are not listed in the 20 cm catalog of Owen & Morrison (2008) because they had  $S/N < 5.0$  (L9, L28, and L36), or they were blended together with nearby radio sources (L17 and L39) during extraction (Owen & Morrison, 2008; Lindner et al., 2011). The sample has a mean redshift of  $\langle z \rangle = 2.6$  (see Table 3.3).



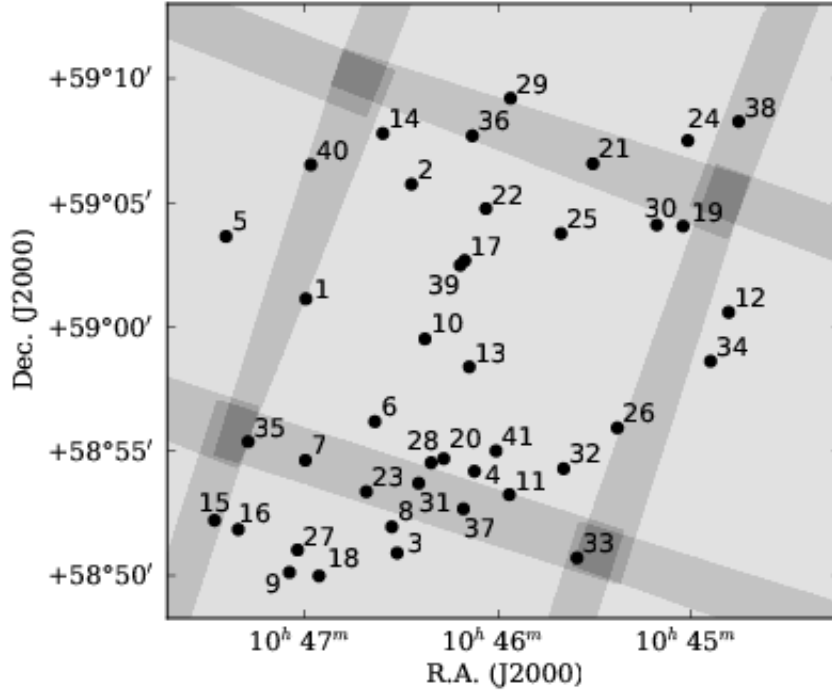


Figure 3.1: SMG positions inside the LHN. The filled circles mark the locations of the stacking targets used in this work and are labeled according to the SMGs’ ID numbers from Table 3.3. The locations of the source without a reliable radio counterpart (L20), the nearby galaxy at  $z = 0.044$  (L29), and the source with a likely X-ray counterpart (L26) are also shown even though they are not used in our stacking analysis. The greyscale image shows the relative *Chandra* effective exposure time across the field.

### 3.2.2 *Chandra* ACIS-I Observations

Our X-ray data are from the  $3 \times 3$ -pointing raster mosaic of the LHN obtained with the Advanced CCD Imaging Spectrometer (ACIS-I; Weisskopf et al., 1996) on the *Chandra* X-ray telescope by Polletta et al. (2006). The final mosaic comprises nine 70 ks pointings arranged with  $\sim 2'$  overlap (see Figure 3.1). It covers a total area of  $\simeq 0.7 \text{ deg}^2$  and has a limiting conventional broad band ( $B_C$ ; 0.5–8.0 keV) sensitivity of  $\sim 4 \times 10^{-16} \text{ erg s}^{-1} \text{ cm}^{-2}$  (Polletta et al., 2006). Fiolet et al. (2009) used these same data to search for a stacked X-ray signal among 33 *Spitzer*  $24 \mu\text{m}$ -selected starburst galaxies, and found no significant 0.3–8 keV-band emission.

Within the sample of 41 MAMBO detections in the LHN, only L26 has a likely X-ray counterpart (CXOSWJ104523.6+585601) in the catalog of Wilkes et al. (2009). This X-ray source has conventional broad band ( $B_C$ ; 0.5–8.0 keV), soft band ( $S_C$ ; 0.5–2.0 keV), and hard band ( $H_C$ ; 2.0–8.0 keV) X-ray fluxes of  $f_{B_C} = 2.53 \times 10^{-15} \text{ erg s}^{-1} \text{ cm}^{-2}$ ,  $f_{S_C} = 1.21 \times 10^{-15} \text{ erg s}^{-1} \text{ cm}^{-2}$ , and  $f_{H_C} = 1.57 \times 10^{-15} \text{ erg s}^{-1} \text{ cm}^{-2}$ , respectively, and a hardness ratio of  $\text{HR} = -0.32^{+0.31}_{-0.34}$ . The hardness ratio is defined by  $\text{HR} = (H_C - S_C)/(H_C + S_C)$ , where  $H_C$  and  $S_C$  are the counts in the *Chandra* conventional hard and soft bands, respectively.

### 3.3 Stacking Analysis

In this section we describe our reduction of the *Chandra* X-ray data products and the methods used in our stacking analysis. We use two techniques: (1) image-based stacking in binned X-ray maps (§3.3.1), and (2) a photon-based spectral stacking procedure using optimized apertures (§3.3.2). The following subsections describe our implementation of these two methods.

#### 3.3.1 Image-based stacking

We generate  $1'' \times 1''$ -pixel gridded maps of the total counts and effective exposure time in the  $B_C$ ,  $S_C$ , and  $H_C$  energy bands using the *Chandra* Interactive Analysis of Observations (CIAO; Fruscione et al., 2006) script `fluximage`. The characteristic energies input to `fluximage` to compute effective areas were 4.00 keV, 1.25 keV, and 5.00 keV for the  $B_C$ ,  $S_C$ , and  $H_C$  bands, respectively. We then used the CIAO scripts `reproject_image` to merge the maps of each observation into one mosaic, and `dmimgcalc` to produce an exposure-corrected flux image in units of  $[\text{photons cm}^{-2} \text{ s}^{-1}]$ .

Figure 3.2 shows the resulting stacked image in each energy band. The  $40'' \times 40''$  S/N postage stamp images are shown with a color stretch from  $\text{S/N} = -4$  to  $+4$ . The peak

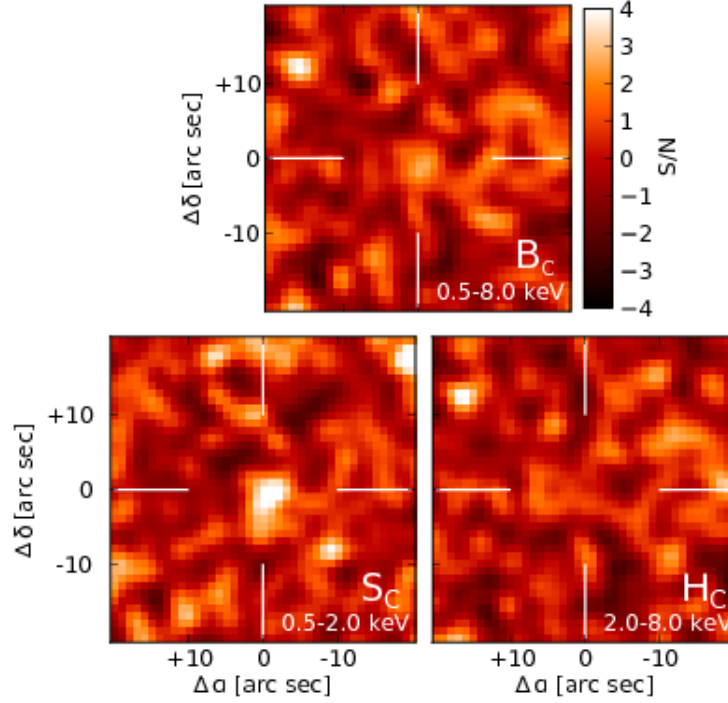


Figure 3.2: Stacked X-ray images showing the S/N in the  $B_C$ ,  $H_C$ , and  $S_C$  *Chandra* energy bands. The white cross hairs mark the stacking center. The color stretch is  $S/N=[-4,+4]$ .

$S/N$  is 3.2, 4.8, and 2.0 in the  $B_C$ ,  $S_C$ , and  $H_C$  bands, respectively. The peak of the strong stacked detection in the  $S_C$  band has an offset from the mean radio counterpart centroid position of  $\lesssim 1''$ .

### 3.3.2 Optimized broad-band stacking

Our second stacking technique does not use a binned X-ray map. Instead, we compute the stacked count rate and flux by directly counting photons at the stacking positions. The photometric aperture at each stacking location is derived using a technique similar to the optimized stacking algorithm presented in Treister et al. (2011, supplementary information).

The size and shape of the aperture at each stacking position is chosen to maximize

the point-source S/N at that position on the ACIS-I chips. The apertures are constructed as follows. For each stacking position (shown in Figure 3.1), we (1) use the CIAO script `mkpsf` to generate a 2D image of the local *Chandra* PSF, (2) convolve this PSF with a Gaussian smoothing kernel (see below), and (3) find the enclosed-energy fraction (EEF) contour  $C_{\text{EEF}}$  that maximizes the S/N of the flux within the aperture. The area enclosed by this contour defines the aperture. Because Poisson noise from the X-ray background is stronger than the flux at each position and the average exposure time does not change rapidly with increasing aperture size, the S/N within the aperture can be parametrized by  $C_{\text{EEF}}$  as

$$\text{S/N} \propto \frac{\text{EEF}}{\sqrt{A(C_{\text{EEF}})}}, \quad (3.1)$$

where  $A(C_{\text{EEF}})$  is the total area enclosed by the contour  $C_{\text{EEF}}$ . This expression is the same as that derived by Treister et al. (2011), except that instead of using only circular apertures, we allow for non-axisymmetric apertures that follow the local shape of the *Chandra* PSF.

We compensate for the change in shape of the *Chandra* PSF with photon energy by generating two optimal apertures at each stacking position, one for each energy band (i.e., for characteristic energies of 1.25 keV and 5 keV). Parts of the LHN *Chandra* mosaic were imaged multiple times due to the overlapping edges of the individual exposures (see Figure 3.1). For these positions we find the total effective aperture by maximizing Equation 3.1 using a linear combination of PSFs, one for each overlapping observation.

We broaden the local *Chandra* PSFs to accommodate photons that do not lie at the stacking centers due to intrinsic wavelength offsets in the galaxies and astrometric errors. Previous X-ray stacking analyses find the optimal aperture radius to be  $\sigma = 1.25\text{--}3.0''$  (Lehmer et al., 2005; Georgantopoulos et al., 2011). We find similarly that

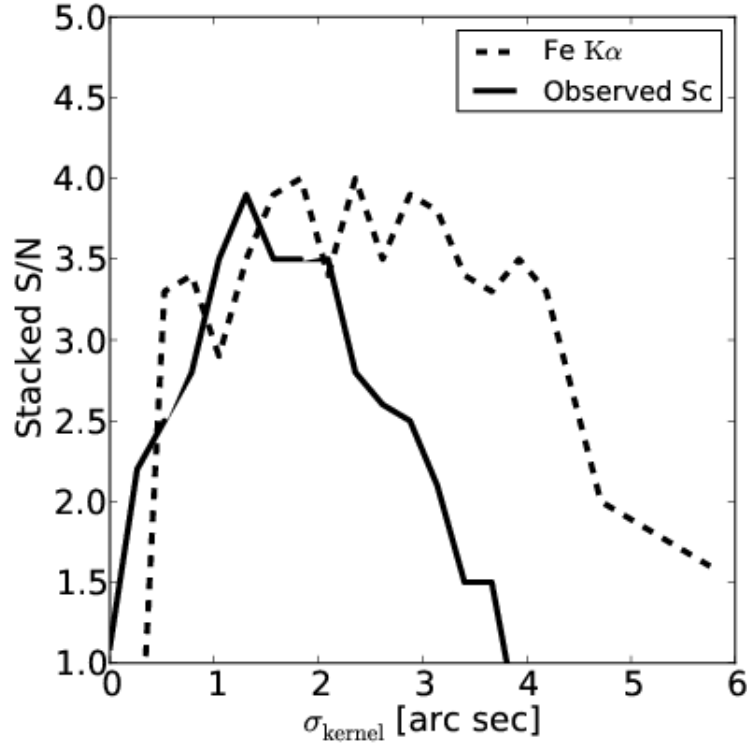


Figure 3.3: Stacked S/N of the observed  $S_C$  and rest-frame Fe  $K\alpha$  line fluxes as a function of the optimal aperture broadening kernel size  $\sigma_{\text{kernel}}$ .

our broad band stacked S/N is maximized with a smoothing kernel radius  $\sigma_{\text{kernel}} = 1.3''$  (see Figure 3.3), so we adopt this value for our subsequent broadband photometry. The smallest angular separation of any pair of stacking targets ( $15''$  for L17 and L39) is larger than the maximum radial extent of the largest X-ray stacking aperture, so we can ignore the effects of X-ray blending within our sample.

The photons used for background subtraction are collected from arrays of large circular apertures positioned next to each stacking target position. The apertures are manually positioned to exclude any bright nearby X-ray sources that could contaminate the background estimate. To avoid possible systematic uncertainties associated with the background subtraction (see, e.g., Treister et al., 2011; Williams et al., 2011), we do not impose any S/N-based clipping or additional filtering in the background regions.

Table 3.1. X-ray Stacking Results

Band	Energy keV	Net Rate $10^{-6} \text{ s}^{-1}$	Flux ( $\Gamma = 1.6$ ) $10^{-17} \text{ erg cm}^{-2} \text{ s}^{-1}$	Flux ( $\Gamma = 1.9$ ) $10^{-17} \text{ erg cm}^{-2} \text{ s}^{-1}$	$L_X$ ( $\Gamma = 1.6$ ) $10^{42} \text{ erg s}^{-1}$
$S_C$	0.5–2.0	$8.0^{+2.1}_{-2.0}$	$4.7^{+1.2}_{-1.2}$	$4.9^{+1.3}_{-1.2}$	—
$H_C$	2.0–8.0	$1.2^{+3.2}_{-2.9}$	$< 9.7$	$< 9.1$	—
$B_C$	0.5–8.0	$9.2^{+3.8}_{-3.5}$	$10.1^{+4.2}_{-3.9}$	$9.0^{+3.7}_{-3.4}$	—
$H_C^{\text{rest}}$	0.55–2.22	$8.0^{+2.1}_{-2.3}$	$4.8^{+1.3}_{-1.4}$	$4.9^{+1.3}_{-1.4}$	$3.0 \pm 1.1$
$H^{\text{rest}}$	0.55–2.78	$8.6^{+2.4}_{-2.5}$	$5.7^{+1.6}_{-1.7}$	$5.7^{+1.6}_{-1.7}$	$3.6 \pm 1.3$

Note. — Unabsorbed fluxes calculated assuming the given photon index with Galactic absorption only. Hydrogen column density taken as that of the central *Chandra* pointing,  $N_H = 6.6 \times 10^{19} \text{ cm}^{-2}$  (Stark et al., 1992). Luminosity calculation uses  $\Gamma = 1.6$ .

Table 3.1 shows the average stacked count rate and energy flux per galaxy in the three broad energy bands. We find a significant stacked detection in the soft band, and no significant detection in the hard band. To convert the stacked count rate into energy flux, we used the web-based CIAO Portable Interactive Multi-Mission Simulator<sup>1</sup> (PIMMS- version 4.4; Cycle 5). The fluxes are corrected for Galactic absorption using the column density in the direction of the LHN center,  $N_H = 6.6 \times 10^{19} \text{ cm}^{-2}$  (Stark et al., 1992). Our non-detection in the hard band leaves our calculation of the hardness ratio relatively unconstrained,  $\text{HR} = -0.68^{+0.51}_{-0.32}$  (setting a limit on the photon index  $\Gamma > 1.2$ ), although it is clear that our sample has a steeply declining photon spectrum characteristic of star-forming galaxies (e.g., Ranalli et al., 2012). This estimate of HR was made after subtracting out the count rate in the soft band that is due to the strong Fe K $\alpha$  line (see §3.3.3), which is a  $\sim 20\%$  contribution for  $1.3''$ -broadened photometric apertures.

A high photon index of  $\Gamma = 1.6$  ( $\text{HR} \simeq -0.37$ ) is found by Laird et al. (2010), who stack on SCUBA-detected SMGs in the *Chandra* Deep Field North (CDF-N). An even steeper photon index of  $\Gamma = 1.9$  ( $\text{HR} \simeq -0.49$ ) is measured by Georgantopoulos et al.

<sup>1</sup> <http://cxc.harvard.edu/toolkit/pimms.jsp>

(2011), who stack on LABOCA-detected SMGs in the Extended Chandra Deep Field South (ECDF-S). We have used values of  $\Gamma = 1.6$  and  $\Gamma = 1.9$  to compute the stacked flux in each energy band (e.g., see Table 3.1), although the difference between the two estimates is less than the Poisson uncertainty (see Table 3.1).

### 3.3.3 Optimized spectral stacking

In addition to stacked broad-band fluxes, we also calculate the observed-frame and rest-frame stacked count-rate spectra for our sample.

For each stacking target, we use redshift information in the following order of priority, subject to availability: (1) spectroscopic (Polletta et al., 2006; Owen & Morrison, 2009; Fiolet et al., 2010), (2) *Herschel*-based photometric (Magdis et al., 2010; Roseboom et al., 2012), (3) *AA*-quality optical-based photometric (Strazzullo et al., 2010), and (4) millimeter/radio photometric estimated using the Carilli & Yun (1999) spectral index  $\alpha_{850\mu\text{m}}^{20\text{cm}}$  technique (Lindner et al., 2011). The redshift distribution of our sample is shown in Figure 3.4.

We use a flat sum of the observed counts at each stacking-target position with no weighting factors. Although this technique gives more weight to the brightest members of the stack, it is necessary given that *none* of our stacking targets are individually detected and therefore S/N-based weights (used in, e.g., Treister et al., 2011) cannot be reliably assigned. For the rest-frame data, we separately coadd, blueshift, and bin the background photons to avoid creating artificial spectral features (see, e.g., Yaqoob, 2006).

The uncertainty in the rest-frame energy of the photons  $\Delta E_{\text{rest}}$  as a function of the observed photon energies  $E_{\text{obs}}$  due to the typical redshift error  $\Delta z$  is estimated by the equation

$$\Delta E_{\text{rest}} = E_{\text{obs}} \frac{\langle \Delta z \rangle}{1 + \langle z \rangle}. \quad (3.2)$$

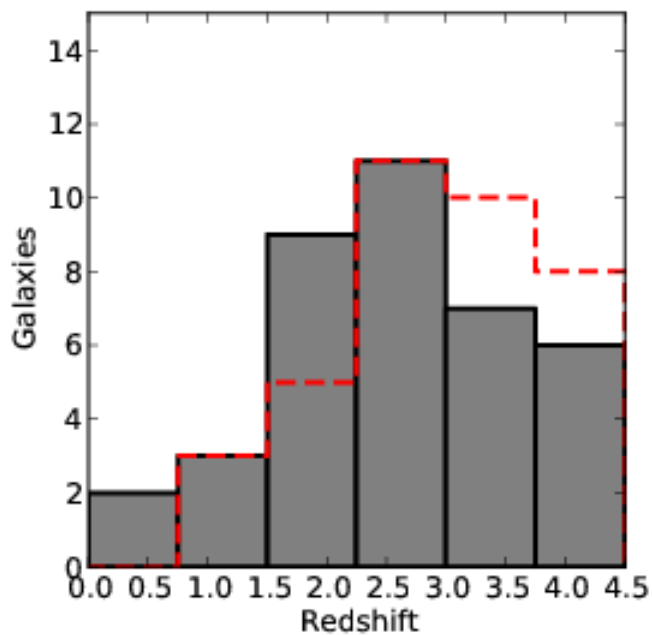


Figure 3.4: Redshift distribution for our sample of 38 SMGs. The filled histogram represents the redshifts used in this work, with  $\langle z \rangle = 2.6$ . The red dashed line represents the values as presented in Lindner et al. (2011), which relied more heavily on spectral index-based photometric redshifts.



Table 3.2. redshift uncertainties

Redshift type	N galaxies	$\Delta z$	References
Spectroscopic	3	$\simeq 0$	Polletta et al. (2006) Fiolet et al. (2010) Owen & Morrison (2009)
Optical-based photometric	3	0.2	Strazzullo et al. (2010)
Infrared-based photometric	23	0.4	Magdis et al. (2010) Roseboom et al. (2012)
Spectral index-based estimate (Carilli & Yun, 1999)	9	0.6	Lindner et al. (2011)

This uncertainty is always larger than the energy resolution of the ACIS-I chips, so we set the rest-frame energy bin widths to match  $\Delta E_{\text{rest}}$  (Equation 3.2) using our sample’s average redshift  $\langle z \rangle = 2.6$  and redshift uncertainty  $\langle \Delta z \rangle = 0.4$  (see Table 3.2).

Figures 3.5 and 3.6 show the net observed and rest-frame count-rate spectra for our SMG sample, respectively. The rest-frame spectrum contains a  $4\sigma$  emission feature with a centroid near 6.7 keV, which we attribute to Fe K $\alpha$  line emission from a mixture of Fe ionization states including Fe XXV (see §3.5.1). It is apparent from this rest-frame spectrum that a significant fraction of the observed soft-band flux is due to the Fe K $\alpha$  emission line. If strong unresolved Fe K $\alpha$  emission is a common feature in the X-ray spectra of other SMG samples, it may artificially lower their measured HR values by inflating their observed soft-band fluxes.

To ensure our stacking signal is not the result of contamination from a few strong targets, we performed a bootstrapping Monte Carlo analysis to recover the probability distribution for the single 6.7 keV-energy bin ( $\text{bin}_{6.7}$ ). The mean number of on-target counts in  $\text{bin}_{6.7}$  is 16, while the mean number of background counts in the bin is 8. Figure 3.7 shows that the resulting distribution closely matches that of an ideal Poisson distribution with a mean of 16, confirming that our stacking signal is characteristic of the entire sample, not a few outliers.

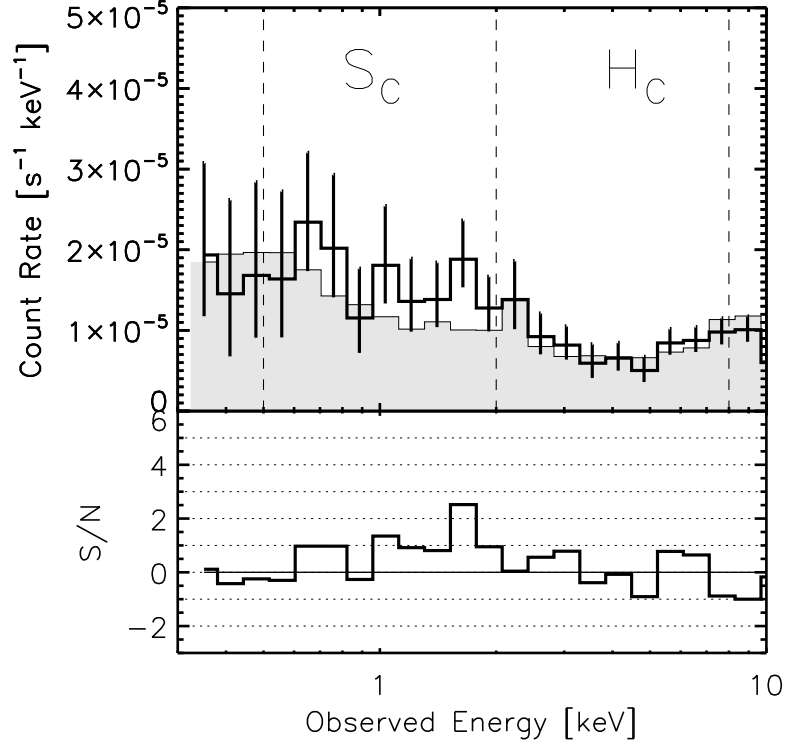


Figure 3.5: Stacked observed-frame X-ray spectrum of our SMG sample. *Above:* Count rate spectrum. The solid line and filled region represent the stacked on-target and background count rates. The error bars show the Poisson 68% double-sided confidence intervals due to the background. The dashed lines mark the extent of the  $S_C$  and  $H_C$  energy bands. *Below:* S/N of each bin in the above spectrum.

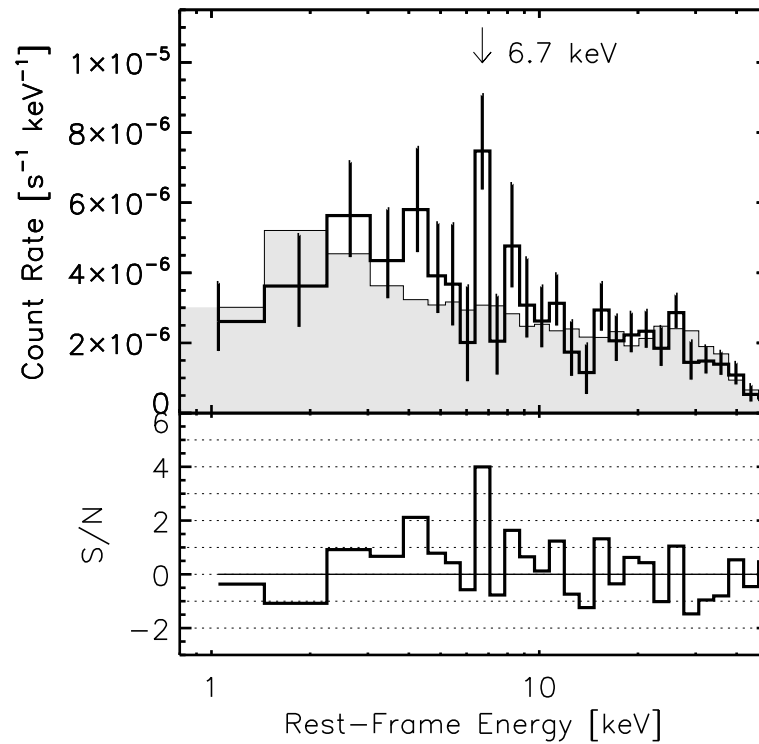


Figure 3.6: Stacked rest-frame X-ray spectrum of our SMG sample. *Above:* Count rate spectrum. The solid line and filled region represent the stacked on-target and background count rates. The error bars show the Poisson 68% double-sided confidence intervals due to the background only. The arrow marks the location of the rest-frame bin that is centered at 6.7 keV. *Below:* S/N of each bin in the above spectrum.

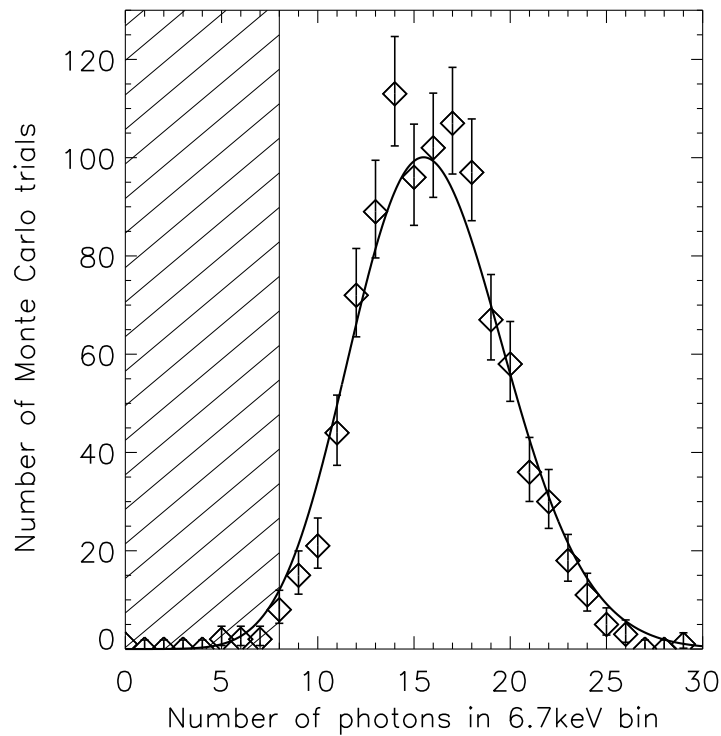


Figure 3.7: Bootstrap-Monte Carlo analysis of the number of  $\text{Fe K}\alpha$  counts in the 6.7 keV-bin of the rest-frame stacked spectrum (Figure 3.6). The histogram represents the total number of Monte Carlo trials returning the given number of total counts when randomly selecting 38 stacking positions from the original 38, with replacement. 16 counts lie in the 6.7 keV bin of the real data, and the mean Monte Carlo result is 15.9 counts. The solid curve shows an ideal Poisson distribution with mean  $\mu = 16$ . The shaded region represents the background level in this bin (8 counts).

### 3.3.4 Estimating $L_X$ and $L_{\text{FeK}\alpha}$

The mean stacked *rest-frame* hard-band X-ray luminosity,  $L_{H_C}$ , of our sample is given by

$$\langle L_{H_C} \rangle = 4\pi f_{H_C} \langle d_L^2 \rangle, \quad (3.3)$$

where  $f_{H_C}$  is the stacked energy flux per galaxy inside the observed 0.56–2.22 keV energy band (the 2.0–8 keV energy band, redshifted by  $\langle z \rangle = 2.6$ ), and  $d_L$  is the luminosity distance at the redshift of each stacking target. We convert the observed count rate to an energy flux using PIMMS. The resulting rest frame X-ray luminosity is  $\langle L_{H_C} \rangle = (3.0 \pm 1.1) \times 10^{42} \text{ erg s}^{-1}$ .

To estimate the equivalent width and line flux of the FeK $\alpha$  feature, we assume that the line emission is contained only within the single elevated bin at 6.7 keV (see Figure 3.6) and estimate the local count-rate continuum around the FeK $\alpha$  feature by averaging together the 8 bins between 3–9 keV (excluding the bin containing the line). This results in an equivalent width of  $\text{EW} = 3.9 \pm 2.5 \text{ keV}$ . Although the EW is relatively unconstrained, it is  $> 1 \text{ keV}$  with 90% confidence. Using the nominal equivalent width and Equation 3.15, we find a mean stacked FeK $\alpha$  line flux of  $\langle f_{\text{FeK}\alpha} \rangle \simeq 2.1 \times 10^{-17} \text{ erg cm}^{-2} \text{ s}^{-1}$ , and a mean line luminosity  $\langle L_{\text{FeK}\alpha} \rangle = (1.3 \pm 0.4) \times 10^{42} \text{ erg s}^{-1}$ .

Figure 3.3 also shows that the S/N of the FeK $\alpha$  signal only drops at a larger radius than the broad-band signal. If we interpret the X-ray continuum as originating from the galaxies' nuclear regions, then this relative offset between the FeK $\alpha$  emission and the X-ray continuum indicates that the FeK $\alpha$  photons in our sample are systematically offset from the galaxies' centers. By measuring the distance between the peaks of the two curves in Figure 3.3, we estimate the radial offset to be  $\sim 1''$ . For our computation of the FeK $\alpha$  line luminosity, we adopt an aperture broadening kernel suited to maximize the S/N of the FeK $\alpha$  emission line,  $\sigma_{\text{kernel}} = 2.4''$ .

We use a two-sample Kolmogorov-Smirnov (KS) test to determine the significance of the apparent angular extension of the FeK $\alpha$  emission relative to the continuum emission. First, we compute the *Chandra* PSF at the location of each stacking target, then sample the PSFs at the positions of their respective collections of optimally-selected photons (see §3.3.3). The PSFs are peak-normalized and smoothed by an amount  $\sigma_{\text{smooth}}$  to reflect intrinsic wavelength offsets and astrometric errors in the photon positions. We then compare the cumulative distributions of the observed soft-band (0.5–2.0 keV) continuum photons (excluding those in the rest-frame FeK $\alpha$  bin) and the rest-frame FeK $\alpha$  photons using the two-sample KS test to determine with what confidence  $1 - p$  ( $p$  is the KS test significance) we can rule out the null hypothesis that the two samples are drawn from a common distribution. When using all 38 stacking positions, we find a maximum confidence of  $1 - p = 0.71$  at  $\sigma_{\text{smooth}} = 0.5''$  (63 continuum counts and 15 FeK $\alpha$  counts). When we use only the stacking positions that have  $\geq 1$  FeK $\alpha$  photon, the maximum confidence occurs at the same value of  $\sigma_{\text{smooth}}$  but has a reduced  $1 - p = 0.45$  (29 continuum counts and 15 FeK $\alpha$  counts). Therefore, the extension in the FeK $\alpha$  emission relative to the continuum emission indicated by Figure 3.3 is a  $\gtrsim 1\sigma$  (71% confidence) effect, whose significance is limited primarily by the small number of FeK $\alpha$  photons.

### 3.4 Obscuration and Star Formation Rate

Two galaxies in our sample have  $L_{\text{IR}}$  [8–1000  $\mu\text{m}$ ] estimated from Magdis et al. (2010), and 12 from Roseboom et al. (2012). For the remaining galaxies without SED fits, we estimate  $L_{\text{IR}}$  by scaling the SED from the nearby, bolometrically-star formation dominated ULIRG, Arp 220:

$$L_{\text{IR}} = L_{\text{IR}}^{\text{Arp220}} \left( \frac{S_{1.2\text{mm}}}{S_{\nu_0}^{\text{Arp220}}} \right) \left[ \frac{d_L(z)}{d_L(z_0)} \right]^2 \left( \frac{1+z_0}{1+z} \right), \quad (3.4)$$

in terms of

$$\nu_0 = 1.2 \text{ mm} \times \left( \frac{1+z}{1+z_0} \right), \quad (3.5)$$

$L_{\text{IR}}^{\text{Arp 220}} = 1.3 \times 10^{12} L_{\odot}$ , the observed 1.2mm flux density  $S_{1.2\text{mm}}$ , luminosity distance  $d_L$ , target redshift  $z$ , and Arp 220 redshift  $z_0 = 0.018$ . The  $L_{\text{IR}}$  values for all stacking targets are presented in Table 3.3; the average value of our whole sample is

$$\langle L_{\text{IR}} \rangle = (2.4 \pm 0.2) \times 10^{46} \text{ erg s}^{-1}. \quad (3.6)$$

The mean 20 cm radio luminosity density  $L_{20\text{ cm}}$  is calculated using our sample's redshift distribution and 20 cm flux densities (Owen & Morrison, 2008; Lindner et al., 2011):

$$\langle L_{20\text{ cm}} \rangle = (2.5 \pm 0.3) \times 10^{31} \text{ erg s}^{-1} \text{ Hz}^{-1}. \quad (3.7)$$

Table 3.3. LHN MAMBO SMGs

ID	Name	RA <sup>a</sup>	Dec <sup>a</sup>	z	z type <sup>b</sup>	z reference <sup>c</sup>	$\log(L_{\text{IR}}/L_{\odot})^d$	L <sub>IR</sub> reference <sup>c</sup>
L1	MM J104700.1 + 590109	161.75083	59.018778	2.562	S	P06	13.3	R12
L2	MM J104627.1 + 590546	161.61192	59.095778	4.09	P-IR	R12	12.9	L12
L3	MM J104631.4 + 585056	161.63112	58.848889	1.8	CY	L11	13.0	L12
L4	MM J104607.4 + 585413	161.53050	58.903889	4.4	CY	L11	12.7	L12
L5	MM J104725.2 + 590339	161.85592	59.060139	3.00	P-O	S10	13.1	R12
L6	MM J104638.4 + 585613	161.66112	58.936806	2.03	S	F10	12.9	R12
L7	MM J104700.1 + 585439	161.75054	58.911500	2.74	P-IR	R12	12.7	L12
L8	MM J104633.1 + 585159	161.63779	58.866417	2.07	P-IR	R12	12.8	L12
L9	MM J104704.9 + 585008	161.77071	58.835750	3.9	CY	L11	12.9	L12
L10	MM J104622.9 + 585933	161.59604	58.993000	3.01	P-IR	R12	12.7	L12
L11	MM J104556.5 + 585317	161.48721	58.888556	1.95	S	F10	12.9	R12
L12	MM J104448.0 + 590036	161.19829	59.009972	2.16	P-O	S10	12.7	R12
L13	MM J104609.0 + 585826	161.53646	58.974583	0.32	P-IR	R12	12.3	L12
L14	MM J104636.1 + 590749	161.64937	59.130139	2.26	P-IR	R12	12.9	R12
L15	MM J104728.3 + 585213	161.86654	58.870583	2.78	P-IR	R12	13.3	R12
L16	MM J104720.9 + 585151	161.83633	58.864722	3.24	P-IR	R12	12.8	L12
L17	MM J104610.4 + 590242	161.54383	59.045000	2.65	P-IR	R12	12.7	L12
L18	MM J104655.7 + 585000	161.73021	58.834444	2.15	P-IR	R12	12.9	L12
L19	MM J104502.1 + 590404	161.25833	59.067583	4.1	CY	L11	12.6	L12



Table 3.3 (cont'd)

ID	Name	RA <sup>a</sup>	Dec <sup>a</sup>	z	z type <sup>b</sup>	z reference <sup>c</sup>	$\log(L_{\text{IR}}/L_{\odot})^{\text{d}}$	L <sub>IR</sub> reference <sup>c</sup>
L20	MM J104617.0 + 585444	161.57058	58.913694	> 4.6	CY	L11	–	–
L21	MM J104530.3 + 590636	161.37575	59.110083	2.52	P-IR	R12	12.6	L12
L22	MM J104603.8 + 590448	161.51763	59.080389	1.44	P-IR	R12	12.3	R12
L23	MM J104641.0 + 585324	161.67129	58.890500	3.6	CY	L11	12.6	L12
L24	MM J104500.5 + 590731	161.25279	59.126000	3.24	P-O	S10	12.7	R12
L25	MM J104540.3 + 590347	161.41679	59.063333	3.5	CY	L11	12.6	L12
L26	MM J104522.8 + 585558	161.34833	58.933611	> 5.0	CY	L11	–	–
L27	MM J104702.4 + 585102	161.76000	58.850861	1.62	P-IR	R12	12.7	L12
L28	MM J104620.9 + 585434	161.58804	58.909722	3.8	CY	L11	12.5	L12
L29	MM J104556.1 + 590914	161.48129	59.154528	0.044	S	O09	8.0	R12
L30	MM J104510.3 + 590408	161.29329	59.068639	0.71	P-IR	R12	12.5	L12
L31	MM J104624.7 + 585344	161.60379	58.896444	2.90	P-IR	R12	12.7	R12
L32	MM J104539.6 + 585419	161.41579	58.906917	2.40	P-IR	M10	12.57	M10
L33	MM J104535.5 + 585044	161.39608	58.847139	2.63	P-IR	R12	12.8	L12
L34	MM J104453.7 + 585838	161.22346	58.978194	2.46	P-IR	R12	12.6	L12
L35	MM J104717.9 + 585523	161.82546	58.923833	2.14	P-IR	R12	12.9	L12
L36	MM J104608.1 + 590744	161.53421	59.129444	4.5	CY	L11	12.5	L12
L37	MM J104610.8 + 585242	161.54575	58.879139	1.72	P-IR	M10	12.81	M10
L38	MM J104444.5 + 590817	161.18704	59.138361	3.6	CY	L11	12.5	L12

We estimate the average star formation rate in our sample using the scaling relations of Kennicutt (1998) in the infrared and Bell (2003) at radio wavelengths, giving  $\text{SFR}_{\text{IR}} \simeq (1100 \pm 100) M_{\odot} \text{yr}^{-1}$  and  $\text{SFR}_{\text{radio}} \simeq (1400 \pm 200) M_{\odot} \text{yr}^{-1}$ , respectively. These values are consistent with each other, but greater than the estimate using the X-ray scaling relation from Vattakunnel et al. (2012),  $\text{SFR}_X \sim (500 \pm 300) M_{\odot} \text{yr}^{-1}$ . All three scaling relations assume a Salpeter (1955) initial mass function with limiting masses of 0.1 and  $100 M_{\odot}$ . The SFR estimated using the X-ray luminosity may be low due to intrinsic absorption. We can derive a lower limit on the average absorbing column in our sample by computing how much obscuration is required to reduce the value of  $\text{SFR}_X$  from an intrinsic value consistent with  $\text{SFR}_{\text{IR}}$  and  $\text{SFR}_{\text{radio}}$ . In this case, we would require  $N_{\text{H}} \sim 2.3 \times 10^{23} \text{cm}^{-2}$  based on our observed flux in the 0.55–2.77 keV band assuming  $\Gamma = 1.6$  and using  $\langle z \rangle = 2.6$ . If we use this argument to estimate the *unabsorbed* X-ray luminosity, we find  $\langle L_{\text{HC}} \rangle \simeq 9.2 \times 10^{42} \text{erg s}^{-1}$ .

### 3.5 Discussion

#### 3.5.1 Comparison to previous surveys

In this section, we compare our results to those of previous X-ray analyses of SMG samples from the CDFN (Alexander et al., 2005a; Laird et al., 2010) and the (E)CDF-S (Georgantopoulos et al., 2011).

#### Detection rate

With only one significant X-ray counterpart in the LHN, the Lindner et al. (2011) SMG sample has an X-ray detection rate of  $2^{+6}_{-2}\%$ . Alexander et al. (2005a) find a high X-ray detection rate of  $85^{+15}_{-20}\%$  among SMGs and submillimeter-targeted radio galaxies (which constitute 70% of their sample) in the CDFN. Laird et al. (2010) find a lower detection rate of  $45 \pm 8\%$  using their purely submillimeter-selected sample derived from

Table 3.3 (cont'd)

ID	Name	RA <sup>a</sup>	Dec <sup>a</sup>	z	z type <sup>b</sup>	z reference <sup>c</sup>	$\log(L_{\text{IR}}/L_{\odot})^{\text{d}}$	$L_{\text{IR}}$ reference <sup>c</sup>
L39	MM J104611.9 + 590231	161.55012	59.042583	2.59	P-IR	R12	12.5	L12
L40	MM J104658.7 + 590633	161.74304	59.109306	0.78	P-IR	R12	12.5	L12
L41	MM J104600.7 + 585502	161.50129	58.917944	1.49	P-IR	R12	12.6	L12

<sup>a</sup>Position of 20 cm radio counterpart

<sup>b</sup>Redshift type: S = spectroscopic, P-IR = *Herschel*-based photometric, P-O = optical-based photometric, CY = estimated using the spectral index  $\alpha_{850\mu\text{m}}^{20\text{cm}}$  (Carilli & Yun, 1999).

<sup>c</sup>References: P06 = Polletta et al. (2006), O09 = Owen & Morrison (2009), F10 = Fiolet et al. (2010), M10 = Magdis et al. (2010), S10 = Strazzullo et al. (2010), L11 = Lindner et al. (2011), R12 = Roseboom et al. (2012), L12 = This Work

<sup>d</sup>8–1000  $\mu\text{m}$

the inhomogenously covered SCUBA supermap (Borys et al., 2003). The LESS sample of Georgantopoulos et al. (2011) is also purely submillimeter-selected and has an X-ray detection rate of  $11^{+4}_{-3}\%$ . However, unlike the SCUBA supermap, the LESS survey is produced with a single observing mode, and with uniform coverage.

We can place these four surveys in a common framework if we ask what fraction of SMGs in each survey have X-ray counterparts above the X-ray detection threshold in the LHN. In this case, we find 11 of 20 ( $55^{+14}_{-13}\%$ ) for Alexander et al. (2005a), 0 of 35 ( $0^{+7}_{-0}\%$ ) for Laird et al. (2010), and 11 of 126 ( $9^{+3}_{-3}\%$ ) for Georgantopoulos et al. (2011). The latter two are in agreement with our sample in the LHN. These results indicate that a lower X-ray detection rate may be more characteristic of strictly submillimeter-detected SMGs from surveys made with uniform coverage.

#### $L_{\text{Fe K}\alpha}$ vs. $L_{\text{IR}}$ vs. $L_{20\text{ cm}}$

Figure 3.8 shows our sample’s average X-ray (corrected only for Galactic absorption), radio, and IR luminosities compared to those of other stacked SMG samples (Laird et al., 2010; Georgantopoulos et al., 2011), individually X-ray-detected SMGs (Alexander et al., 2005a; Laird et al., 2010; Georgantopoulos et al., 2011), and nearby LIRGs and ULIRGs (sample drawn from Iwasawa et al., 2009). Where available, we use the  $L_{\text{IR}}$  value from Table A2 of Pope et al. (2006) for the SMGs from the CDFN. For the twelve SMGs in Alexander et al. (2005a) that are not in the catalog of Pope et al. (2006), we scale  $L_{\text{FIR}} \rightarrow L_{\text{IR}}$  using the average conversion factor  $f$  for the eight SMGs common between the two samples,  $f = 1.42$ . The  $870\text{ }\mu\text{m}$ -detected SMGs from the (E)CDF-S are plotted with  $L_{\text{IR}} = 10\text{--}1000\text{ }\mu\text{m}$ . The local LIRGs and ULIRGs from Iwasawa et al. (2009) also have their  $L_{\text{FIR}}(40\text{--}400\text{ }\mu\text{m})$  estimates scaled by  $f = 1.42$ . We also show the total sample luminosity average for Laird et al. (2010), including the contribution from their stacked SMGs that were not individually detected in the X-ray.

The average properties of our stacking sample are in agreement with the total luminosities of Laird et al. (2010).

Figures 3.8 and 3.9 also indicate the AGN classification of each galaxy. Galaxies whose mid-IR or X-ray spectral properties are consistent with emission produced entirely by star formation are plotted in red, while those requiring the presence of an AGN are shown in blue. Georgantopoulos et al. (2011) divide their sample by using a probabilistic approach; those galaxies requiring the presence of a torus-dust component in their mid-IR SED according to an F-test are categorized as AGN. Laird et al. (2010) and Alexander et al. (2005a) separate out the AGN based on the most favored model of their X-ray spectra according to the Cash (1979) statistic. The sample of Iwasawa et al. (2009) is divided based on hardness ratio.

The division between AGN and non-AGN systems can be roughly determined based on the X-ray scaling relations of purely star-forming galaxies in the local universe (Ranalli et al., 2003; Vattakunnel et al., 2012), shown as solid black lines. The average properties of our stacking sample lie very near the Ranalli et al. (2003) relation. Considering the substantial intrinsic scatter in the spectral classifications of the Laird et al. (2010) sample, our stacking sample also probably contains a substantial fraction of both star-formation-only and AGN-required systems.

### **Fe K $\alpha$ emission properties**

The Fe K $\alpha$  photons in our stacking sample may be more spatially extended than the continuum photons by  $\sim 1''$  (see §3.3.4). Extended and misaligned Fe K $\alpha$  emission has been observed in Arp 220 (Iwasawa et al., 2005) and NGC 1068 (Young et al., 2001). We may also be blending together the emission from multiple components of merging systems of which only one component has strong Fe K $\alpha$  emission (like, e.g., Arp 299;

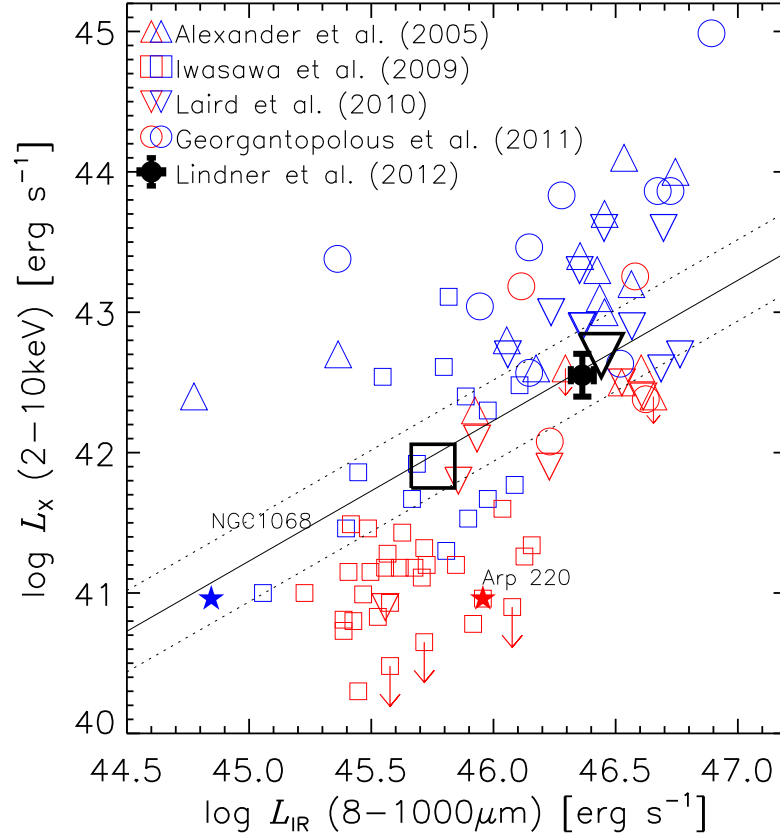


Figure 3.8: Log X-ray luminosity vs. log infrared ( $8\text{--}1000\mu\text{m}$ ) luminosity for our SMG sample compared to other stacked and individually detected SMGs, LIRGs, and ULIRGs from the literature: SMGs in the CDF-N from Alexander et al. (2005b, triangles) and Laird et al. (2010, upside-down triangles), SMGs in the ECDFS from Georgantopoulos et al. (2011, circles), and nearby LIRGs and ULIRGs from Iwasawa et al. (2009, squares). Red and blue symbols represent galaxies with “star formation-only” or “AGN-required” X-ray spectral classifications, respectively. The line represents the relation for star-forming galaxies in the local Universe (Ranalli et al., 2003). The black hollow symbols represent the average luminosities of all LIRGs/ULIRGs (Iwasawa et al. 2009, square), and all SMGs (including the stacked contribution) of the SCUBA supermap detections in the CDFN (Laird et al. 2010, upside-down triangle).

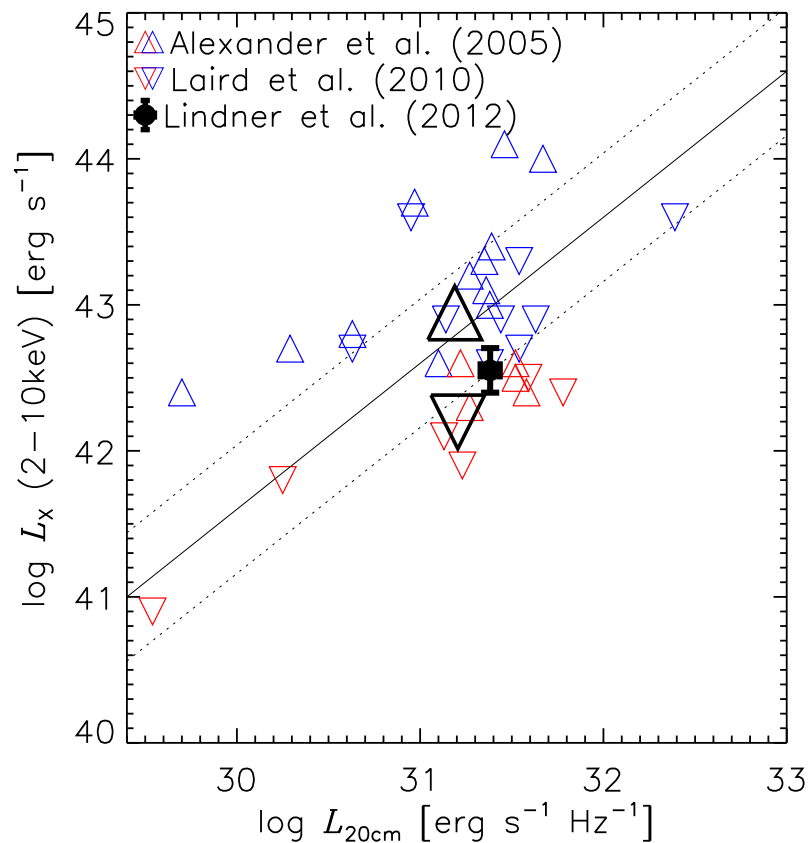


Figure 3.9: X-ray luminosity versus 20 cm spectral power. The symbols and colors are the same as in Figure 3.8. The over-plotted solid and dashed lines show the correlation between  $L_X$  and  $L_{20\text{cm}}$  along with  $1\sigma$  errors for star-forming galaxies (Vattakunnel et al., 2012).

Ballo et al., 2004).

The bin width in our stacked rest-frame X-ray spectrum, which is set by the redshift uncertainties of our SMG sample, is larger than the rest energy separation between Fe K $\alpha$  emission from neutral and highly-ionized iron (0.3 keV); therefore, it is difficult to determine the average Fe ionization fraction in our sample. Close inspection of the photons near the rest-frame Fe K $\alpha$  line (see Figure 3.10) reveals a range of values between 6.4 keV–7.2 keV, with a local maximum at 6.7 keV. Given that the Fe line photons are contributed fairly evenly by the 38 targets in our stacking sample, and have been assigned to their bins based on a wide variety of redshift estimation techniques (spectroscopic, optical-photometric, *Herschel*-photometric, millimeter/radio-photometric), they are unlikely all to be systematically biased high or low. Therefore, a significant fraction of the detected Fe K $\alpha$  photons likely originate from the highly-ionized species of FeXXV or FeXXVI. However, the  $\sim 10\%$  rest-frame uncertainty in the energy of each photon implies an uncertainty in the centroid of the line profile of  $\sigma_{\text{centroid}} = (\text{FWHM})/(\text{SNR}) \simeq 398 \text{ eV}$ , insufficient to determine the relative fractions of each ionization state with certainty.

Strong emission ( $\text{EW} = 1.8 \pm 0.9$ ) from highly ionized Fe K $\alpha$  has been observed in the nearby ULIRG Arp 220 by Iwasawa et al. (2005) using *XMM-Newton*. Iwasawa et al. (2009) also find strong 6.7 keV emission ( $\text{EW} = 0.9 \pm 0.3 \text{ keV}$ ) from the stacked spectrum of nearby ULIRGs (including Arp 220) that have no evidence of AGN emission (termed X-ray-quiet ULIRGs). Alexander et al. (2005a) detected strong ( $\text{EW} \simeq 1 \text{ keV}$ ) Fe K $\alpha$  emission in the stacked SMG spectrum of the six SMGs in their sample with  $N_H > 5 \times 10^{23} \text{ cm}^{-2}$ , and find that the line centroid is between 6.7 keV and 6.4 keV, indicating a substantial contribution from highly ionized gas.

In Figure 3.11 we compare the relation between  $L_{\text{K}\alpha}$  and  $L_{\text{IR}}$  in our sample with



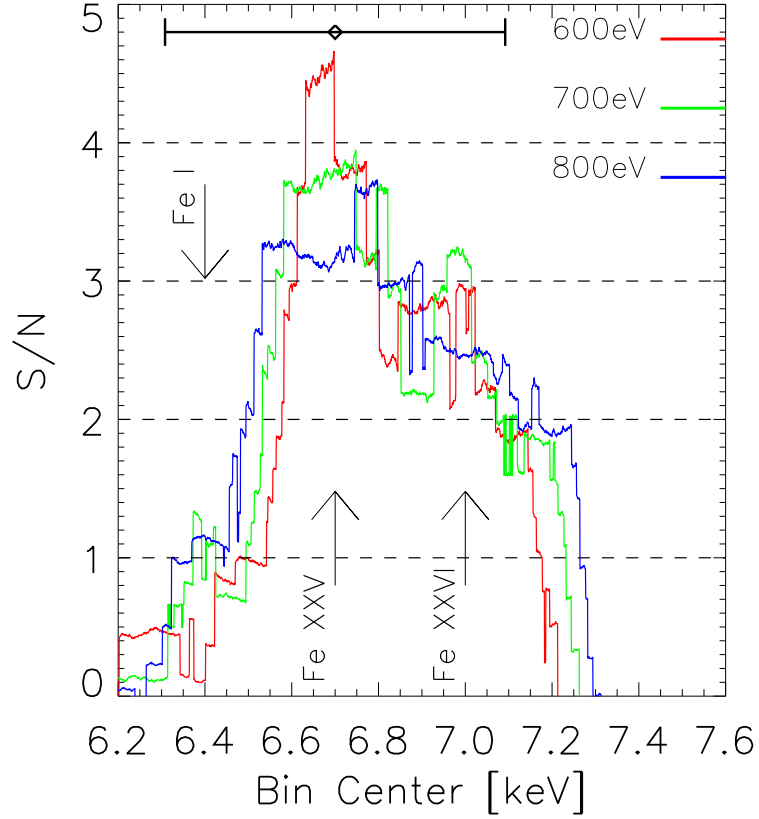


Figure 3.10: S/N of the Fe K $\alpha$  emission as a function of bin position and width. The red, green, and blue lines use bin widths of 600 eV, 700 eV, and 800 eV (the bin width used in the rest frame spectrum in Figure 3.6 is 698 eV and is determined by the typical redshift uncertainty in our sample). The black arrows mark the energies of K $\alpha$  photons from Fe I (6.4 keV), Fe XXV (6.7 keV) and Fe XXVI (7.0 keV). The horizontal error bar shows the formal uncertainty in the line centroid  $\sigma_{\text{centroid}} = \pm 398$  eV centered on 6.7 keV.

those for other individual systems and stacked samples with measured  $\text{Fe K}\alpha$  line luminosities and bolometrically dominant energy sources that are well understood. The dashed line represents a linear slope between  $L_{\text{K}\alpha}$  and  $L_{\text{IR}}$  and has been normalized to NGC 1068, a nearby prototypical Seyfert II LIRG. Red symbols represent systems that do not have significant observed AGN bolometric contributions, like SMGs and local X-ray quiet ULIRGs; the blue symbols represent systems that have significant bolometric AGN contributions. Figure 3.11 shows that the relative  $\text{Fe K}\alpha$ /infrared luminosity fraction,  $L_{\text{K}\alpha}/L_{\text{IR}}$ , increases with increasing  $L_{\text{IR}}$ . If the  $\text{Fe K}\alpha$  emission is due to AGN activity, then this result may be in agreement with the observed trend that LIRGs/ULIRGs tend to be increasingly AGN-dominated with increasing  $L_{\text{IR}}$  (e.g., Tran et al., 2001).

### 3.5.2 Origin of the $\text{Fe K}\alpha$ emission

This section discusses three possible physical origins for the  $\text{Fe K}\alpha$  emission detected in our stacked SMG sample: supernovae, galactic-scale winds, and AGNs. Because a significant fraction of our sample's  $\text{Fe K}\alpha$  emission likely originates from the highly-ionized species  $\text{Fe XXV}$  (see, e.g., Figure 3.10) and because evidence for highly-ionized  $\text{Fe K}\alpha$  emission from other (U)LIRGs exists at both high (Alexander et al., 2005a) and low (e.g., Iwasawa et al., 2005) redshifts, the following sections focus on the origin of this high-ionization component.

#### Supernovae

Here we consider if the observed  $\text{Fe K}\alpha$  feature can be attributed to X-ray luminous supernovae. X-ray observations of the supernova SN 1986J in the nearby spiral galaxy NGC 831 reveal strong hard-band emission and a significant 6.7 keV ( $\text{EW} \lesssim 500 \text{ eV}$ ) line (Houck et al., 1998). Supernova 1986J decayed in the 2–10 keV band as  $\sim t^{-2}$

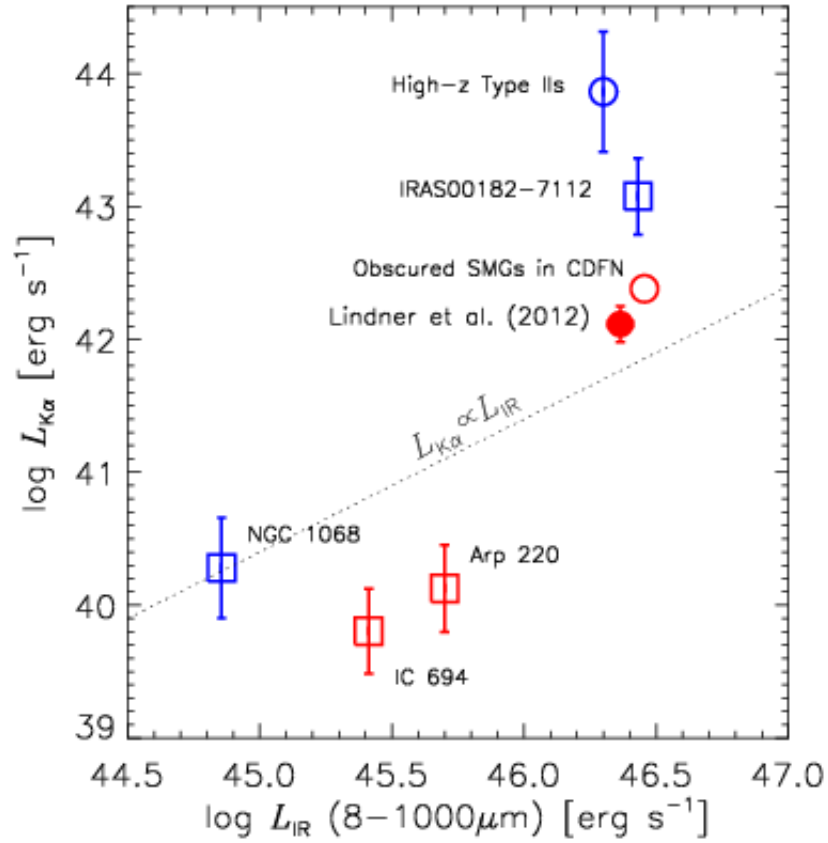


Figure 3.11: Fe K $\alpha$  line luminosity  $L_{\text{K}\alpha}$  versus  $L_{\text{IR}}$  for our results (filled red circle), stacked SMGs in the CDF-N (empty red circle; Alexander et al., 2005a), and stacked high- $z$  Type II AGN (empty blue circle; Iwasawa et al., 2011). The squares represent the LIRG NGC 1068 (Young et al., 2001), the HyLIRG IRAS 00182-7112 (Nandra & Iwasawa, 2007), and the merger component IC 694 (Ballo et al., 2004). The dashed line represents a linear relation that is normalized to NGC 1068. Blue (red) symbols denote samples/systems that do (do not) show strong AGN bolometric signatures.

from 1991 to 1996. We will take a conservative approach and use only the luminosity information in this time interval for our calculation. Given the X-ray luminosity and decay rate of SN 1986J (Houck et al., 1998), and assuming the star formation rate of our sample of order  $\text{SFR} = 10^3 M_{\odot} \text{yr}^{-1}$  giving a supernova rate of  $10 \text{ SN yr}^{-1}$ , we would expect  $\sim 50$  X-ray luminous supernovae to be visible at any given time. The combined supernova X-ray luminosity is therefore  $L_{H_C, \text{SNR}} \simeq 10^{42} \text{ erg s}^{-1}$ . Considering the fact that prior to 1991 SN 1986J was probably still dimming at a rate close to  $\propto t^{-2}$ , this calculation is an underestimate. Therefore, supernovae like 1986J can satisfy the bolometric requirements for explaining the hard X-ray emission *and* the Fe K $\alpha$  line that we see in our stacked SMG sample.

However, if the supernovae associated with massive star formation are visible, then so must be high-mass X-ray binaries given the short time lifetimes of massive stars. These systems would dominate the hard X-ray emission from star-forming regions, and would severely dilute the Fe K $\alpha$  emission (see, e.g., Iwasawa et al., 2009). We therefore rule out X-ray luminous supernovae and supernova remnants as the source of the Fe K emission in our sample.

### Galactic-scale winds

As discussed in Iwasawa et al. (2005), who consider the 6.7 keV emission line in Arp 220, a starburst-driven galactic-scale superwind of hot gas is energetically plausible as the source of the Fe K $\alpha$  emission. Large outflows could also explain why the the Fe K $\alpha$  line emission appears more extended than the X-ray continuum emission in our stacking sample. To explore this scenario, we used the X-ray spectral-fitting package XSPEC (Arnaud, 1996) to model an absorbed diffuse thermal X-ray (`zphabs * mekal`) spectrum and estimate the gas metallicity required to produce the strong high-ionization

Fe K $\alpha$  emission detected in our SMG sample. We computed the model EW values using the spectral window 6.35–7.05 keV, the same energy width as the bin containing the Fe K $\alpha$  emission in our stacked rest-frame spectrum (Figure 3.6), which includes all Fe K $\alpha$  ionization states. We fixed the gas temperature to Arp 220’s best-fit value  $kT = 7.4$  keV (Iwasawa et al., 2005), the gas density to  $n = 1$  cm $^{-3}$ , the redshift to our sample’s average  $\langle z \rangle = 2.6$ , and the obscuring hydrogen column density to  $2.3 \times 10^{23}$  cm $^{-2}$  (§3.4). Both the Fe K $\alpha$  line luminosity and the continuum intensity vary linearly with  $Z$ , allowing us to express the relation between EW and  $Z$  as

$$\text{EW} = \frac{6.67}{1 + \frac{Z'}{Z}} \text{ keV}, \quad (3.8)$$

where  $Z' = 5.29 Z_{\odot}$ . EW is approximately proportional to  $Z$  for  $Z \ll Z'$  and approaches the constant value 6.67 keV for  $Z \gg Z'$ . Because of this non-linear behavior, an abundance of  $0.94 Z_{\odot}$  can produce EW = 1 keV (90% confidence lower-limit) while a significantly greater abundance  $Z \simeq 7.5 Z_{\odot}$  is needed to explain our nominal value EW  $\simeq 3.9$  keV. If a significant amount of our rest-frame 2–10 keV luminosity is from X-ray binaries, incapable of generating the observed line emission, then the required metallicity would be even higher. While the lower limit on our measured EW can be explained by thermal emission from a diffuse ionized plasma, especially considering the extreme enrichment taking place in systems like SMGs, generating an EW with a value close to our nominal measurement would require an unrealistic degree of high- $z$  enrichment.

### AGN activity

AGNs hidden behind large hydrogen column densities may be responsible for the observed Fe K $\alpha$  emission in our sample. The Fe K $\alpha$  emission line is the signature spectral feature of the reprocessed (reflected) spectrum of an AGN (Matt et al., 2000). As the ionizing luminosity increases, so does the ionization fraction of the gas, shifting the

dominant emission feature from 6.4 keV (neutral and intermediate ionization states) to 6.7 keV (helium-like Fe XXV) and 6.9 keV (hydrogen-like Fe XXVI).

Some insight into the properties of SMGs can be gained from reviewing the well-studied Fe K $\alpha$  emission properties of AGN and nearby ULIRGs. Strong (EW  $\simeq 1$  keV) 6.7 keV emission has been observed in systems that are bolometrically AGN-dominated, like IRAS 00182-7112 (Nandra & Iwasawa, 2007) and NGC 1068 (Young et al., 2001), as well as systems that appear to be energetically AGN-free, like Arp 220 (Iwasawa et al., 2005) and IC 694 (Ballo et al., 2004). However, direct evidence of a black hole accretion disk has been observed in Arp 220 by Downes & Eckart (2007) with the detection of a compact ( $0.19'' \times 0.13''$ ) 1.3 mm continuum source in the center of the west nucleus torus. This source has a surface luminosity of  $\sim 5 \times 10^{14} L_{\odot} \text{ kpc}^{-2}$ , which is energetically incompatible with being powered by even the most extreme compact starbursts known. Only an accretion disk can be responsible for heating the dust. Highly ionized Fe K $\alpha$  emission has also been observed in the AGN systems Mrk 273 (Balestra et al., 2005), NGC 4945 (Done et al., 2003), and NGC 6240 (Boller et al., 2003), along with a neutral Fe K $\alpha$  component.

The narrow 6.4 keV “cold” Fe K $\alpha$  emission line is a ubiquitous feature in the spectra of optically-selected active galaxies out to high redshift (e.g., Corral et al., 2008; Iwasawa et al., 2011; Falocco et al., 2012). However, Iwasawa et al. (2011) also find evidence for highly ionized Fe K $\alpha$  emission in two subsets of their X-ray selected AGN sample: Type I AGN with the highest Eddington ratios, and Type II AGN with the highest redshifts. The subsamples with highly ionized K $\alpha$  emission show no evidence of a broad line Fe K $\alpha$  feature; therefore, the highly-ionized Fe K $\alpha$  photons probably do not originate from the accretion disk, but from more distant and tenuous outflowing gas. This scenario may also explain why the Fe K $\alpha$  photons in our sample appear spatially extended with respect to the X-ray continuum photons.

A significant caveat is that it remains difficult to reconcile the power source required to produce offsets as large as  $1''$  in the photon distribution of our sample's stacked Fe K $\alpha$  emission (relative to the nuclear continuum; see §3.3.4) given the sample's low average X-ray luminosity. For example, we can calculate the maximum radial distance out to which low-density gas can remain highly photoionized by a single ionizing source by assuming that our sample's stacked infrared luminosity is produced by deeply-buried AGNs, i.e.,  $L_{\text{ion}} \simeq L_{\text{IR}} = 2.4 \times 10^{46} \text{ erg s}^{-1}$ . Using the ionization parameter  $\xi \equiv L_{\text{ion}}/nR^2$  ( $\log \xi \geq 2.8$  is required for a significant Fe XXV ionization fraction: Kallman et al., 2004) with  $n = 1 \text{ cm}^{-3}$ , we find  $R_{\text{max}} = \sqrt{L_{\text{IR}}/n\xi} \simeq 2.0 \text{ kpc}$ . At our sample's average redshift of  $\langle z \rangle = 2.6$ , this corresponds to a typical angular offset of  $0.24''$ . Angular offsets larger than  $0.24''$ , like those tentatively indicated by our sample (see Figure 3.3), can be explained by SMGs that host multiple distributed ionizing sources. In particular, the radio continuum emission (defining our stacking positions) might be more closely associated with the X-ray continuum than with Fe K $\alpha$  line emission in a complex, multi-component system. These results highlight the importance of resolving the sizes and morphologies of SMGs with high-resolution (sub)millimeter imaging (e.g., Tacconi et al., 2006).

If the high-ionization Fe K $\alpha$  emission is ultimately due to star-formation processes (shocked gas from SNe), and the SFR is traced by the  $L_{\text{IR}}$ , then we should expect a linear relation between  $L_{\text{K}\alpha}$  and  $L_{\text{IR}}$ . If the systems with the highest  $L_{\text{IR}}$  have an infrared contribution from obscured AGN that are not also emitting Fe K $\alpha$  photons, then we would expect a slope that is even less than unity. However, Figure 3.11 shows that  $L_{\text{K}\alpha}$  is relatively much more dominant in SMGs and high- $z$  AGN than in their lower-luminosity, lower-redshift analogues. This distinction indicates that highly ionized Fe K $\alpha$  emission cannot be explained solely by star-formation processes and is more likely to be the result of AGN activity.

### 3.6 Conclusions

We analyze the X-ray properties of a complete sample of SMGs with radio counterparts from the LHN. This sample’s X-ray detection rate of  $2^{+6}_{-2}\%$  is consistent with those for other uniformly-mapped, submillimeter-detected samples, considering the depth of our X-ray data. The X-ray undetected SMGs show a strong stacked detection in the  $S_C$  band, and no significant detection in the  $H_C$  band, similar to results from SMG stacking in the CDF-N (Laird et al., 2010) and CDF-S (Georgantopoulos et al., 2011).

We also use the available redshift information of our SMGs to compute the rest-frame, stacked count-rate spectrum of our sample. The rest-frame spectrum shows strong ( $EW > 1$  keV) emission from  $\text{Fe K}\alpha$ , possibly with contributions from  $\text{Fe XXV}$  and  $\text{Fe XXVI}$ . A comparison with other high-ionization  $\text{Fe K}\alpha$ -emitting systems from the literature indicates that accretion onto obscured AGNs is the likely explanation for the strong  $\text{Fe K}\alpha$  emission line. In our sample, the  $\text{Fe K}\alpha$  emission is responsible for  $\sim 20\%$  of the observed soft-band X-ray flux. Therefore, if strong Fe line emission is a common feature in other SMG samples, it would significantly decrease the measured values of HR and lead to overestimates of the continuum spectral index  $\Gamma$ .

We find a tentative indication (71% confidence) that our sample’s stacked distribution of  $\text{Fe K}\alpha$  photons is more spatially extended than that of the X-ray continuum. If confirmed by future studies, this result can help determine the physical origin of the prominent  $\text{Fe K}\alpha$  emission in SMGs.



### 3.7 Appendix

#### 3.7.1 Detailed descriptions of calculations

##### Optimized spectral stacking method

We begin by labeling all the photons within the optimized apertures (see Section 3.3.1) of all of the  $N = 38$  stacking targets with the index  $i$ , and those within the background regions for the  $N$  targets  $i'$ .  $E_i$  is the energy of the  $i^{th}$  photon, and  $T_i$  is the total effective exposure time in the mosaic at the position of  $i$ . The notation  $i \in j$  refers to all the photons that have energies located the  $j^{th}$  energy bin. The stacked mean count rate in the  $j^{th}$  energy bin,  $R_j$ , is then

$$R_j = \frac{1}{N} \sum_{i \in j} \frac{1}{T_i \kappa_i} \quad (3.9)$$

where  $\kappa_i$  is the aperture correction for the optimal aperture of the energy band of the  $i^{th}$  photon. The background mean count rate in the  $j^{th}$  bin is

$$R'_j = \frac{1}{N} \sum_{i' \in j} \frac{1}{T_{i'} \kappa_{i'} c_{i'}}, \quad (3.10)$$

where  $c_{i'}$  is the ratio of the areas of the background region of the stacking position of the  $i'^{th}$  photon, and of the optimal aperture of that stacking position. It follows that the expected number of background counts in the  $j^{th}$  bin,  $\tilde{N}_j$ , is

$$\eta_j = \langle T_i \rangle_{i \in j} \times R'_j. \quad (3.11)$$

We use the double-sided 68%-confidence upper and lower limits,  $\eta_j^{\text{high}}$ , and  $\eta_j^{\text{low}}$  (Gehrels, 1986), to compute the  $1\sigma$  count rate deviations in the  $j^{th}$  bin due to the background,  $\sigma^{\text{hi/low}}$ :

$$\sigma_j^{\text{hi/low}} = \frac{|\eta_j^{\text{hi/low}} - \eta_j|}{\langle T_{i \in j} \rangle_i} \quad (3.12)$$

Therefore, the net count rate density per galaxy in the  $j^{th}$  bin,  $\mathbf{R}_j$ , is

$$\mathbf{R}_j = \frac{(R_j - \tilde{R}_j)}{\Delta E_j} \frac{+ \sigma(R)_j^{\text{hi}} / \Delta E_j}{- \sigma(R)_j^{\text{low}} / \Delta E_j} [\text{s}^{-1} \text{keV}^{-1}], \quad (3.13)$$

where  $\Delta E_j$  is the width of the  $j^{th}$  energy bin. We calculate the corresponding rest-frame spectrum  $\mathbf{R}_j^{\text{rest}}$  by binning the photons according to their rest-frame energies,  $E_i^{\text{rest}} = E_i (1 + z_i)$ , where  $z_i$  is the redshift of the stacking target associated with the photon.

### Fe K $\alpha$ energy flux

We use the CIAO script `eff2evt` to tabulate the local effective area  $A_i$  ( $A_{i'}$ ), and quantum efficiency  $Q_i$  ( $Q_{i'}$ ), for each photon in the on-target (background) apertures.

The mean stacked on-target and background photon fluxes in the  $j^{th}$  bin,  $F_j$ , and  $F'_j$ , are then

$$F_j = \frac{1}{N} \sum_{i \in j} \frac{1}{T_i A_i Q_i \kappa_i}, \quad (3.14)$$

and

$$F'_j = \frac{1}{N} \sum_{i' \in j} \frac{1}{T_{i'} A_{i'} Q_{i'} \kappa_{i'} c_{i'}}, \quad (3.15)$$

respectively.

## Chapter 4

### The LABOCA/ACT Survey of Clusters at All Redshifts

#### 4.1 Introduction

Galaxy clusters produce a spectral distortion in the cosmic microwave background (CMB) known as the Sunyaev Zel'dovich effect (SZE; Zeldovich & Sunyaev, 1969; Sunyaev & Zeldovich, 1970). The thermal SZE signal, quantified by  $Y_{\text{SZ}} \equiv \int y d\Omega$  in terms of the Compton parameter

$$y = \int \sigma_T n_e kT_e / m_e c^2 dl \quad (4.1)$$

is insensitive to cluster redshift, allowing for the unbiased detection of massive clusters out to very large distances. This selection is complementary to that of surveys using optical richness or X-ray flux, which generally yield lower-redshift cluster samples (for a review of SZE cluster cosmology, see e.g., Carlstrom et al., 2002). The mass function of SZE-selected galaxy clusters has been used to constrain the properties of dark energy, as well as the mean matter density  $\Omega_m$  and amplitude of fluctuations  $\sigma_8$  (e.g., Sehgal et al., 2011; Benson et al., 2013; Planck Collaboration et al., 2013 XX).

The number of known SZE-selected clusters is rising rapidly. Initial samples of  $\sim 10$ – $20$  blind SZE-detected clusters were presented by Vanderlinde et al. (2010) and Marriage et al. (2011). Recently, Menanteau et al. (2013) reported 68 SZE-selected clusters from an equatorial Atacama Cosmology Telescope (ACT) survey, and  $\sim 1200$  more all-sky SZE cluster candidates have been catalogued by the Planck Collaboration et al. (2013 XXIX). As the sky coverage of high-resolution SZE surveys like ACT

and the South Pole Telescope (SPT) increases, all massive clusters out to arbitrarily high redshifts can in principle be detected through the SZE. Yet with samples of just nine and eighteen clusters, respectively, Sehgal et al. (2011) and Benson et al. (2013) find that the statistical errors on  $w$  and  $\sigma_8$  are already smaller than systematic errors due to uncertainties in the  $Y_{\text{SZ}}$ -to-mass scaling relation. Therefore, to further improve constraints from SZE-cluster cosmology using these larger samples, we need a better understanding of the scaling between integrated SZE signal and cluster mass in individual systems.

A number of physical processes are known to cause deviations from equilibrium scaling relations. Cluster mergers are predicted to cause departures from hydrostatic equilibrium, and can produce transient pressure enhancements that boost the SZE signal (e.g., Wik et al., 2008). Such pressure enhancements were invisible in initial X-ray observations of the massive cluster RXJ1347-1145, for example, but were revealed through high-resolution SZE-imaging to contribute  $\sim 10\%$  of the bulk signal (Komatsu et al., 2001; Kitayama et al., 2004; Mason et al., 2010). Kinematic Sunyaev Zel’dovich (kSZ) signals due to clusters’ peculiar velocities can also introduce additional scatter to  $Y_{\text{SZ}}$  measurements. Hand et al. (2012) recently achieved a direct statistical detection of kSZ signals from ACT, but the peculiar velocity distribution of clusters remains unconstrained. Mroczkowski et al. (2012) found some evidence for large kSZ distortions in the triple merger system MACSJ0717.5+3745, a result that might indicate high-velocity substructures in merging clusters introduce additional transient deviations to  $Y_{\text{SZ}}$ . Ruan et al. (2013) predict these transient deviations could bias  $Y_{\text{SZ}}$  results by  $\sim 10\%$ . The emission from bright galaxies near the clusters (in projection) can further bias the SZE signal. Synchrotron emission from star-forming galaxies and active galactic nuclei may “fill in” SZE decrements. Reese et al. (2012) estimate contamination from synchrotron sources to be  $\lesssim 20\%$  in the SZE decrement based on high-resolution

90 GHz imaging of two ACT clusters. SZE increments, on the other hand, can be artificially enhanced by the strong infrared emission from dusty, high-redshift star-forming submillimeter galaxies (SMGs; for a review, see Blain et al., 2002). Gravitational lensing by the clusters’ potentials may increase contamination by lensed SMGs (e.g., Knudsen et al., 2008; Johansson et al., 2011) or introduce deficits in surface brightness at the location of the cluster (Zemcov et al., 2013). Benson et al. (2003) conclude that direct measurements of cluster peculiar velocities in maps with angular resolution  $\gtrsim 1$  arcmin will be limited by SMG contamination.

The number counts of the rarest, most massive clusters have the most power to constrain cosmological parameters. Unfortunately, these systems will also tend to be affected the most by the above processes. The massive systems will produce large gravitational lensing fields, and in our hierarchical universe, they also tend to be more commonly disrupted by recent merging activity. To better understand how these processes affect the observed SZE signals in clusters, we need high-resolution submillimeter and radio imaging of large and representative samples of SZE-selected clusters.

In this work we present new observations at 345 GHz (19.2'' resolution) with the Large APEX Bolometer Camera (LABOCA) on the Atacama Pathfinder EXperiment (APEX) telescope and at 2.1 GHz (5'' resolution) with the Australia Telescope Compact Array (ATCA) of a sample of massive SZE-selected galaxy clusters. We use these data to measure the properties of the clusters’ spatially-resolved SZE increment signals, and quantify the degree of background and foreground radio and infrared galaxy contamination. Section 4.2 describes our cluster sample, Section 4.3 presents observations and data reduction techniques, Section 4.4 assesses the SZE contamination by point sources, Section 4.5 uses the point-source subtracted multi-wavelength SZE maps to place constraints on cluster peculiar velocities, and Section 4.6 reviews our conclusions. In our calculations, we assume a *WMAP* cosmology with  $H_0 = 70 \text{ km s}^{-1} \text{ Mpc}^{-1}$ ,  $\Omega_M = 0.27$ ,

and  $\Omega_\lambda = 0.73$  (Komatsu et al., 2011).

## 4.2 Cluster sample

Our sample consists of eleven clusters with signal-to-noise (S/N)  $> 4.7$  from the Atacama Cosmology Telescope (ACT; Kosowsky, 2006; Fowler et al., 2007) southern survey (Menanteau et al., 2010; Marriage et al., 2011). Among the 15 highest-S/N ACT southern clusters, this set includes 9 of 10 clusters not known before ACT or SPT, and excludes the only cluster with  $z < 0.15$  and three clusters that had been previously mapped with AzTEC. Their coordinates and other properties are listed in Table 4.1. The sample spans a large redshift range between  $z = 0.3$ – $1.1$  and has masses  $M_{500c} \geq 3 \times 10^{14} M_\odot$  (Menanteau et al., 2010; Sifón et al., 2013), where  $M_{500c} = 500 (4\pi/3) \rho_c r_{500c}^3$ , and  $r_{500c}$  is the radius enclosing a mass density equal to  $500\times$  the critical density of the Universe at the redshift of the cluster. We define the angular radius  $\theta_{500c} = r_{500c}/D_A$ . Each SZE detection has been confirmed to be a rich optical cluster through followup imaging by Menanteau et al. (2010). Included in the sample are the notable cluster mergers ACT J0102-4915, also known as “El Gordo” (Menanteau et al., 2012), and 1E0657-56 (ACT J0658-5557), the original “Bullet” cluster (Markevitch et al., 2002).

## 4.3 Observations and data reduction

### 4.3.1 345 GHz APEX/LABOCA

We have obtained new 345 GHz,  $19.2''$  resolution imaging of ten clusters between 2010–2011 (see Table 4.2) using the Large APEX Bolometer Camera (LABOCA; Siringo et al., 2009) on the Atacama Pathfinder Experiment<sup>1</sup> (APEX) telescope. The LABOCA

---

<sup>1</sup> This publication is based on data acquired with the Atacama Pathfinder Experiment (APEX). APEX is a collaboration between the Max-Planck-Institut für Radioastronomie, the European Southern

Table 4.1. Cluster sample

Name	R.A. <sup>a</sup> (h:m:s)	Dec. <sup>a</sup> (° : ′ : ″)	$z$	$\theta_{500c}$ (′)
ACT-CL J0102–4915	01:02:53	-49:15:19	0.870 <sup>b</sup>	2.50
ACT-CL J0215–5212	02:15:18	-52:12:30	0.480 <sup>c</sup>	3.16
ACT-CL J0232–5257	02:32:45	-52:57:08	0.556 <sup>c</sup>	2.42
ACT-CL J0235–5121	02:35:52	-51:21:16	0.278 <sup>c</sup>	5.18
ACT-CL J0245–5302	02:45:33	-53:02:04	0.300 <sup>e</sup>	3.08 <sup>f</sup>
ACT-CL J0330–5227	03:30:54	-52:28:04	0.442 <sup>c</sup>	4.08
ACT-CL J0438–5419	04:38:19	-54:19:05	0.421 <sup>c</sup>	4.53
ACT-CL J0546–5345	05:46:37	-53:45:32	1.066 <sup>c</sup>	1.75
ACT-CL J0559–5249	05:59:43	-52:49:13	0.609 <sup>c</sup>	3.08
ACT-CL J0616–5227	06:16:36	-52:28:04	0.684 <sup>c</sup>	2.60
ACT-CL J0658–5557	06:58:30	-55:57:04	0.296 <sup>d</sup>	3.44 <sup>g</sup>

<sup>a</sup>SZE decrement centroid from Marriage et al. (2011)

<sup>b</sup>Menanteau et al. (2012)

<sup>c</sup>Sifón et al. (2013)

<sup>d</sup>Tucker et al. (1998)

<sup>e</sup>Edge et al. (1994)

<sup>f</sup> $r_{500c}$  for ACT-CL J0245–5302 was estimated using its velocity dispersion  $\sigma \simeq 900 \text{ km s}^{-1}$  (Edge et al., 1994), giving  $M_{200} \sim 5 \times 10^{14} M_{\odot}$  and  $r_{200} = 1260 \text{ kpc}$ .

<sup>g</sup> $r_{500c}$  from Zhang et al. (2006)

data for an eleventh cluster that is also detected by ACT (ACT-CL J0658–5557; Bullet) were downloaded from the European Southern Observatory (ESO) archive. The following subsections describe the algorithms used to reduce the LABOCA data and extract SZE signals.

### LABOCA observations

Observations were taken using the standard raster spiral mode, in which the telescope traces out one spiral in equatorial coordinates every 35 seconds at each of four raster points defining a square with  $27''$  sides. In polar coordinates  $(r, \phi)$ , the spiral track has an initial radius  $r_0 = 18''$ , a constant radial speed  $\dot{r} = 2.2'' \text{ s}^{-1}$ , and a constant angular rate  $|\dot{\phi}| = \frac{\pi}{2} \text{ rad s}^{-1}$  (see Figure 4.1). The 345 GHz zenith opacity is interpolated between skydip measurements that punctuate observing sessions, and is used to correct for line-of-sight atmospheric absorption. Flux calibration is determined by observations of Neptune before each scan, and the telescope pointing is monitored throughout the observations with periodic scans of bright quasi-stellar objects (QSOs). Scans that either had abnormally-high RMS array sensitivities or had been taken during rapidly-changing atmospheric conditions were removed from the analysis. The total remaining on-target integration times for the clusters are listed in Table 4.2.

The main lobe of the LABOCA beam has a half-power beam width (HPBW) of  $19.2''$  and solid angle  $\Omega = 9.87 \pm 0.26 \text{ nsr}$ . The full beam<sup>2</sup> includes broader, low-level wings, with total  $\Omega = 12.17 \pm 0.43 \text{ nsr}$ . We use the  $\sim 20\%$  larger solid angle of the full beam when computing integrated flux densities of extended emission. For point sources, we directly fit the data to 2D Gaussian profiles of the main lobe.

---

Observatory, and the Onsala Space Observatory.

<sup>2</sup> <http://www.apex-telescope.org/bolometer/laboca/calibration/>



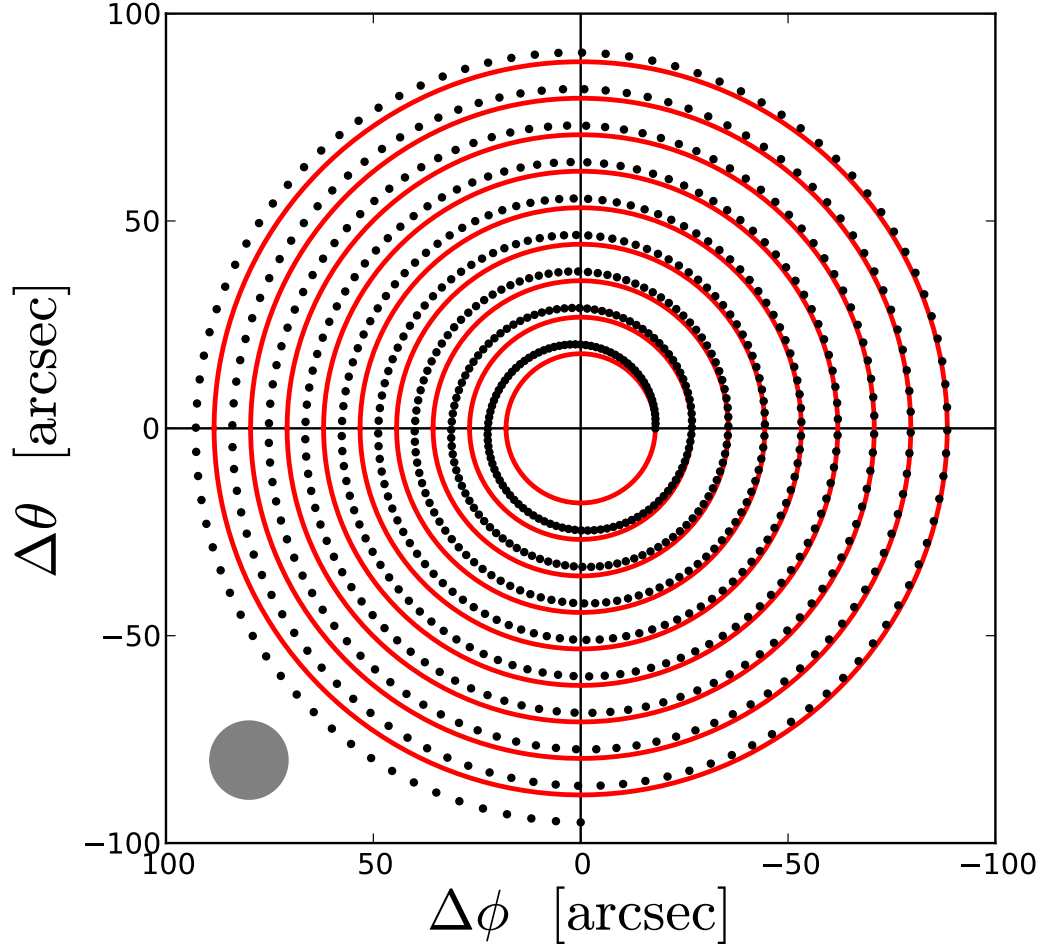


Figure 4.1: Sampling pattern of a single channel during a 35 second APEX/LABOCA spiral scan with 25 Hz data sampling. The coordinates  $(\phi, \theta)$  represent telescope azimuth and elevation. The origin represents one of four vertices in the raster pattern, offset to an arbitrary channel in the focal plane. Solid circles represent the approximation to this scan pattern that is used in computing the expected SZE signal in the ACT 148 and 218 GHz maps. The lower left circle represents the FWHM of the LABOCA 345 GHz beam ( $19.2''$ ).

Table 4.2. LABOCA 345 GHz observations

Project ID	Target	$t_{\text{obs}}^{\text{a}}$ (hr)	map RMS (mJy beam $^{-1}$ )
C-086.F-0668A-2011	ACT-CL J0546–5345	16.3	3.5
C-087.F-0012A-2011	ACT-CL J0559–5249	13.3	6.7
C-088.F-1772A-2011	ACT-CL J0215–5212	17.6	4.3
E-086.A-0972A-2010	ACT-CL J0330–5227	8.1	4.5
	ACT-CL J0438–5419	18.3	3.3
M-087.F-0037-2100	ACT-CL J0102–4915	11.3	5.4
M-088.F-0003-2011	ACT-CL J0245–5302	11.6	4.8
O-086.F-9302A-2010	ACT-CL J0232–5257	17.0	3.6
O-087.F-9300A-2011	ACT-CL J0235–5121	12.2	4.9
O-088.F-9300A-2011	ACT-CL J0616–5227	14.8	4.0
E-380-A-3036A-2007	ACT-CL J0658–5557	16.5	5.0
O-079.F-9304A-2007			

<sup>a</sup>Total un-flagged, on-target integration time

### LABOCA data reduction

We reduced the LABOCA data using the Python-based Bolometer Array Analysis Software (BoA<sup>3</sup>) package. The data time-stream  $T(c, t)$ , a function of channel  $c$  and time  $t$ , is first flux calibrated and corrected for atmospheric absorption. Next, median filtering at each time step is applied to all channels, then to each of twelve subgroups of channels that share readout cabling, then to each of four subgroups that share amplifier boxes (see Figure 4.2). Despiking is performed between stages of median filtering, before a linear baseline is subtracted from each channel; channels with RMS noise greater than  $4\times$  the median value are flagged. Low-frequency “ $1/f$ ” noise is removed using BoA’s noise whitening algorithm `flattenFreq`, which sets the magnitudes of Fourier modes with frequencies less than some cutoff frequency  $f < f_c$  to the average magnitude of those in the range  $f_c < f < 1.2 \times f_c$ . Because the celestial scanning velocity increases

<sup>3</sup> <http://www.apex-telescope.org/bolometer/laboca/boa/>

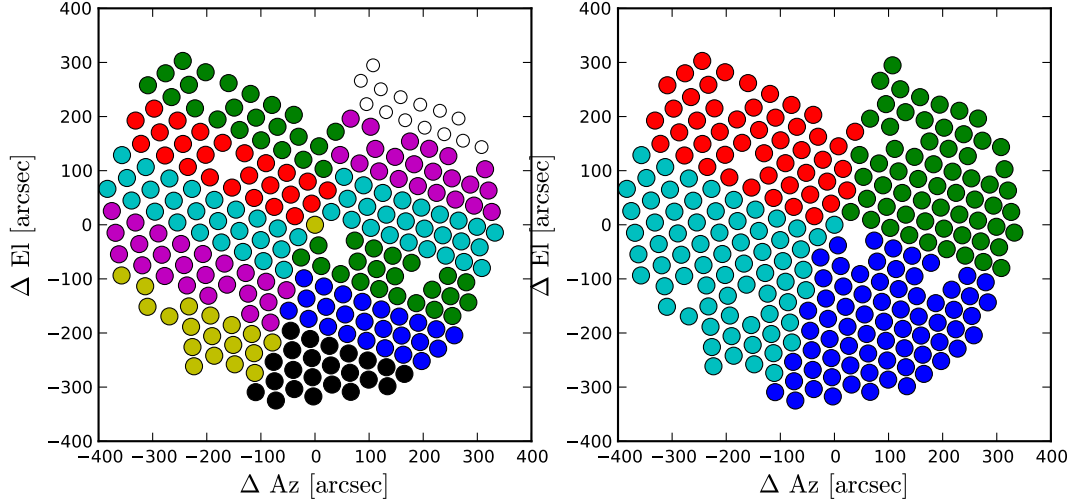


Figure 4.2: Spatial arrangement of LABOCA channels in horizontal coordinates. The color coding is repeated and represents different contiguous groups of channels that share a common cable box (*left*) or amplifier box (*right*).

as a function of time during each scan as  $v(t) \simeq |\dot{\phi}|(r_0 + \dot{r}t)$ , `flattenFreq` filters out all emission on angular scales larger than the cutoff scale  $s_c(t)$  given by

$$s_c(t) = v(t)/f_c = (3.5 \times t + 28) f_c^{-1} [\text{arcsec}], \quad (4.2)$$

with  $t$  in seconds and  $f_c$  in  $\text{Hz}^4$ . The data are then gridded onto an equatorial  $0.3^\circ \times 0.3^\circ$  image with  $3.6''$  pixels (oversampling the beam by a factor of five in each direction). The resulting central RMS sensitivities of the full-resolution maps are presented in Table 4.2.

The above reduction steps, represented by  $\mathcal{R}$ , operate on time-stream data and return a gridded map, i.e.,  $I(\alpha, \delta) = \mathcal{R}[T(c, t), l]$ , where the parameter  $l$  is determined by the noise whitening properties and represents the largest source size to which the entire scan remains responsive. The corresponding  $f_c$  is found from Equation 4.2 by setting  $s_c$  at  $t = 0$  (where it achieves its minimum value) equal to  $l$  convolved with the

---

<sup>4</sup> In Equation 4.2, the term  $\dot{r}^2$  in the full equation for the scanning velocity,  $v^2 = \dot{r}^2 + (r_0 + \dot{r}t)|\dot{\phi}|^2$ , is ignored because  $\dot{r}^2 \ll (r_0 + \dot{r}t)|\dot{\phi}|^2$  during the entire scan.

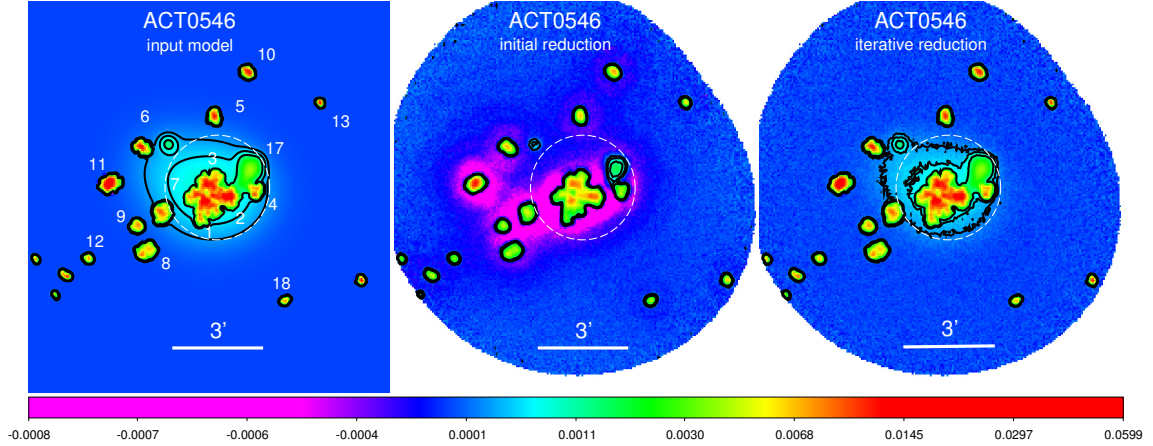


Figure 4.3: Example of iterative reduction performance in ACT-CL J0546–5345. *Left:* Input 345 GHz model based on the converged model components from the real data. *Center:* Output image after a single reduction (no iteration). *Right:* Output image after running the iterative pipeline. The numbered sources correspond to those presented in Figure 4.5. The white dashed circle is centered on the ACT 148 GHz decrement (Marriage et al., 2011) with radius equal to the projected  $\theta_{500c}$  ( $105''$ ) (Sifón et al., 2013). The black contours represent 345 GHz intensity levels of 0.2, 0.5, and 1 mJy beam $^{-1}$ .

LABOCA beam  $\theta_{\text{beam}}$ :

$$f_c(l) = \frac{28}{\sqrt{l^2 + \theta_{\text{beam}}^2}} [\text{Hz}], \quad (4.3)$$

for  $l$  and  $\theta_{\text{beam}}$  in arcsec.

### Iterative multi-scale algorithm

The filtering steps described above, primarily median filtering on cabling subgroups and noise whitening (Section 4.3.1), can remove astrophysical emission from the data along with atmospheric noise (e.g., see Figure 4.3). To recover this lost signal, we have developed an iterative, multi-scale pipeline. Our approach is inspired by techniques used by Enoch et al. (2006) and Nord et al. (2009). One important difference is that we maximize our sensitivity to low-level extended emission by using a series of matched filters to search for signal at multiple cluster-sized spatial scales, similar in nature to adaptive filtering algorithms (e.g., Scoville et al., 2007).

The first step of the pipeline is reducing the data with aggressive filtering by setting the angular scale of fully-preserved emission to  $l = 0''$ . This first image,  $I_1^{l=0''}$ , is minimally affected by  $1/f$  noise, although it has complete responsiveness only to point sources. High-significance structures in this first image are located by producing a S/N image  $S(\alpha, \delta)$  using a spatial matched filter (e.g., Serjeant et al., 2003).

$$S = \frac{I \otimes k}{\sqrt{W \otimes k^2}}, \quad (4.4)$$

where  $k$  is a 2D Gaussian kernel with  $\text{FWHM} = \sqrt{l^2 + \theta_{\text{beam}}^2}$ , and  $W(\alpha, \delta)$  is a weight map defined by the inverse variance of time stream data within each pixel. Pixels where  $S(\alpha, \delta) < S_{\text{thresh}}$  are set to zero in  $I_1^{l=0''}$ . The significance level  $S_{\text{thresh}}$  is chosen so that there are  $\leq 0.3$  spurious sources in the S/N map, and therefore depends on  $l$  and the image size. This clipped image is then smoothed to the angular scale of interest by convolving with a normalized 2D Gaussian with  $\text{FWHM} = l$  to produce a model image  $M_1^{l=0''}$ . For the case of  $l = 0''$ , a small amount of smoothing,  $\text{FWHM} = 7''$ , is still applied to help reduce sharp discontinuities in the model image. If the model image  $M_1^{l=0''}$  is not empty, iteration proceeds and  $M_1^{l=0''}$  is transformed into time stream data  $\mathcal{T}[M_1^{l=0''}]$  and subtracted from the original time stream. This residual time stream  $T - \mathcal{T}[M_1^{l=0''}]$  is then reduced using the procedure from Section 4.3.1, and the resulting residual image is added to  $M_1^{l=0''}$  to produce the next image,  $I_2 = \mathcal{R}[T - \mathcal{T}[M_1]] + M_1$ . This process is carried out until the signal in the map converges,  $(\Sigma(I_n - I_{n-1}) \simeq 0)$ , and we are left with a final image  $I_N$  and model  $M_N$ . Ten iterations are sufficient for the model image to converge.

Now we begin to search for larger spatial scale emission.  $M_N^{l=0''}$  (the final, converged model image with  $l = 0''$  filtering) is subtracted from the original time streams, and the residual time stream is reduced with a relaxed filtering, initially,  $l = 30''$ . If high-significance  $30''$ -scale emission is located using a matched filter, iteration begins again. This process is carried out for  $l = 0'', 30'', 60''$  and  $120''$ ; the final image is the sum of

all converged models, plus any residual low-level signal and the remaining noise:

$$I_{\text{final}} = M_f + \mathcal{R}(T - \mathcal{T}[M_f]), \quad (4.5)$$

where  $M_f$  is the sum of all scales’ converged model images  $M_f = \Sigma_l M_N^l$ . The array loses sensitivity quickly for angular scales that are larger than the typical size of contiguous subsets of channels that share cabling (i.e.,  $\gtrsim 6.7'$ ; see Figure 4.2); therefore, the pipeline is limited to  $l \leq 120''$ , which allows for recovery of emission on scales up to  $\langle s_c(t, l = 120'') \rangle \leq 6.5'$ .

The final, converged, iteratively-reduced 345 GHz images of all eleven clusters are shown in Figure 4.4. We detect bright SMGs in all clusters and strong SZE increment signals ( $S/N > 3.5$ ) in six clusters (see Table 4.5).

### Systematic uncertainties of iterative pipeline

In Figure 4.3, we show the results when a noise-free<sup>5</sup> model image (that of ACT-CL J0546–5345) is transformed to time stream data and passed through the full iterative pipeline. We define the transfer function efficiency as the ratio of flux densities of structures in the final iterated map divided by their “true” flux densities in the input model image. Point-source flux densities are measured using a least-squares fit to a circular Gaussian profile with a floating constant offset, and integrated SZE signal is measured as the integrated flux density within  $r_{500c}$  after subtraction of point sources. We find that both compact and extended structures are recovered accurately by the iterative process, while a single-pass reduction leaves the compact sources attenuated and the extended emission almost completely removed. Figure 4.3 displays the initial model, a single (non-iterative) reduction, and the final iterated image.

---

<sup>5</sup> Our “noise-free” data actually have a non-zero RMS noise of 1% that of the real data, due to constraints of the BoA software package. Realistic correlations in the simulated noise are produced by convolving a Gaussian random sequence with the square of the autocorrelation function of real data.

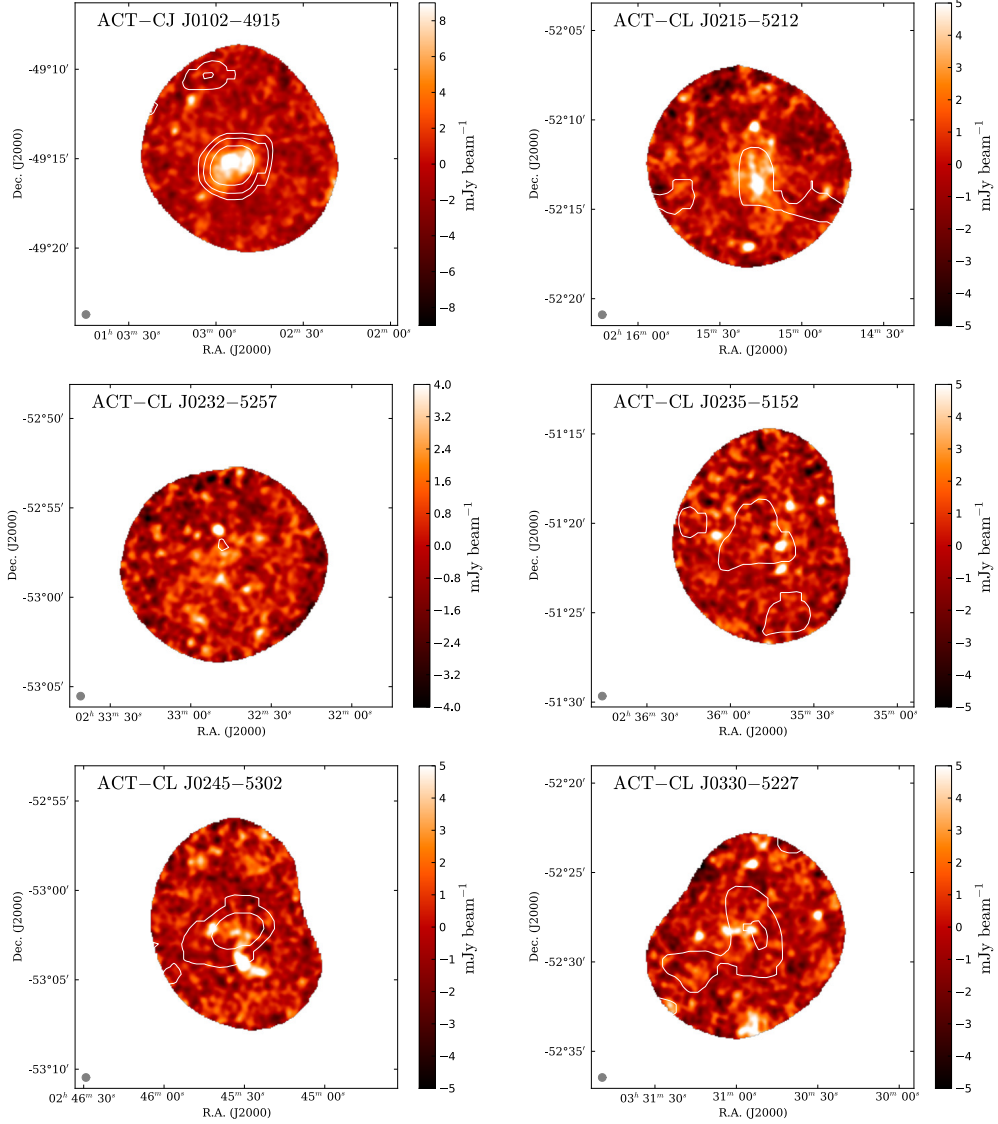


Figure 4.4: LABOCA 345 GHz maps. The color scale images represent 345 GHz flux density in the beam-smoothed, iteratively-reduced maps. The white contours represent the 1.4'-resolution LABOCA-filtered ACT 148 GHz decrement intensities with levels  $\Delta T_{\text{CMB}} = -[20, 50, 100] \mu\text{K}$ . The grey circle at the lower left represents the effective angular resolution of the beam-smoothed LABOCA maps (27.2'').

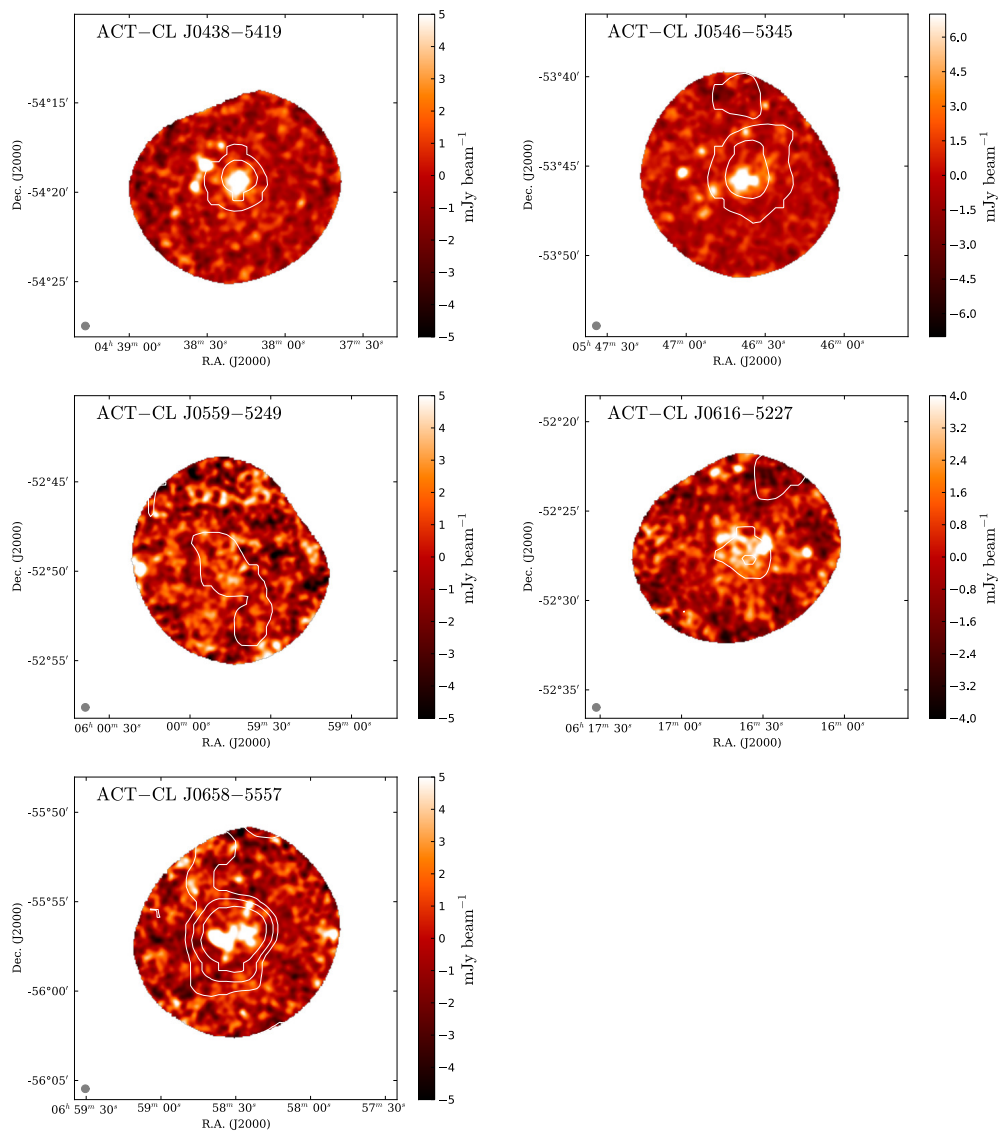


Figure 4.4: Continued



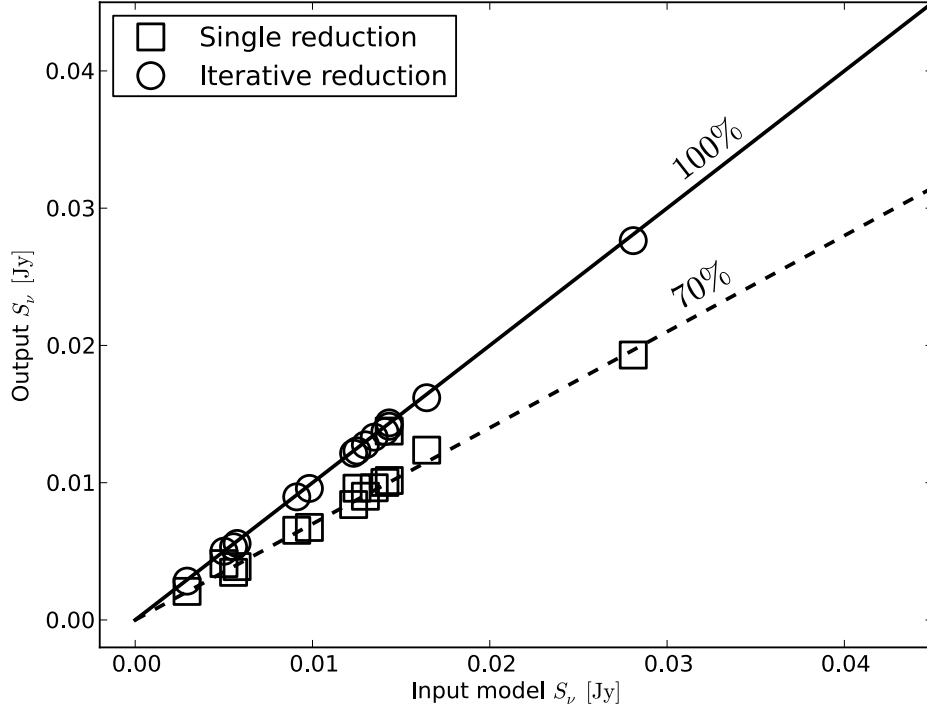


Figure 4.5: Transfer function efficiency of the LABOCA reduction pipeline. The squares and circles represent the input and output flux densities of point sources in the field of ACT-CL J0546–5345 (see Figure 4.3) for a single run of the reduction pipeline (squares), and for a full iterative reduction (circles). The average flux recovery fractions for single and iterative reductions are  $0.73 \pm 0.08$  and  $0.98 \pm 0.01$ , respectively.

Figure 4.5 displays the flux densities of point sources from Figure 4.3 after a single-pass reduction and after the iterative reduction. The transfer function efficiency  $e_T$  of the first-pass reduction is independent of the target cluster field and the intensity of simulated noise, with a value  $e_T \simeq 70\%$  for compact emission, and a value  $e_T \sim 52\%$  for extended emission on  $l = 120''$  scales. After the iteration process, the average  $\langle e_T(0) \rangle = 98 \pm 1\%$ , indicating that the flux that remains lost after iteration is much lower than the typical statistical uncertainty of our measurements and can be ignored.  $e_T(120)$  is estimated from the fractional increase in signal in  $l = 120$  model images of real data, while  $e_T(0)$  is read off Figure 4.5. The transfer function efficiency is lower for larger angular scales because of the increased effects of median filtering and noise whitening on these scales. After the iteration process, we find no significant bias in the observed flux densities of compact sources or integrated SZE signals.

Notwithstanding this encouraging result, the integrated flux density within  $r_{500c}$  will remain an underestimate in images that do not trigger the iteration process. The worst-case scenario would correspond to emission that after being folded through the reduction pipeline remains just below the threshold for iteration, corresponding to  $S_\nu^{\text{missing}} = \sigma_{120} S_{\text{thresh}}^{120} \Omega (e_T(120)^{-1} - 1)$ , where  $\sigma_{120}$  is the RMS noise in the  $l = 120''$  match-filtered image,  $S_{\text{thresh}}^{120}$  is corresponding S/N threshold, and  $\Omega$  is the solid angle of the photometric aperture. This additional systematic uncertainty applies to SZE non-detections that are too weak to trigger iteration, and will not affect our high-S/N SZE detections.

### 4.3.2 148 GHz and 218 GHz ACT

We can also use the ACT 148 and 218 GHz maps to constrain the SZE spectra of the clusters. Before extracting the integrated flux densities  $S_{148}$  and  $S_{218}$  for each cluster, we filter the raw ACT maps to mimic the transfer function of our LABOCA observations,

which attenuates emission from spatial scales larger than  $\gtrsim 120''$ . This filtering is done by first taking the 2D Fourier transform of  $1 \text{ deg}^2$  cutouts around the clusters in the ACT maps. We then apply the same frequency-domain filtering in 2D space for the ACT maps that the algorithm `FlattenFreq` performed on the 1D LABOCA time streams. To transform between temporal and spatial frequencies, we use the angular scanning speed of the LABOCA observations. We approximate the full 35 second APEX raster spiral as a collection of 9 circles (Figure 4.1), each of constant radius representing one spiral loop at a constant scanning velocity. One Fourier-filtered map is produced for each scanning speed and then transformed back to spatial coordinates. The final filtered map that is used to extract 148 GHz and 218 GHz flux densities is the average of all nine individually Fourier-filtered images. Uncertainties are then computed using the effective number of ACT beams in each aperture. Beam solid angles at 148 and 218 GHz are taken from Hincks et al. (2010). The ACT maps are originally gridded with  $50''$  pixels, and therefore the additional Poisson noise (Gehrels, 1986) of computing photometric quantities using small numbers ( $\lesssim 20$  pixels) of pixels are included in the uncertainties.

### 4.3.3 2.1 GHz ATCA

#### ATCA Observations

We acquired 2.1 GHz Australia Telescope Compact Array (ATCA) observations of the ten clusters in our sample with new LABOCA observations. We used the 16 cm-band receiver with the Compact Array Broadband Backend (CABB) giving 2049 1 MHz-wide channels spanning 1.1–3.1 GHz. Observations were made in January 2011 (PI: Baker), December 2011 (PI: Baker), and April 2012 (PI: Lindner). All clusters have been observed with the 6A antenna configuration (baseline range  $B = 628\text{--}5939 \text{ m}$ ), and ACT J0102-4915 has additional data in the 1.5B configuration ( $B = 31\text{--}4301 \text{ m}$ ). For

Table 4.3. ATCA 2.1 GHz observations

Month	Target	Phase cal	$t_{\text{obs}}^{\text{b}}$ (hr)	Configuration
Jan 2011	ACT-CL J0232–5257	J0214-522	19.8	6A
	ACT-CL J0546–5345	J0539-530	21.0	6A
Dec 2011	ACT-CL J0102–4915	J0047-579	12.1	6A
	ACT-CL J0215–5212	J0214-522	8.6	6A
	ACT-CL J0235–5121	J0214-522	8.5	6A
	ACT-CL J0245–5302	J0214-522	10.3	6A
	ACT-CL J0330–5227	J0334-546	8.8	6A
	ACT-CL J0438–5419	J0522-611	8.1	6A
	ACT-CL J0559–5249	J0539-530	8.9	6A
	ACT-CL J0616–5227 <sup>a</sup>	J0539-530	7.8	6A
		J0522-611		6A
		J0647-475		6A
Apr 2012	ACT-CL J0102–4915	J0047-579	6.8	1.5B

<sup>a</sup>Observations used three phase calibrators.

<sup>b</sup>Total un-flagged, on-source integration time.

flux and bandpass calibration we used PKS 1934-638 (Reynolds, 1994). The Australia Telescope National Facility (ATNF) on-line calibrator database<sup>6</sup> was used to choose suitably bright, nearby, and compact phase calibrators for each cluster, which are listed in Table 4.3.

The software package MIRIAD (Sault et al., 1995) was used to calibrate, flag, invert, and clean the visibility data. Radio frequency interference (RFI) that affected all channels at a given time or at all times for a certain channel was removed manually using `pgflag` and `blflag`. Transient RFI was removed using the automated flagging algorithm `mirflag` (Middelberg, 2006). Baseline 1–2 in the April 2012 data contained powerful broad-spectrum RFI and was entirely flagged. First-order multi-frequency synthesis images with robust parameter `robust`= 0 were made using `invert` and `mfclean`.

<sup>6</sup> <http://atoa.atnf.csiro.au>

Table 4.4. ATCA map properties

Target	$\langle\nu\rangle^a$ (GHz)	$\theta_{\text{major}}^b$ ( $''$ )	$\theta_{\text{minor}}^c$ ( $''$ )	P.A. <sup>d</sup> ( $^\circ$ )	map RMS <sup>e</sup> ( $\mu\text{Jy beam}^{-1}$ )
ACT-CL J0102–4915	2.15	6.13	3.09	-1.9	7.5
ACT-CL J0215–5212	2.16	4.66	2.93	-21.0	11.0
ACT-CL J0232–5257	2.13	4.80	3.06	6.0	8.1
ACT-CL J0235–5121	2.17	5.26	2.71	-10.0	10.9
ACT-CL J0245–5302	2.16	4.44	2.97	4.3	10.5
ACT-CL J0330–5227	2.17	5.06	2.73	17.7	11.7
ACT-CL J0438–5419	2.15	5.30	2.80	-19.6	11.9
ACT-CL J0546–5345	2.13	4.66	3.21	-3.1	6.9
ACT-CL J0559–5249	2.15	5.35	2.86	-13.1	9.6
ACT-CL J0616–5227	2.15	4.99	2.98	26.2	12.0

<sup>a</sup>Effective frequency<sup>b</sup>Synthesized beam major axis<sup>c</sup>Synthesized beam minor axis<sup>d</sup>Synthesized beam position angle<sup>e</sup>RMS noise at the image phase center

Two rounds of self-calibration were then carried out, one solving for phase only, and one for both phase and amplitude together. The final RMS sensitivities at phase center range from 6.9–12  $\mu\text{Jy beam}^{-1}$  (see Table 4.4).

#### 4.3.4 *Herschel*/SPIRE observations

We have also acquired new *Herschel* Space Observatory (Pilbratt et al., 2010) imaging with the Spectral and Photometric Receiver (SPIRE; Griffin et al., 2010) and the Photodetector Array Camera (PACS; Poglitsch et al., 2010) of a subset of the cluster sample. PACS observations have angular resolution 5–7 $''$  and use integration times of 1.6 h per cluster, corresponding to RMS sensitivities above the confusion limit of 1.8 and 3.4 mJy beam $^{-1}$ , respectively, in the 100  $\mu\text{m}$  and 60  $\mu\text{m}$  bands. SPIRE observations have

angular resolution  $18.2\text{--}36.3''$  and integration times of 0.6 h for RMS map sensitivities of 2.0, 1.7, and  $2.4 \text{ mJy beam}^{-1}$  in the  $250 \mu\text{m}$ ,  $350 \mu\text{m}$ , and  $500 \mu\text{m}$  bands, respectively.

Currently, the SPIRE imaging for ACT-CL J0102–4915 is reduced, and we use these data to help constrain the high-frequency end of the SZE spectrum when deriving the cluster’s peculiar velocity (Section 4.5). Relative intensities of typical SZE increment signals compared to those at 345 GHz are 0.05%, 2%, and 34%, respectively, in the SPIRE 250, 350, and  $500 \mu\text{m}$  bands.

The high sensitivity and comparatively low angular resolution of *Herschel* SPIRE make the images confusion-limited, i.e., the brightness fluctuations in the images are primarily due to the blending together of bright, unresolved sources. Zemcov et al. (2010) presented an algorithm that uses the SPIRE  $250 \mu\text{m}$  image as a template to subtract out the confused point source emission from the longer-wavelength bands using knowledge of the typical spectrum of  $250 \mu\text{m}$  point sources. We have used the Zemcov et al. (2010) algorithm on our data with the *Herschel* Interactive Processing Environment (Ott et al., 2006) to remove the confused infrared background from our  $350 \mu\text{m}$  and  $500 \mu\text{m}$  images when extracting SZE signals.

#### 4.3.5 The Sunyaev Zel’dovich effect

The deflection in CMB intensity due to the thermal SZE for a single temperature gas is (Carlstrom et al., 2002)

$$\Delta I_{\text{tSZ}} = y I_0 g(x, T_e), \quad (4.6)$$

in terms of the scaled frequency  $x \equiv h\nu/kT_{\text{CMB}}$ ,  $I_0 = 2(kT_{\text{CMB}})^3/(hc)^2 = 22.87 \text{ Jy arcmin}^{-2}$ , and electron temperature  $T_e$ . The Compton parameter

$$y \equiv \frac{kT_e}{m_e c^2} \int \sigma_T n_e dl, \quad (4.7)$$

where  $m_e$  is the mass of the electron, and  $\sigma_T$  is the Thompson cross section. The optical depth to electron scattering  $\tau = \int \sigma_T n_e dl$ . The function  $g(\nu, T_e)$  is the derivative of

the Planck function ( $dB_\nu/dT$ ) multiplied by the SZE spectrum,

$$g(x, T_e) = \frac{x^4 e^x}{(e^x - 1)^2} \left( x \frac{e^x + 1}{e^x - 1} - 4 \right) [1 + \delta_{\text{SZE}}(x, T_e)], \quad (4.8)$$

where  $\delta_{\text{SZ}}$  represents relativistic corrections that become important at high electron temperatures, especially when  $x \gg 1$ .

The change in CMB intensity due to the kSZ effect is given by

$$\begin{aligned} \Delta I_{\text{kSZ}} &= -\tau_e I_0 \left( \frac{v_p}{c} \right) \frac{dB_\nu}{dT} \\ &= -\tau_e I_0 \left( \frac{v_p}{c} \right) \frac{x^4 e^x}{(e^x - 1)^2}, \end{aligned} \quad (4.9)$$

where  $v_p$  is the cluster line-of-sight peculiar velocity with respect to the CMB in the cluster rest frame.

We compute predicted SZE signals using the numerical integration **C++** package **SZPACK** (Chluba et al., 2012, 2013), which allows for quick computations of SZE signals with  $10^{-5}$  precision for temperatures up to  $T_e \simeq 25 \text{ keV}$  at frequencies up to and including the high-frequency *Herschel* SPIRE bands ( $x \lesssim 20$ ).

## 4.4 Point source contamination

### 4.4.1 Radio sources

Radio and IR-bright sources can potentially “fill in” SZE decrement signals and artificially enhance SZE increment signals in the  $1.5'$ -resolution SZE maps typically used to detect clusters. With our high-resolution 2.1 GHz and 345 GHz imaging, we can disentangle the signals of point sources from those of the true SZE signal, allowing us to derive more robust measurements of cluster mass and thus unbiased limits on cluster peculiar velocities. In this section, we quantify the degrees of radio and submillimeter contamination of the SZE signal.

## 2.1 GHz number counts

We use the Astronomical Image Processing System (AIPS) task **SAD** to fit Gaussian profiles to all bright sources in the ATCA maps down to a significance of  $4\sigma$  and out to the 75% primary beam power radius at the effective frequency of 2.1 GHz (7.2'). We consider sources only within this radius to avoid large uncertainties in the beam-corrected flux densities of sources lying far from the pointing center caused by variation in their spectral shapes. We adopt a primary beam profile based on the spectrum-weighted mean frequency of 1.96 GHz assuming a fiducial power-law spectrum with  $\alpha = 1$ , where the spectral index  $\alpha$  is defined by  $S_\nu \propto \nu^{-\alpha}$ . To minimize radial selection bias, we only consider sources that have primary beam-corrected flux densities above the detection threshold at *all* radii, i.e.  $> 4\sigma/0.75 = 64 \mu\text{Jy}$ . These selections result in a total of 1279 radio sources spanning a flux density range between  $64 \mu\text{Jy}$  and  $0.24 \text{ Jy}$ .

Fainter sources have an increased chance of having their flux densities scattered below the detection threshold by noise, thus lowering their completeness. Because the noise in the 2.1 GHz maps is nearly Gaussian, we correct completeness using an analytic correction in the following way. The completeness probability  $C$  that a source with true flux density  $S_\nu$  will be detected above a threshold of  $N\sigma$  is given by

$$C = 1 - \Phi\left(\frac{N\sigma - S_\nu}{\sigma}\right), \quad (4.10)$$

where  $\Phi(x)$  is the cumulative normal distribution function. The completeness correction is then implemented by computing number counts using a weighted histogram with weights  $w_i = C_i^{-1}$ .

Figure 4.6 shows combined and individual 2.1 GHz number counts in nine log-spaced flux density bins. The power-law index of the counts  $\delta$ , where  $dN/dS \propto S^{-\delta}$ , is  $\delta \simeq 1.7$ . We measure the counts inside concentric circles centered on the clusters in Figure 4.7, revealing that there is an enhanced density of radio sources with radial distance  $r < 2'$



from the cluster centers. For the typical cluster in the sample, this radius lies inside  $\theta_{500c}$ . We next compute the number counts in three disjoint regions defined by the clusters' individual  $\theta_{500c}$  values, and find that the enhancement in number counts is due primarily to sources at  $r < 0.35 \theta_{500c}$  (Figure 4.8). This enhanced source density in cluster interiors is likely due to the presence of both radio-loud cluster member galaxies and (possibly) gravitationally-lensed background AGNs and star forming-galaxies. We have also checked for variation in the counts of the top, bottom, left, and right halves of the radio images and find no significant differences.

### Radio contamination extrapolated to 148 GHz

We use our 610 MHz Giant Metre-wave Radio Telescope (GMRT) image of ACT-CL J0102–4915 to compute the radio spectral index  $\alpha_{610}^{2.1}$  distribution of 2.1 GHz sources, which allows us to extrapolate their flux densities to the higher frequencies of the SZE decrement. We find 105 for 2.1 GHz/610 MHz pairs of sources with  $< 1''$  separation and  $> 4\sigma$  significance out to the  $> 20\%$  radius of the primary beam in the ACT-CL J0102–4915 field and compute their spectral indices

$$\alpha_{610}^{2.1} = -\log(S_{2.1}/S_{610})/\log(2.1/610). \quad (4.11)$$

The distribution  $\alpha_{610}^{2.1}$  is shown in Figure 4.9. We find a median spectral index  $\alpha_{610\text{ median}}^{2.1} = 0.99$  with inner quartile range 0.80–1.20.

We detect 387 2.1 GHz sources with  $S_{2.1} > 4\sigma$  within  $\theta_{500c}$  of our ten clusters with ATCA imaging, corresponding to a mean 2.1 GHz flux density within  $\theta_{500c}$  per cluster of  $45.7_{-8.2}^{+9.2}$  mJy. After scaling the flux density to the 148 GHz SZE decrement using  $\alpha_{610\text{ median}}^{2.1} = 0.99$  and including an additional uncertainty based on the spectral index inner quartile range, the typical contaminating radio signal from 2.1 GHz-detected synchrotron radio sources is estimated to lie between 0.23–1.82 mJy in the 148 GHz SZE decrement.

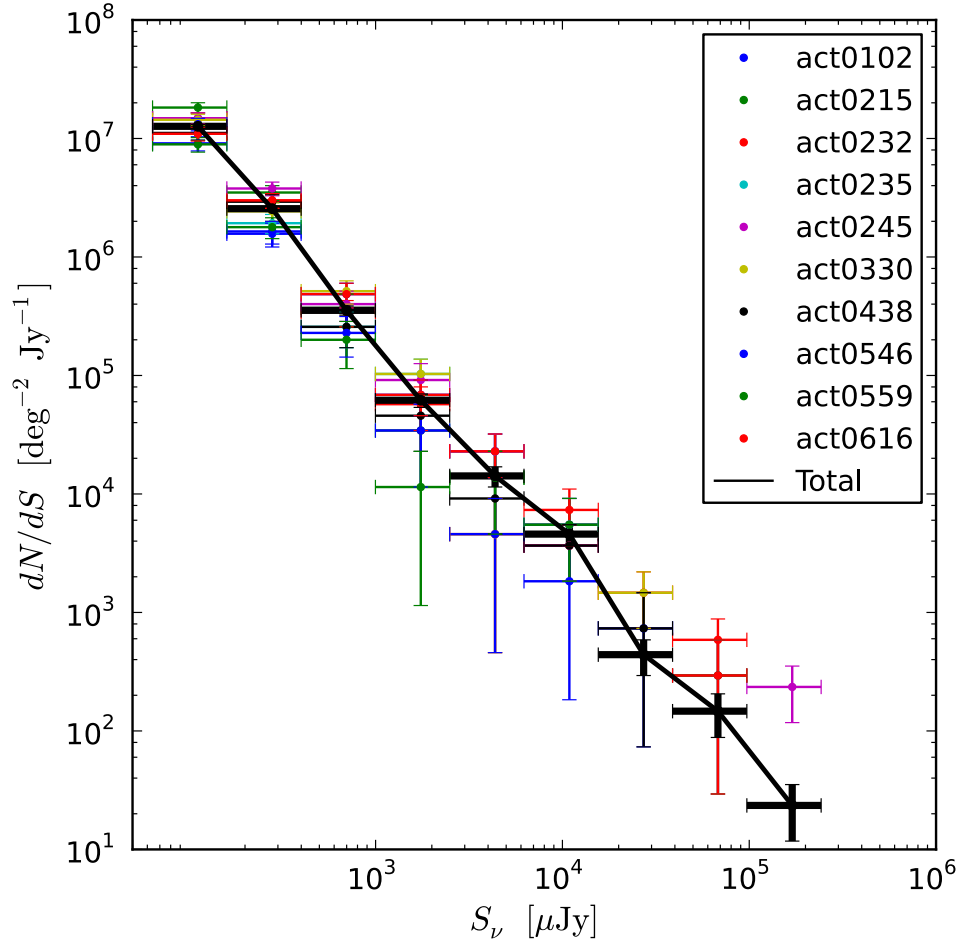


Figure 4.6: Total 2.1 GHz differential number counts towards the clusters out to a maximum search radius of  $r_{\text{max}} = 8.2'$ . The different series of colored error bars represent the counts around individual clusters. The connected black error bars represent the cumulative counts across all clusters. The horizontal error bars represent the bin limits, which are logarithmically-spaced between  $64 \mu\text{Jy}$  and  $0.24 \text{ Jy}$ .

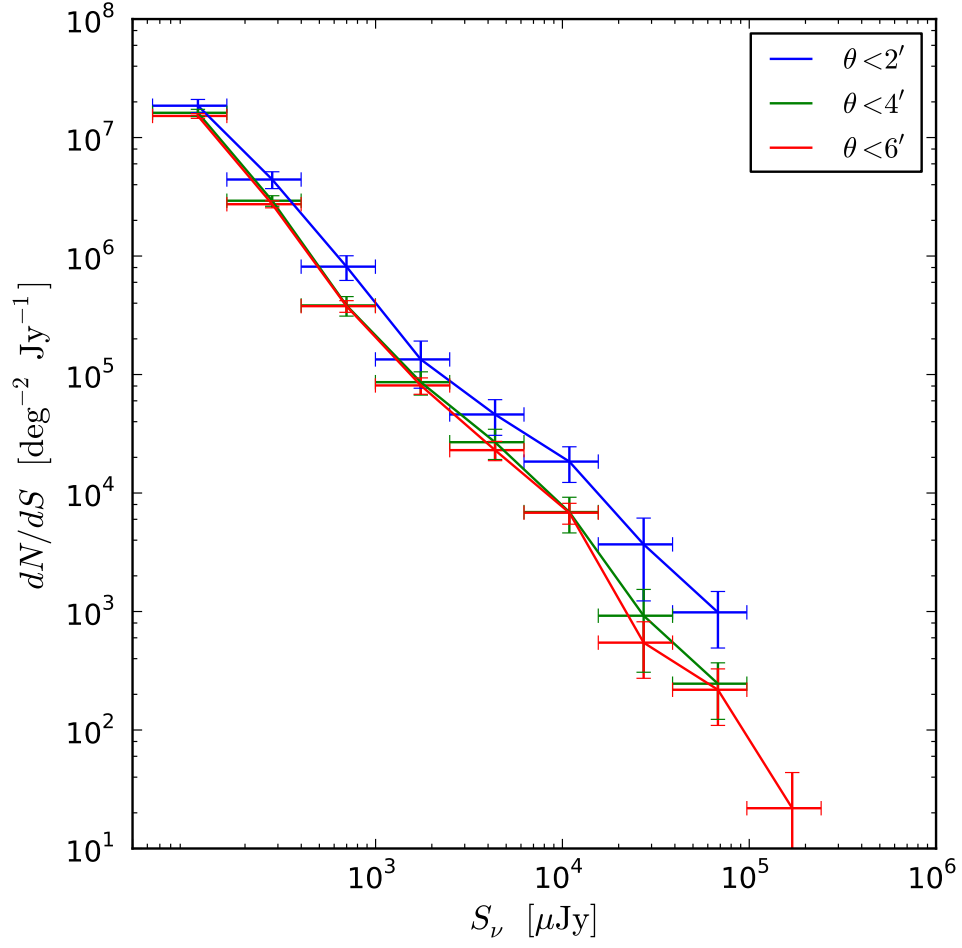


Figure 4.7: 2.1 GHz differential number counts as a function of cluster-centric radius. The connected points and error bars represent number counts and Poisson uncertainties inside circles centered on the clusters with angular radii  $2'$  (blue),  $4'$  (green), and  $6'$  (red). The bins are the same as in Figure 4.6.

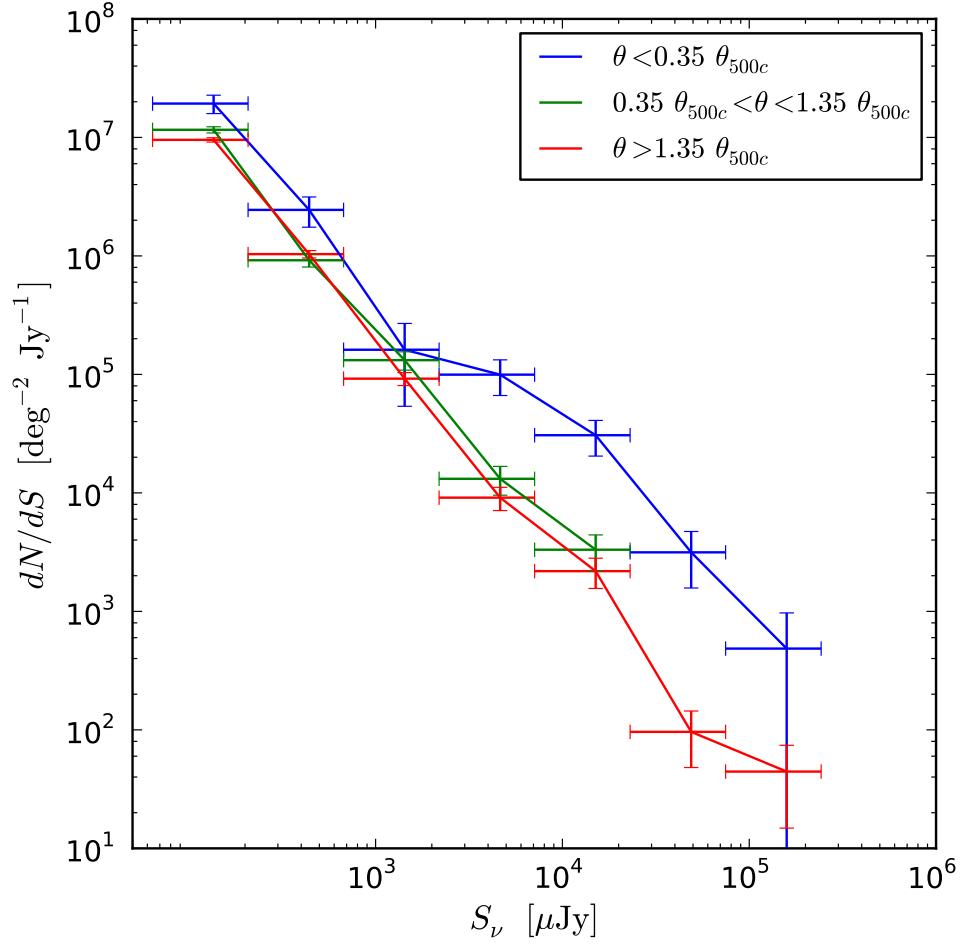


Figure 4.8: 2.1 GHz differential number counts as a function of physical clustercentric projected radius. The connected points and error bars represent number counts and Poisson uncertainties inside a circle with projected radius  $r \leq 0.35 r_{500c}$  (blue), inside an annulus with radii  $0.35 r_{500c} < r \leq 1.35 r_{500c}$  (green), and inside an outer annulus with radii  $1.35 r_{500c} < r \leq r_{\text{max}}$  (red), where  $r_{\text{max}} = 8.2'$  is the maximum search radius. The bins are the same as in Figure 4.6.

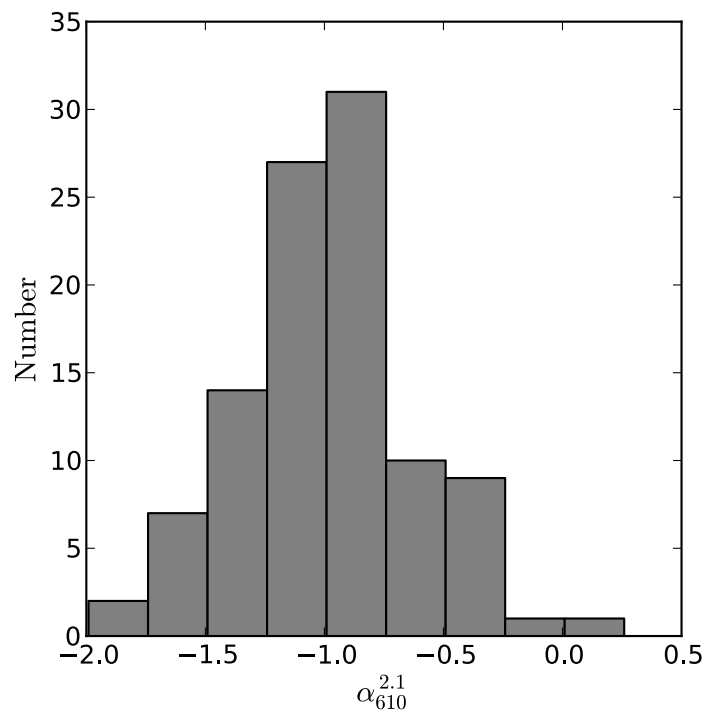


Figure 4.9: Spectral index  $\alpha_{610}^{2.1}$  of 105 pairs of  $> 4\sigma$  significance 2.1 GHz and 610 MHz sources within a  $19.4'$  radius of ACT-CL J0102–4915. The median and inner-quartile range are  $\alpha_{610\text{median}}^{2.1} = 0.99$  and 0.80–1.20, respectively.

Inside the photometric apertures used to constrain the clusters’ peculiar velocities, the estimated contaminating 148 GHz signal is  $S_\nu = 0.5 \text{ mJy}$ , which is 0.6% of the typical decrement signal in our sample.

#### 4.4.2 SMGs

In the iteratively-reduced LABOCA images, we find bright SMGs superposed on the clusters’ extended SZE emission. A complete analysis of the statistical properties of the detected SMG population will be presented in Aguirre et al. (2013). Here we consider only the brightest sources nearest to the cluster centers, and their effects on measured SZE increment signals. Potentially contaminating SMGs are selected to lie within  $\theta_{500c}$  of the cluster centers and have  $S_\nu > 10 \text{ mJy}$ . The existence of a 2.1 GHz radio counterpart is used to discriminate between SZE fluctuations and SMG emission when a source is blended with cluster SZE signal. ACT-CL J0102–4915 and ACT-CL J0546–5345 each contain two bright, blended SMGs with radio counterparts. We detect a total of 23  $S_\nu > 10 \text{ mJy}$  point sources within  $\theta_{500c}$  of our 10 cluster centers with deep ATCA imaging, giving an estimated total flux density per cluster in high-significance SMGs of  $54^{+68}_{-33} \text{ mJy}$ . Using the combined area of  $0.10 \text{ deg}^2$ , this sample has cumulative number counts of  $N(> 10 \text{ mJy}) = 230^{+59}_{-48} \text{ deg}^{-2}$ , which is 6–10 times greater than that of sources with comparable brightness in blank fields (Weiß et al., 2009). Due to the negative k-corrections and high redshifts of SMGs, the number density enhancement is likely due to gravitational lensing by the clusters’ gravitational potentials. Gravitational lensing does not alter the average integrated flux density of the projected SMG population, but it does increase the Poisson “shot noise” variance (e.g., Refregier & Loeb, 1997). Lima et al. (2010) predict that due to lensing, the Poisson noise from  $z = 2$  SMGs projected through the interiors of  $10^{14.2} \text{--} 10^{14.6} M_\odot$  clusters at  $z = 0.5$  is comparable to the clusters’ 345 GHz SZE increment signals.

The 345 GHz flux density in bright SMGs inside the smaller apertures used in our analysis of the SZE (Section 4.5) is  $21^{+49}_{-18}$  mJy, corresponding to  $6^{+15}_{-5}$  mJy at 218 GHz and  $2^{+5}_{-2}$  mJy at 148 GHz. The scaling to lower frequencies is done using a modified Planck function with parameters  $\beta = 1.5$  and  $T_D = 37.4$  K, values of typical blank-field 345 GHz-selected SMGs (Wardlow et al., 2011). The contaminating SMG signal represents  $15^{+36}_{-13}\%$  of the SZE signal at 345 GHz, and  $2^{+6}_{-2}\%$  at 148 GHz, respectively. The contaminating SMGs are fit by circular Gaussian profiles and subtracted from the maps before further analysis. The Gaussian fits use a floating offset that preserves the underlying 1–5 mJy spatially-extended SZE signal.

#### 4.5 Peculiar velocities

In addition to its Hubble-flow velocity, a galaxy cluster can have a velocity offset with respect to its local CMB rest-frame, known as the peculiar velocity  $v_p$ . As well as being interesting in its own right as a statistical cosmological probe of large-scale structure (e.g., Doré et al., 2003),  $v_p$  distorts the SZE spectrum, thereby possibly affecting the scaling between  $Y_{SZ}$  and cluster mass.

Mroczkowski et al. (2012) report that their 268 GHz data of the triple-merger cluster MACSJ0717.5+3745 only adequately fits their SZE model when allowing for a strong kSZ distortion from a high-velocity subcomponent. It is unclear whether strong kSZ distortions like those seen by Mroczkowski et al. (2012) are common in merging clusters. Recent results from Planck Collaboration et al. (2013 XIII) only constrain the RMS fluctuations in  $v_p$  to be  $\leq 800 \text{ km s}^{-1}$  (95% confidence) for a sample of Meta Catalogue X-ray Detected Clusters (MCXC). If transient kSZ distortions are common in merging cluster systems, then the  $Y_{SZ}$ –mass relation in SZE clusters may be significantly affected. For example, Sifón et al. (2013) find at least one indication of dynamical substructure in  $81^{+19}_{-22}\%$  (13/16) of a representative sample of ACT clusters (nine of which overlap

with this work).

We use our point source-subtracted multi-band data to constrain the peculiar velocities in our sample by parametrizing the observed SZE signal with  $v_p$  and a new quantity we refer to as  $Y'_{\text{SZ}}$ . The iterative pipeline (Section 4.3.1) faithfully recovers extended emission only up to angular scales of  $\sim 2'$ , while  $\theta_{500c}$  values can be much larger. Therefore, to strengthen constraints while fitting for  $v_p$ , we choose circular apertures for each cluster (typically 1.5–2' radii) that contain the observed scale of emission in the 345 GHz images.  $Y'_{\text{SZ}}$  is therefore the effective integrated SZ signal within each of these apertures. We have recently obtained new *Chandra* imaging (PI: Hughes) for many clusters in our sample and will use these data to independently measure  $T_e$  in these systems. For the current analysis, we set  $kT_e = 5 \text{ keV}$  (see Table 4.5) for clusters with unknown gas temperatures.

For each integrated flux density measurement  $S_{\text{SZ},i}$  at  $x_i = h\nu_i/kT_e$  we compute the expected SZE signal  $S_{\text{SZ}}^{\text{model}}(Y'_{\text{SZ}}, x_i, v_p, T_e)$ . We fit the data to the multi-band model using a grid-based search. The noise in all images is nearly Gaussian, and therefore the conditional probability density of obtaining measurements  $S_{\text{SZ},i}$ , given the model parameters  $\theta = (Y'_{\text{SZ}}, v_{\text{pec}})$  is

$$p_i(x_i; \theta) \propto e^{-(S_{\text{SZ},i} - S_{\text{SZ},i}^{\text{model}})^2 / 2\sigma_i^2}. \quad (4.12)$$

The joint probability density of obtaining all measurements is then given by  $P(x; \theta) \propto \prod_i p_i$ . We take as the best-fit parameters those that maximize the likelihood function, and the final quoted  $1\sigma$  uncertainties in  $v_p$  and  $Y'_{\text{SZ}}$  are found by marginalizing over the 2D likelihood parameter space and integrating the resulting 1D probability functions out to  $\pm 34.1\%$  in each direction. The best-fit peculiar velocities and corresponding 68.2% confidence intervals are presenting in Table 4.5. We find a mean peculiar velocity  $\langle v_p \rangle = 230 \pm 330 \text{ km s}^{-1}$ , consistent with the limits of  $72 \pm 60 \text{ km s}^{-1}$  found by Planck Collaboration et al. (2013 XIII) using the variance of the CMB towards X-ray detected



Table 4.5. SZE properties

Name	$T_e$ (keV)	$v_p$ (km s <sup>-1</sup> )	$S_{345}(< \theta_{500c})$ (mJy)	$Y_{500c}^a$ (10 <sup>-10</sup> sr)	S/N <sup>b</sup>
S/N $\geq 3.5$					
ACT-CL J0102–4915	6.6 <sup>c</sup>	400 <sup>+500</sup> <sub>-500</sub>	340 ± 73	1.5 ± 0.2	6.6
ACT-CL J0215–5212	5.0	-300 <sup>+1100</sup> <sub>-600</sub>	202 ± 76	1.1 ± 0.5	5.0
ACT-CL J0438–5419	5.0	300 <sup>+600</sup> <sub>-600</sub>	99 ± 98	0.7 ± 0.7	4.3
ACT-CL J0546–5345	8.54 <sup>+1.38</sup> <sub>-1.05</sub> <sup>d</sup>	-600 <sup>+700</sup> <sub>-700</sub>	185 ± 33	1.1 ± 0.2	5.3
ACT-CL J0616–5227	5.0	-500 <sup>+600</sup> <sub>-600</sub>	243 ± 57	1.4 ± 0.4	4.5
ACT-CL J0658–5557	10.8 ± 0.9 <sup>e</sup>	3000 <sup>+1200</sup> <sub>-900</sub>	134 ± 93	1.3 ± 1.0	3.5
S/N < 3.5					
ACT-CL J0232–5257	5.0	-200 <sup>+1500</sup> <sub>-1500</sub>	55 ± 50	0.3 ± 0.4	1.9
ACT-CL J0235–5121	5.0	400 <sup>+2200</sup> <sub>-2200</sub>	37 ± 139	0.2 ± 1.3	0.7
ACT-CL J0245–5302	5.0	700 <sup>+1100</sup> <sub>-700</sub>	26 ± 92	0.2 ± 0.8	1.4
ACT-CL J0330–5227	4.32 <sup>+0.21</sup> <sub>-0.19</sub> <sup>d</sup>	300 <sup>+1200</sup> <sub>-1200</sub>	32 ± 105	0.2 ± 0.9	1.9
ACT-CL J0559–5249	8.09 ± 0.75 <sup>d</sup>	-900 <sup>+1800</sup> <sub>-1800</sub>	21 ± 120	0.1 ± 0.8	1.2

<sup>a</sup>For clusters with unknown  $T_e$ ,  $Y_{500c}$  is computed assuming  $T_e = 5.0$  keV.

<sup>b</sup>S/N based on integrated  $S_{345}$  inside  $Y'_{SZ}$  apertures using the point-source subtracted iteratively-reduced maps.

<sup>c</sup>El Gordo has an integrated X-ray temperature of  $14.5 \pm 0.1$  keV (Menanteau et al., 2012). However, we adopt the lower temperature of El Gordo’s cold “bullet” (6.6 keV; Menanteau et al., 2012) in this analysis because it provides a significantly better quality of fit (e.g., see Figure 4.10).

<sup>d</sup>Menanteau et al. (2010)

<sup>e</sup>Mass-weighted temperature from Halverson et al. (2009)

clusters.

Figure 4.10 shows the best-fit SZE spectra for all clusters, with the  $\chi^2$  per degree of freedom ( $\chi^2/\nu$ ) and  $p$  values indicated in the panels. The fits for El Gordo assuming the integrated X-ray gas temperature  $kT_e = 14.5$  keV, and also the minimum value found in El Gordo’s “cold bullet”  $kT_e = 6.6$  keV (Menanteau et al., 2012), are shown in the first panel. We find that  $kT_e = 6.6$  keV ( $\chi^2/\nu = 2.5/3$ ) provides a better fit to the data than 14.5 keV ( $\chi^2/\nu = 6.8/3$ ;  $v_p = 1300 \pm 1100$  km s $^{-1}$ ). Figure 4.11 shows the likelihood parameter-space of El Gordo’s fit assuming  $kT_e = 6.6$  keV (Menanteau et al., 2012) when we use only ACT+LABOCA data, and when we include *Herschel* SPIRE 350  $\mu$ m and 500  $\mu$ m data as well. The SPIRE data points significantly improve constraints on the electron optical depth  $\tau$  through  $Y'_{\text{SZ}}$ .

Our data favor the lower temperature of 6.6 keV for the violent merger system El Gordo. This result is similar to that of Halverson et al. (2009), who determine that the mass-weighted SZE temperature measured for the Bullet cluster ( $10.8 \pm 0.9$  keV; Halverson et al., 2009) is significantly lower than that derived from the X-ray (13.9 keV; Govoni et al., 2004). When using the SZ-temperature from Halverson et al. (2009), we derive a large peculiar velocity for the Bullet cluster of  $3000^{+1200}_{-900}$  km s $^{-1}$  (Figure 4.10). This signal is unlikely to be caused by contamination of sources fainter than  $S_{345} < 10$  mJy, because positive signal contamination acts to push  $v_{\text{pec}}$  to more negative values. In the Bullet cluster, Markevitch (2006) find a central “bullet” collision velocity of 4700 km s $^{-1}$ . Our signal may be due to a kSZ distortion related to this high-velocity subcomponent, similar to the findings of Mroczkowski et al. (2012) in MACS J0717.5+3745.

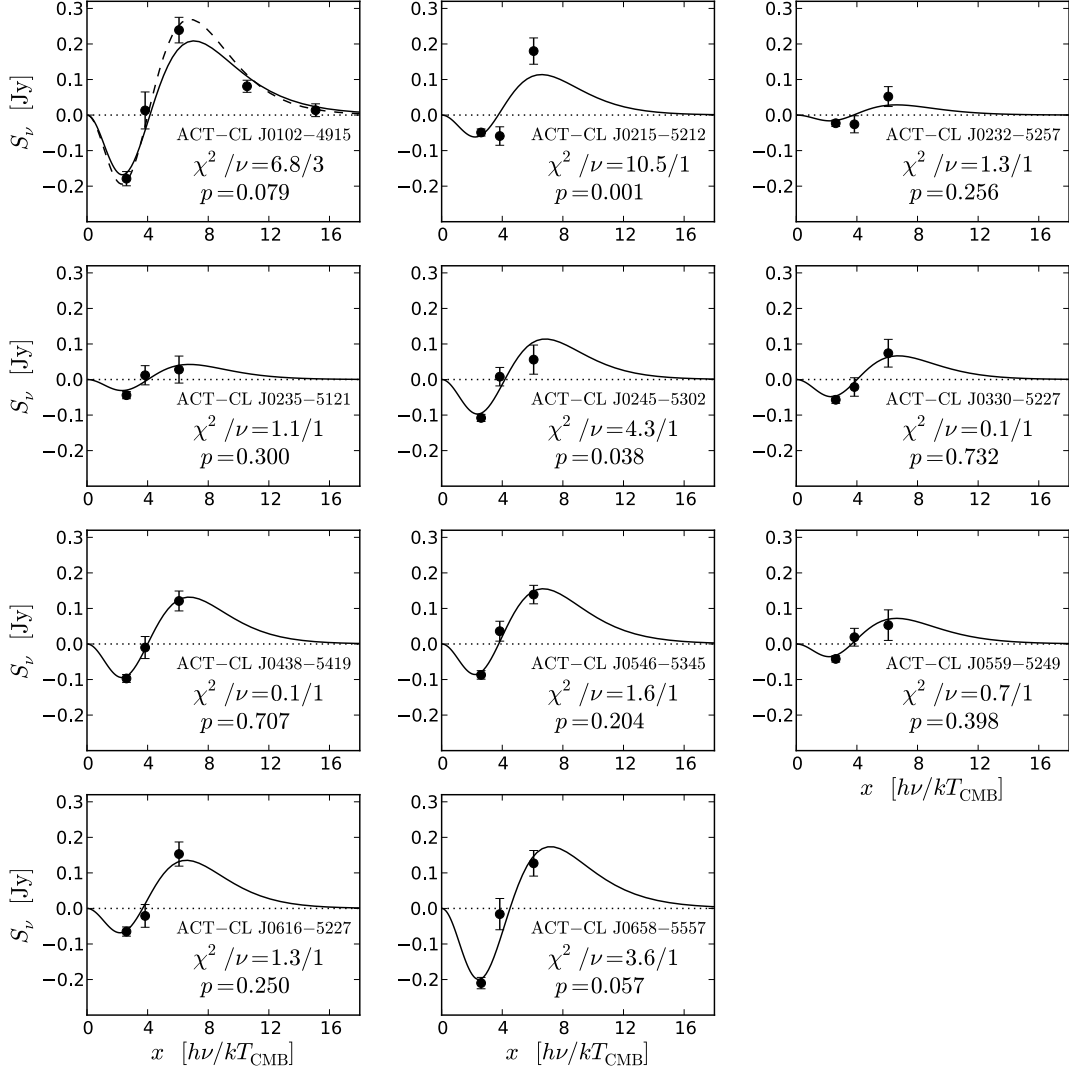


Figure 4.10: Best-fit SZE spectra for all 11 clusters with the fit quality ( $\chi^2/\nu$ ) for each solid curve indicated in the panels. The solid and dashed curves in the first panel represent the best-fit parametrization when assuming  $kT_e = 14.5$  keV and 6.6 keV, respectively (for  $kT_e = 6.6$  keV,  $\chi^2/\nu=2.5/3$ ). From left to right, the data points are ACT 148 GHz, ACT 218 GHz, LABOCA 345 GHz, (and for ACT-CJ J0102–4915) SPIRE 500  $\mu\text{m}$ , and SPIRE 350  $\mu\text{m}$ .

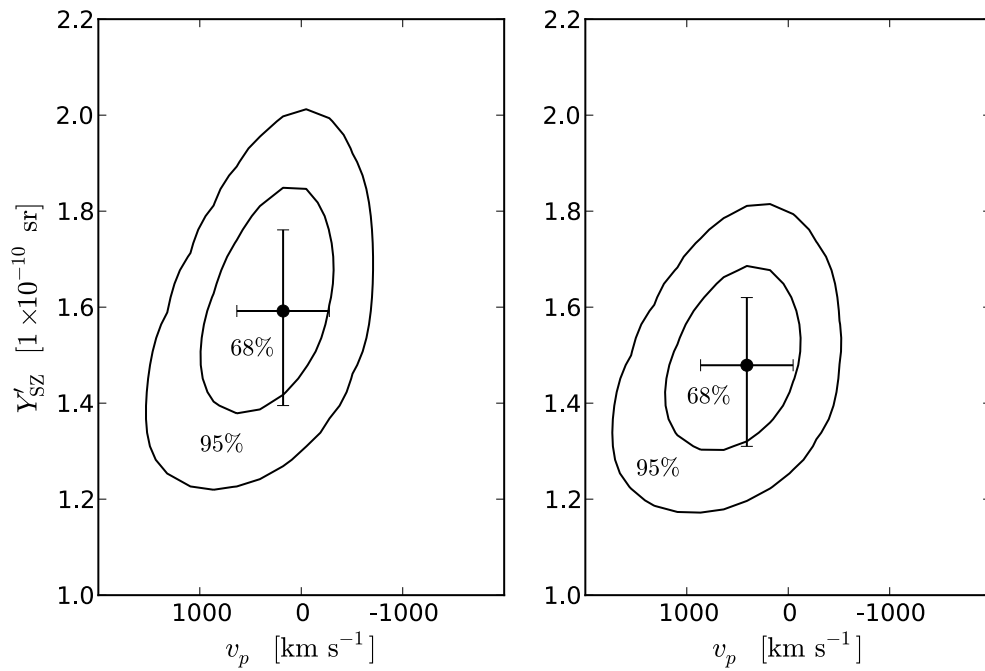


Figure 4.11: Likelihood space of  $Y'_{SZ}$  vs.  $v_p$  for ACT J0102-4915 when using only ACT+LABOCA data (*left*) and when including SPIRE 500  $\mu\text{m}$  and 350  $\mu\text{m}$  data (*right*). The black points and error bars represent the marginalized maximum likelihood values and 68% confidence intervals.

## 4.6 Conclusions

We present new high-resolution 345 GHz LABOCA and 2.1 GHz ATCA imaging of eleven massive SZE-selected clusters from the ACT southern survey (Marriage et al., 2011; Menanteau et al., 2010). We use these data to constrain the levels of radio source and SMG contamination of the SZE signals of the clusters, and also to constrain the cluster peculiar velocities using the kSZ effect.

We find that the contamination from 2.1 GHz radio sources in the SZE decrement is small, at a level of  $S_\nu = 0.5$  mJy per cluster, or only  $\sim 0.6\%$  of the SZE decrement signal in our analysis. In contrast, the typical contamination from bright, unresolved SMGs is significant compared to the SZE signals, with per-cluster typical contaminating fluxes of  $21_{-18}^{+49}$  mJy per cluster at 345 GHz, which is  $15_{-13}^{+36}\%$  and  $2_{-2}^{+6}\%$  of the SZE increment and decrement signals, respectively. This contamination may contribute to the scatter found in the  $Y_{\text{SZ}}$ -to-mass scaling relation of SZE clusters.

After subtraction of the bright SMGs, we use our multi-band data to constrain the peculiar velocities of the clusters and find  $\langle v_p \rangle = 230 \pm 330 \text{ km s}^{-1}$ . For clusters with high significance SZE detections, the typical uncertainty in  $v_p$  is  $\pm 700 \text{ km s}^{-1}$ . We place the tightest constraints on the notable cluster merger ACT-CL J0102–4915 (Menanteau et al., 2012), for which we have additional SPIRE photometry available. For this system, we find  $v_p = 400_{-500}^{+500} \text{ km s}^{-1}$ .

## 4.7 Appendix

### 4.7.1 “La Flaca” and El Gordo

El Gordo has two bright point sources projected at small clustercentric radii, the brighter of the two ( $S_\nu = 36 \pm 2$  mJy) we refer to as “La Flaca.” La Flaca is located at  $\alpha = 15.732207^\circ$   $\delta = -49.252415^\circ$  and has an extremely faint radio counterpart

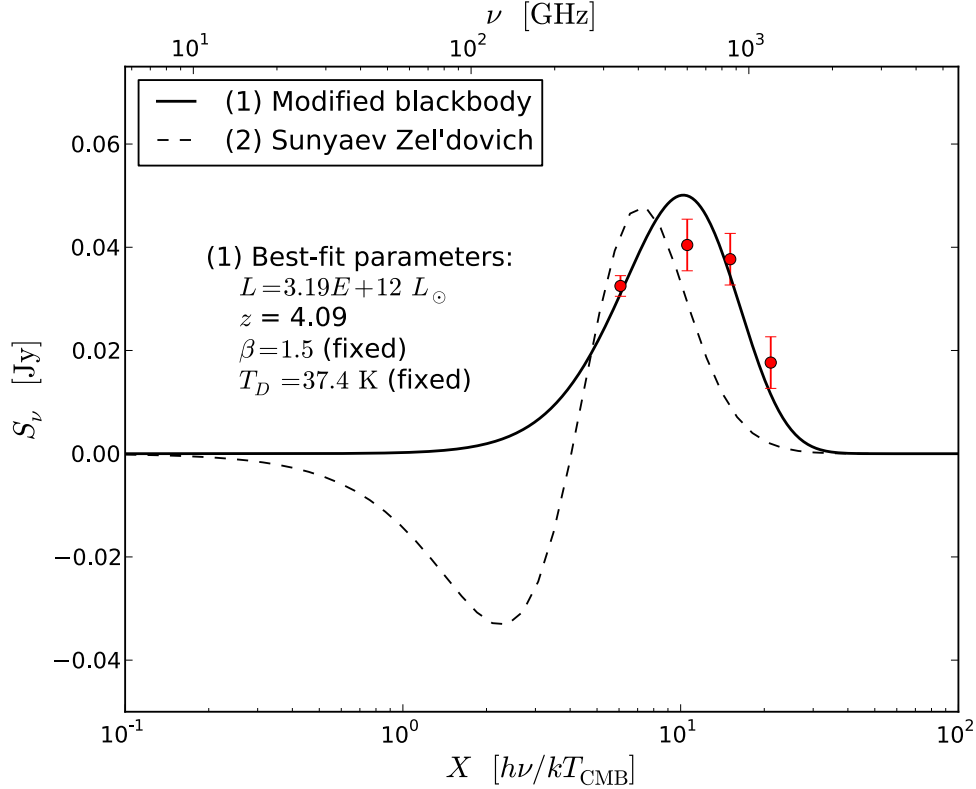


Figure 4.12: Observed photometry and best-fit thermal and SZE spectra for J010256–491509 (“La Flaca”). From left to right, the red points represent LABOCA 345 GHz and SPIRE 500  $\mu\text{m}$ , 350  $\mu\text{m}$ , and 250  $\mu\text{m}$  data. The solid black line represents the least-squares fit to the data using a modified black-body spectrum with fixed parameters  $T_d = 37.4\text{ K}$  and  $\beta = 1.5$ , which are adopted from Wardlow et al. (2011). The best fit redshift and infrared luminosity are  $z = 4.09$  and  $L_{\text{IR}} = 3.19 \times 10^{12} L_{\odot}$ . The dashed curve represents the best-fitting thermal SZE SED assuming  $T_e = 25\text{ keV}$ , which is formally unsatisfactory.

with  $S_{2.1} = 24 \pm 7\ \mu\text{Jy}$ . To test the possibility that La Flaca is a local SZE enhancement, we compare the spectral fits of the source’s LABOCA+SPIRE photometry using a modified black body spectrum and thermal SZE spectrum. Figure 4.12 shows the best-fit curves for each model. We find that the SZE spectral shape is incompatible with the data, therefore La Flaca is more likely to be a high-redshift dusty star-forming galaxy rather than a compact SZE enhancement.

The best-fit modified Planck function parameters are  $z = 4.1$  and  $L_{\text{IR}} = 3.2 \times 10^{12} L_{\odot}$ , assuming the median observed  $T_D = 37.4\text{ K}$  and  $\beta = 1.5$  from the LABOCA

Extended-CDFS SMG survey (LESS; Weiß et al., 2009; Wardlow et al., 2011). Using the 610 MHz image, we derive a radio spectral index of  $\alpha \sim -1.3$ , giving a Carilli & Yun (1999) radio-to-far IR spectral index redshift estimate of  $z = 4.0$ , in agreement with that of the spectral fit and further evidence that La Flaca is a high-redshift SMG.

## Chapter 5

### The Radio Halo and Relics of El Gordo, a Massive $z = 0.870$ Cluster Merger

#### 5.1 Introduction

Galaxy clusters grow out of peaks in the primordial matter distribution of the early Universe and gain mass by accreting gas from their environment and by merging with other clusters and groups of galaxies. Because the physical properties and dynamical state of the intracluster medium (ICM) are affected by its merger history, observations of the ICM can be used to study clusters' growth and evolution. Cluster mergers can inject large amounts of gravitational potential energy ( $\sim 10^{64}$  erg) into the ICM, and observations of cluster-scale radio synchrotron emission, particularly in merging and dynamically disturbed systems (Cassano et al., 2011), indicate that some fraction of this energy is directed into accelerating cosmic ray electrons to ultra-relativistic ( $\gamma \sim 10^3$ – $10^4$ ) energies. The resulting non-thermal radio emission is seen as a radio halo, i.e., diffuse axisymmetric emission centered on the cluster, or as radio relics, narrow, extended, filamentary structures located near the cluster outskirts (for reviews, see Ferrari et al. 2008 and Feretti et al. 2012). By studying the spectral, morphological, and polarization properties of radio halos and relics, we can probe the poorly understood non-thermal properties of galaxy clusters like cosmic ray acceleration and magnetic field profiles. The geometry of relic systems can also be used to constrain the collision parameters of cluster mergers (van Weeren et al., 2011a).



One challenge in using relics and halos to probe the energy content and magnetic field properties of clusters is their relative rarity. Only  $\simeq 30\%$  of X-ray luminous clusters host halos (Cassano et al., 2011). Their presence is correlated with cluster mass and dynamical state, with the most massive and most dynamically disturbed clusters showing the highest frequencies of halos and relics. Large radio relics, arcs with lengths  $\geq 1$  Mpc, are found only in massive, merging clusters, and even rarer double-relic systems are found only in binary cluster mergers occurring in the plane of the sky.

The paucity of massive high-redshift clusters combined with the steep observed spectral index<sup>1</sup>  $\alpha$  of the non-thermal emission ( $\alpha \simeq 1.5$ ; Ferrari et al., 2008) make the study of halos and relics at high redshifts especially difficult. Additionally, energy losses of the relativistic electrons to cosmic microwave background photons through inverse Compton scattering are expected to reduce the radiative lifetimes, and therefore detectability, of synchrotron-emitting regions. Because of the above limitations, catalogs of known radio halo and relic clusters only extend to low redshifts; the highest-redshift halo cluster discovered to date is MACS0717.5+3745 ( $z = 0.546$ ; van Weeren et al., 2009). Nuza et al. (2012) predict that many more  $z > 0.3$  relics should exist than are currently catalogued, with the deficit likely due to lack of observations. To understand the nature of non-thermal emission in clusters throughout cosmic time, we need to increase the sample of known relics and halos at high redshift.

In this work, we present new 610 MHz and 2.1 GHz observations of the extremely massive,  $z = 0.870$  cluster ACT-CL J0102-4915 (also known as “El Gordo,” and hereafter referred to by that name; Menanteau et al., 2012), which reveal an associated radio halo and double radio relics. As the highest redshift radio-halo cluster now known, El Gordo can help fill in the gaps in our knowledge about non-thermal cluster physics

---

<sup>1</sup>  $S_\nu \propto \nu^{-\alpha}$

at high redshift when the Universe was only half its current age. Section 5.2 describes El Gordo, Section 5.3 describes our observations and data reduction algorithms, Sections 5.4 and 5.5 present our analyses of and results for the relics and halo, respectively, and Section 5.6 presents our conclusions. In our calculations, we assume a *WMAP* cosmology with  $H_0 = 70 \text{ km s}^{-1} \text{ Mpc}^{-1}$ ,  $\Omega_M = 0.27$ , and  $\Omega_\lambda = 0.73$  (Komatsu et al., 2011). At  $z = 0.870$ ,  $D_A = 1618 \text{ Mpc}$ ,  $D_L = 5656 \text{ Mpc}$  and 1 arcmin corresponds to 0.47 Mpc.

## 5.2 ACT J0102-4915, “El Gordo”

El Gordo was discovered through its 148 GHz Sunyaev-Zel’dovich effect (SZE; Sunyaev & Zeldovich, 1972) decrement by the Atacama Cosmology Telescope (ACT; Fowler et al., 2007) collaboration. With a SZE centroid at  $01^{\text{h}}02^{\text{m}}53^{\text{s}} -49^{\circ}15'19''$  (J2000) and the strongest SZE signal in the  $455 \text{ deg}^2$  southern ACT survey (Marriage et al., 2011), El Gordo was optically confirmed as a bona fide galaxy cluster at  $z = 0.870$  (Menanteau et al., 2010) with a “bullet”-like merger morphology revealed in *Chandra* X-ray imaging (Menanteau et al., 2012). El Gordo’s collision axis, identified by elongation in the X-ray surface brightness and the relative positions of two optical galaxy density peaks, is in the northwest-to-southeast direction at a position angle of  $136^\circ$  (Menanteau et al., 2012). Based on the morphology and galaxy velocity distribution, Menanteau et al. (2012) predict the inclination angle (between the collision axis and the plane of the sky)  $\phi$  to be shallow, in the range  $\phi = 0\text{--}30^\circ$ . The cluster is also the most significant detection in the (overlapping)  $2500 \text{ deg}^2$  survey (Williams et al., 2011) of the South Pole Telescope (SPT; Carlstrom et al., 2011). El Gordo has an observed-frame 0.5–2.0 keV X-ray luminosity of  $L_X = (2.19 \pm 0.11) \times 10^{45} h_{70}^{-2} \text{ erg s}^{-1}$  and an integrated X-ray temperature of  $k_B T_{\text{gas}} = 14.5 \pm 0.1 \text{ keV}$  (Menanteau et al., 2012). By combining X-ray, SZE, and velocity dispersion measurements, Menanteau et al. (2012) estimate a

Table 5.1. Radio observations

Telescope	Frequency (GHz)	Configuration	Obs date	$t_{\text{obs}}$ (hr)
ATCA	2.1GHz	6A	Dec 2011	12
		1.5B	April 2012	8
GMRT	610MHz	fixed	Aug 2012	12

total mass<sup>2</sup> within  $r_{500c}$ , the radius containing  $500\times$  the critical density of the universe, of  $M_{500c} = (1.17 \pm 0.17) \times 10^{15} h_{70}^{-1} M_{\odot}$ .

### 5.3 Observations and data reduction

#### 5.3.1 2.1 GHz ATCA

We used the Australia Telescope Compact Array (ATCA) to acquire 2.1GHz imaging of El Gordo. The Compact Array Broadband Backend (CABB; Wilson et al., 2011) has 2048 1 MHz-wide channels that span 1.1–3.1 GHz. The observations were obtained in two installments (see Table 5.1): 12 hours in the extended 6A configuration in December 2011 (PI: Baker), and 8 hours in the compact 1.5B configuration in April 2012 (PI: Lindner). Calibration used the flat-spectrum radio-loud quasars PKS 1934-638 (band-pass and flux calibration) and PKS 0047-579 (initial phase calibration). Observations of PKS 1934-638 bracketed each observing session, while phase tracking observations of PKS 0047-579 were taken every 30 minutes. We used the software package MIRIAD (Sault et al., 1995) to calibrate, flag, invert, and clean the visibility data.

Radio frequency interference (RFI) is significant in the 2.1 GHz band at the ATCA. We removed RFI from the data both manually using the MIRIAD tasks `pgflag` and

<sup>2</sup> The mass estimate assumes a conversion factor  $f = M_{200a}/M_{500c} = 1.85$  (Menanteau et al., 2012).

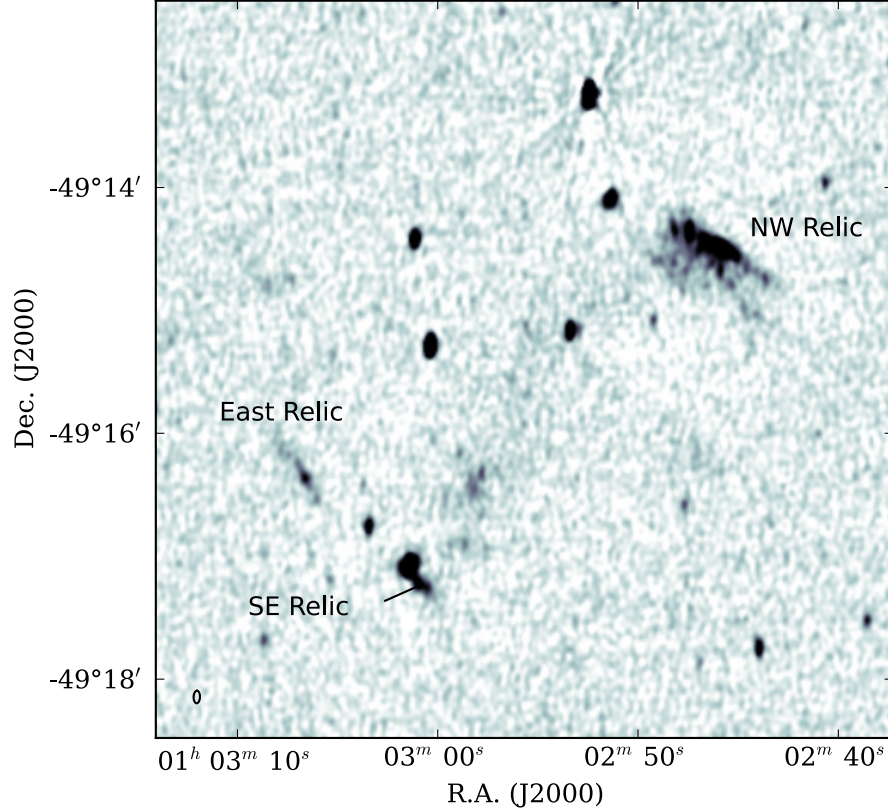


Figure 5.1: 2.1 GHz ATCA image of El Gordo. The color stretch is  $[-80, 80] \mu\text{Jy beam}^{-1}$ . Labels mark the locations of the NW, SE, and E relics. The synthesized beam is shown in the lower left corner.

`blflag`, and automatically using the MIRIAD task `mirflag` (Middelberg, 2006). Baseline 1–2 in the 2012 observations contained powerful broad-spectrum RFI and was entirely flagged. In total, 22% of visibilities were flagged. We produced continuum images using multi-frequency synthesis (MFS) with tasks `invert` and `mfclean`. The data were then self-calibrated, first allowing the phase to vary, then phase and amplitude together. The final image was made with `robust=0` *uv* weighting, giving a synthesized beam with dimensions  $6.1'' \times 3.1''$  and a position angle  $\text{PA} = -1.9^\circ$ . The image RMS noise at phase center is  $\sigma_{2.1} = 8.2 \mu\text{Jy beam}^{-1}$  for an effective frequency of  $\nu = 2.15 \text{ GHz}$ . The 2.1 GHz map of El Gordo is shown in Figure 5.1.

The 2011 and 2012 observations have parallactic angle coverages of  $120^\circ$  and  $230^\circ$ ,

respectively. Schnitzeler et al. (2011) note that the instrumental polarization leakage across the CABB bandpass varies with frequency. Therefore, during gain calibration, we solved for leakage corrections separately in each of eight 256 MHz-wide subbands using the `gpcal` option `nfbn`.

### 5.3.2 610 MHz GMRT

We used the 30-antenna Giant Metre-wave Radio Telescope (GMRT) to acquire 610 MHz imaging of El Gordo. Observations were carried out in August 2012 (PI: Lindner) in three four-hour tracks. The data have 256 130 kHz-wide channels for a total bandwidth of 33 MHz and an effective frequency of 607.7 MHz. The  $uv$  data were calibrated and imaged using the Common Astronomy Software Applications (CASA) package (Version 4.0.0)<sup>3</sup>. Tracks were visually inspected to remove powerful RFI spikes that were constant in either time or channel, and transient RFI signals were removed using the automated flagging algorithm AOFLAGGER (Offringa et al., 2010, 2012).

The non-coplanar  $uv$  dataset was imaged using three facets and 512  $w$ -projection planes. The final self-calibrated map is shown in Figure 5.2 and has an RMS sensitivity of  $\sigma_{610} = 26 \mu\text{Jy beam}^{-1}$  and a synthesized beam of  $11.0'' \times 4.0''$  at position angle  $-4.3^\circ$ . The elongated synthesized beam is due to the low maximum elevation ( $\simeq 20^\circ$ ) when El Gordo is observed from the GMRT site.

## 5.4 Radio relics

Menanteau et al. (2012) identified two 843 MHz sources on opposite sides of El Gordo in the archival data from the Sydney University Molonglo Sky Survey (SUMSS; Mauch et al., 2003) that were aligned with the collision axis and coincided with the locations of possibly shocked thermal gas, as traced by an unsharp-masked image of the *Chandra*

---

<sup>3</sup> <http://casa.nrao.edu/>

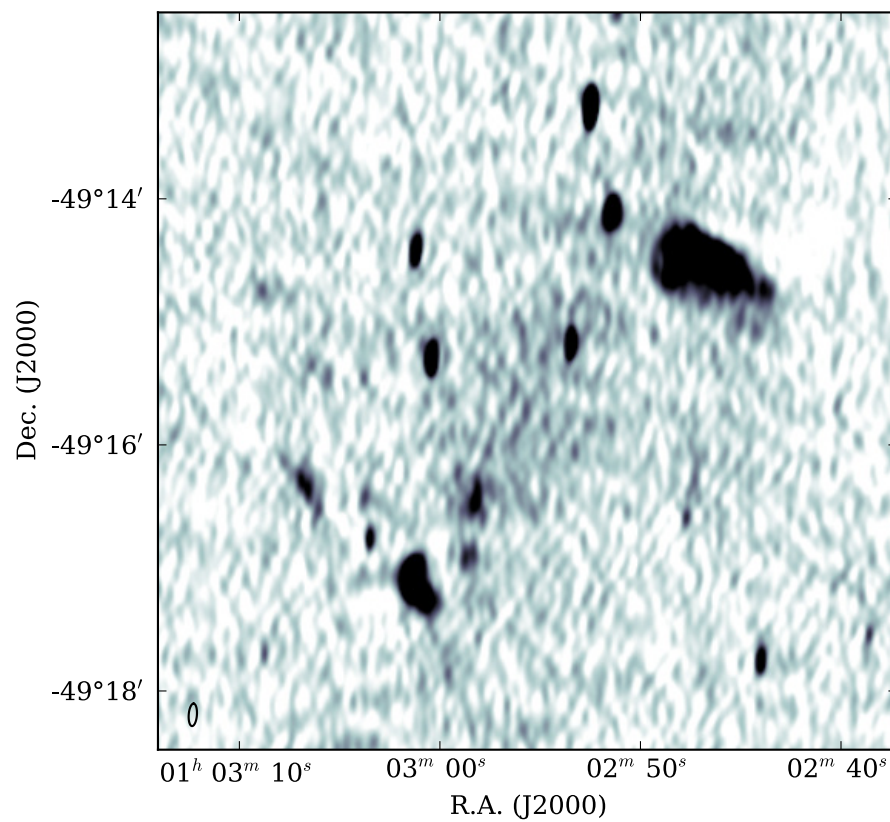


Figure 5.2: 610 GHz GMRT image of El Gordo. The color stretch is  $[-30, 300] \mu\text{Jy beam}^{-1}$ . The synthesized beam is shown in the lower left corner.

0.5–2.0 keV X-ray map. This morphology is the signature arrangement of well-studied double radio relics in binary major cluster mergers at lower redshifts (e.g., van Weeren et al., 2011b). Table 5.2 lists the photometric properties of the relics.

#### 5.4.1 Geometries

Our high-resolution imaging reveals the northwest SUMSS source to be an extended radio relic (hereafter referred to as the NW relic), which is resolved in both length and width by our observations. The NW relic has a total width of  $34''$  (0.27 Mpc), and a bright, unresolved ridge of emission on its northeast outer edge. The internal structure of the NW relic is complex, and contains a trailing unresolved filament that is extended in a direction that is offset from the angle of the NW relic leading edge. The flux from the southeast SUMSS source is due to a compact radio source ( $S_{2.1} = 1.3$  mJy) superposed on a much fainter extended emission component, which we interpret as a likely radio relic (hereafter referred to as the SE relic). A third component of extended filamentary emission located  $\sim 1'$  northeast of the SE relic we will refer to as the E relic. The E and SE relics and the bright leading edge of the NW relic are all unresolved by our observations, indicating very narrow shocked regions of  $d_{\text{shock}} \leq 23$  kpc. The elongation direction for all relics is perpendicular to the collision axis, suggesting they are created by shock waves in the ICM of the cluster merger (Ensslin et al., 1998).

#### 5.4.2 Spectral indices

Our multi-wavelength data allow us to produce a 610 MHz/2.1 GHz spectral index ( $\alpha_{610}^{2.1}$ ) map using the full GMRT and ATCA images, and a 1.6 GHz/2.6 GHz spectral index ( $\alpha_{1.6}^{2.6}$ ) map using the upper and lower halves (1.1 – 2.1 and 2.1 – 3.1 GHz) of the ATCA bandpass. We need not worry about the recovery of large-scale emission in the relics because the largest linear size of the larger NW relic ( $1.3'$ ) is still smaller than the

Table 5.2. Relic and halo properties

Name	R.A. h:m:s	Dec. o : ' : "	$S_{610}$ (mJy)	$S_{843}^a$ (mJy)	$S_{2100}$ (mJy)	$\alpha_{610}^{2100}$	$\alpha_{1.6}^{2.6}$
NW Relic	01 : 02 : 46	-49 : 14 : 43	$19.4 \pm 0.17$	18.2	$4.3 \pm 0.1$	$1.22 \pm 0.01$	$1.98 \pm 0.09$
E Relic	01 : 03 : 07	-49 : 16 : 16	$1.22 \pm 0.09$	-	$0.41 \pm 0.03$	$0.88 \pm 0.08$	$1.1 \pm 0.4$
SE Relic	01 : 03 : 01	-49 : 17 : 14	-	-	-	-	-
Halo	01 : 02 : 55	-49 : 15 : 37	$28.4 \pm 0.59^b$	-	$2.12 \pm 0.07$	$1.24 \pm 0.03$	-

<sup>a</sup>Flux density from SUMSS (Mauch et al., 2003)<sup>b</sup>After folding through the ATCA  $uv$  coverage,  $S_{610} = 9.8 \pm 0.1$  mJy.



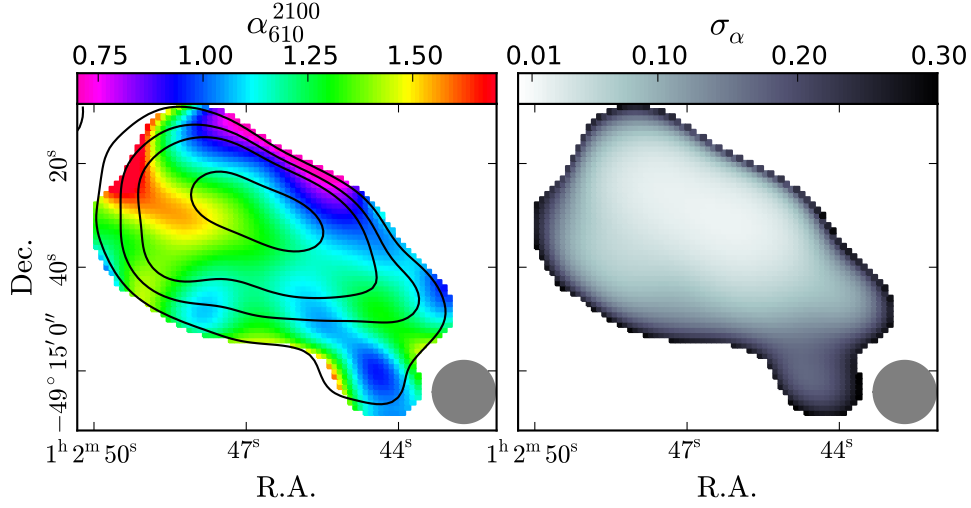


Figure 5.3: Spectral index ( $\alpha_{610}^{2.1}$ ) map of the NW relic (left) and corresponding uncertainty (right). Contours=[0.3,0.6,1.0,3.0] mJy beam<sup>-1</sup>. The filled grey circle represents the effective resolution (12'').

angular scale on which we expect the ATCA to begin resolving out emission ( $\gtrsim 1.9'$ ) given the minimum  $uv$  distance (1.8 k $\lambda$ ) of the high-frequency end of the bandpass. The GMRT data extend to a lower  $uv$  distance and preserve emission on scales even larger than the cluster. The pairs of images were smoothed to a common circular beam (11'' for  $\alpha_{2.1}^{610}$  and 8'' for  $\alpha_{1.6}^{2.6}$ ) and then clipped at a  $4\sigma$  level before we computed the spectral index  $\alpha = -\log(S_{\nu_1}/S_{\nu_2})/\log(\nu_1/\nu_2)$ .

Figures 5.3 and 5.4 present the  $\alpha_{610}^{2.1}$  and  $\alpha_{1.6}^{2.6}$  spectral index maps of the NW relic. The integrated spectral indices are  $\langle \alpha_{610}^{2.1} \rangle = 1.22 \pm 0.01$  and  $\langle \alpha_{1.6}^{2.6} \rangle = 1.98 \pm 0.09$ . Figure 5.5 shows  $\alpha_{610}^{2.1}$  for the the E and SE relics. The E relic has integrated spectral index values of  $\langle \alpha_{610}^{2.1} \rangle = 0.88 \pm 0.08$  and  $\langle \alpha_{1.6}^{2.6} \rangle = 1.1 \pm 0.4$ . For both the NW and E relics,  $\alpha_{1.6}^{2.6}$  is steeper than  $\alpha_{610}^{2.1}$  due to spectral aging effects. The E relic resembles the leading edge of the NW relic in its narrow width and flatter spectral index, which are likely due to decreased projection effects and recent energy injection.

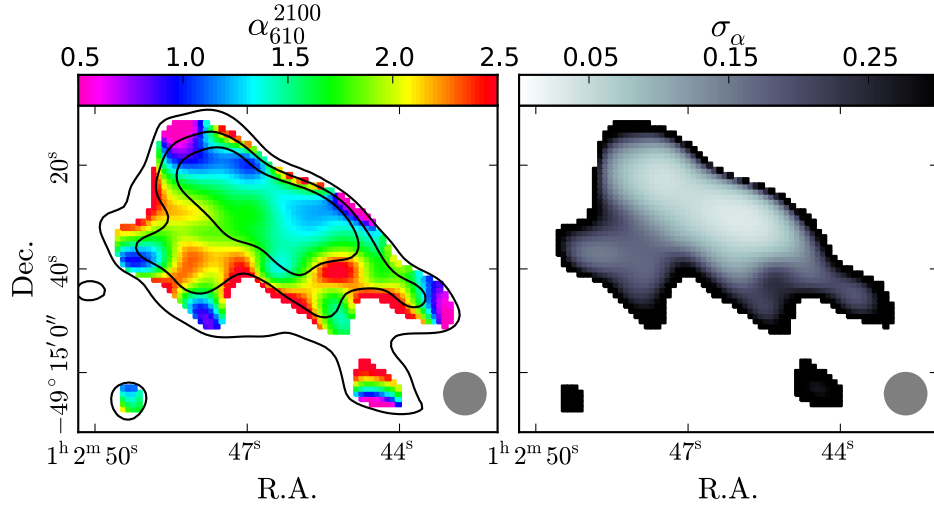


Figure 5.4: Spectral index ( $\alpha_{1.6}^{2.6}$ ) map of the NW relic (left) and corresponding uncertainty (right). Contours represent 2.1 GHz intensity levels of 30, 100, and 200  $\mu\text{Jy beam}^{-1}$ . The grey circle represents the effective resolution (8'').

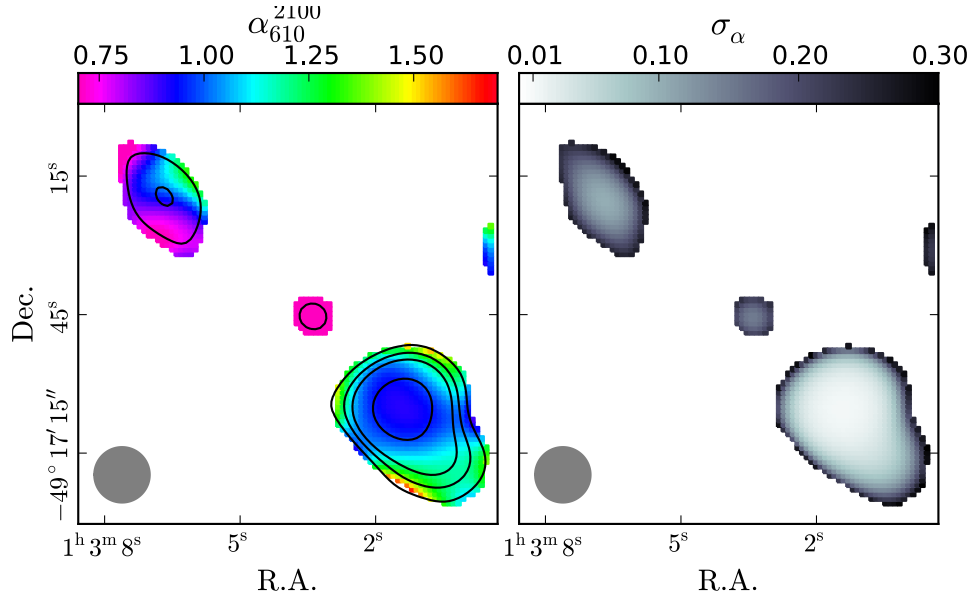


Figure 5.5: Spectral index ( $\alpha_{610}^{2.1}$ ) map of the E and SE relics (left) and uncertainties (right). Contours represent 610 MHz intensity levels of [0.3, 0.6, 1.0, 3.0] mJy beam $^{-1}$ . The grey circle represents the effective resolution (12'').

### 5.4.3 Rotation measure and $B_{\parallel}$

Magnetized plasma along the line of sight to polarized emission will cause Faraday rotation of the polarization angle of the emitted photons by an amount  $\Delta\Psi = \text{RM} \times \lambda^2$ , where  $\Psi$  is the polarization angle ( $\Psi = 0.5 \tan^{-1}(U/Q)$ ),  $\lambda$  is the wavelength of observation, and RM is the rotation measure (RM). Our wide bandwidth, full polarization ATCA data allow us to measure the RM through the cluster outskirts to the polarized relic signal and constrain the integrated product of the parallel component of the magnetic field and the free electron density at a projected distance of  $\sim 1$  Mpc from the cluster center. For a single source of polarized emission, the rotation measure is equal to the Faraday depth  $\phi = 0.81 \int_{\text{source}}^{\text{observer}} n_e B_{\parallel} dl$  (Burn, 1966), with  $B_{\parallel}$  in  $\mu\text{G}$ ,  $n_e$  in  $\text{cm}^{-3}$ , and  $dl$  in pc. To avoid “ $n\pi$ ” errors and to allow for the detection of multiple RM components, we compute the Faraday spectrum, the complex polarized surface brightness per unit Faraday depth  $F(\phi)$  [ $\text{Jy beam}^{-1} \phi^{-1}$ ], using the RM synthesis algorithm (Brentjens & de Bruyn, 2005) as implemented by the Astronomical Image Processing System (AIPS<sup>4</sup>) in the task **FARS**.

We first produced 10 MHz-wide  $Q$  and  $U$  images with  $3''$  pixels, which were then individually corrected for the varying primary beam attenuation across the wide CABB bandwidth, smoothed to a common resolution with a circular synthesized beam of FWHM  $11''$ , and assembled into a single data cube before running **FARS**. The region of maximum sensitivity is a circle with radius  $\sim 14'$ , entirely covering the cluster, which is set by the high-frequency end of the bandpass. The 10 MHz-wide channel maps were then weighted by the inverse variance of the noise within a central  $8'$  box. The effective  $\langle \lambda^2 \rangle$  of the data is  $\langle \lambda^2 \rangle = 0.20 \text{ m}^2$ . The FWHM of the RM transfer function (RMTF), shown in Figure 5.6, is  $\delta_{\text{RM}} = 145 \text{ rad m}^{-2}$ .

The spatially-integrated rotation measure spectrum for the polarized emission in

---

<sup>4</sup> <http://www.aips.nrao.edu/>

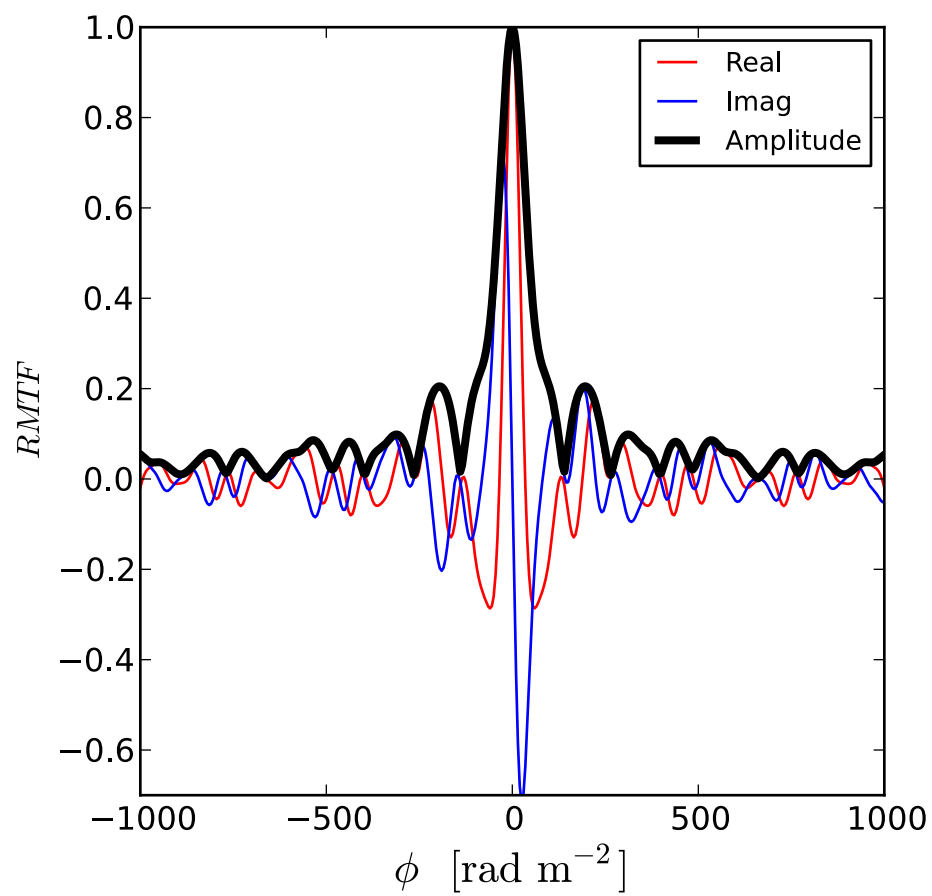


Figure 5.6: Rotation measure transfer function. The red and blue lines represent the real and imaginary components; the black line represents the total amplitude.

the NW relic is shown in Figure 5.7. We find that the polarized signal in each channel is consistent with a single, dominant Faraday component. Therefore, the polarized emission from the NW relic is likely originating from a single plane behind the magnetized plasma of the cluster and foreground material. We find no other significant Faraday components out to  $\pm 10^4 \text{ rad m}^{-2}$ . We next used the AIPS task **AFARS** to produce an image showing the RM value of the dominant component in each pixel across the relic (Figure 5.8). The RM values across the relic span a range from  $-5 \text{ rad m}^{-2}$  to  $+25 \text{ rad m}^{-2}$ . The uncertainty in each RM value is given by  $\sigma_{\text{RM}} = \delta_{\text{RM}}/(2 \times \text{SNR})$ . For the pixels shown in Figure 5.8,  $\sigma_{\text{RM}}$  lies in the range of  $5\text{--}10 \text{ rad m}^{-2}$ . Therefore, the spread in RM values significantly exceeds the width of the RMTF, and is likely reflecting the changing magnetic field strength and orientation ( $\int B_{\parallel} dl$ ) in the ICM.

The RM contribution from the Galaxy is estimated using the RM maps of Oppermann et al. (2012). Within a  $2^\circ$ -radius circle centered on El Gordo, the mean Galactic RM value is  $1.0 \text{ rad m}^{-2}$ , with a range between  $-0.1 \text{ rad m}^{-2}$  and  $+1.9 \text{ rad m}^{-2}$ . Therefore there is little fluctuation in RM values near El Gordo, however there may be a large systematic offset of  $\pm 8 \text{ rad m}^{-2}$ .

Recently, O’Sullivan et al. (2012) studied the Faraday spectra of four bright ( $> 1 \text{ Jy}$ ) radio-loud active galactic nuclei using the ATCA/CABB at  $2.1 \text{ GHz}$  and obtained RMTF widths of  $\delta_{\text{RM}} \simeq 60 \text{ rad m}^{-2}$ . In contrast, our goal of detecting the  $< 1 \text{ mJy}$  polarized emission from faint relic structure in El Gordo leaves us more susceptible to low-level RFI. RFI generally increases at low frequencies, thereby reducing the weights of the high- $\lambda^2$  coverage and increasing the width of the RMTF, given by  $\delta_{\text{RM}} = 2\sqrt{3}/(\lambda_{\text{max}}^2 - \lambda_{\text{min}}^2)$ . We note that when we use equal instead of inverse-variance weighting across the  $\lambda^2$  channels, our RMTF becomes significantly narrower with  $\delta_{\text{RM}} = 79 \text{ rad m}^{-2}$ , although the RM centroid uncertainties  $\sigma_{\text{RM}}$  are not improved due to the increased noise from including all low-frequency channels.

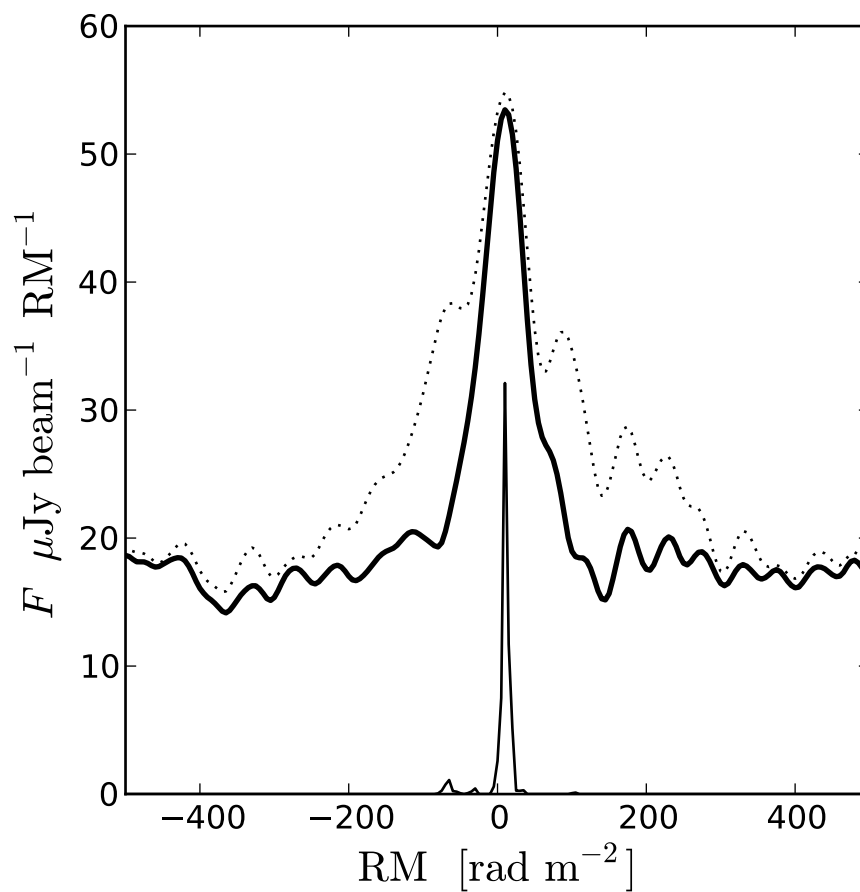


Figure 5.7: Integrated RM synthesis spectrum for the NW relic. The dotted and thick solid lines show the uncleaned and cleaned spectra, respectively. The thin solid line below represents the cleaned model components (amplitudes have been scaled by  $\times 3$  for visual clarity).

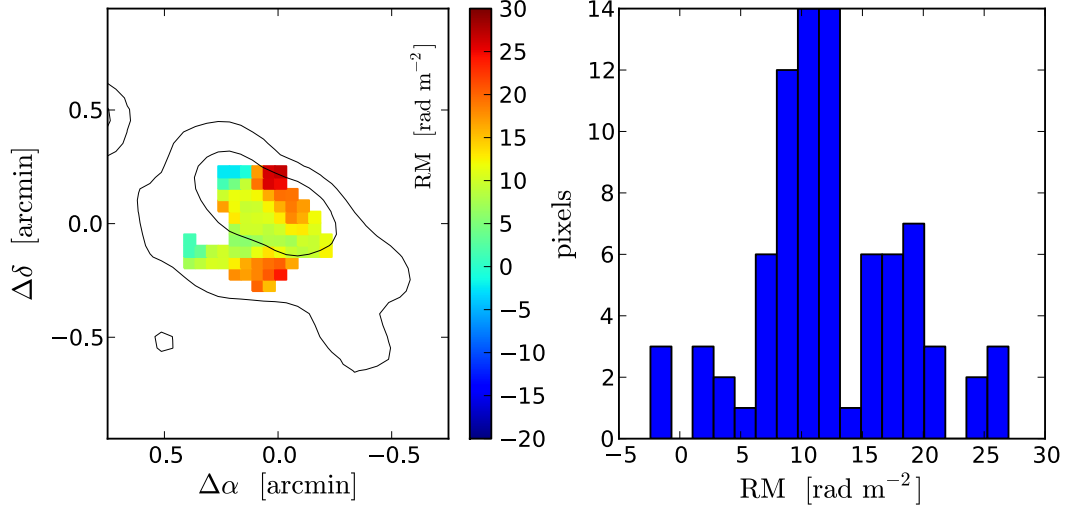


Figure 5.8: *Left:* RM value of dominant RM component in each pixel across the NW relic. RM values are clipped at  $> 3\sigma$  in the polarized signal image. Stokes  $I$  contours are shown at  $30$  and  $300 \mu\text{Jy beam}^{-1}$ . *Right:* Distribution of RM values in the left panel. The uncertainty in RM centroid of a given component ranges between  $5\text{--}10 \text{ rad m}^{-2}$ .

Based on the X-ray analysis of Menanteau et al. (2012), the electron density near the NW relic in the outskirts of El Gordo is  $n_e \simeq 2 \times 10^{-4} \text{ cm}^{-3}$ . To obtain an electron column density, we integrate for a line-of-sight distance equal to the radial offset of NW relic from the cluster center, 871 kpc. If we interpret the variation in RM across the relic as variation in the magnetic field in the vicinity of the relic, then the typical amplitude  $B_{\parallel} \sim 0.2 \mu\text{G}$ .

#### 5.4.4 Polarization

Highly polarized synchrotron emission is evidence of highly aligned magnetic fields in the emitting region. Such alignment can be caused by shocks sweeping up ICM material at the locations of radio relics. The total amplitude of linearly polarized emission  $P = \sqrt{Q^2 + U^2}$  and the total fractional polarization is given by  $f_P = P/I$ . Uncertainties in  $P$  and  $f_P$  follow a Rice distribution, which has non-zero mean. In our maps, we account for this bias using multiplication by a correction factor  $f_R =$

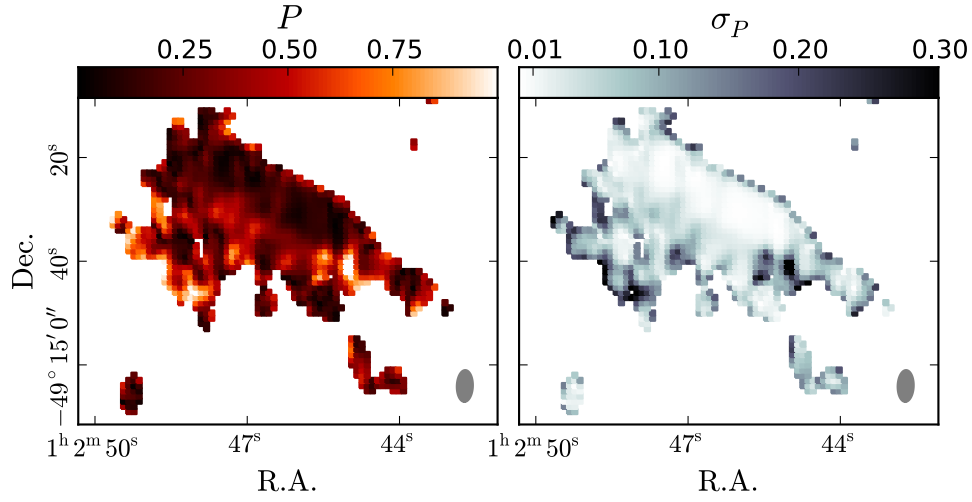


Figure 5.9: Polarization fraction  $f_P$  across the NW relic (left), with corresponding uncertainty (right).

$$\sqrt{1 - \text{SNR}^{-2}} \text{ (Wardle \& Kronberg, 1974).}$$

Figure 5.9 presents the fractional polarization across the NW relic. Polarization is lower at the leading edge of the shock and higher in the trailing regions, possibly due to increased alignment of the magnetic field in the post-shock region, projection effects, or to a steeper particle spectrum due to spectral aging in this area. The NW and E relics have similar integrated polarization values  $33 \pm 1\%$  and  $33 \pm 3\%$ , respectively.

We use the RM map to “derotate” the  $Q$  and  $U$  datasets to produce an image of the intrinsic polarization angle  $\Psi$  across the relic. Figure 5.10 shows the polarization angles after further rotation by  $90^\circ$  so that the line segments indicate the direction of the projected magnetic field. We find that the projected magnetic field is aligned with the relic’s elongation axis in the NW relic, and at least partially aligned in the weaker E and SE relics as well.



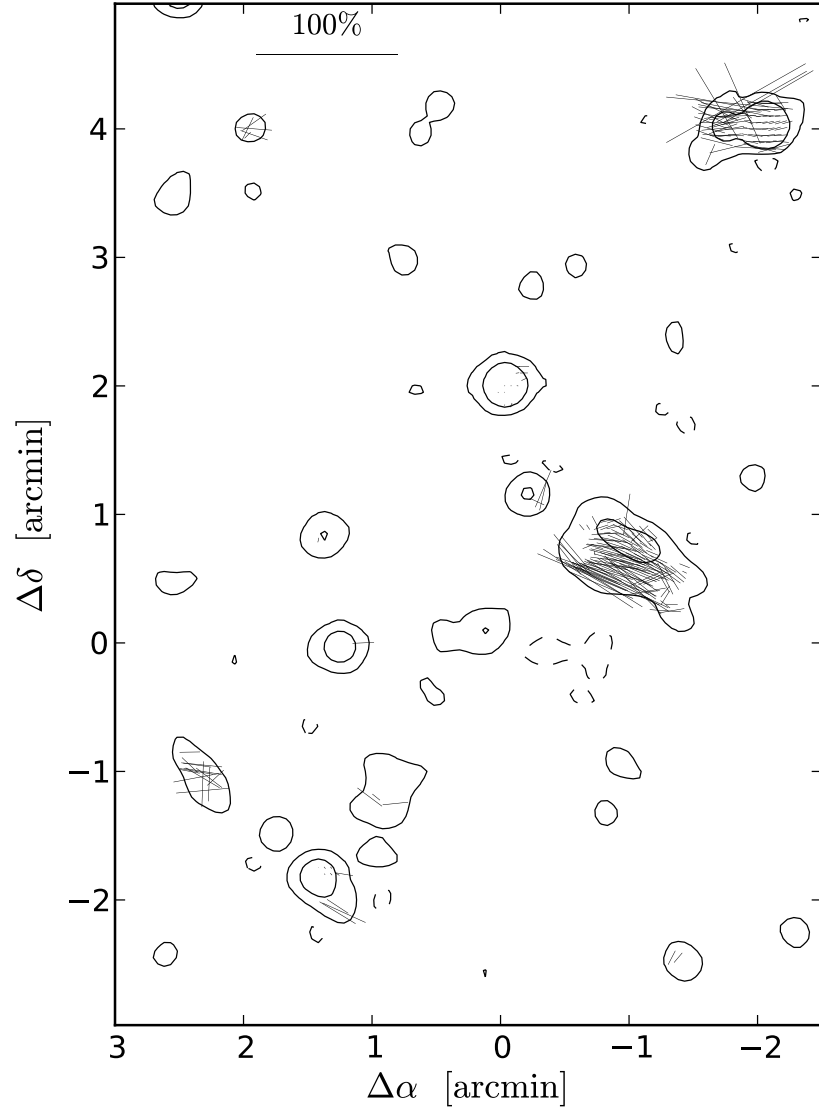


Figure 5.10: Polarization fraction  $f_P$  and angle  $\Psi$  of relic emission. Polarization angles have been corrected for rotation measure and further rotated  $90^\circ$ , indicating the direction of  $B_\perp$ . The polarized source in the northwest is SUMSS J010240-491118 with  $S_{843} = 1.3 \text{ mJy}$ , and is not associated with the cluster. The  $f_P = 100\%$  scale bar is shown at the top of the panel. The RMS noise in the corresponding stokes  $I$  image is  $\sigma = 17 \mu\text{Jy beam}^{-1}$ . The polarization computation is clipped when  $S_I < 5\sigma$ . Contours are drawn at  $-2.5\sigma$ ,  $+2.5\sigma$ , and  $500 \mu\text{Jy beam}^{-1}$ .

### 5.4.5 Shock properties and $B_{\perp}$

We constrain the perpendicular component of the magnetic field at the location of the NW relic using the shock width and spectral index (e.g., van Weeren et al., 2010). We assume a thin shock with upstream and downstream speeds  $v_1$  and  $v_2$ , respectively, propagates along the collision axis. If the electrons are energized by the first-order Fermi acceleration mechanism (Drury, 1983), the compression ratio  $r$  determines the index of the particle energy distribution function  $p = (r + 2)/(r - 1)$ , which is related to the spectral index of the synchrotron emission via  $\alpha = (p - 1)/2$ . The compression ratio is related to the Mach number of a thin shock through the Rankine-Hugoniot jump condition:

$$\frac{1}{r} = \frac{\gamma - 1}{\gamma + 1} + \frac{2}{\gamma + 1} \frac{1}{\mathcal{M}^2}, \quad (5.1)$$

where we assume  $\gamma \equiv c_P/c_V = 5/3$  for a monatomic gas. For the leading edge (up to an offset of  $6''$ ),  $\langle \alpha \rangle = 0.85$ , giving  $p = 2.7$ , and  $r = 2.8$ . The estimated Mach number  $\mathcal{M}$  of the shock is therefore  $\mathcal{M} \sim 2.6$ . The integrated gas temperature of El Gordo is  $kT_e = 14.5 \text{ keV}$ . However, the gas temperature can be elevated above the average value behind a shock front, and in the outer regions of El Gordo, temperatures rise to  $\gtrsim 20 \text{ keV}$  (Menanteau et al., 2012). Therefore, we adopt a value of  $20 \text{ keV}$  in computing the down-stream velocity  $v_2 = 1540 \text{ km s}^{-1}$ .

The downstream velocity combined with the width of the shock constrains  $B_{\perp}$  via  $d_{\text{relic}} = v_2 \times t_{\text{sync}}$ , where  $t_{\text{sync}}$  is the characteristic timescale of synchrotron radiation (van Weeren et al., 2011b):

$$t_{\text{sync}} = 3.2 \times 10^{10} \frac{B_{\perp}^{1/2}}{B_{\perp}^2 + B_{\text{CMB}}^2} \frac{1}{\sqrt{\nu(1+z)}} \text{ yr}, \quad (5.2)$$

with  $\nu$  in MHz, and  $B$  and  $B_{\text{CMB}}$  in  $\mu\text{G}$ .

For El Gordo,  $z = 0.870$ ,  $\nu = 2100$  MHz,  $B_{\text{CMB}} = 11.2 \mu\text{G}$ , and the relics are unresolved with  $d_{\text{shock}} \leq 23$  kpc.  $B_{\text{CMB}}$  parametrizes electron energy loss by inverse Compton scattering off cosmic microwave background (CMB) photons through an equivalent synchrotron power with magnetic field  $B_{\text{CMB}} = 3.2 \mu\text{G} (1+z)^2$ . Figure 5.11 presents an average profile of the NW relic showing the leading unresolved edge followed by an extended trail of low-level signal likely caused by the spherical projection of a 3D shock structure and filamentary substructures in the shock material. Similar extended tails are seen in simulations of cluster mergers by van Weeren et al. (2011a). As shown in Figure 5.12, the expected range of shock width is lower than the upper limits provided, and therefore the  $B_{\perp}$  remains unconstrained. Additional radio imaging with angular resolution  $< 1''$  will be required to place meaningful limits on  $B_{\perp}$ .

## 5.5 Radio halo

El Gordo has a powerful radio halo that is detected at both 610 MHz and 2.1 GHz, allowing it to join an exclusive club of clusters known to host both double radio relics and halos. Other members include CL0217+70 ( $z = 0.0655$ ; Brown et al., 2011), RXCJ1314.4-2515 ( $z = 0.2439$ ; Feretti et al., 2005), and CIZA J2242.8+5301 ( $z = 0.1921$ ; van Weeren et al., 2010).

We isolated the 610 MHz halo emission by first producing an image with `robust` =  $-1$  from data with  $uv$  distance  $d_{uv} > 3.4 \text{ k}\lambda$ , corresponding to angular scales  $\lesssim 1'$ . This image, containing only point-source emission, was then reinverted and subtracted from the  $uv$  data before re-imaging with 1<sup>st</sup>-order MFS. This second pass used `robust` =  $+1$ , a  $uv$ -taper of  $30''$ , and multi-scale clean (Abrantes et al., 2009) with scales of  $0''$ ,  $30''$ , and  $90''$ . The final image has surface brightness sensitivity of  $129 \mu\text{Jy arcmin}^{-2}$  with a synthesized beam of  $60.7'' \times 48.9''$  at P.A. =  $37^\circ$ . To remove residual relic emission from the regions where the relics join the halo near the ends of the cluster collision axis, we

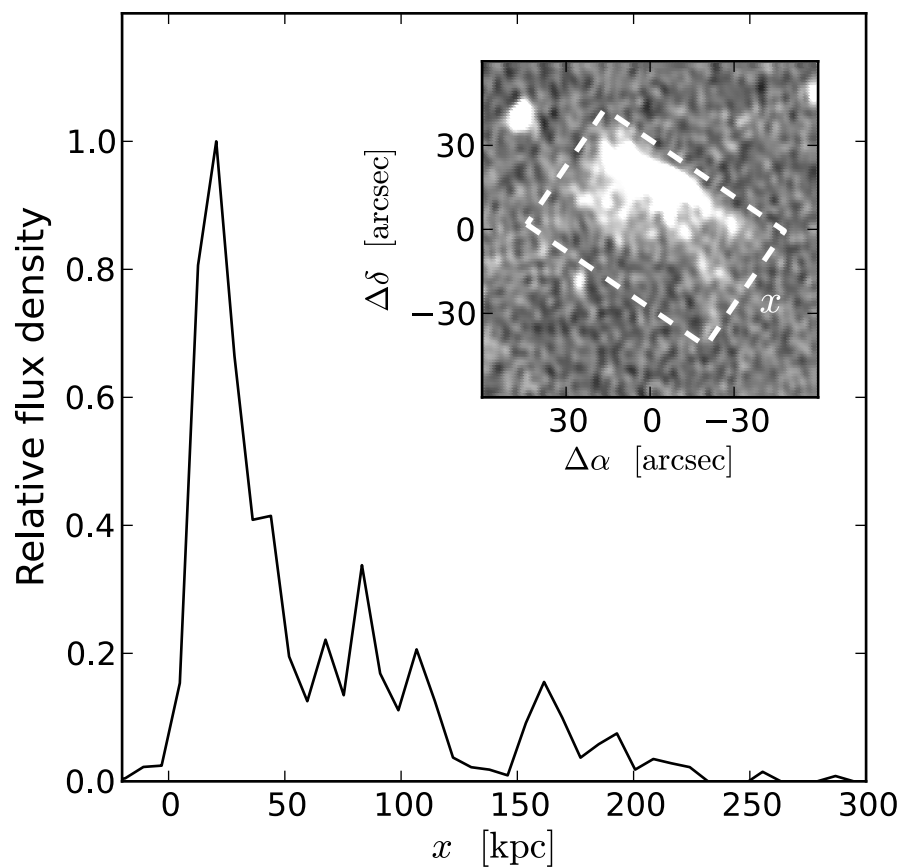


Figure 5.11: Projected radial profile of NW relic. The projection region is a  $1.3' \times 0.8'$  box at P.A.= $55^\circ$ , shown in the inset. The bright leading edge drops quickly, and an extended tail of emission continues out to  $\sim 200$  kpc. The extended tail is due to projection and to the superposition of multiple fainter filaments.

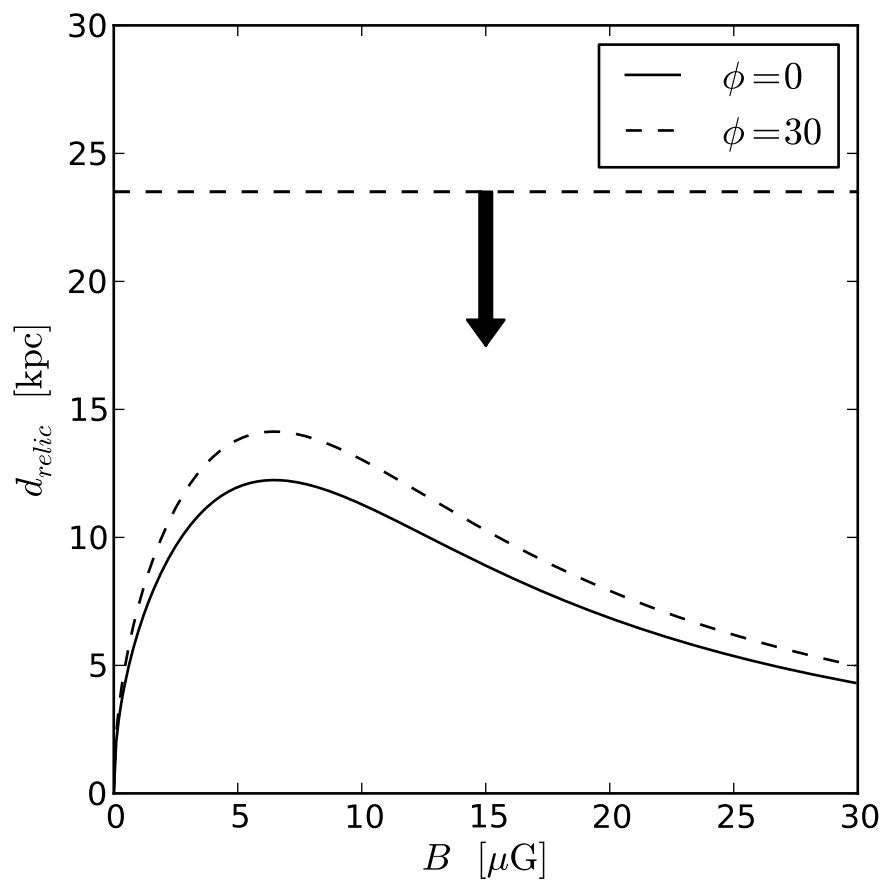


Figure 5.12: Predicted shock width as a function of magnetic field strength. The solid and dashed curves show predictions of  $d_{\text{shock}}$  using projection angles  $\phi = 0$  and  $30^\circ$ , respectively. The horizontal dashed line and downward arrow represent the upper limit placed on the shock width from our 2.1 GHz imaging ( $d_{\text{shock}} \leq 23 \text{ kpc}$ ).

subtracted the  $0''$ -scale clean components from the multi-scale clean model.

The 2.1 GHz halo emission was isolated using the same steps as for the 610 MHz data, with the exception that 2<sup>nd</sup>-order MFS was needed to subtract out the point source emission. In the ATCA 2.1 GHz data, the edge of the primary beam ranges from  $14'$  to  $42'$ . Many bright radio sources fall within this annulus and their spectra are accordingly attenuated by the Gaussian response of the primary beam. These sources are not well-modeled by only a single Taylor coefficient in the MFS algorithm, so 2<sup>nd</sup>-order MFS was used instead. The 2.1 GHz image has a synthesized beam of  $38.4'' \times 24.7''$  at P.A. =  $-2.9^\circ$ . The halo emission has higher S/N in the 610 MHz data, so we use that map for our morphology and luminosity analyses, and the 2.1 GHz map only to measure the halo spectral index. Table 5.2 lists the photometric properties of the halo.

### 5.5.1 Geometry

The halo is elongated in the direction of the collision axis, as has also been observed in the cluster merger systems 1E0657-56 (Bullet cluster; Markevitch et al., 2002) and Abell 520 (Girardi et al., 2008). The emission bridges the entire gap between the two relics lying on opposite sides of the cluster (see Figure 5.2). Such a complete emission bridge has been seen in other cluster mergers with radio halos (e.g., Bonafede et al., 2012). At 610 MHz, the halo fills a large fraction of the projected cluster area. If we define the effective radius of the halo  $r_H$  as that of a circle containing all the  $> 3\sigma$  halo emission (after subtracting point sources), then  $r_H \simeq 1.1$  Mpc, which fills 85% of the projected area within  $r_{500c}$  ( $1177 \pm 92$  kpc; Sifón et al., 2013)<sup>5</sup>. Cassano et al. (2007) predict that halo emission in clusters will not be self-similar, and that the fractional volume occupied by the halo will increase with cluster mass. El Gordo falls very near the Cassano et al. (2007) relation, which predicts  $R_H \sim 0.87^{+3.3}_{-0.69}$  Mpc and gives the

---

<sup>5</sup> Sifón et al. (2013) report  $r_{200a}$ , which we convert to  $r_{500c}$  using the conversion factor  $f = 1.52$  (Nagai et al., 2007).

system one of the larger halos known.

### 5.5.2 Spectral index

The  $uv$  coverage is different for the ATCA and GMRT datasets. The scale at which emission begins to be resolved out of the ATCA data ( $\sim 1.9'$ ) is also similar to the size of the halo itself. We therefore made an unbiased comparison between the two frequencies by folding the GMRT data through the ATCA  $uv$  coverage before smoothing both images to a common resolution and computing the spectral index in each pixel.

Figure 5.13 presents the spectral index  $\alpha_{610}^{2.1}$  image of the El Gordo halo. The spectral index is shallowest nearest the collision axis and steepens with increasing distance from the center. The spectral index also flattens to the north end of the halo where there is additional signal from the NW relic. The flattest spectral index values that do not adjoin regions containing residual relic emission ( $\alpha_{610}^{2.1} \sim 0.75$ ) are located near the “cold bullet” of the merger system. The integrated halo spectral index is  $\langle \alpha \rangle = 1.24 \pm 0.03$ . We note the importance of matching the  $uv$  coverage between observations, without which we would have instead derived an incorrect steeper mean spectral index ( $\alpha \sim 1.95$ ). Using recent radio halo samples, Feretti et al. (2012) find that clusters with  $T_{\text{gas}} > 10$  keV on average have spectral indices of  $\sim 1.2$ . El Gordo is in agreement with this trend, suggesting the halo emission is associated with the recent energy injection caused by the ongoing merger. Similar merger-related spectral index structure has been seen in A 665 and A 2163 (Feretti et al., 2004).

There exists a correlation between average gas temperature and average halo spectral index in galaxy clusters with radio halos (e.g., Feretti et al., 2012), indicating a connection between energy injection in the ICM and halo emission. The spatially-resolved correlation is less well studied but remains important for understanding systems that

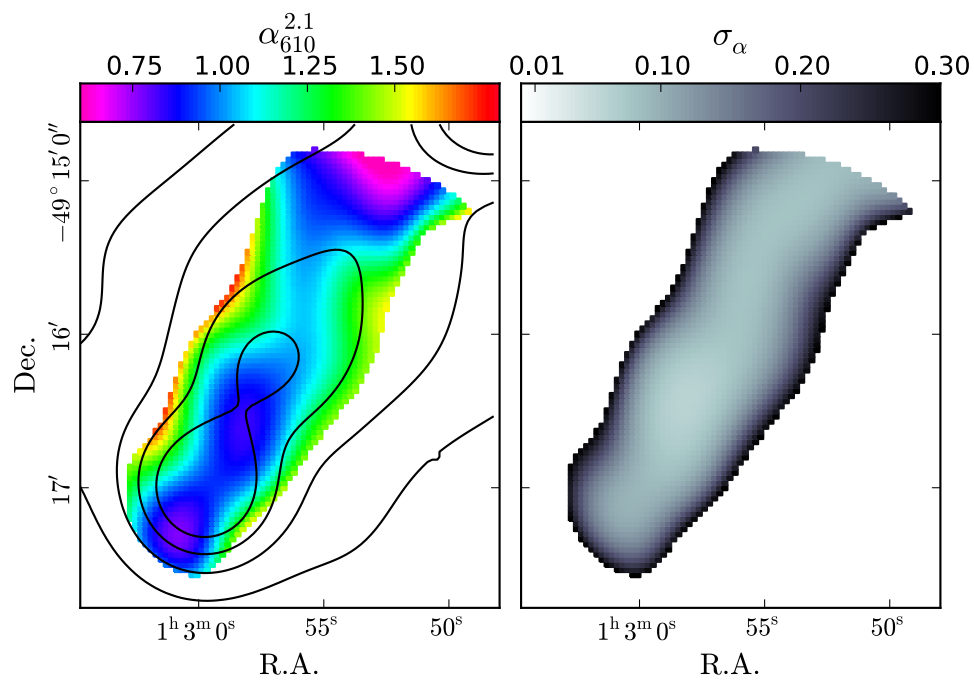


Figure 5.13: Spectral index  $\alpha_{610}^{2.1}$  image of El Gordo's radio halo. The spectral index and the uncertainty per pixel  $\sigma_\alpha$  are shown in the left and right panels, respectively. Contours represent the 610 MHz halo intensity with levels 1, 2, 3, and 4 mJy beam<sup>-1</sup>.



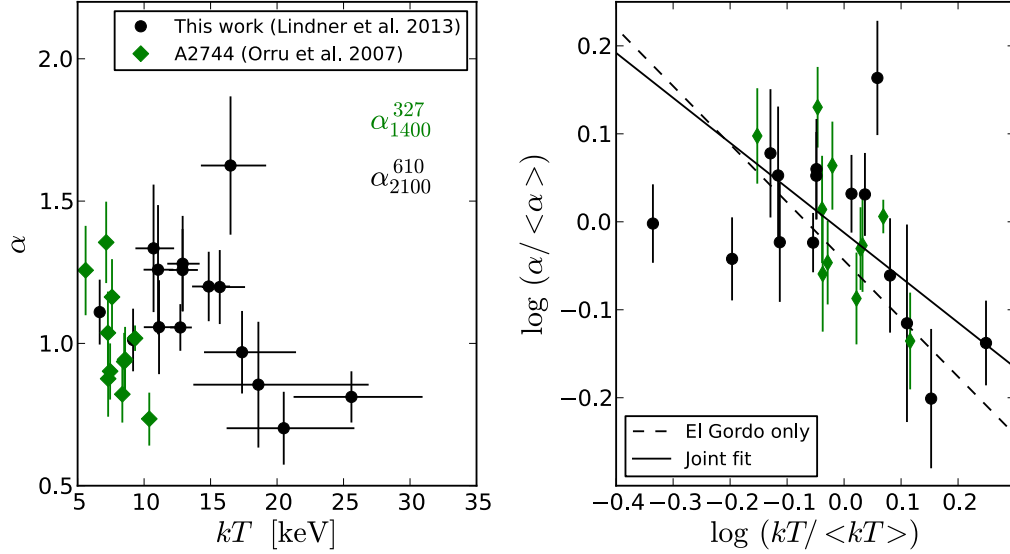


Figure 5.14: *Left*: Radio spectral index versus X-ray gas temperature for El Gordo (black points) compared to A2744 (Orrú et al., 2007). *Right*: Linear fits to the log of data in the left panel after scaling by the means. The dashed line shows the best-fit when we use El Gordo data only (power-law slope  $B \simeq -0.7$ ), and the solid line shows the best-fit when we use both datasets together ( $B \simeq -0.5$ ).

are not in equilibrium; these represent a large fraction of halo clusters. Recent observations have identified a resolved correlation between cluster gas temperature and halo spectral index in Abell 2744, at  $z = 0.31$  (Orrú et al., 2007). El Gordo’s spectral index map, combined with the temperature information derived from new *Chandra* observations, allow us to characterize the spatial correlation in a system with gas temperatures up to  $\sim 20$  keV. Figure 5.14 presents a comparison of the halo  $\alpha_{610}^{2.1}$  versus the X-ray gas temperature  $T_e$  within a tiling of nearly independent  $30''$  boxes. We find that the spectral index becomes flatter with increasing gas temperature. We fit a line to the scaled parameterized relation

$$\log(\alpha / \langle \alpha \rangle) = A + B \times \log(T_e / \langle T_e \rangle), \quad (5.3)$$

and find a best-fit power-law slope  $B = -0.7$  using the El Gordo data alone, and  $B = -0.5$  when we include the data from Orrú et al. (2007).

### 5.5.3 Luminosity

We compute the rest-frame 1.4 GHz spectral power  $L_{1.4}$  of the radio halo using the 610 MHz flux density,  $S_{610} = (28.4 \pm 0.59)$  mJy, which we extract from a  $2.7'$ -radius circle centered on the point-source-subtracted halo image. After adopting the integrated spectral index  $\langle\alpha\rangle = 1.24 \pm 0.03$  for the  $k$ -correction, we find  $\log(L_{1.4}/\text{W Hz}^{-1}) = 25.65 \pm 0.07$ , making El Gordo’s one of the most powerful radio halos known. Figure 5.15 shows  $L_{1.4}$  versus  $L_X$  for El Gordo compared with other clusters from the literature. Only MACSJ0717.5+3745 has greater luminosity,  $\log L_{1.4} \simeq 25.70$ , and spectral index  $\alpha_{610}^{4900} = 1.24 \pm 0.05$  (van Weeren et al., 2009). Another SZE-selected cluster that hosts a radio halo is PLCK171.9-40.7 ( $\log L_{1.4} = 24.70$ ; Giacintucci et al., 2013).

## 5.6 Conclusions

We present new 610 MHz and 2.1 GHz observations of El Gordo, the highest redshift ( $z = 0.870$ ) radio halo/relic cluster known, thereby providing important constraints on the non-thermal emission properties of clusters at high redshift.

El Gordo’s double radio relic morphology is characteristic of other massive cluster mergers occurring in the plane of the sky. The bright leading edges of all relics remain unresolved in our images, implying extremely thin shock widths of  $d_{\text{shock}} \leq 23$  kpc.

El Gordo’s radio halo is among the largest ( $r_{\text{H}} \simeq 1.1$  Mpc) and most powerful ( $\log(L_{1.4}/\text{W Hz}^{-1}) = 25.65 \pm 0.07$ ) known. The halo spectral index varies with position, being flattest in the center along the collision axis and steeper away from this axis. This spectral index morphology, along with the shallow integrated spectral index ( $\langle\alpha\rangle = 1.24 \pm 0.03$ ), strongly suggests the mechanism of Fermi 2<sup>nd</sup>-order reacceleration associated with the ongoing merger and high gas temperatures ( $T_e \simeq 14.5$  keV; Menanteau et al., 2012) as the origin of the halo emission.

RM-synthesis was carried out using the broad-bandwidth polarimetry capabilities

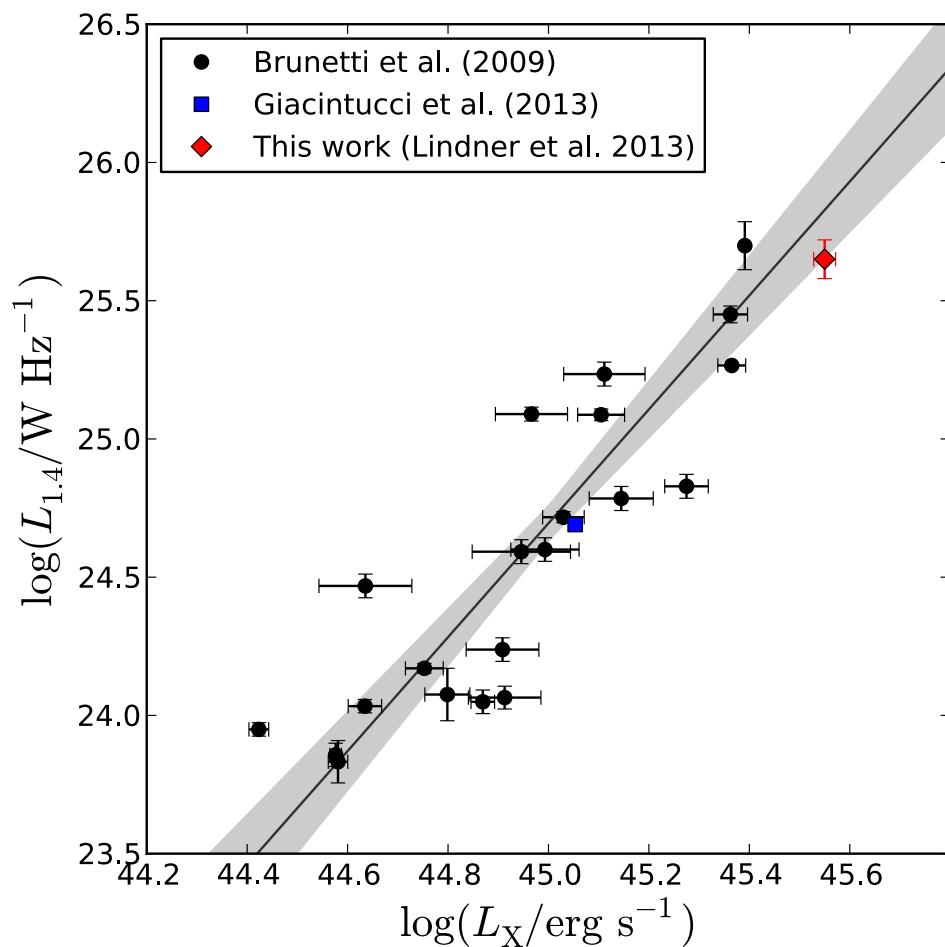


Figure 5.15: Rest-frame 20 cm spectral power vs  $L_X$  for El Gordo's and other halos from the literature. Errors in  $\log L_{1.4}$  include the uncertainty in  $\alpha_{610}^{2.1}$  used in the k-correction. The line and shaded region show the fit best correlation and  $\pm 1\sigma$  uncertainties from Brunetti et al. (2009).

of the ATCA/CABB. We find variation between  $-5$  and  $+25 \text{ rad m}^{-2}$  ( $\pm 8 \text{ rad m}^{-2}$ ) in the RM across the spatially-extended NW relic, likely due to structure in the projected magnetic field ( $\int B_{\parallel} dl$ ). Using an estimate of the column density of electrons along the line of sight from X-ray observations, we estimate typical magnetic field amplitudes of  $B_{\parallel} \sim 0.2 \mu\text{G}$ .

The significant energy losses due to Compton scattering off CMB photons at this redshift, parameterized by the effective synchrotron magnetic field strength,  $B_{\text{CMB}} = 11.2 \mu\text{G}$ , severely limits the radiative lifetime of cosmic ray electrons, and radio observations with angular resolution  $< 1''$  will be required to place meaningful constraints on  $B_{\perp}$  at these redshifts.

## Chapter 6

### Conclusions

This research presents a survey of the growth of galaxies and galaxy clusters at high redshift using radio, sub/millimeter, and X-ray observations. Episodes of rapid growth can be triggered by mergers, which occur frequently in the theory of hierarchical structure formation. These events are identifiable from great distances and can be used to constrain the mass assembly history of galaxies and clusters.

High-redshift galaxy-galaxy mergers of gas-rich progenitor systems can trigger intense starbursts, called submillimeter galaxies (SMGs). In Chapter 2, we present a deep 1.2 mm survey of the inner 566 arcmin<sup>2</sup> of the Lockman Hole North (LHN) to search for SMGs. We detect 41 sources with  $S/N > 4.0$  and  $S_\nu \simeq 2\text{--}5$  mJy, of which  $93^{+4}_{-7}\%$  have robust counterparts in the LHN's deep 20 cm radio imaging (Owen & Morrison, 2008). This high radio-counterpart identification rate has allowed us to produce an unbiased estimate of the 1.2 mm-selected SMG redshift distribution ( $z_{\text{median}} = 2.9$ ). We also detect significant angular correlation between the sources, which is the first discovery of clustering in 1.2 mm-selected SMGs. Using a  $P(D)$  analysis, we constrain the 2.1 mm number counts down to 0.05 mJy, far below the nominal detection threshold. This work has significantly improved our knowledge of the statistical properties of the 1.2 mm SMG population and provides constraints for models of galaxy formation and evolution.

Mergers between galaxies can also dump large amounts of matter into galaxies' nuclei, growing central super-massive black holes, which then shine as AGNs. In Chapter

3 we study the X-ray properties of the LHN 1.2 mm detections to search for signatures of this accretion in a statistically-complete sample of SMGs. In the stacked, rest-frame X-ray spectrum, we detect strong Fe K $\alpha$  emission with EW > 1 keV. The mean Fe K $\alpha$  line luminosity of  $(1.3 \pm 0.4) \times 10^{42} \text{ erg s}^{-1}$  is high compared to those of star-formation-only systems with comparable  $L_{\text{IR}}$ , indicating that accretion is likely responsible for the Fe K $\alpha$  line, and that rapid black-hole growth may be occurring in these high-redshift starburst systems.

Galaxy clusters are the largest gravitationally-bound structures in the Universe, and their observed growth through cosmic time can be used to constrain cosmological parameters. With the Sunyaev Zel'dovich Effect (SZE), massive clusters can be detected out to (in principle) arbitrarily high redshifts. However, the scaling between SZE signal and mass remains the limiting uncertainty in constraining cosmological parameters. In Chapter 4, we investigate to what degree the SZE signal in a sample of massive clusters from the Atacama Cosmology Telescope southern survey (Menanteau et al., 2010; Marriage et al., 2011) is affected by contamination from radio sources and SMGs. We find that synchrotron emission from 2.1 GHz-selected radio galaxies contaminates the 148 GHz SZE decrement by < 1%, and higher-frequency observations by a negligible amount. At 345 GHz, SMGs contaminate the SZE signal by  $15^{+36}_{-13}\%$  and  $2^{+6}_{-2}\%$  in the SZE 345 GHz and 148 GHz bands, respectively. This significant contamination by SMGs may add systematic scatter to the  $Y_{\text{SZ}}$ -mass scaling relation. With the contaminating SMGs subtracted, we derive peculiar velocity constraints for the clusters and obtain a typical precision  $\sigma_{v_{\text{pec}}} \simeq 700 \text{ km s}^{-1}$  in clusters with SZE S/N > 3.5. We find an average peculiar velocity  $\langle v_p \rangle = 230 \pm 330 \text{ km s}^{-1}$  for the sample.

Galaxy clusters gain mass predominantly through merging, and cluster-cluster mergers are some of the most energetic events in the Universe. Some of this released energy is directed into accelerating cosmic ray particles, which emit non-thermal radiation that

reveals information about the magnetic field properties and energy content of the intracluster medium. In Chapter 5, we present a detailed analysis of the non-thermal radio emission in the massive cluster merger ACT-CL J0102–4915 (“El Gordo”; Menanteau et al., 2012). We detect a giant radio halo with effective radius  $r_{\text{H}} \simeq 1.1 \text{ Mpc}$  and rest-frame 1.4 GHz luminosity  $\log(L_{1.4}/\text{W Hz}^{-1}) = 25.65 \pm 0.07$ . We also detect three radio relics that have geometries, spectral index properties, and polarization fractions consistent with their being produced by first-order Fermi acceleration in shock fronts generated by the cluster collision. The shock widths as traced by the unresolved leading edges of the relics are among the narrowest known,  $d_{\text{shock}} \leq 23 \text{ kpc}$ . The Faraday rotation measure across the brightest radio relic shows significant variation between  $-5$  and  $+25 \text{ rad m}^{-2}$ , likely caused by the intrinsic variation in magnetic fields along the line-of-sight with typical amplitudes  $B_{\parallel} \sim 0.2 \mu\text{G}$ . At  $z = 0.870$  (Menanteau et al., 2012), El Gordo is the highest-redshift radio halo/relic cluster known, and this work supplies badly-needed constraints on the non-thermal physics in clusters beyond  $z \gtrsim 0.3$ .

## Bibliography

- Abrantes, F., Lopes, C., Rodrigues, T., et al. 2009, *Geochemistry, Geophysics, Geosystems*, 10, 9
- Adler, R. J. 1981, *The Geometry of Random Fields* (Wiley)
- Aguirre, P., Baker, A. J., Menanteau, F., Lutz, D., & Tacconi, L. J. 2013, *ApJ*, 768, 164
- Alexander, D. M., Bauer, F. E., Chapman, S. C., et al. 2005a, *ApJ*, 632, 736
- Alexander, D. M., Smail, I., Bauer, F. E., et al. 2005b, *Nature*, 434, 738
- Alexander, D. M., Bauer, F. E., Brandt, W. N., et al. 2003, *AJ*, 125, 383
- Arnaud, K. A. 1996, in *Astronomical Society of the Pacific Conference Series*, Vol. 101, *Astronomical Data Analysis Software and Systems V*, ed. G. H. Jacoby & J. Barnes, 17
- Arnaud, M., Pratt, G. W., Piffaretti, R., et al. 2010, *A&A*, 517, A92
- Austermann, J. E., Aretxaga, I., Hughes, D. H., et al. 2009, *MNRAS*, 393, 1573
- Austermann, J. E., Dunlop, J. S., Perera, T. A., et al. 2010, *MNRAS*, 401, 160
- Balbus, S. A., & Hawley, J. F. 1991, *ApJ*, 376, 214
- Balestra, I., Boller, T., Gallo, L., Lutz, D., & Hess, S. 2005, *A&A*, 442, 469
- Ballo, L., Braito, V., Della Ceca, R., et al. 2004, *ApJ*, 600, 634



- Barger, A. J., Cowie, L. L., Sanders, D. B., et al. 1998, *Nature*, 394, 248
- Baugh, C. M., Lacey, C. G., Frenk, C. S., et al. 2005, *MNRAS*, 356, 1191
- Bell, E. F. 2003, *ApJ*, 586, 794
- Benson, B. A., Church, S. E., Ade, P. A. R., et al. 2003, *ApJ*, 592, 674
- Benson, B. A., de Haan, T., Dudley, J. P., et al. 2013, *ApJ*, 763, 147
- Bertoldi, F., Carilli, C., Aravena, M., et al. 2007, *ApJS*, 172, 132
- Best, P. N. 2004, *MNRAS*, 351, 70
- Best, P. N., Kauffmann, G., Heckman, T. M., et al. 2005, *MNRAS*, 362, 25
- Béthermin, M., Dole, H., Beelen, A., & Aussel, H. 2010, *A&A*, 512, A78
- Béthermin, M., Dole, H., Lagache, G., Le Borgne, D., & Penin, A. 2011, *A&A*, 529, A4
- Biggs, A. D., Ivison, R. J., Ibar, E., et al. 2011, *MNRAS*, 413, 2314
- Bigiel, F., Leroy, A., Walter, F., et al. 2008, *AJ*, 136, 2846
- Blain, A. W., Smail, I., Ivison, R. J., Kneib, J.-P., & Frayer, D. T. 2002, *Physics Reports*, 369, 111
- Boller, T., Keil, R., Hasinger, G., et al. 2003, *A&A*, 411, 63
- Bonafede, A., Brüggén, M., van Weeren, R., et al. 2012, *MNRAS*, 426, 40
- Borys, C., Chapman, S., Halpern, M., & Scott, D. 2003, *MNRAS*, 344, 385
- Borys, C., Scott, D., Chapman, S., et al. 2004, *MNRAS*, 355, 485
- Brentjens, M. A., & de Bruyn, A. G. 2005, *A&A*, 441, 1217
- Brown, S., Duisterhoeft, J., & Rudnick, L. 2011, *ApJL*, 727, L25

- Brunetti, G., Blasi, P., Reimer, O., et al. 2012, MNRAS, 426, 956
- Brunetti, G., Cassano, R., Dolag, K., & Setti, G. 2009, A&A, 507, 661
- Brunetti, G., Setti, G., Feretti, L., & Giovannini, G. 2001, MNRAS, 320, 365
- Brusa, M., Gilli, R., & Comastri, A. 2005, ApJL, 621, L5
- Burn, B. J. 1966, MNRAS, 133, 67
- Calabrese, E., Hlozek, R. A., Battaglia, N., et al. 2013, Physical Review D, 87, 103012
- Carilli, C. L., & Yun, M. S. 1999, ApJL, 513, L13
- . 2000, ApJ, 530, 618
- Carlstrom, J. E., Holder, G. P., & Reese, E. D. 2002, ARA&A, 40, 643
- Carlstrom, J. E., Ade, P. A. R., Aird, K. A., et al. 2011, PASP, 123, 568
- Cash, W. 1979, ApJ, 228, 939
- Cassano, R., Brunetti, G., Setti, G., Govoni, F., & Dolag, K. 2007, MNRAS, 378, 1565
- Cassano, R., Brunetti, G., & Venturi, T. 2011, Journal of Astrophysics and Astronomy, 32, 519
- Chapin, E. L., Pope, A., Scott, D., et al. 2009, MNRAS, 398, 1793
- Chapman, S. C., Blain, A. W., Ivison, R. J., & Smail, I. R. 2003, Nature, 422, 695
- Chapman, S. C., Blain, A. W., Smail, I., & Ivison, R. J. 2005, ApJ, 622, 772
- Chapman, S. C., Smail, I., Blain, A. W., & Ivison, R. J. 2004, ApJ, 614, 671
- Chapman, S. C., Ivison, R. J., Roseboom, I. G., et al. 2010, MNRAS, 409, L13

- Chaudhary, P., Brusa, M., Hasinger, G., Merloni, A., & Comastri, A. 2010, *A&A*, 518, A58
- Chluba, J., Nagai, D., Sazonov, S., & Nelson, K. 2012, *MNRAS*, 426, 510
- Chluba, J., Switzer, E., Nelson, K., & Nagai, D. 2013, *MNRAS*, arXiv:1211.3206
- Comastri, A. 2004, in *Astrophysics and Space Science Library*, Vol. 308, *Supermassive Black Holes in the Distant Universe*, ed. A. J. Barger, 245
- Condon, J. J. 1974, *ApJ*, 188, 279
- . 1992, *ARA&A*, 30, 575
- Condon, J. J., Cotton, W. D., Greisen, E. W., et al. 1998, *AJ*, 115, 1693
- Connolly, A. J., Szalay, A. S., Dickinson, M., Subbarao, M. U., & Brunner, R. J. 1997, *ApJL*, 486, L11
- Conselice, C. J., Chapman, S. C., & Windhorst, R. A. 2003, *ApJL*, 596, L5
- Coppin, K., Halpern, M., Scott, D., Borys, C., & Chapman, S. 2005, *MNRAS*, 357, 1022
- Coppin, K., Chapin, E. L., Mortier, A. M. J., et al. 2006, *MNRAS*, 372, 1621
- Corral, A., Page, M. J., Carrera, F. J., et al. 2008, *A&A*, 492, 71
- Davé, R., Finlator, K., Oppenheimer, B. D., et al. 2010, *MNRAS*, 404, 1355
- Dennison, B. 1980, *ApJL*, 239, L93
- Dodelson, S. 2003, *Modern cosmology* (Academic Press)
- Dole, H., Lagache, G., Puget, J.-L., et al. 2006, *A&A*, 451, 417
- Done, C., Madejski, G. M., Życki, P. T., & Greenhill, L. J. 2003, *ApJ*, 588, 763

- Doré, O., Knox, L., & Peel, A. 2003, *ApJL*, 585, L81
- Downes, A. J. B., Peacock, J. A., Savage, A., & Carrie, D. R. 1986, *MNRAS*, 218, 31
- Downes, D., & Eckart, A. 2007, *A&A*, 468, L57
- Draine, B. T. 2006, *ApJ*, 636, 1114
- Draine, B. T., Dale, D. A., Bendo, G., et al. 2007, *ApJ*, 663, 866
- Drury, L. O. 1983, *Reports on Progress in Physics*, 46, 973
- Edge, A. C., Boehringer, H., Guzzo, L., et al. 1994, *A&A*, 289, L34
- Engel, H., Tacconi, L. J., Davies, R. I., et al. 2010, *ApJ*, 724, 233
- Enoch, M. L., Young, K. E., Glenn, J., et al. 2006, *ApJ*, 638, 293
- Ensslin, T. A., Biermann, P. L., Klein, U., & Kohle, S. 1998, *A&A*, 332, 395
- Falocco, S., Carrera, F. J., Corral, A., et al. 2012, *A&A*, 538, A83
- Feretti, L., Giovannini, G., Govoni, F., & Murgia, M. 2012, *Astronomy and Astrophysics Reviews*, 20, 54
- Feretti, L., Orrù, E., Brunetti, G., et al. 2004, *A&A*, 423, 111
- Feretti, L., Schuecker, P., Böhringer, H., Govoni, F., & Giovannini, G. 2005, *A&A*, 444, 157
- Ferrarese, L., & Merritt, D. 2000, *ApJL*, 539, L9
- Ferrari, C., Govoni, F., Schindler, S., Bykov, A. M., & Rephaeli, Y. 2008, *Space Science Reviews*, 134, 93
- Fiolet, N., Omont, A., Polletta, M., et al. 2009, *A&A*, 508, 117

- Fiolet, N., Omont, A., Lagache, G., et al. 2010, *A&A*, 524, A33
- Fixsen, D. J., Dwek, E., Mather, J. C., Bennett, C. L., & Shafer, R. A. 1998, *ApJ*, 508, 123
- Fowler, J. W., Niemack, M. D., Dicker, S. R., et al. 2007, *Applied Optics*, 46, 3444
- Frayer, D. T., Ivison, R. J., Scoville, N. Z., et al. 1998, *ApJL*, 506, L7
- . 1999, *ApJL*, 514, L13
- Fruscione, A., McDowell, J. C., Allen, G. E., et al. 2006, in *Society of Photo-Optical Instrumentation Engineers (SPIE) Conference Series*, Vol. 6270
- Gawiser, E., van Dokkum, P. G., Herrera, D., et al. 2006, *ApJS*, 162, 1
- Gebhardt, K., Bender, R., Bower, G., et al. 2000, *ApJL*, 539, L13
- Gehrels, N. 1986, *ApJ*, 303, 336
- Georgantopoulos, I., Rovilos, E., & Comastri, A. 2011, *A&A*, 526, A46
- Giacintucci, S., Kale, R., Wik, D. R., Venturi, T., & Markevitch, M. 2013, *ApJ*, 766, 18
- Girardi, M., Barrena, R., Boschini, W., & Ellingson, E. 2008, *A&A*, 491, 379
- Glenn, J., Conley, A., Béthermin, M., et al. 2010, *MNRAS*, 409, 109
- Govoni, F., Markevitch, M., Vikhlinin, A., et al. 2004, *ApJ*, 605, 695
- Greve, T. R., Ivison, R. J., Bertoldi, F., et al. 2004, *MNRAS*, 354, 779
- Greve, T. R., Pope, A., Scott, D., et al. 2008, *MNRAS*, 389, 1489
- Greve, T. R., Bertoldi, F., Smail, I., et al. 2005, *MNRAS*, 359, 1165

- Griffin, M. J., Abergel, A., Abreu, A., et al. 2010, *A&A*, 518, L3
- Gunn, J. E., & Gott, III, J. R. 1972, *ApJ*, 176, 1
- Halverson, N. W., Lanting, T., Ade, P. A. R., et al. 2009, *ApJ*, 701, 42
- Hand, N., Addison, G. E., Aubourg, E., et al. 2012, *Physical Review Letters*, 109, 041101
- Hatsukade, B., Kohno, K., Aretxaga, I., et al. 2011, *MNRAS*, 411, 102
- Hayward, C. C., Kereš, D., Jonsson, P., et al. 2011, *ApJ*, 743, 159
- Hill, G. J., & Lilly, S. J. 1991, *ApJ*, 367, 1
- Hincks, A. D., Acquaviva, V., Ade, P. A. R., et al. 2010, *ApJS*, 191, 423
- Hogg, D. W., & Turner, E. L. 1998, *PASP*, 110, 727
- Holland, W. S., Robson, E. I., Gear, W. K., et al. 1999, *MNRAS*, 303, 659
- Houck, J. C., Bregman, J. N., Chevalier, R. A., & Tomisaka, K. 1998, *ApJ*, 493, 431
- Hubble, E. 1926, *Contributions from the Mount Wilson Observatory / Carnegie Institution of Washington*, 324, 1
- Hughes, D. H., Serjeant, S., Dunlop, J., et al. 1998, *Nature*, 394, 241
- Ibar, E., Ivison, R. J., Best, P. N., et al. 2010, *MNRAS*, 401, L53
- Ibar, E., Ivison, R. J., Biggs, A. D., et al. 2009, *MNRAS*, 397, 281
- Ivison, R. J., Smail, I., Barger, A. J., et al. 2000, *MNRAS*, 315, 209
- Ivison, R. J., Smail, I., Le Borgne, J.-F., et al. 1998, *MNRAS*, 298, 583
- Ivison, R. J., Greve, T. R., Smail, I., et al. 2002, *MNRAS*, 337, 1

- Iverson, R. J., Smail, I., Dunlop, J. S., et al. 2005, MNRAS, 364, 1025
- Iverson, R. J., Greve, T. R., Dunlop, J. S., et al. 2007, MNRAS, 380, 199
- Iwasawa, K., Sanders, D. B., Evans, A. S., et al. 2009, ApJL, 695, L103
- . 2005, MNRAS, 357, 565
- Iwasawa, K., Sanders, D. B., Teng, S. H., et al. 2011, A&A, 529, A106
- Johansson, D., Sigurdarson, H., & Horellou, C. 2011, A&A, 527, A117
- Kallman, T. R., Palmeri, P., Bautista, M. A., Mendoza, C., & Krolik, J. H. 2004, ApJS, 155, 675
- Kennicutt, Jr., R. C. 1998, ApJ, 498, 541
- Kim, S.-H., Martin, P. G., & Hendry, P. D. 1994, ApJ, 422, 164
- Kitayama, T., Komatsu, E., Ota, N., et al. 2004, Publications of the ASJ, 56, 17
- Klein, U., Wielebinski, R., & Morsi, H. W. 1988, A&A, 190, 41
- Knudsen, K. K., van der Werf, P. P., & Kneib, J.-P. 2008, MNRAS, 384, 1611
- Komatsu, E., Matsuo, H., Kitayama, T., et al. 2001, Publications of the ASJ, 53, 57
- Komatsu, E., Smith, K. M., Dunkley, J., et al. 2011, ApJS, 192, 18
- Kormendy, J., & Kennicutt, Jr., R. C. 2004, ARA&A, 42, 603
- Kosowsky, A. 2006, New Astronomy Review, 50, 969
- Kreysa, E., Gemuend, H.-P., Gromke, J., et al. 1998, in Society of Photo-Optical Instrumentation Engineers (SPIE) Conference Series, ed. T. G. Phillips, Vol. 3357, 319–325

- Kroupa, P. 2001, MNRAS, 322, 231
- Lacey, C., & Cole, S. 1993, MNRAS, 262, 627
- Laird, E. S., Nandra, K., Pope, A., & Scott, D. 2010, MNRAS, 401, 2763
- Landy, S. D., & Szalay, A. S. 1993, ApJ, 412, 64
- Laurent, G. T., Aguirre, J. E., Glenn, J., et al. 2005, ApJ, 623, 742
- Lehmer, B. D., Brandt, W. N., Alexander, D. M., et al. 2005, AJ, 129, 1
- Leroy, A. K., Walter, F., Brinks, E., et al. 2008, AJ, 136, 2782
- Lima, M., Jain, B., & Devlin, M. 2010, MNRAS, 406, 2352
- Lin, Y.-T., Stanford, S. A., Eisenhardt, P. R. M., et al. 2012, ApJL, 745, L3
- Lindner, R. R., Baker, A. J., Beelen, A., Owen, F. N., & Polletta, M. 2012, ApJ, 757, 3
- Lindner, R. R., Baker, A. J., Omont, A., et al. 2011, ApJ, 737, 83
- Longair, M. S. 2011, High Energy Astrophysics (Cambridge University Press)
- Lonsdale, C. J., Smith, H. E., Rowan-Robinson, M., et al. 2003, PASP, 115, 897
- Lynden-Bell, D. 1967, MNRAS, 136, 101
- Magdis, G. E., Elbaz, D., Hwang, H. S., et al. 2010, MNRAS, 409, 22
- Magnelli, B., Lutz, D., Berta, S., et al. 2010, A&A, 518, L28
- Magorrian, J., Tremaine, S., Richstone, D., et al. 1998, AJ, 115, 2285
- Maloney, P. R., Glenn, J., Aguirre, J. E., et al. 2005, ApJ, 635, 1044
- Markevitch, M. 2006, in ESA Special Publication, Vol. 604, The X-ray Universe 2005, ed. A. Wilson, 723



- Markevitch, M., Gonzalez, A. H., David, L., et al. 2002, *ApJL*, 567, L27
- Markwardt, C. B. 2009, in *Astronomical Data Analysis Software and Systems XVIII*, ed. D. A. Bohlender, D. Durand, & P. Dowler, Vol. 411, 251
- Marriage, T. A., Acquaviva, V., Ade, P. A. R., et al. 2011, *ApJ*, 737, 61
- Marsden, G., Chapin, E. L., Halpern, M., et al. 2011, *MNRAS*, 417, 1192
- Mason, B. S., Dicker, S. R., Korngut, P. M., et al. 2010, *ApJ*, 716, 739
- Matt, G., Fabian, A. C., Guainazzi, M., et al. 2000, *MNRAS*, 318, 173
- Mauch, T., Murphy, T., Buttery, H. J., et al. 2003, *MNRAS*, 342, 1117
- Menanteau, F., González, J., Juin, J.-B., et al. 2010, *ApJ*, 723, 1523
- Menanteau, F., Hughes, J. P., Sifón, C., et al. 2012, *ApJ*, 748, 7
- Menanteau, F., Sifón, C., Barrientos, L. F., et al. 2013, *ApJ*, 765, 67
- Menéndez-Delmestre, K., Blain, A. W., Alexander, D. M., et al. 2007, *ApJL*, 655, L65
- Menéndez-Delmestre, K., Blain, A. W., Smail, I., et al. 2009, *ApJ*, 699, 667
- Merritt, D., & Ferrarese, L. 2001, *MNRAS*, 320, L30
- Middelberg, E. 2006, *Publications of the Astron. Soc. of Australia*, 23, 64
- Morrison, R., & McCammon, D. 1983, *ApJ*, 270, 119
- Mroczkowski, T., Dicker, S., Sayers, J., et al. 2012, *ApJ*, 761, 47
- Nagai, D., Kravtsov, A. V., & Vikhlinin, A. 2007, *ApJ*, 668, 1
- Nandra, K., & Iwasawa, K. 2007, *MNRAS*, 382, L1

- Narayanan, D., Cox, T. J., Hayward, C. C., Younger, J. D., & Hernquist, L. 2009, MNRAS, 400, 1919
- Narayanan, D., Hayward, C. C., Cox, T. J., et al. 2010, MNRAS, 401, 1613
- Navarro, J. F., Frenk, C. S., & White, S. D. M. 1997, ApJ, 490, 493
- Neri, R., Genzel, R., Ivison, R. J., et al. 2003, ApJL, 597, L113
- Niemack, M. D., Ade, P. A. R., Aguirre, J., et al. 2010, in Society of Photo-Optical Instrumentation Engineers (SPIE) Conference Series, Vol. 7741
- Nord, M., Basu, K., Pacaud, F., et al. 2009, A&A, 506, 623
- Nuza, S. E., Hoeft, M., van Weeren, R. J., Gottlöber, S., & Yepes, G. 2012, MNRAS, 420, 2006
- Offringa, A. R., de Bruyn, A. G., Biehl, M., et al. 2010, MNRAS, 405, 155
- Offringa, A. R., van de Gronde, J. J., & Roerdink, J. B. T. M. 2012, A&A, 539, A95
- Oliver, S. J., Wang, L., Smith, A. J., et al. 2010, A&A, 518, L21
- Oppermann, N., Junklewitz, H., Robbers, G., et al. 2012, A&A, 542, A93
- Orrú, E., Murgia, M., Feretti, L., et al. 2007, A&A, 467, 943
- O’Sullivan, S. P., Brown, S., Robishaw, T., et al. 2012, MNRAS, 421, 3300
- Ott, S., Bakker, J., Brumfitt, J., et al. 2006, in Astronomical Society of the Pacific Conference Series, Vol. 351, Astronomical Data Analysis Software and Systems XV, ed. C. Gabriel, C. Arviset, D. Ponz, & S. Enrique, 516
- Owen, F. N. 2013a, In prep.
- . 2013b, In prep.

- Owen, F. N., & Morrison, G. E. 2008, *AJ*, 136, 1889
- . 2009, *ApJS*, 182, 625
- Owen, F. N., Morrison, G. E., Klimek, M. D., & Greisen, E. W. 2009, *AJ*, 137, 4846
- Patanchon, G., Ade, P. A. R., Bock, J. J., et al. 2009, *ApJ*, 707, 1750
- Penner, K., Pope, A., Chapin, E. L., et al. 2011, *MNRAS*, 410, 2749
- Penzias, A. A., & Wilson, R. W. 1965, *ApJ*, 142, 419
- Perera, T. A., Chapin, E. L., Austermann, J. E., et al. 2008, *MNRAS*, 391, 1227
- Pilbratt, G. L., Riedinger, J. R., Passvogel, T., et al. 2010, *A&A*, 518, L1
- Planck Collaboration, Ade, P. A. R., Aghanim, N., et al. 2013 XIII, *ArXiv e-prints*, arXiv:1303.5090
- . 2013 XVI, *ArXiv e-prints*, arXiv:1303.5076
- . 2013 XX, *ArXiv e-prints*, arXiv:1303.5080
- . 2013 XXIX, *ArXiv e-prints*, arXiv:1303.5089
- Poglitsch, A., Waelkens, C., Geis, N., et al. 2010, *A&A*, 518, L2
- Polletta, M. d. C., Wilkes, B. J., Siana, B., et al. 2006, *ApJ*, 642, 673
- Pope, A., Scott, D., Dickinson, M., et al. 2006, *MNRAS*, 370, 1185
- Pope, A., Chary, R.-R., Alexander, D. M., et al. 2008, *ApJ*, 675, 1171
- Press, W. H., & Schechter, P. 1974, *ApJ*, 187, 425
- Puget, J.-L., Abergel, A., Bernard, J.-P., et al. 1996, *A&A*, 308, L5
- Ranalli, P., Comastri, A., & Setti, G. 2003, *A&A*, 399, 39

- Ranalli, P., Comastri, A., Zamorani, G., et al. 2012, *A&A*, 542, A16
- Reese, E. D., Mroczkowski, T., Menanteau, F., et al. 2012, *ApJ*, 751, 12
- Refregier, A., & Loeb, A. 1997, *ApJ*, 478, 476
- Reynolds, J. 1994, A Revised Flux Scale for the AT Compact Array
- Riess, A. G., Macri, L., Casertano, S., et al. 2011, *ApJ*, 732, 129
- Roseboom, I. G., Ivison, R. J., Greve, T. R., et al. 2012, *MNRAS*, 419, 2758
- Rowan-Robinson, M. 2009, *MNRAS*, 394, 117
- Ruan, J. J., Quinn, T. R., & Babul, A. 2013, *MNRAS*, 432, 3508
- Rybicki, G. B., & Lightman, A. P. 1979, *Radiative processes in astrophysics* (Wiley-Interscience)
- Salpeter, E. E. 1955, *ApJ*, 121, 161
- Sarazin, C. L. 1988, *X-ray emission from clusters of galaxies* (Cambridge University Press)
- Sault, R. J., Teuben, P. J., & Wright, M. C. H. 1995, in *Astronomical Society of the Pacific Conference Series*, Vol. 77, *Astronomical Data Analysis Software and Systems IV*, ed. R. A. Shaw, H. E. Payne, & J. J. E. Hayes, 433
- Sayers, J., Czakon, N. G., Mantz, A., et al. 2013, *ApJ*, 768, 177
- Schechter, P. 1976, *ApJ*, 203, 297
- Schinnerer, E., Smolčić, V., Carilli, C. L., et al. 2007, *ApJS*, 172, 46
- Schmidt, M. 1959, *ApJ*, 129, 243

- Schnitzeler, D., Banfield, J., Emonts, B., et al. 2011, Calibrating linear polarization data at 16 cm with ATCA/CABB
- Scott, D., & Tout, C. A. 1989, MNRAS, 241, 109
- Scott, K. S., Austermann, J. E., Perera, T. A., et al. 2008, MNRAS, 385, 2225
- Scott, K. S., Yun, M. S., Wilson, G. W., et al. 2010, MNRAS, 405, 2260
- Scott, S. E., Dunlop, J. S., & Serjeant, S. 2006, MNRAS, 370, 1057
- Scoville, N., Aussel, H., Benson, A., et al. 2007, ApJS, 172, 150
- Scoville, N. Z., Sargent, A. I., Sanders, D. B., & Soifer, B. T. 1991, ApJL, 366, L5
- Sehgal, N., Trac, H., Acquaviva, V., et al. 2011, ApJ, 732, 44
- Serjeant, S., Dunlop, J. S., Mann, R. G., et al. 2003, MNRAS, 344, 887
- Sharon, C. E., Baker, A. J., Harris, A. I., & Thomson, A. P. 2013, ApJ, 765, 6
- Sifón, C., Menanteau, F., Hasselfield, M., et al. 2013, ApJ, in press, arXiv:1201.0991
- Siringo, G., Kreysa, E., Kovács, A., et al. 2009, A&A, 497, 945
- Smail, I., Ivison, R. J., & Blain, A. W. 1997, ApJL, 490, L5
- Smith, A. J., Wang, L., Oliver, S. J., et al. 2012, MNRAS, 419, 377
- Soifer, B. T., Neugebauer, G., Helou, G., et al. 1984, ApJL, 283, L1
- Springel, V., White, S. D. M., Jenkins, A., et al. 2005, Nature, 435, 629
- Stark, A. A., Gammie, C. F., Wilson, R. W., et al. 1992, ApJS, 79, 77
- Strazzullo, V., Pannella, M., Owen, F. N., et al. 2010, ApJ, 714, 1305
- Sunyaev, R. A., & Zeldovich, Y. B. 1970, Astrophysics and Space Science, 7, 20

- . 1972, *Comments on Astrophysics and Space Physics*, 4, 173
- Tacconi, L. J., Neri, R., Chapman, S. C., et al. 2006, *ApJ*, 640, 228
- Tielens, A. G. G. M. 2005, *The Physics and Chemistry of the Interstellar Medium* (Cambridge University Press)
- Toomre, A., & Toomre, J. 1972, *ApJ*, 178, 623
- Tran, Q. D., Lutz, D., Genzel, R., et al. 2001, *ApJ*, 552, 527
- Treister, E., Schawinski, K., Volonteri, M., Natarajan, P., & Gawiser, E. 2011, *Nature*, 474, 356
- Tucker, W., Blanco, P., Rappoport, S., et al. 1998, *ApJL*, 496, L5
- Urry, C. M., & Padovani, P. 1995, *PASP*, 107, 803
- Valiante, E., Lutz, D., Sturm, E., Genzel, R., & Chapin, E. L. 2009, *ApJ*, 701, 1814
- Valiante, E., Lutz, D., Sturm, E., et al. 2007, *ApJ*, 660, 1060
- Valiante, E., Ade, P. A. R., Bock, J. J., et al. 2010, *ApJS*, 191, 222
- van Weeren, R. J., Brüggen, M., Röttgering, H. J. A., & Hoeft, M. 2011a, *MNRAS*, 418, 230
- van Weeren, R. J., Hoeft, M., Röttgering, H. J. A., et al. 2011b, *A&A*, 528, A38
- van Weeren, R. J., Röttgering, H. J. A., Brüggen, M., & Cohen, A. 2009, *A&A*, 505, 991
- van Weeren, R. J., Röttgering, H. J. A., Brüggen, M., & Hoeft, M. 2010, *Science*, 330, 347
- Vanderlinde, K., Crawford, T. M., de Haan, T., et al. 2010, *ApJ*, 722, 1180

- Vattakunnel, S., Tozzi, P., Matteucci, F., et al. 2012, MNRAS, 420, 2190
- Veilleux, S., Kim, D.-C., & Sanders, D. B. 2002, ApJS, 143, 315
- Vikhlinin, A., Kravtsov, A., Forman, W., et al. 2006, ApJ, 640, 691
- Voss, H., Bertoldi, F., Carilli, C., et al. 2006, A&A, 448, 823
- Wake, D. A., Croom, S. M., Sadler, E. M., & Johnston, H. M. 2008, MNRAS, 391, 1674
- Wardle, J. F. C., & Kronberg, P. P. 1974, ApJ, 194, 249
- Wardlow, J. L., Smail, I., Coppin, K. E. K., et al. 2011, MNRAS, 415, 1479
- Wei, A., Kovács, A., Coppin, K., et al. 2009, ApJ, 707, 1201
- Weisskopf, M. C., O’dell, S. L., & van Speybroeck, L. P. 1996, in Society of Photo-Optical Instrumentation Engineers (SPIE) Conference Series, ed. R. B. Hoover & A. B. Walker, Vol. 2805, 2–7
- Wik, D. R., Sarazin, C. L., Ricker, P. M., & Randall, S. W. 2008, ApJ, 680, 17
- Wilkes, B. J., Kilgard, R., Kim, D.-W., et al. 2009, ApJS, 185, 433
- Williams, C. C., Giavalisco, M., Porciani, C., et al. 2011, ApJ, 733, 92
- Williamson, R., Benson, B. A., High, F. W., et al. 2011, ApJ, 738, 139
- Wilson, W. E., Ferris, R. H., Axtens, P., et al. 2011, MNRAS, 416, 832
- Yaqoob, T. 2006, in IAU Symposium, Vol. 230, Populations of High Energy Sources in Galaxies, ed. E. J. A. Meurs & G. Fabbiano, 461–462
- Young, A. J., Wilson, A. S., & Shopbell, P. L. 2001, ApJ, 556, 6
- Yun, M. S., & Carilli, C. L. 2002, ApJ, 568, 88

Zeldovich, Y. B., & Sunyaev, R. A. 1969, *Astrophysics and Space Science*, 4, 301

Zemcov, M., Rex, M., Rawle, T. D., et al. 2010, *A&A*, 518, L16

Zemcov, M., Blain, A., Cooray, A., et al. 2013, *ApJL*, 769, L31

Zhang, Y.-Y., Böhringer, H., Finoguenov, A., et al. 2006, *A&A*, 456, 55